Luminescent Nanocrystals

Line broadening and formation mechanisms

Johanna C. van der Bok

Luminescent Nanocrystals

Line broadening and formation mechanisms

PhD thesis, Utrecht University
Luminescent Nanocrystals: line broadening and formation mechanisms
Johanna C. van der Bok, 2023

Printed by Proefschriftenmaken.nl
ISBN 978-94-6473-137-8

Cover: composition of data and schematically visualized nanocrystals

Luminescent Nanocrystals

line broadening and formation mechanisms

Luminescente Nanokristallen

Lijnverbreding en vormingsmechanismen

(met een samenvatting in het Nederlands)

Proefschrift

ter verkrijging van de graad van doctor aan de Universiteit Utrecht op gezag van de rector magnificus, prof.dr. H.R.B.M. Kummeling, ingevolge het besluit van het college voor promoties in het openbaar te verdedigen op

maandag 3 juli 2023 des middags te 14.15 uur

door

Johanna Cornelia van der Bok

geboren op 14 maart 1991 te Dirksland

Promotoren:
Prof. dr. A. Meijerink
Prof. dr. D.A.M. Vanmaekelbergh

Dit proefschrift werd mogelijk gemaakt met financiële ondersteuning van de Nederlandse Organisatie voor Wettenschappelijk Onderzoek (NWO) met het project genaamd 'Superfical Superstructures: Control of Colloidal Ordering at Interfaces' (projectnummer 718.015.002).

Table of contents

Chapter 1

Introduction

1.1 Introduction

Nanomaterials are an exciting class of materials that hold promise for a myriad of applications. The strength of nanomaterials lies in the ability to tune their optical, electronic, or magnetic properties by simply adjusting their size. For example, materials with optical tunability are essential for creating high-quality LCDs.[1] Additionally, the small dimensions and relatively high surface area of nanomaterials can be utilized in catalysis.[2] The use of nanoparticles (NPs) is not limited to these examples but spans a wide range of fields. Recent application-based examples of research on nanomaterials include the use of NPs in IR-photodetectors to lower the fabrication cost and allow for detectors that do not require challenging low-temperature operating conditions,[3] incorporation of NPs in rechargeable batteries to increase the energy density, withstand volume changes upon charging and allow the use of sodium ions instead of lithium ions,[4,5] utilizing NPs as luminophores for luminescent solar concentrators to establish transparent solar cell elements and thereby transform windows, next to rooftops, in energy harvesting surfaces.[6] Lastly, research on NPs is also conducted in the medical field for imaging and targeted drug delivery.[7]

The broad usability of NPs has resulted in the synthesis of a wide variety of nanomaterials. This thesis will focus on two types of nanomaterials: cadmium-based semiconductor NPs and $NaYF_4$ NPs doped with rare earths. For both materials, the optical properties and NP formation mechanism make them intriguing. An in-depth understanding of the formation mechanism is necessary to improve the optical performance of these materials. The origin of their fascinating optical properties and use in applications differ between these two materials. The semiconductor NPs exhibit size-dependent optical properties, whereas the $NaYF_4$ NPs serve as a host material for trivalent lanthanide ions and have largely size-independent optical properties. The following sections discuss these two materials and their applications separately.

1.1 Cadmium-based semiconductor NPs

Semiconductor NPs receive special attention because the bandgap, and thereby the wavelength of absorbed and emitted light, can be tuned by changing the dimensions of a NP. For instance, the light emitted by CdSe quantum dots (QDs) can be changed from blue to red by increasing the NP size from two to six nm. The size dependence of the bandgap is caused by the spatial confinement of the charge carriers (electron and hole) and is called the quantum confinement effect.

Next to the size-dependent optical properties, the emission of these QDs is also color pure, meaning the emission linewidth is narrow. This property makes semiconductor QDs that emit visible light valuable materials for lighting and display applications. The most widely used phosphors to convert blue LEDs to white LEDs, $Y_3Al_5O_{12}:Ce^{3+}$ (YAG:Ce^{3+}) and $CaAlSiN_3:Eu^{2+}$ (CASN:Eu^{2+}), have broad emission bands ranging from ~475 nm to beyond 700 nm, as is shown in Figure 1.1A. This figure also displays the human eye sensitivity, which drops significantly for wavelengths longer than 630 nm.[8] The conventional material for white LEDs thus partly emits light to which the human eye is not sensitive, lowering the efficiency of LEDs. The red emitter should have a narrow emission linewidth to ensure high efficiency and simultaneously generate pleasant warm, white-LED light. Red emitting QDs, which are inherently more color pure than most conventional LED phosphors, can thus be used to enhance the efficiency of white LEDs.

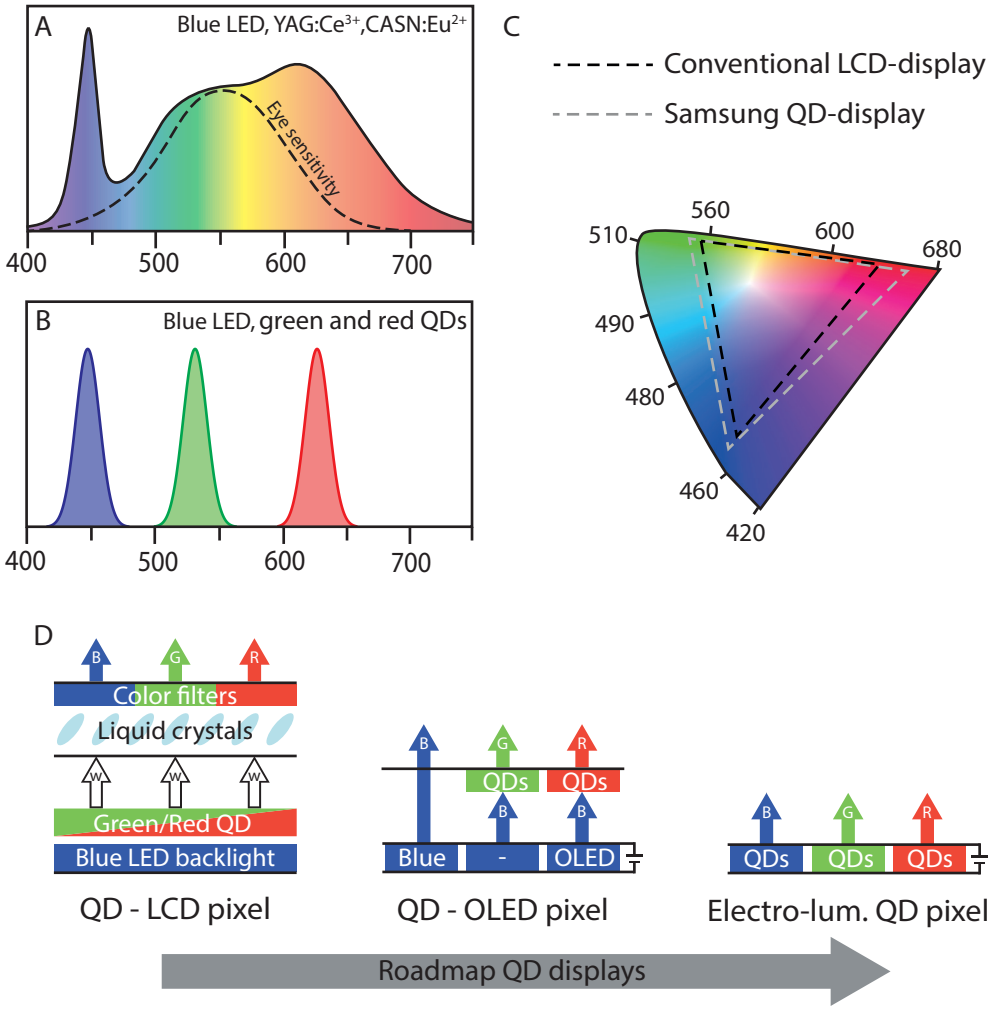

Figure 1.1 (A) Emission spectrum of a white LED with a sharp feature around 450 nm from the blue LED and a broad emission band of the YAG:Ce^{3+} and CASN:Eu^{2+} phosphors, which convert part of the blue light of the LED to green and red light. The dashed line indicates the human eye sensitivity.[8] **(B)** The spectrum of a QD-display with a blue LED and green- and red-emitting QDs. **(C)** The color gamut for QD displays (gray dashed) is larger than for displays using conventional materials and color filters (black dashed).[9] **(D)** Road map for QD displays.[10] From left to right: green and red QDs convert part of blue LED backlight in LCD screens, green or red QDs are used in an OLED subpixel, QDs are directly used to generate blue, green, and red subpixels in electro-luminescent QD displays.

Not only narrow-band red emitters but also narrow-band blue and green emitters are needed for displays to generate color pure light in each display pixel (Figure 1.1B). Other colors are realized by adjusting the relative intensities of red, blue, and green. The colors visible to the human eye are represented by the CIE chromaticity diagram (Figure 1.1C). The locus represents single wavelengths, and the enclosed colors within a triangle formed by any three points on the color map indicate which colors can be generated by mixing these components. This is referred to as the color gamut. The larger the color gamut, the more lifelike and vibrant the viewer will perceive the display. The difference in color gamut between a conventional display without narrow-band emitters and a QD display by Samsung is shown in Figure 1.1C by the black-dashed and gray-dashed triangles, respectively.[9] The narrow-band emission of the QDs results in a larger color gamut.

Although QD displays are already on the market, there is a continuous endeavor to enhance the performance by reducing energy consumption, extending the color gamut, fabricating thinner displays, and allowing other functionalities such as a flexible display.[11] Figure 1.1D presents the roadmap of the pixel's architecture within a QD display.[10] The first QD displays were LCD screens with a blue-LED backlight and a film with embedded green and red QDs to generate white light. The blue, green, and red subpixels were created using liquid crystals and color filters. More recently, the QDs were enclosed in a polymer matrix on top of the liquid crystal layer, making color filters redundant. In 2022, multiple companies released QD-OLED screens. In these screens, the subpixels consist of blue organic LEDs (OLEDs) combined with green or red QDs. The OLEDs, and thereby the subpixels, can be switched on or off by applying a voltage, which can be more efficient than using a backlight and makes the (sub)pixel completely black when turned off. This provides a superior contrast in comparison with LCDs, where still some light can leak out from pixels that are turned off.

The fabrication cost of OLEDs is high because it requires vacuum deposition with high precision. QDs can be deposited with solution-based processes, which is much less costly.[10] Hence, the ultimate goal is to create electro-luminescent QD displays. In these displays, only QDs are used for the subpixels while retaining the ability to control the subpixel by applying a voltage.

As the development of displays and lamps is still ongoing, it is key to understand and map the properties of semiconductor NPs and control the growth of these NPs. As mentioned, the emission linewidth of the emitter should be small, which is the case for most semiconductor NCs. However, the operating temperature in displays and lamps can range from 60 ^{0}C to 150 ^{0}C, and the local temperature affects both the linewidth and the emission wavelength. Much is still unknown about this temperature dependence, especially at elevated temperatures. Furthermore, more and more types of NCs are synthesized with different compositions, shapes, and properties. CdSe nanoplatelets are particularly intriguing because they exhibit an even narrower emission linewidth than CdSe QDs. However, the formation mechanism of these nanoplatelets is not fully understood yet. Therefore, this thesis includes studies on the temperature-dependent luminescence line broadening and formation of CdSe nanoplatelets.

1.2 $NaYF_4$ NPs doped with rare earths

The second type of material this thesis focuses on is $NaYF_4$ NPs doped with rare earth ions (the group of elements consisting of lanthanides, yttrium, and scandium). The luminescence of these materials is not inherent to the material's band structure and size, as for semiconductor NPs,

but stems from individual luminescent centers: trivalent lanthanide ions. $NaYF_4$ is an insulator and serves as a host material for these lanthanides because of its high chemical stability and low phonon energies. The latter reduces the probability of non-radiative decay of excited lanthanide ions.

The luminescence of lanthanide ions usually originates from intraconfigurational f-f transitions, that is, the redistribution of the electrons over the 4f orbitals without a change in the $4f^n$ electron configuration. The electrons in the 4f orbitals can be distributed in $\binom{14}{n}$ ways, where n is the electron population of the 4f orbitals ($n = 0 - 14$). The number of distributions becomes enormous, especially for lanthanide ions in the middle of the f-block of the periodic table, and results in many possible states. These states differ in energy due to varying Coulombic electron-electron interactions and spin-orbit coupling. The states are labeled with a term symbol $^{2S+1}L_J$, which gives the total orbital angular momentum L, the total spin angular momentum S, and the total angular momentum J of the state.

The f-block trivalent ions have useful properties for applications; first, the energies of the states are hardly affected by the surroundings because the 4f-orbitals have a smaller radial extension than the 5p and 5s orbitals. The 4f orbitals are thus shielded from the surroundings, resulting in host-independent luminescence and long lifetimes of the excited states. Due to the host independence, an overview of the energy levels of trivalent lanthanides can be given, called the Dieke diagram, which is valid in any type of host lattice. Figure 1.2A shows the energy levels and term symbols of Yb^{3+} ($4f^{13}$) and the lowest energy levels of Er^{3+} ($4f^{11}$).

Second, f-f transitions have sharp absorption and emission features because the f-orbitals do not participate in the chemical bonding with the surrounding anions. Therefore, there is no change in the average bond length for excited state ions compared to the ground state, and consequently, only transitions between the zero vibration states occur (see also section 2.2.4 and Figure 2.7A).

Third, the long lifetimes and multiple occurrences of similar spacing between the energy levels in the Dieke diagram make materials doped or co-doped with lanthanides efficient upconversion materials. Upconversion materials convert two low-energy photons to one high-energy photon. In $NaYF_4$ co-doped with Yb^{3+} and Er^{3+} (Figures 1.2A and 1.2B), two Yb^{3+} ions absorb a near-infrared (NIR) photon (dark red arrows). This energy is transferred to a nearby Er^{3+} ion, thereby exciting the ion to the $^4F_{7/2}$ state (gray arrows). After fast initial non-radiative decay from the $^4F_{7/2}$ state to the nearby $^2H_{11/2}$, $^4S_{3/2}$, and $^4F_{9/2}$ states, the Er^{3+} ion decays back to the ground state from one of the excited states by emitting a visible (Vis) photon (green or red arrow).

An important application for upconversion NPs is deep tissue imaging. The optimal wavelength window for fluorescence imaging is 700 to 1000 nm because hemoglobin, water, and lipids absorb the least in this region.[12] NIR thus travels deeper into the specimen than UV, Vis, or IR light. Additionally, NIR light experiences less light scattering than UV or Vis light. NIR dyes can be used for deep tissue imaging but have poor stability.[13] Upconversion materials are an excellent replacement for dyes because of their high stability and almost zero-background signal, as there is no NIR-to-Vis upconversion in tissue. Absorption/scattering of the emitted upconversion emission can be minimized by enhancing the red $^4F_{9/2}$ emission because its nearer to the optimal wavelength window for imaging.

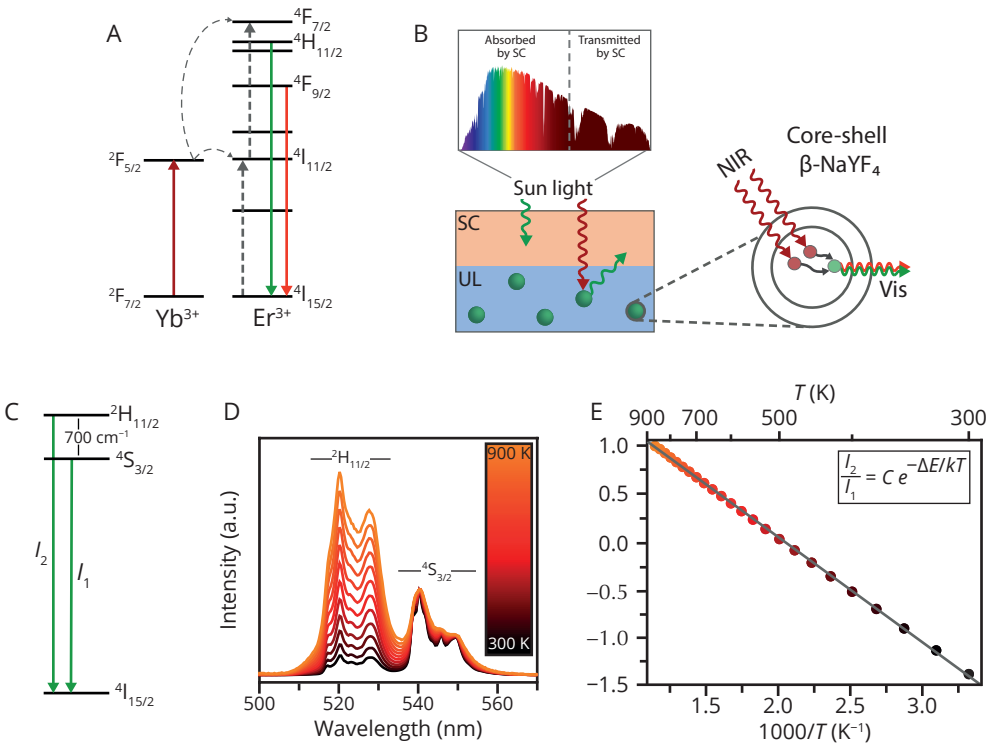

Figure 1.2 (A) Upconversion mechanism of Yb^{3+} and Er^{3+}, converting NIR light (dark red) to visible light (green and red arrow). **(B)** core-shell β-$NaYF_4$:Yb^{3+},Er^{3+} NPs can be used to enhance the efficiency of a solar cell. The transmitted NIR light by the solar cell (SC) is converted in the upconversion layer (UL) beneath the solar to visible light, which can then be absorbed by the solar cell. **(C and D)** The Boltzmann equilibrium between the closely packed excited states, $^2H_{11/2}$ and $^4S_{3/2}$, results in a temperature-dependent relative emission intensity from these states to the $^4I_{15/2}$ ground state of Er^{3+}. The temperature can be mapped using a calibration curve **(E)** constructed from the data in D. D and E have been duplicated with permission from ref. [16].

Another application for upconversion NPs is the enhancement of a solar cell's efficiency (Figure 1.2B). Part of the solar spectrum cannot be absorbed by semiconductors used in a solar cell because the energy of the photons is too low to promote electrons over the bandgap. Therefore, part of the solar spectrum is transmitted, and the energy is lost. A layer with upconversion NPs underneath the solar cell can enhance the performance by absorbing these transmitted photons and converting these to photons of higher energy, which the semiconductor in the solar cell can absorb. One of the most efficient upconverters is core-shell β-$NaYF_4$ NPs co-doped with ytterbium and erbium (Figure 1.2B).[14] The core-shell structure reduces losses by non-radiative decay of ions close to the NP surface.

Lastly, $NaYF_4$:Yb^{3+},Er^{3+} NPs can be used as luminescent nanothermometers. The intensity ratio of emission from two closely spaced energy levels can be used to determine the temperature of the local surroundings. Thermal energy is sufficient to ensure fast relaxation between two

closely spaced energy levels, resulting in a Boltzmann equilibrium between these states. Hence, the relative population, and thereby photoluminescence intensity, of the states depends on the temperature. The $^4S_{3/2}$ and $^2H_{11/2}$ states of Er^{3+} are good examples (Figure 2C); The temperature dependence of the relative emission intensity for these two states is shown in Figure 2D. From these measurements, a calibration curve can be constructed (Figure 2E), which can be used to extract the temperature *in situ* during experiments. For instance, $NaYF_4$:Yb^{3+},Er^{3+} NPs can be added to a catalytic or microfluidic reactor to map the temperature with a high resolution by evaluating the relative intensity of emission from the $^4S_{3/2}$ and $^4H_{11/2}$ states. Due to the small size of the NPs, they can also diffuse into a porous material, giving better insight into the temperature distribution in porous catalysts.[15]

1.3 Motivation and outline

Cd-based semiconductor NPs and $NaYF_4$ NPs can and are used for various applications as set out above. The NP properties should be well-controlled to ensure a high performance. This control can only be achieved if their luminescence properties and formation mechanism are well-understood. In this thesis, the formation mechanism of CdSe NPLs and β-$NaYF_4$ will be discussed, as well as the temperature-dependent luminescence properties of cadmium-based NPs. The relevant theoretical background on luminescence, NP nucleation and growth, and NP characterization techniques are discussed in Chapter 2.

For semiconductor NPs in LEDs and displays, narrow emission bands are preferred. The linewidth is affected by the composition, size variation, and temperature due to coupling with lattice vibrations (exciton-phonon coupling). The strength of this coupling and, thereby, the temperature dependence of the photoluminescence needs to be investigated, considering that displays and lamps operate at elevated temperatures.

As was briefly mentioned above, CdSe NPLs have a superior narrow emission linewidth compared to CdSe QDs. Typically, core NPs are encapsulated with a larger band gap semiconductor to enhance the luminescence, upon which the desired narrow emission linewidth of the core NPLs is lost. The loss of the desired linewidth, as well as the overall temperature dependence of the linewidth and spectral shift for various cadmium-based NPs in the high-temperature regime that is relevant for applications in light-emitting devices, are the topic of Chapter 3. In addition, the linewidth, spectral shift, tuneability, and stability are compared to conventional phosphors used in white LEDs.

The mechanism behind the formation of CdSe NPLs and β-$NaYF_4$ NPs has been the topic of various studies but is not yet understood. The formation of CdSe NPLs with atomically flat thickness is intriguing because anisotropic growth is unexpected for a material with a cubic crystal structure. Acetate has been shown to play a pivotal role in the formation of NPLs. In Chapter 4, the NPL formation is investigated with *in situ* absorption and small-angle X-ray scattering using a specially designed setup, mimicking realistic laboratory synthesis conditions. The experiments show that the formation of NPLs is not solely due to the presence of an acetate salt, but both acetate and myristate ligands play a crucial role in the growth kinetics and formation of NPLs with large lateral dimensions. However, NPLs with small lateral dimensions are shown to be also formed without adding an acetate salt.

Chapter 5 discusses the formation of monodisperse hexagonal β-phase $NaYF_4$ NPs from smaller nanometer-sized cubic α-phase $NaYF_4$ NPs. This process was monitored *in situ* using wide-angle X-ray scattering (WAXS) to probe the crystal structure of the NPs and small-angle X-ray scattering (SAXS) to extract the size and concentration of the different types of NPs over time. Previous studies proposed that β-$NaYF_4$ NPs nucleate and grow as α-$NaYF_4$ NPs start to dissolve, or that a crystal structure change occurs in a subset of the α-$NaYF_4$ NPs to the β-phase. After that, the β-$NaYF_4$ NPs continue to grow at the expense of α-$NaYF_4$.[17, 18] The *in situ* SAXS and WAXS data in Chapter 5 combined with TEM analysis show that both large α-phase particles as β-phase are present in the reaction mixture. This reveals that there is not only growth of β-$NaYF_4$ NCs but also of α-$NaYF_4$ NCs while smaller α-$NaYF_4$ NCs dissolve, giving rise to a bimodal particle size distribution. The phase transition to the β-phase does not initiate the observed bimodal distribution of particle sizes. With simulations, we show that a narrowing of the size distribution of NCs can originate from a distribution of growth rates for the NCs present in the reaction mixture. This distribution of growth rates also gives rise to a bimodal distribution of the NCs sizes during the reaction and, finally, one distribution of sizes with a low polydispersity, as observed with the SAXS measurements.

References

1. Supran, G. J.; Shirasaki, Y.; Song, K. W.; Caruge, J.-M.; Kazlas, P. T.; Coe-Sullivan, S.; Andrew, T. L.; Bawendi, M. G.; Bulović, V., QLEDs for displays and solid-state lighting. *MRS Bulletin* **2013,** *38* (9), 703-711.
2. Astruc, D., Introduction: Nanoparticles in Catalysis. *Chemical Reviews* **2020,** *120* (2), 461-463.
3. Wang, F.; Zhang, Y.; Gao, Y.; Luo, P.; Su, J.; Han, W.; Liu, K.; Li, H.; Zhai, T., 2D Metal Chalcogenides for IR Photodetection. *Small* **2019,** *15* (30), 1901347.
4. Liu, J.; Wang, S.; Kravchyk, K.; Ibáñez, M.; Krumeich, F.; Widmer, R.; Nasiou, D.; Meyns, M.; Llorca, J.; Arbiol, J.; Kovalenko, M. V.; Cabot, A., SnP nanocrystals as anode materials for Na-ion batteries. *Journal of Materials Chemistry A* **2018,** *6* (23), 10958-10966.
5. Park, M.-G.; Lee, D.-H.; Jung, H.; Choi, J.-H.; Park, C.-M., Sn-Based Nanocomposite for Li-Ion Battery Anode with High Energy Density, Rate Capability, and Reversibility. *ACS Nano* **2018,** *12* (3), 2955-2967.
6. Moraitis, P.; Schropp, R. E. I.; van Sark, W. G. J. H. M., Nanoparticles for Luminescent Solar Concentrators - A review. *Optical Materials* **2018,** *84*, 636-645.
7. Wahajuddin; Arora, Superparamagnetic iron oxide nanoparticles: magnetic nanoplatforms as drug carriers. *International Journal of Nanomedicine* **2012**, 3445.
8. Vos, J., Colorimetric and Photometric Properties of a 2 Degree Fundamental Observer. *Color Research & Application* **2007,** *3*, 125-128.
9. Samsung Quantum dot, why QD display? https://www.samsungdisplay.com/eng/tech/quantum-dot.jsp (accessed 16 July 2022).
10. Ishida, T.; Nakanishi, Y.; Izumi, M.; Berryman-Bousquet, V., How Will Quantum Dots Enable Next-Gen Display Technologies? *Information Display* **2020,** *36* (6), 14-18.
11. Panfil, Y.; Oded, M.; Waiskopf, N.; Banin, U., *Material Challenges for Colloidal Quantum Nanostructures in Next Generation Displays*. 2020.
12. Wu, X.; Chen, G.; Shen, J.; Li, Z.; Zhang, Y.; Han, G., Upconversion Nanoparticles: A Versatile Solution to Multiscale Biological Imaging. *Bioconjugate Chemistry* **2015,** *26* (2), 166-175.
13. Song, C.; Zhang, S.; Zhou, Q.; Hai, H.; Zhao, D.; Hui, Y., Upconversion nanoparticles for bioimaging. *Nanotechnology Reviews* **2017,** *6* (2), 233-242.
14. Homann, C.; Krukewitt, L.; Frenzel, F.; Grauel, B.; Würth, C.; Resch-Genger, U.; Haase, M., NaYF 4 :Yb,Er/NaYF 4 Core/Shell Nanocrystals with High Upconversion Luminescence Quantum Yield. *Angewandte Chemie International Edition* **2018,** *57* (28), 8765-8769.

15. Geitenbeek, R. G.; Nieuwelink, A.-E.; Jacobs, T. S.; Salzmann, B. B. V.; Goetze, J.; Meijerink, A.; Weckhuysen, B. M., In Situ Luminescence Thermometry To Locally Measure Temperature Gradients during Catalytic Reactions. *ACS Catalysis* **2018,** *8* (3), 2397-2401.
16. Geitenbeek, R. G. Luminescence Thermometry, Fundamentals and Applications. Utrecht University, Utrecht, 2018.
17. May, P. B.; Suter, J. D.; May, P. S.; Berry, M. T., The Dynamics of Nanoparticle Growth and Phase Change During Synthesis of β-NaYF4. *The Journal of Physical Chemistry C* **2016,** *120* (17), 9482-9489.
18. Voss, B.; Haase, M., Intrinsic Focusing of the Particle Size Distribution in Colloids Containing Nanocrystals of Two Different Crystal Phases. *ACS Nano* **2013,** *7* (12), 11242-11254.

Chapter 2

Theoretical background

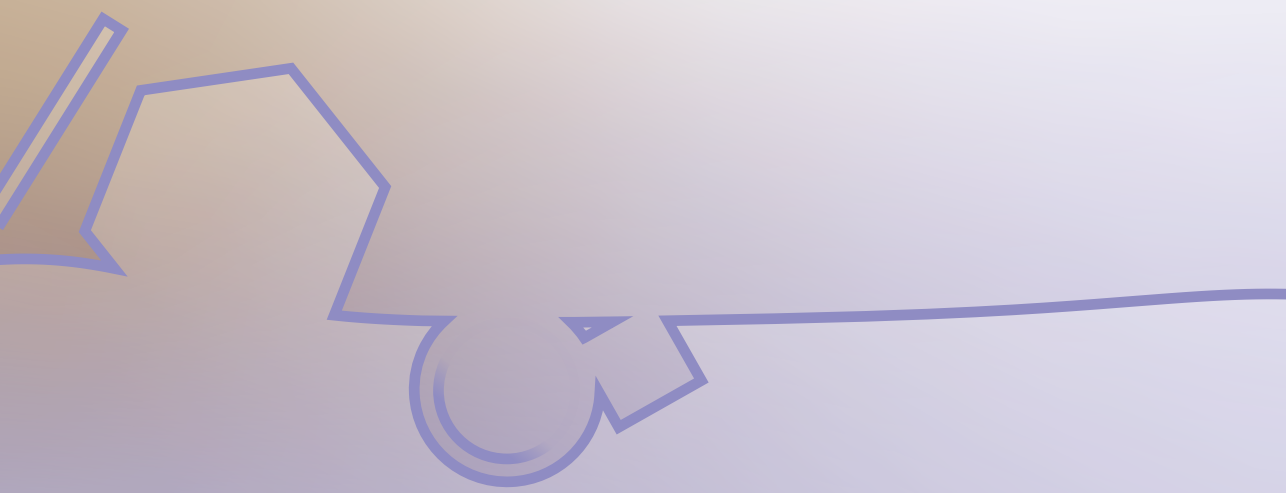

2.1 Versatility of nanomaterials

Nanomaterials form a rapidly growing class of materials when it comes to research and applications. They are classified as materials with at least one dimension smaller than 100 nm. Their common feature is that they behave differently than their bulk counterpart. Nanoparticles (NPs) have been used, often unknowingly, for centuries. For example, to make stained-glass windows or intricate patterns on ceramics.[1, 2] An outstanding example is the Lycurgus cup dating from the 4th century. Gold-silver alloy NPs in the cup make the glass dichroic, changing its color from opaque green to translucent ruby-red depending on the lighting conditions.[3] An entirely different accidental use of NPs in history are Fe_3C nanowires and carbon nanotubes in Damascus blades.[4] Impurities in the ingredients facilitate the formation of these nanowires and nanotubes in steel, producing blades with exceptionally sharp edges and strength.

These diverse examples underline that the class of nanomaterials is immensely versatile. NPs can have various chemical compositions and can be used for widely different physical properties. Their common ground and what makes them so exciting is the ability to tune these physical properties by adjusting their size. Apart from this, nanomaterials generally act differently due to the large surface-to-volume ratio compared to bulk. Surface atoms differ from the inner atoms of a particle. They have fewer neighbors and, therefore, unsaturated chemical bonds. As a result, surface atoms are more reactive and make nanomaterials more suitable for, amongst others, catalytic reactions.[5] Moreover, reactions occur at the surface; thus, a higher surface-to-volume ratio will be beneficial for accelerating chemical reactions. Their small size also ensures that nanoparticles can diffuse into porous materials. For example, $NaYF_4$ doped with lanthanides can potentially be used as nanothermometers to map the temperature profile in a porous catalyst.[6]

The tunability of their physical properties is what makes nanomaterials truly compelling. Semiconductors possess size-dependent properties on the nanoscale. The color of absorbed and emitted light can be tuned by changing the size of a semiconductor NP. This is referred to as the quantum confinement effect and makes these materials especially appealing for displays,[7] lighting applications,[8, 9] and detectors.[10]

The optical properties of metal NPs can also be tuned. Metal NPs, like gold and silver NPs, absorb and scatter light differently depending on their size. The free electrons resonate with the oscillating electromagnetic field of light, called surface plasmon resonance.[11] The variation in the coupling strength through the electromagnetic spectrum depends on the NP's size and shape and is also influenced by the surroundings. For example, the attachment of biosystems to metal NPs can be detected by spectral shifts of the absorption maxima. These NPs can thus be used for chemical and biochemical sensing.[12]

In some cases, even magnetic properties can be changed. Bulk ferromagnetic materials, *e.g.*, iron oxide, have multiple magnetic domains with different magnetization directions. Ferromagnetic NPs exhibit a single magnetic domain when smaller than ~100 nm.[13] These NPs are more resilient to demagnetization by an external magnetic field than bulk ferromagnetic materials.[14] When the particles are made even smaller (10 – 20 nm), the magnetization direction of this single domain will fluctuate rapidly due to temperature, resulting in no net magnetization when no magnetic field is applied.[13] These superparamagnetic NPs have a stronger and more rapid response to an applied magnetic field than larger crystals. Superparamagnetic NPs do not aggregate as larger crystals do in the absence of a magnetic field because they preserve no

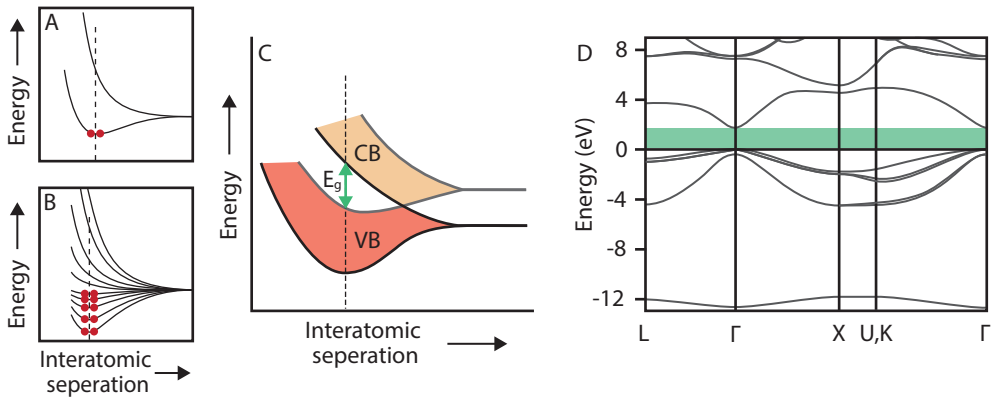

Figure 2.1 Molecular energy levels as a function of the interatomic separation for a system consisting of two atoms **(A)**, multiple atoms **(B)**, and many atoms **(C)**. Occupied energy levels are indicated with red dots (electron pairs). In C, the energy levels form energy bands with a continuum of energy levels. The valence band (VB) occupied with electrons and the empty conduction band (CB) are indicated in red and yellow, respectively. The dashed line in A – C shows the equilibrium distance between the atoms. **(D)** Band structure of bulk zinc blende CdSe obtained from Tight binding calculations. The band gap between the VB and CB is indicated in green in C and D and corresponds to ~1.7 eV. Figures adapted from references [18, 19].

residual magnetic interaction upon removing the magnetic field.[15] Superparamagnetic particles are therefore more suitable as drug delivery vehicles as they offer better control over the NPs' aggregation by applying or removing a magnetic field.[15, 16]

To summarize, different physical properties can be tuned depending on the NPs' composition. As a result, NPs can be used in many applications and fields of research. This thesis will focus on two topics related to NPs: the formation mechanism of CdSe NPLs and $NaYF_4$ NPs, and the spectral line broadening of CdSe NPLs compared to other cadmium-based NPs. This chapter will provide a theoretical background to be able to grasp these topics better. First, the optical properties of semiconductor NPs and the role of quantum confinement will be explained in more detail. The optical characteristic of CdSe QDs, NPLs, and heterostructures, as well as the cause of spectral line broadening, will be addressed. Next, the focus will shift to the theory of particle growth and (*in situ*) techniques to monitor the nucleation and growth of NPs, namely transmission electron microscopy, absorption spectroscopy, and X-ray scattering techniques.

2.2.1 Semiconductor band structure and the quantum confinement effect

Bulk semiconductors consist of at least ~10^7 atoms, considering an average density of ~10^{22} atoms/cm^3 for solids[17] and dimensions exceeding 100 nm. Whereas single atoms have discrete energy levels, the energy levels of large crystals cannot be individually distinguished due to the large number of atoms. This is illustrated in Figures 2.1A – C. The wavefunctions of valance electrons overlap when two atoms bind. Consequently, the atomic energy levels split into a bonding and an anti-bonding molecular energy level. The energy of these levels depends on the distance between the atoms (Figure 2.1A). The dashed lines in the figures give the equilibrium distance between the atoms. The red dots represent electrons and indicate populated energy

levels. When bigger clusters form consisting of N atoms, then the atomic energy levels split into N non-degenerate molecular levels (Figure 2.1B). For solids, the individual energy levels can no longer be distinguished. Energy bands are formed with a quasi-continuous density of states (DOS), as shown in Figure 2.1C.

The valence band (VB, red) is the highest occupied energy band, and the highest empty or partially occupied band is known as the conduction band (CB, yellow). These bands are separated by a band gap E_g, a region of forbidden energies for the electrons. The conductive properties of solids depend on the occupation of the energy bands. Materials with an empty CB, separated from the VB by a band gap, cannot conduct electricity. These materials are insulators unless the band gap is small enough to allow the promotion of an electron to the empty CB, for example, by means of heat, applying a current, or illuminating the material with light. These materials are appropriately named semiconductors.

Figure 2.1C gives a simple depiction of the energy band formation in solids. This model provides no insight into band structure differences between crystal structures because the crystal periodicity is disregarded. The periodicity is accounted for by the nearly free-electron model. This model shows that the band gaps result from the periodic potential imposed on the electron wavefunctions by the periodic arrangement of ions in the crystal lattice.[20]

The electron wavefunctions in solids are propagating waves; hence, the probability of finding an electron is equal everywhere in the crystal. However, standing waves are obtained when the wave vector k is equal to $\frac{n\pi}{a}$, where a is the lattice constant. These wavefunctions have either a high electron density near the ions or in between the ions in the lattice. The electrons experience a reduced potential energy near the ions, resulting in a difference in energy for these two situations and the formation of a gap in the dispersion relation $E(k)$ at the Brillouin zone for $k = \frac{n\pi}{a}$.

A three-dimensional representation of the band structure of zinc blende CdSe is given in Figure 2.1D.[19] The x-axis corresponds to different directions in the first Brillouin zone and, likewise, different directions in the crystal in real space. The band gap above the VB is indicated in green. The figure shows that the direct band gap is present at the Γ-point (k = (0,0,0)) and corresponds to an energy E_g of 1.76 eV. Note that the band structure in Figure 2.1D results from Tight Binding calculations. In this model, the electrons are more strongly associated with their respective atom, and the overlap between the atomic orbitals is calculated.[21] This approximation more accurately represents the band structure for more covalently bound materials than the nearly free electron model.[18]

Absorption of light with an energy equal to, or higher than, E_g can excite an electron to the CB. Removing a negatively charged electron from the VB leaves a positively charged hole behind. The electron and hole attract each other by Coulomb forces and form a quasi-particle: an exciton. The average distance between the electron-hole pair, the spatial extension of the exciton, is called the exciton Bohr radius. The exciton Bohr radius is an intrinsic material constant for bulk materials. For semiconductors, the values range from a few to a hundred nanometers (*e.g.*, CdSe: 5.6 nm,[22] PbTe: 150 nm[23]).

Due to these relatively large values, a semiconductor nanocrystal can physically be made small enough that its size is similar to or smaller than the exciton Bohr radius. Once the size approaches the exciton Bohr radius, the exciton becomes confined (weak confinement regime).

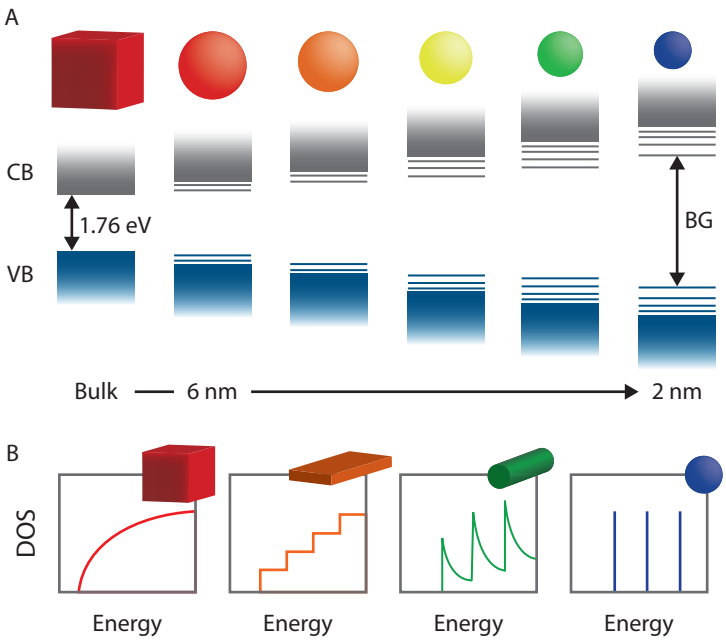

Figure 2.2 (A) Schematic representation of the quantum confinement effect. The band gap increases compared to bulk (CdSe: 1.76 eV)[24] when the size of the NC is decreased. Consequently, the emission wavelength of CdSe QDs can be adjusted from red to blue by changing the size from 6 to 2 nm. Additionally, discrete energy levels emerge at the edges of the valence band (VB) and the conduction band (CB). **(B)** The density of states (DOS) for bulk, nanoplatelets, nanorods, and quantum dots. The DOS for bulk is quasi-continues and scales with $E^{-1/2}$ at the band edges (red). Confinement in three dimensions results in discrete energy levels for QDs (blue and A). Charge carriers in nanoplatelets (orange) and nanorods (green) are confined in one and two dimensions, giving a stepwise and saw-like DOS, respectively. Figure adapted from reference [25].

When the size becomes (much) smaller than the exciton Bohr radius, we speak of the strong confinement regime. This confinement drastically alters the electronic structure compared to bulk. Figure 2.2A gives a schematic representation of the VB and CB and the effect of exciton confinement in three dimensions on the band structure. The size of the band gap increases when the particles become smaller. Furthermore, discrete energy levels appear at the edges of the VB and CB.

Theoretically, this change in band structure can be understood by solving the Schrödinger equations for a particle in an infinite spherical potential well. The electron or hole energy levels are given by equation 2.1, where $m_{e,h}$ are the effective masses of the electron or hole, R the radius of the nanocrystal, $\chi_{l,n}$ and the *n*th root of the spherical Bessel function of order *l*. *n* and *l* are both quantum numbers and have integer values.[26] The energies given by equation 2.1 are thus quantized.

$$E_{l,n}^{e,h} = \frac{\hbar^2 \chi_{l,n}^2}{2 m_{e,h} R^2} \tag{2.1}$$

The QDs, studied in this thesis, have a size smaller than the exciton Bohr radius and therefore fall in the strong confinement regime. In this regime, the confinement of the electron and hole can be treated separately because the confinement term dominates over the Coulomb interactions. The energy of the bandgap only needs to be slightly corrected for changes in the Coulomb interaction between the electron and the hole (E_c). The lowest energy transition is then given by equation 2.2 and is the sum of the fundamental bandgap (E_g, 1.76 eV for CdSe), the confinement energy of the lowest electron and hole states, and the Coulomb correction term E_c. The latter is equal to $\sim \frac{1.8e^2}{\varepsilon a}$ for the first excited state, where ε is the dielectric constant of the semiconductor.[27] Equation 2.2 indeed shows that the size of the bandgap is strongly size-dependent and becomes larger for QDs with smaller radii.

$$E = E_g + \frac{\hbar^2\pi^2}{2m_eR^2} + \frac{\hbar^2\pi^2}{2m_hR^2} - E_c \tag{2.2}$$

The expression in equation 2.1 means that the DOS is no longer quasi-continuous near the band edges. For bulk, the DOS at the edges scales with $E^{-1/2}$, whereas the DOS of QDs features discrete energy levels near the band edges. The exciton can also be confined in less than three dimensions. The first Cd-chalcogenide QDs were synthesized in a glass matrix, [28,29] but since the development of a synthesis method for colloidal CdSe QDs by Murray, Norris, and Bawendi,[30] a wide variety of semiconductor NP shapes have been fabricated. For example, nanoplatelets (NPLs)[31] and nanorods[32] for which the exciton is confined in only one or two dimensions, respectively. The DOS for these structures has a saw-like shape for rods and a stepwise shape for NPLs.[33] The DOS of bulk and NPs of different shapes are shown in Figure 2.2B. The optical properties of Cd-chalcogenide QDs and NPLs are the topic of chapters 3 and 4. Therefore, the electronic structure of these NPs and its relation to the absorption and emission spectra will be discussed in more detail in the following sections.

2.2.2 Optical characteristics of QDs and NPLs

Equations 2.1 and 2.2 give insight in the observed size-dependent bandgap and the discrete energy states of QDs. The equations only hold for band structures with simple parabolic dispersions relations ($E \propto k^2$). Only the bottom of the CB has this parabolic dispersion.[26] For calculating the energy states of QDs, the actual band structure should be considered. In Figure 2.3A, the band structure of zinc blende CdSe is shown in gray. We focus on the position of the direct band gap at the Γ point (Figure 2.1D). The figure shows that the VB consists of three sub-bands. The two sub-bands are degenerate at $k = 0$, but their dispersion differs for other k values due to a difference in effective mass. These two bands are called the heavy and light hole sub-bands and are both two-fold degenerate. The third sub-band is the spin-orbit split off sub-band and is also two-fold degenerate.

In a QD, these three valence sub-bands mix, and the VB and CB couple with each other for semiconductors with a small bandgap. Therefore, the expressions to calculate the electronic structure of semiconductor QDs are more advanced than those given in the previous section and are discussed in refs [26,34-36]. A schematic representation of the lowest hole and electron states in CdSe QDs are superimposed on the band structure in Figure 2.3A. The states are labeled nL_J, with n an integer number, L the orbital angular momentum (S, P, D, etc.), and J the total angu-

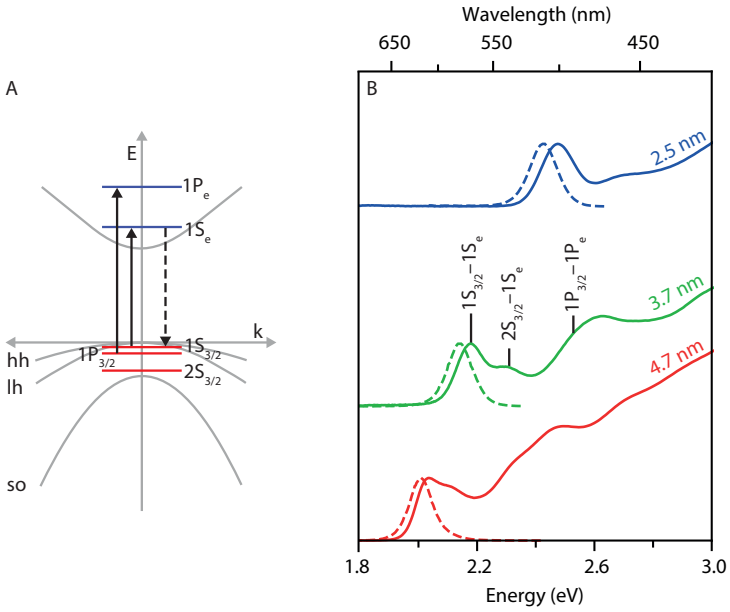

Figure 2.3 (A) Schematic representation of the bulk band structure at the Γ-point of a semiconductor with a zinc blende crystal structure (gray). The heavy hole sub-band (hh), light hole sub-band (lh), and the spin-orbit split off sub-band (so) are labeled. CB electron states and VB hole states of a QD are shown in blue and red. **(B)** Absorption (solid) and emission (dashed) spectra of CdSe QDs. The spectra shift to lower energies for quantum dots with larger diameters. A few transitions are labeled for the QDs with a 3.7 nm diameter.

lar momentum.[37] The hole states are spaced closer together than the electron states due to the contribution of the three valence sub-bands. CdSe is a wide bandgap semiconductor, therefore, coupling of the VB and CB can be neglected.[26]

In early research, Norris and Bawendi assigned the transitions in excitation spectra of CdSe QDs for a large variety of sizes.[37] This work showed the agreement between the theoretical model by Efros *et al.*[22] and experimental data on high-quality colloidal CdSe QDs. In Figure 2.3B, absorption and emission spectra of differently sized QDs are plotted. As an example, a few dipole-allowed transitions (S–S and P–P) are labeled for the intermediate-sized QDs plotted in green.

In 2008, Ithurria *et al.*[31] reported a synthesis method for two-dimensional CdSe NPs with atomically flat thicknesses. These NPLs exhibit narrow absorption and emission linewidth, as can be observed by comparing Figures 2.3B and 2.4B. The assignment of the distinctive features in NPLs absorption spectra differs significantly from QD absorption spectra. First of all, the density of states has a stepwise function due to the confinement in only one dimension. Secondly, the band structure is affected by the anisotropic shape of the NPLs. The symmetry of a zinc blende crystal structure causes a heavy hole (hh) and light hole (lh) degeneracy at $k = 0$ (at the Γ-point). The strong one-dimensional confinement in NPL breaks this symmetry. As a result, the degeneracy is lifted at $k = 0$ for the hh and lh sub-band (Figure 2.4A). Absorption spectra of NPLs are therefore characterized by transitions between the hh or lh sub-bands and the CB.[38-40]

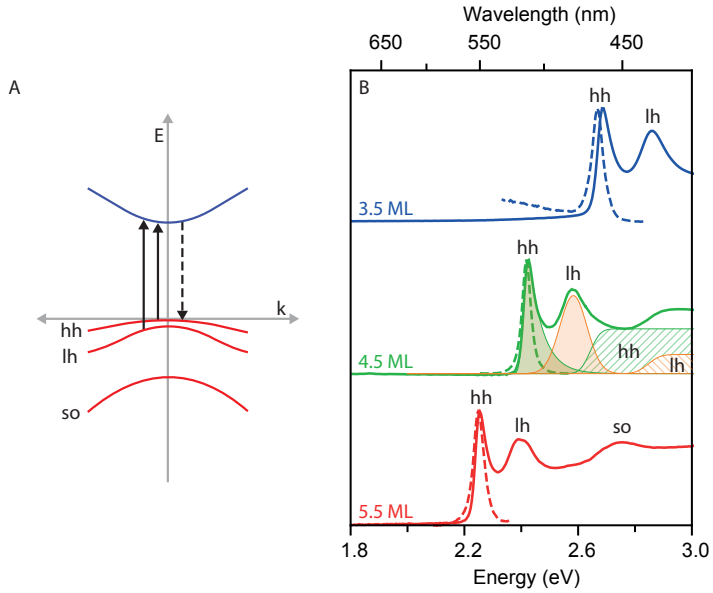

Figure 2.4 (A) Schematic representation of band structure of zinc blende CdSe NPLs with heavy hole (hh) sub-band, light hole (lh) sub-band, and the spin orbit (so) split off sub-band. The arrows represent free carrier generation and radiative recombination. **(B)** Absorption spectra (solid) and emission spectra (dashed) of 3.5 ML, 4.5 ML, and 5.5 ML NPLs. Spectra shift to lower energies for thicker NPLs. The contribution of the two excitonic transitions (solid) and the free carrier absorption (striped) of the hh and lh transitions are indicated with green and orange, respectively, for the 4.5 ML NPLs.[45] The emission spectrum of the 3.5 ML NPLs shows the onset of trap emission below ~2.6 eV, often more apparent in thinner NPLs.

NPLs with a thickness of 3.5 to 5.5 monolayers (MLs) of CdSe can be synthesized using the standard synthesis methods.[41] The use of half a monolayer in the naming indicates that the top and bottom facets are both cadmium terminated. That is, there is one additional cadmium layer compared to selenium layers. The hh and lh transitions for NPLs of different thicknesses are shown in Figure 2.4B.

At high energies, the step-shaped profile (see DOS in Figure 2.2B) of the free carrier absorption in can be observed. The hh and lh absorption are shown in green and orange, respectively. The intense peaks at lower energies are excitonic hh and lh transitions (not shown in Figure 2.4A). The electron-hole Coulomb interactions are stronger in two-dimensional structures compared to bulk, which is ascribed to the reduced screening of the attractive electrostatic interactions by the low dielectric constant of the surrounding ligands and solvent.[42] For example, an exciton binding energy of 190 meV for the hh transition in 4.5 ML thick NPLs has been extracted compared to 15 meV in bulk.[39, 43] This large exciton binding energy results in a large shift of the excitonic transitions compared to the free carrier transitions at higher energy.[38, 39]

The stronger exciton binding leads to a smaller exciton Bohr radius of 1.5 nm in NPLs.[44] Hence, the NPL lateral dimensions quickly exceed the confinement regime, and the band gap is predominantly affected by the NPLs thickness. The effect of the NPL thickness can be seen

in Figure 2.4B. The spectra shift to lower energy when the NPLs thickness increases from 3.5 to 5.5 ML.

2.2.3 Heterostructure NC designs

Nanoparticles with high luminescence quantum yields (QYs) are a necessity for many applications such as LEDs,[46] displays,[8, 47] luminescence solar concentrators for solar cells,[48, 49] or lasers.[50, 51] The surface of the NC needs to be well-passivated to achieve high QYs. Surface passivation is one of the roles of the organic ligands that are attached to the surface. These ligands also reduce aggregation of the NC due to steric hindrance or Coulombic repulsion, thereby ensuring that the dispersion is colloidally stable. Still, the NC surface often contains many defects or oxidizes over time, which results in the trapping of the charge carriers at the surface, thereby lowering the QY of semiconductor NC and doped NC with dopants in the vicinity of the surface.

An effective method to increase the QY is to surround the NC with an inert shell that separates the charge carriers or dopant ions from the surface. The QY of doped $NaYF_4$ can, for example, be enhanced by adding a shell of undoped $NaYF_4$.[52-54] For semiconductors NC, hetero NC can be made by encapsulating the core with a different semiconductor material. Different types of hetero NCs can be created by tuning the bandgap offset between the core and shell material. The band gap offsets for three types of heterostructures are shown in Figure 2.5. For a type I material, both the electron and hole are localized in the core, while for a type II structure, only one charge carrier is localized in the core and the other in the shell. A type $I^{1/2}$ heterostructure classifies materials where one charge carrier is confined to the core, and the other charge carrier is delocalized over the entire structure.

Type I materials will give the best passivation because both charge carriers are confined to the core, and thus, the overlap with trap states at the surface is minimal. With Type $I^{1/2}$ and Type II, the overlap between the electron and hole wavefunction can be tuned. Hence, next

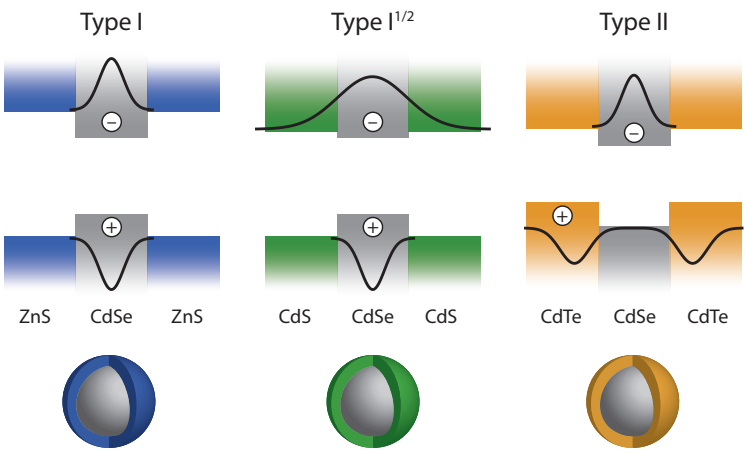

Figure 2.5 Schematic representation of the band gap offset in heterostructure NCs. For type I materials, the electron and hole are localized in the core (*e.g.*, CdSe/ZnS NC). In type $I^{1/2}$ materials, one charge carrier is localized in the core, and one is delocalized over the entire structure (*e.g.*, CdSe/CdS NC). In Type II materials, one charge carrier is localized in the core and the other in the shell material (*e.g.*, CdSe/CdTe NC).

to increasing the QY, these heterostructure designs unlock possibilities to tailor the exciton lifetime,[55, 56] Auger recombination rate,[57-59] reabsorption strength,[49, 60] photoluminescence (PL) wavelength,[56, 61, 62] and exciton phonon coupling[63-65] for semiconductor NC. The tuneability of these electronic properties is beneficial for adjusting the NC for specific applications. For example, reducing the reabsorption strength is essential for increasing the efficiency of luminescent solar concentrators,[66] high QY, and control over PL wavelength are necessary for displays, and reducing the Auger recombination rate is needed to enhance LED brightness.[67]

2.2.4 Spectral line broadening

One of the most important aspects for LEDs and displays is the spectral line width of the emitted light.[7, 9, 68] For the red contribution, this line width should be narrow to achieve warm, white-LED light with high efficacy. For displays with a wide color gamut, narrow line widths in the blue, green, and red are needed, as discussed in the introduction. The spectral line broadening in NC can differ tremendously. Compare, for example, the linewidth of the absorption features in Figures 2.3B and 2.4B. One can easily observe that the NPL absorption and emission features are significantly narrower than the QD features. This is caused by the size dispersion within an ensemble and the size-dependent bandgap of semiconductor NCs. The variation in sizes causes variation in the bandgap energy, resulting in inhomogeneous broadening of the spectra (Figure 2.6A). In a QD, this broadening is affected by variation in size in three dimensions. In a NPLs, the exciton is only confined in one dimension. Variations in the lateral dimensions will not cause inhomogeneous broadening because these dimensions are much larger than the exciton Bohr radius. Additionally, the NPL thickness is atomically exact and therefore gives no inhomogeneous broadening for NPLs.[69]

Spectra also broaden on the single particle level (Figure 2.6B) due to closely spaced energy levels, giving rise to exciton fine structure, which cannot be spectrally resolved. For example, the eight-fold degenerate lowest excited state in QDs ($1S_{3/2} - 1S_e$), splits in an optically active (bright) and passive (dark) state due to electron-hole interactions. Also, in slightly anisotropic QDs the degeneracy of the hh and lh sub-bands is lifted, but to a lesser extent than in NPLs.[26, 70, 71] Hence,

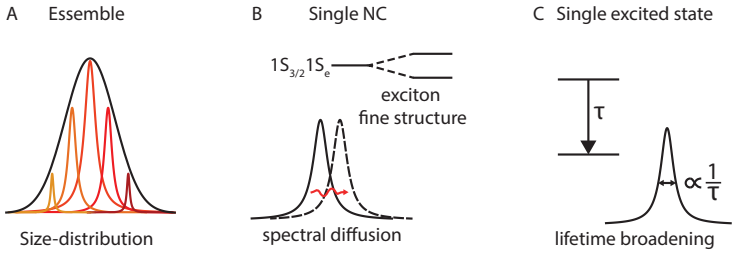

Figure 2.6 Spectral line broadening processes in semiconductor NC. **(A)** The size-dependent band gap and size distribution within an ensemble of NCs cause inhomogeneous broadening of the spectra. **(B)** The PL of a single NC broadens due to closely spaced energy levels (exciton fine structure) which cannot be spectrally resolved. The spectrum of a single NC can also shift to different energies (spectral diffusion) by local fluctuations, *e.g.*, in the electric field. Longer integration times will result in broader spectra, especially for single dots measurements at low temperatures. **(C)** The PL of a two-level system will broaden due to the finite coherence lifetime of the ground and excited state. The fwhm is inversely proportional to the coherence lifetime.

this will cause the spectra to broaden instead of appearing as two distinguishable features. Even over time, the PL spectrum can shift in energy due to spectral diffusion. Consequently, the full width half maximum (fwhm) will depend on the integration time. Spectral diffusion can be caused by local fluctuations of the electric field presumably induced by the surroundings, ligands, or charges on the NC and is most noticeable in single dots measurements at low temperatures where the homogeneous linewidth is very small.[65, 72, 73]

Finally, even the emission spectrum of a single two-level system will broaden because of the finite coherence lifetime of the excited state and ground state. A variety of dephasing processes reduces the coherence lifetime. The finite (coherence) lifetime ($\Delta\tau$) results in an uncertainty in the transition energy between the ground and excited state as is dictated by the Heisenberg uncertainty relation ($\Delta E \Delta\tau \gtrsim \hbar/2$) and is known as the Fourier transform limited linewidth.[74] For CdSe NPs, with an excited state lifetime in the range of nanoseconds, this gives a fwhm in the order of μeV. A line width of 120 μeV has, for example, been measured at 10 K for single CdSe QDs overcoated with ZnS, but it was clear that this linewidth was imposed by the spectral resolution of the set-up and that the actual (Fourier transform limited) linewidth is much narrower.[75]

At room temperature, a significantly larger fwhm of 70 meV has been measured for single CdSe QDs.[76] This increase in emission linewidth at elevated temperatures is caused by loss of coherence by the coupling to phonons, *i.e.*, vibrations of the crystal lattice. Phonon-induced dephasing is strongly temperature dependent as the phonon population increases with temperature. A variety of phonon-induced dephasing processes are known, including one-phonon direct relaxation, two-phonon Raman scattering, two-phonon Orbach process, or intrinsic Raman broadening.[77] Each of the processes has a different temperature dependence. Examples of phonon dephasing processes are shown in Figure 2.7B.

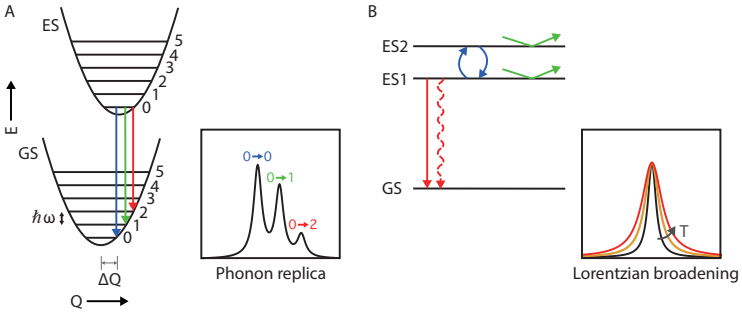

Figure 2.7 Exciton phonon coupling processes in NCs causing homogeneous broadening for PL spectra. **(A)** configuration coordinate diagram: decrease of the bond strength in the excited state due to changes in the electronic configuration causes the potential energy curve to shift to a larger equilibrium distance (Q). Consequently, electronic transitions to different vibrational states of the ground state (GS) will occur, resulting in phonon replicas in the PL spectra. The number of phonon replicas, and thus the broadening, depends on the relative shift of the excited state (ES) potential energy curve. **(B)** The PL spectra also broaden due to the loss of coherence of the induced polarization upon excitation. Loss of coherence is caused by radiative and non-radiative decay to the GT (red) or, more importantly, by coupling to phonons without loss of the excited state population, *e.g.*, by a transition to higher (virtual) excited states (blue) or Raman scattering processes (green). The loss of coherence by coupling to phonons depends strongly on the temperature, broadening the PL with increased temperature.

Excitons can couple to acoustic or optical phonons. The first type of phonons are in-phase motions of neighboring atoms, while the latter are out-of-phase motions of oppositely charged neighboring atoms within a unit cell. In the case of polar semiconductors like CdSe, the cadmium and selenium atoms move out of phase for optical phonons creating an oscillating dipole moment that can couple to an electromagnetic field. An electric field in the NC can be induced by the separation of the charge carriers. Hence, coupling to optical phonons is expected to increase when the overlap between the electron and hole wavefunctions is reduced in type $I^{1/2}$ and type ll hetero nanostructures.[65, 78] Acoustic phonons have a lower energy, and coupling to acoustic phonons is therefore more prominent at lower temperatures (below 200 K for CdSe), while at higher temperatures, dephasing processes due to coupling to optical phonons become dominant.[79-81]

The homogeneous broadening due to phonon interactions is two-fold. Exciton-phonon coupling reduces the coherence lifetime and thus increases the spectral linewidth. The spectra also broaden due to the presence of phonon replicas corresponding to spectral emission (absorption) lines with a lower (higher) energy than the zero-phonon line with integer phonon energy steps of $\hbar\omega$. A phonon replica progression is shown in Figure 2.7A. The phonon replicas stem from a difference in equilibrium geometry between the atoms in the ground state and excited state due to a change in the electronic configuration. The change in equilibrium geometry shifts the harmonic potentials in the configuration coordination diagram by ΔQ (Figure 2.7A). The larger this displacement, the broader the absorption and emission features. This is expressed in large values for the Huang-Rhys parameter S.

Theoretically, exciton-phonon coupling and the Huang-Rhys parameter are size dependent,[82, 83] and in accordance, broader spectra are obtained for small CdSe clusters relative to CdSe QDs. The shape and size of these clusters are well-defined, and therefore, there is little inhomogeneous broadening. However, the low number of atoms results in a large change in the average bond length between the atoms upon excitation and therefore broader spectra.[84-86] Typically, small values for S ranging from ~0.1 to ~0.5 are extracted for CdSe QDs with radii above 2 nm based on the relative intensity of the first phonon replica line to the strong zero-phonon line.[79, 87] The small S values for larger structures can be understood from the distribution of the change in bond length over many atoms. Nevertheless, it should be noted that relatively large discrepancies in S-values have been reported for CdSe QDs and the size-dependency of S is greatly disputed.[80, 88-90] Explanations for these discrepancies could be the use of different techniques to extract S-values such as single-particle spectroscopy, four-wave mixing, fluorescence line narrowing, or Raman spectroscopy, while also ligand coverage and trap states at the surface, which differ from batch to batch or even from NC to NC within a batch, likely affect the results.[65]

The various phonon-induced dephasing processes will cause the zero-phonon line to broaden at elevated temperatures without reducing the excited state population. This is referred to as pure dephasing and typically reduces the coherence lifetime to the fs – ps regime, thereby increasing the spectral linewidth to several tens of meVs.[70] The total dephasing rate is the sum of half the population decay rate and the pure dephasing rate.[91] This gives an exponential decay of the coherence and results in a Lorentzian line shape, known as homogeneous broadening.

The processes causing homogeneous broadening or inhomogeneous broadening are categorized rather loosely in literature. Spectral diffusion and exciton fine structure are sometimes

classified as homogeneous broadening as they affect the broadening of a single NCs. However, spectral diffusion is influenced by the environment and also depends on the timescale of the measurement (longer time allows for more spectral diffusion and would thus give a larger 'homogeneous' linewidth). Spectral diffusion would therefore be better classified as inhomogeneous broadening. The exciton fine structure involves transitions to or from different excited states and is the sum of multiple linewidths. A stricter definition of homogeneous broadening is the linewidth following from the Heisenberg uncertainty principle and caused by all dephasing processes, such as population radiative decay and dephasing induced by exciton-phonon coupling. At high excitation power, exciton-exciton coupling can induce additional (power-dependent) homogeneous broadening.[74]

2.3.1 Nucleation and growth of NC

Control over NC growth is of great importance for tailoring and optimizing the NC properties for scientific research and implementation in applications. Not only are narrow size distributions needed to reduce inhomogeneous broadening of their emission, but also control over shape and composition allows customization of NCs and their optical properties. The development of synthesis procedures generating colloidally stable NC dispersions also paved the way for easier post-synthesis alterations, *e.g.*, the synthesis of heterostructures or ligand exchanges.[92-94] Over many decennia, an impressive variety of types and shapes of NCs have been synthesized using numerous synthesis methods. The reported synthesis procedures for colloidal *semiconductor* NCs emerged after a method, generating colloidal suspensions of CdSe NCs with low polydispersity and high luminescence efficiency, was reported by Murray *et al.* in 1993. The ability to synthesize colloidal CdSe NCs had a large impact on the development of the semiconductor NC field.[30]

The $NaYF_4$:RE and Cd-chalcogenide NC discussed in this thesis are formed using the common colloidal synthesis procedures known as hot-injection and heating-up methods. Both methods rely on a series of reactions between precursor molecules to form monomers. Often surfactants are added to control the growth and prevent aggregation of the NC. In the case of CdSe NCs, the formation of CdSe monomers involves the reaction of cadmium carboxylates, cadmium oxide, or dimethylcadmium with phosphine selenides or elemental selenium in a high boiling solvent, *e.g.*, 1-octadecene (ODE) and/or trioctylphosphine oxide (TOPO).[95-97] For the formation of $NaYF_4$:RE NCs, rare-earth oleates are combined with sodium oleate and ammonium fluoride in ODE. First, small cubic α-phase $NaYF_4$ NCs are formed, but prolonged heating at 300^{0}C will eventually lead to larger NCs with a hexagonal β-phase crystal structure. β-$NaYF_4$ NCs can also be formed in a two-step synthesis by isolating the α-$NaYF_4$ NCs and reheating them in a mixture of oleic acid and ODE. The latter method improves the reproducibility of the synthesis.[98-100]

In the initial phase of NC formation, a critical level of supersaturation needs to be achieved to spontaneously form nuclei from the monomers. A sudden increase in monomer concentration can be established by injecting a cold and concentrated precursor solution into a hot reaction mixture. The high temperature ensures a fast conversion of precursors to monomers, and the drop in temperature reduces the solubility of the monomers. In a heat-up synthesis, the supersaturation is achieved by a fast temperature ramp and using precursors with low reactivity at low temperatures.

Spontaneous nucleation (in the thermodynamic sense) can occur when the formation of NCs results in a reduction of the total free energy. Classical Nucleation Theory (CNT) defines the free energy of a NC as the sum of the volume and surface free energy of the NCs.[101, 102] For a spherical particle, the expression for the free energy is given by equation 2.3, where ρ is the density and, γ the interfacial tension between the particle surface and the surrounding solution. $\Delta\mu$ is the chemical potential difference for the NC building blocks in the nanocrystals and as monomers in solution, which is also affected by the temperature and level of supersaturation. The first term in equation 2.3 reduces the total free energy with increasing r, because the formation of a larger volume is energetically favorable. The creation of new surface is, however, not energetically favorable. The two competing terms produce a critical nucleus radius corresponding to a maximum in the free energy of the system, thus a critical free energy barrier. Thus, nuclei with a smaller radius decompose into monomers, while nuclei with a larger radius can grow out to NCs, corresponding to a reduction of the free energy.

$$\delta G = \Delta G_v + \Delta G_s = \frac{4}{3}\pi r^3 \rho \Delta\mu + 4\pi r^2 \gamma \tag{2.3}$$

The evolution of NC growth has traditionally been described to follow three stages.[103, 104] During the induction phase (I), the concentration of monomers increases, as is shown in Figure 2.8. Also, small clusters may form during this stage, but these clusters are still unstable and will decompose back to monomers. Once the supersaturation reaches a critical level (S_{crit}), stable nuclei will form. In this nucleation phase (II), the monomer concentration drops because the monomers are rapidly consumed by nucleation. Once the concentration drops below the critical level, no new nuclei form, and the nucleation phase ends. A short nucleation phase is beneficial for achieving small size distributions and can be obtained using either the hot-injection or heating-up method.[105] After fast nucleation, all nuclei will grow at a similar rate to reach a similar final size which can explain the narrow size distribution.

After the nucleation phase, only NCs exceeding a critical radius will continue to grow by the addition of monomers or coalescence of NCs (phase III). Depending on the reaction conditions, growth by monomer addition can be either diffusion-controlled or reaction-controlled. High monomer concentrations typically result in reaction-controlled growth.[104] Once most monomers are consumed by NC growth, the dissolution rate will become significant compared to the growth rate. In the long time limit, the monomer concentration remains constant at S_0. The reaction is usually quenched before this point is reached because at low monomer concentration, the size distribution starts to increase due to Ostwald ripening.[106]

LaMer and Dinegar proposed this three-phase model for NC formation in 1950 to explain the formation of monodisperse colloidal sulfur particles.[107] With the use of CNT, they were one of the first to derive a growth model for NCs. However, to derive a growth model for monodisperse particles, certain approximations needed to be implemented by LaMer.[108] For example, the nucleation had to be instantaneous, and the growth diffusion controlled. In reality, the nucleation phase is often not short-lived but can even be continuous.[103, 109, 110] Recently, using the setup described in chapters 4 and 5, an increase in NC concentration was measured over a time range of 60s while still obtaining a low size distribution of ~6%.[111] Also, far slower growth rates are often measured than expected for diffusion-controlled growth.[96]

CNT also has shortcomings as it treats the NCs as a bulk material and does not consider the effect and role of surfactants.[96, 97, 108, 110] Both ΔG_v and γ for NCs likely differ from macroscopic

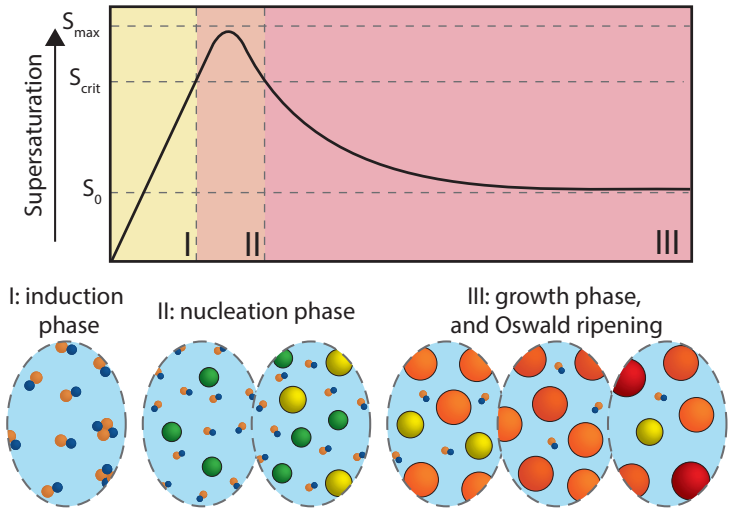

Figure 2.8 The traditional model for NC growth follows three stages: The induction phase (I), the nucleation phase (II), and the growth phase (III). The plot shows the level of supersaturation during the three stages. The images give a schematic representation of the NC growth. During stage I, monomers and small clusters form. In stage II, when a critical supersaturation (S_{crit}) level is reached, stable nuclei form. The supersaturation drops in stage III, no new nuclei form, and existing particles grow in size. When the supersaturation drops to a certain level, the size distribution of the particles increases due to Oswald ripening.

systems, especially for tiny nuclei. The surfactants affect the stability of the monomers, stabilize certain nanocrystal facets, and can also play a role in the chemical reactions to form monomers. Surfactants not only prevent aggregation of the colloids but also affect the nucleation and growth of NCs.

Even though LaMers model and CNT are too simplified and have well-known shortcomings, they are still used to describe NCs growth nowadays. For a variety of (semiconductor) NCs, they give a qualitatively correct view on the nucleation and growth. Formulation of better models takes time because experimental verification of models for the nucleation and growth of NCs is challenging. These studies require *in situ* tracking of the NC formation and a fast time resolution. It should be noted that more realistic models have been proposed in the last decade; these models are based on *in situ* and real time monitoring of nanocrystal nucleation and growth, see *e.g.*, Ref. [111] and references therein.

Another hurdle in investigating NC growth mechanism is that NC synthesis are notoriously difficult to reproduce. For instance, the ramp rate has a profound effect on the results of a heat-up reaction,[112] and impurities in the precursors and surfactants can affect the reaction kinetics. In some cases, it was later discovered that the presence of impurities in the chemicals was, in fact, a key ingredient for obtaining high reaction yields or the desired NC shape. Examples are octylphosphine impurities in trioctylphosphine for PbSe QD synthesis, dioctylphosphine impurities in trioctylphosphine oxide (TOPO), which assist the growth of CdSe QDs, or phosphonic acids in TOPO for the formation of CdSe nanorods, nanowires, and tetrapods.[104, 113, 114]

2.3.2 Models for anisotropic growth of CdSe NPLs

NC Synthesis is undeniably complex because the nucleation and growth of NCs depend on many factors, *e.g.*, precursor concentration, type of precursors, temperature, surfactants, solvent, crystal structure, and NC facets. The formation mechanism is, therefore, often not fully understood yet. The complexity is emphasized by the variety of known formation pathways leading to anisotropic growth resulting in, *e.g.*, nanorods, stars, or platelets. Three completely different growth mechanisms have even been suggested for zinc blende CdSe nanoplatelets, *i.e.*, templated growth,[115] oriented attachment,[116] or continuous growth by monomers addition.[41, 117] A schematic representation of these mechanisms is shown in Figure 2.9. The proposed mechanisms and experimental evidence given by the authors will be outlined in this section. In chapter 4, these mechanisms will be discussed in relation to our obtained *in situ* absorption and X-ray scattering data.

Figure 2.9A shows the mechanism for templated growth. The solvent or surfactant molecules in the reaction mixture can form a lamellar mesophase. The lamellar mesophase constrains the growth of nuclei or magic-sized clusters to dimensions dictated by the dimensions of the lamellar structure, *i.e.*, the spacing *d*. Mesophases of the added surfactants or precursors are typically only stable until temperatures up to ~100°C – 180°C.[115, 118, 119] Templated growth is, therefore, a more plausible mechanism for low-temperature synthesis. The stability of the lamellar structure can, in some cases, be enhanced by the addition of halides, resulting in anisotropic growth at higher temperatures.[118] Multiple examples of two-dimensional growth postulated to occur via this mechanism have been reported, *e.g.*, PbS NPLs,[120] $Cu_{2-x}S$ nanosheets,[118] or wurtzite CdSe quantum belts.[121] As noted, templated growth has been suggested for zinc blende CdSe NPLs.[115] However, it was not experimentally validated in the study that the crystal structure of these NPLs was zinc blende.

Anisotropic growth via oriented attachment can also lead to two-dimensional nanostructures. This mechanism starts with the formation of NCs. These NCs self-organize to a two-dimensional structure before they attach. The driving forces behind self-organization are attractive dipolar interactions induced by anion- and cation-terminated opposing facets in a NC or an uneven distribution of charged ligands.[122, 123] The self-organization can also be facilitated by soft templating.[124] After self-organization, the NC facets orient and attach to form two-dimensional structures. The ligands on the NC surface heavily influence the attachment process; attachment via specific facets can be inhibited by a high ligand density or enhanced by the destabilization of specific facets by ligands.[122, 125] Well-known examples of oriented attachment are PbS and PbSe QDs forming two-dimensional sheets or square and honeycomb lattices.[126]

For zinc blende CdSe NPLs, oriented attachment was suggested as the formation mechanism by Peng *et al.*[116] In the synthesis procedure used for the study, first, spherical seed-NCs with a 1.8 nm diameter were synthesized and purified. These purified seed-NCs were injected into a reaction mixture of ODE, cadmium stearate, and cadmium acetate. They identified absorption features of three kinds of particles during the synthesis: 2D intermediates, 2D embryos, and NPLs (Figure 2.9B). They proposed that intraparticle ripening transforms the seed-NCs into NCs with nearly flat basal planes. These 2D intermediates undergo attachment via more reactive (110) side facets forming 2D embryos, which are doubled in size. The 2D embryos have more defined (100) and (110) facets and will continue to grow by attachment via the (110) facets. At-

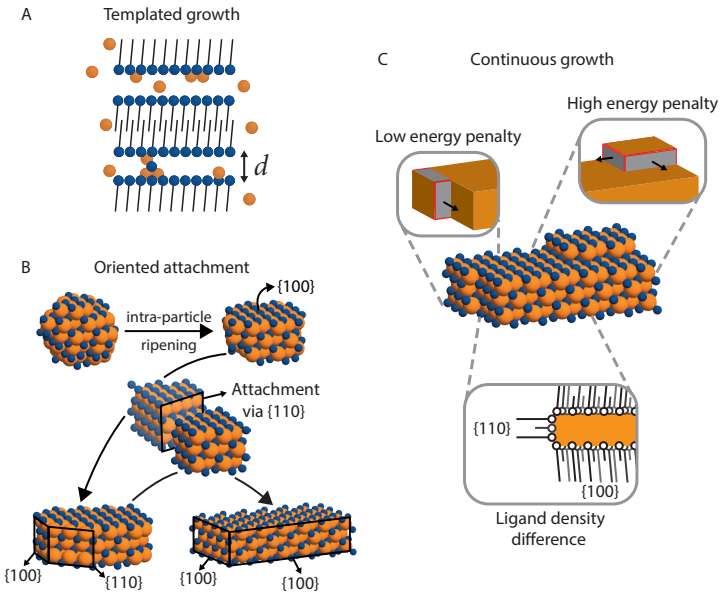

Figure 2.9 Proposed formation mechanisms for CdSe NPLs. **(A)** Templated growth: solvent or surfactant molecules form a lamellar mesophase. The dimensions (*e.g.*, *d*) constrain the growth of nuclei or magic-sized clusters and promotes two-dimensional growth. **(B)** Oriented attachment: intra-particle ripening of purified seed NCs occurs when heated in a reaction mixture of ODE and cadmium carboxylate, forming 2D intermediates. These intermediates attach via (110) facets to form larger 2D structures (2D embryos), which continue to grow via the (110) facets by attachment to form larger NPLs terminated with (100) side facets. **(C)** Continuous growth: two different mechanisms with continuous addition of monomers have been proposed. Bottom: two-dimensional growth occurs due to high ligand density on the top and bottom facets that can only be reached when short-chain ligands are added to the reaction mixture. Top: anisotropic particles can grow under nucleation-limited growth when the formation of new surface has a lower energy penalty than the formation of new edges. The new layer on the small facets quickly spans the width of the facets. As a result, less new edge length is formed (shown in red) compared to the edges formed on a new layer on the large top/bottom facets. Consequently, growth on the large facet has a higher energy penalty than on a small side facet, which promotes two-dimensional growth.

tachment via the basal planes, (100) facets, is prevented by the long-chain carboxylate ligands stabilizing these planes. At the end of the reaction, NPLs are obtained with (100) side facets.

Dubertret *et al.*[41] and Norris *et al.*[117] both hypothesize that zinc blende CdSe NPLs grow by continuous addition of CdSe monomers. Dubertret *et al.* have shown that large nanosheets with dimensions up to one micron can be made by continuously adding precursors to small NPLs.[127] No small QDs were observed during the growth, and therefore they exclude oriented attachment. The proposed mechanism behind two-dimensional growth differs between these authors. Dubertret *et a*l. suggest that two-dimensional growth occurs due to high ligand density on the bottom and top facets (Figure 2.9C, bottom). Steric hindrance prevents the addition of new monomers to these facets.[128] The authors varied ligand concentration and alkyl chain length and studied the effects with electron microscopy and absorption spectroscopy. They observed

larger lateral dimensions when ligands with shorter alkyl chain lengths were added. They hypothesize that long alkyl chain carboxylates cannot match the density of the cadmium-rich top and bottom facets due to steric hindrance, while a high ligands density is needed to counterbalance the charge of the additional cadmium layer in CdSe NPLs. According to the authors, the charges can likely only be counterbalanced if short-chain ligands are added. This would explain why larger NPLs could form when short-chain ligands are added.

Norris *et al*. suggest that NPLs form only if the cadmium precursor does not fully dissolve in the reaction mixture.[117] They show that more NPLs form in a reaction mixture when the chain length, and thus the solubility, is reduced (octanoate to butanoate). Longer chain lengths (oleate) result in the formation of only QDs. The authors show that NPLs could even be synthesized with only short- or long-chain ligands in a solvent-free environment, and nucleation-limited growth in the concentrated droplets of an insoluble precursor is proposed to form NPLs. Nucleation-limited growth results in anisotropic growth under two conditions. First, the energy cost for the nucleation of a new layer on larger facets should be sufficiently high compared to the reaction temperature. Second, the formation of new edges (red, Figure 2.9C) must be energetically expensive, whereas new surface (gray, Figure 2.9C) must be energetically less expensive.[117] The latter condition ensures that growth on larger facets is energetically less favorable than on small facets because a newly formed island on a large facet has more edges, as is shown in Figure 2.9C in red. A new layer on small facets quickly spans the length of the facet and has, therefore, less new edge length. Slight differences in facet size greatly affect the energy barrier for the growth of an additional layer. Thus, random fluctuations during the growth can initiate the formation of NPLs from an isotropic crystal structure. The calculations show that only NPLs with a limited number of ML can be synthesized. For CdSe NPLs, 2.5 MLs to 5.5 MLs can be synthesized under standard reaction conditions.

2.3.3 Growth models for $NaYF_4$ NCs

Hexagonal $NaYF_4$ NCs have attracted increasing attention since the discovery of efficient upconversion in Er^{3+}, Yb^{3+} doped $NaYF_4$ nanocrystals. This also triggered extensive research into understanding and optimizing the formation mechanism. In the early stages of the reaction, cubic α-phase $NaYF_4$ NCs form with a large size distribution, while at the end of the reaction, hexagonal β-phase $NaYF_4$ NCs with a small size distribution are obtained. Multiple variations on the synthesis method have been investigated to clarify the mechanism behind the transition from a large to a small size distribution while also undergoing a change in the crystal structure. This section gives an overview of proposed models and the role of variations in synthesis conditions.

The $NaYF_4$ NC are formed using a heat-up method with a mixture of ODE, oleic acid, sodium oleate, ammonium fluoride, yttrium acetate, and other lanthanide acetates for doped NCs.[129] There are multiple variations on this synthesis using, for example, oleates instead of acetates or different sodium or fluoride sources.[130-132] First, a high number of small α-phase particles form during the heating. After prolonged heating at 300°C, the α-phase particles start to dissolve, and β-phase particles are observed. At this stage, both cubic and hexagonal particles are present in the reaction mixture. There is a large discrepancy in the time needed to reach this stage in the reaction (25 min – 90 min).[129] Once enough β-phase particles have formed, the α-phase particles start to dissolve rapidly, resulting in a reaction mixture with only β-phase par-

ticles within ~15 min.[98, 129] Larger particles with a lower concentration are obtained compared to the preceding α-phase particles.

It is still unclear if the β-phase particles nucleate from the monomers released by the dissolving α-phase particles or if a change in the crystal structure occurs for a subset of the α-phase particles. No experimental evidence has yet been found to distinguish between these two mechanisms. Even though the exact mechanism is unknown, simulations have been performed to explain the small size distribution while the particles grow by Oswald ripening which typically leads to larger size distributions.

Haase *et al.* showed that a small size distribution could be obtained for growing β-particles in the presence of α-particles if the bulk solubility or surface tension of the two phases is sufficiently different. This leads to a large difference in the critical radius for the cubic α-phase and hexagonal β-phase particles and, therefore, reaction conditions where the α-phase particles dissolve and the β-phase particles grow under size-focusing conditions.[133] Berry *et al.* used a model that assumes that β-phase particles form by a phase transition of α-particles that reached a critical size where the transition from α to β phase is thermodynamically favored.[134] With both models, the experimental results can be simulated using reasonable parameters, but the mechanism responsible for forming the hexagonal β-phase is not yet known.

The time needed for the phase transition and whether or when the transition from α to β phase occurs depends strongly on the temperature, concentration of ligands, and ratio between sodium and rare earth ion precursors. For example, DFT simulations have shown that oleate ligands absorb more strongly on an yttrium site than on a sodium site, which affects the organization of yttrium ions in the cubic phase. Consequently, according to these calculations, a higher oleate concentration reduced the energy barrier for the phase transition. Experimentally, a higher concentration of oleate indeed results in shorter reaction times and also in smaller β-phase particles because more β-phase particles form.[135, 136] Next, the stoichiometry between sodium and yttrium in the α-particles influences the reaction as well. A high ratio of sodium to rare-earths results in a larger number of β-particles, while with sodium deficient α-particles as a precursor, the formation of β-particles can be suppressed entirely.[100]

To gain insight into the growth mechanism of the NCs and the crystal structure, *in situ* studies combining small- and wide-angle X-ray scattering under realistic reaction conditions are reported in chapter 5.

2.4.1 NC Characterization techniques

All the differences and uncertainties in the models for the two-dimensional growth of NPLs and growth of hexagonal $NaYF_4$ NPs reviewed in the previous sections show that the reaction mechanism for both is still insufficiently understood. Characterization of NC growth is vital for better understanding NC formation mechanisms. Unfortunately, the small size of NCs makes their characterization not straightforward. The size and shape cannot be studied with conventional light microscopy because the wavelength of visible light by far exceeds the typical NC size. A higher resolution is required, which can be achieved using electromagnetic radiation or particles with a shorter wavelength, *e.g.*, x-rays or electrons.

Electron microscopy techniques use the interactions of electrons with the specimen to image the particles. The electrons are first accelerated using a voltage of 20-200 keV to establish a high resolving power because the associated wavelength is inversely proportional to the par-

ticle's momentum. The De Broglie wavelength of a 200 keV electron is 2.74 pm and allows for imaging with atomic resolution. The electrons can interact with the specimen in a variety of ways. They can be scattered, refracted, lose energy, or eject electrons from atoms in the specimen. All these processes are used in electron microscopy to extract information on NC size, shape, crystal structure, organization of NCs in 2D superlattices, or chemical composition.[137-140]

Several strategies can be used for imaging with electron microscopy. In this thesis specifically, transmission electron microscopy (TEM) and high-angle annular dark-field scanning transmission electron microscopy (HDAAF-STEM) are used. With TEM, a relatively wide electron beam is used to probe the sample. TEM gives a 2D projection of the NCs where the NCs appear darker than empty regions because fewer electrons are transmitted due to scattering and diffraction by the atoms in the NCs. Another option is to use the scattered electrons for imaging, which is done with HDAAF-STEM. This technique uses a focused electron beam and scans the specimen from spot to spot. The scattered electrons are detected at an angle by a circular detector below the specimen. The NCs appear bright, whereas the surroundings are dark. The contrast depends on the electron density for both techniques. Both techniques are thus more sensitive to heavy elements.

For semiconductor NCs valuable information can be obtained from the optical absorption spectra as features depend on the NC size. Sizing curves enable direct extraction of the size and concentration from absorption spectra. The position of the absorption maximum can be related to the NC size using TEM- or small-angle X-ray scattering (SAXS) analysis. The size-dependent extinction coefficient of the NCs is determined by combining size information with inductive coupled plasma spectroscopy (ICP). With the latter, the concentration of an element (*e.g.*, cadmium) in the sample can be determined, and the NC concentration can be calculated from the measured element concentration (obtained with ICP) and size (from TEM or SAXS analysis).

Sizing curves have been established for several semiconductor NCs,[141-145] and are convenient to characterize synthesized NCs quickly. Note that these sizing curves are typically determined at RT and cannot be used at elevated temperatures due to the temperature-dependent position of the absorption maxima and spectral line broadening.

2.4.2 Characterization using X-ray scattering techniques

Analogous to electron microscopy, X-ray scattering techniques rely on the difference in electron density at the interface between particles and the surroundings or periodic density variations inside (nano)crystals. In contrast to electron microscopy, no real image of the NCs is generated but a 2D scattering image containing reciprocal space data (Figure 2.10A). X-ray scattering techniques generate a weak scattering signal. A high X-ray flux is therefore needed to conduct experiments, which can be generated at a synchrotron facility. At a synchrotron, X-rays are generated by altering the trajectory of high-energy electrons with a magnetic field. A bright and coherent X-ray source can be generated when the direction of the electron beam is wiggled with a small amplitude. This is achieved using an undulator magnet, which applies a magnetic field with a consecutive alternating direction. The wavelength of the X-rays is determined by the periodicity of the alternating magnetic field and the beam energy.

The generated X-ray beam can interact with the specimen, resulting in the absorption or scattering of the X-rays. Dominant elastic scattering, scattering without energy loss, occurs when the energy of the photons is much higher than the absorption edge. The angle at which

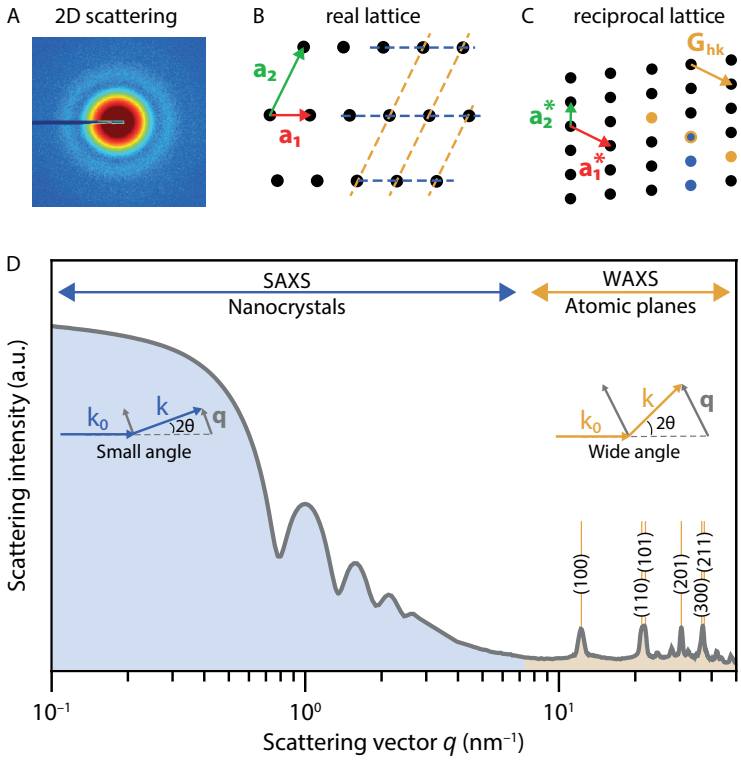

Figure 2.10 (A) 2D scattering data of an *in situ* CdSe QD synthesis. The scattering intensity increased from blue to red and is isotropic because the NCs can freely rotate in solution. In black, the beam stop is visible, which prevents damage to the detector from the direct beam. **(B)** A 2D lattice in real space is composed of many repeating unit cells defined by the lattice parameters a_1 and a_2. **(C)** Same lattice in reciprocal space. Small distances in real space correspond to large distances in reciprocal space. The planes in real space (orange and blue dashed lines) are represented with points in reciprocal space (orange and blue dots). The reciprocal lattice vector $\mathbf{G}_{hk}$, here $\mathbf{G}_{01}$, represents the family of planes in real space (orange dashed). The reciprocal vector is perpendicular to the corresponding planes in real space. **(D)** 2D scattering data is azimuthally averaged to generate a 1D scattering curve. The data displayed originates from an *in situ* measurement of hexagonal β-phase $NaYF_4$ NCs with a diameter of ~11 nm and a polydispersity of <5%. In blue, the scattering at small angles/q-values (SAXS) is displayed, which probes relatively large distances in real space to determine the size, shape, and concentration of the NCs. In orange, the scattering at large angles/q-values (WAXS) is displayed, which probes the inter-atomic distances in the NCs and provides information on the crystal structure. A few Bragg peaks, which originated from constructive interference, are labeled with the corresponding Miller indices (h, k, l) of the planes.[150, 151]

scattering is observed depends inversely on the distance in real space. Scattering at wide angles is caused by short distances (~0.1–1 nm) in real space, corresponding to distances between atomic planes in a crystal. At small angles, the scattering due to density variations over large distances (~1–100 nm) in real space is probed. In this regime, the size and shape of nanome-

ter-sized particles can be extracted due to the differences in electron density between the NCs and the solvent.

NCs in a dispersion can freely rotate. Consequently, the scattering intensity in a 2D scattering image is isotropic and is azimuthally averaged to generate a 1D scattering curve. The scattering vector q is typically used instead of the scattering angle 2θ, where $\mathbf{q} = \mathbf{k} - \mathbf{k_0}$ and its magnitude $q = 4\pi \sin(\theta)/\lambda$. $\mathbf{k_0}$ and $\mathbf{k}$ are the wavevectors of the incoming and scattered wave, respectively. As an example, the scattering intensity of hexagonal $NaYF_4$ particles as function q is shown in Figure 2.10D. The regions where the atomic distances and nanocrystal dimensions are probed are indicated with orange and blue, respectively.

The crystal structure, shape, size, size-dispersion, and concentration of the NCs can be extracted from the scattering pattern in Figure2.10D. To explain how, we will first look at the scattering intensity of a two-body system and then discuss the mathematical equations describing the scattering intensity of a crystal (WAXS region) and a dispersion of NCs (SAXS region) as a function of q. The theory and experimental examples are also discussed extensively in references [146, 147, 148, 149].

The scattering amplitude for a system with two scatterers, one at the origin and one at a position $\boldsymbol{r}$, is given by[149]:

$$A(\mathbf{q}) = f_1 + f_2 e^{i\mathbf{q}\cdot\mathbf{r}} \tag{2.4}$$

The first term in equation 2.4 gives the scattering amplitude f_1 of the scatterer at the origin and the second term of a scatterer at a certain distance r. The scattering is weak, meaning that the scatterers only scatter the incident beam. The phase difference between the waves scattered by the two scatterers will result in constructive or destructive interference depending on the scattering angle and the distance between the scatterers. This phase difference is accounted for with the phase factor $e^{i\mathbf{q}\cdot\mathbf{r}}$. For a system with more scatterers, equation 2.4 simply becomes a sum over many scattering amplitudes f_j (form factors) multiplied with a phase vector.[149] This expression for the scattering amplitude is mathematically named a Fourier transform; real space (the charge density) is converted to reciprocal space (the scattering amplitude/pattern). $f_j(\mathbf{q})$ is the atomic form factor if the scatterers are atoms and then represents the electron distribution $\rho(\boldsymbol{r})$ around a nucleus. Note that the measured intensity in an experiment is the square modulus of $A(\mathbf{q})$, *i.e.*, $I(\mathbf{q}) = |A(\mathbf{q})|^2 = A(\mathbf{q})A(\mathbf{q})^*$. Therefore, the information on the phase is lost in the scattering data.

In the WAXS region, $I(\mathbf{q})$ scales with the square modulus of the structure factor amplitude $F^{\text{crystal}}(\mathbf{q})$. The structure factor amplitude of a crystalline material is, as before, the sum of many atomic form factors f_l multiplied by a phase factor:

$$F^{\text{crystal}}(\mathbf{q}) = \sum_{l}^{\text{all atoms}} f_l(\mathbf{q}) e^{i\mathbf{q}\cdot\mathbf{r}_l} \tag{2.5}$$

A crystalline material can be described with a repeating unit cell with lattices parameter a_i. An example of a two-dimensional crystal structure with lattice parameters a_1 and a_2 is shown in Figure 2.10B. Due to the repeating unit cells in a crystalline material, the sum in equation 2.5 can be split in two terms by writing the position vector $\mathbf{r}_l$ as the sum of the lattice vector $\mathbf{R}_n = n_1\mathbf{a}_1 + n_2\mathbf{a}_2 + n_3\mathbf{a}_3$ and the position of an atom, r_j, within a unit cell:

$$F^{\text{crystal}}(\mathbf{q}) = \sum_{l}^{\text{all atoms}} f_l(\mathbf{q}) e^{i\mathbf{q}\cdot(\mathbf{R}_n+\mathbf{r}_j)} = \sum_{n} e^{i\mathbf{q}\cdot\mathbf{R}_n} \sum_{j} f_j(\mathbf{q}) e^{i\mathbf{q}\cdot\mathbf{r}_j} \tag{2.6}$$

The first term, the lattice sum, is only large when the scattering vector **q** coincides with a reciprocal lattice vector $\mathbf{G} = h\mathbf{a}_1^* + k\mathbf{a}_2^* + l\mathbf{a}_3^*$. When this criterion is met, then the scalar products of **q** and $\mathbf{R}_n$ are equal to integers times 2π and the value of the sum will therefore scale with the number of unit cells N ($|F(\mathbf{q})|^2 \propto N^2$). If this condition is not met, then the terms in the sum will cancel each other, and the sum will remain small. The reciprocal lattice vector **G** represents a family of parallel lattice planes in a real lattice with the **G**-vector perpendicular to it (Figures 2.10B and 2.10C). Hence, it is unsurprising that the criteria for intense or vanishing signals are analogous to Bragg's law for constructive and destructive interference ($n\lambda = d \sin\theta$) and produce sharp peaks in the WAXS region.

The sharp peaks will only be observed when the second sum in equation 2.6, named the unit cell structure factor, is nonzero. The second sum describes the scattering of the atoms in a unit cell. The atomic form factor f_j will differ when the unit cell contains non-identical atoms, but if the atoms are identical, this factor can be placed before the sum, as will be done for the example below.

The structure factor of a monoatomic body-centered cubic (bcc) crystal will be considered as an example. A bcc crystal has a reciprocal lattice vector equal to $\mathbf{G} = \frac{2\pi}{a}(h,k,l)$ and it can be deconstructed into a simple cubic crystal structure with a two-atom basis, one at the origin $\mathbf{r}_1 = (0,0,0)$ and one at half the unit cell $\mathbf{r}_2 = \left(\frac{1}{2},\frac{1}{2},\frac{1}{2}\right)a$. The structure factor of a bcc crystal is then given by:

$$S_{\text{bbc}}(\mathbf{q}) = f_j(\mathbf{q}) \sum_{j} e^{i\mathbf{G}\cdot\mathbf{r}_j} = f_j(\mathbf{q})\left(e^{i\cdot 0} + e^{i\frac{2\pi}{a}\cdot\frac{a}{2}(h+k+l)}\right) = f_j(\mathbf{q})\left(1 + (-1)^{h+k+l}\right) \tag{2.7}$$

$S_{\text{bcc}}(\mathbf{q})$ and thereby $F^{\text{bcc}}(\mathbf{q})$ in equation 2.6, is nonzero when the sum of the Miller indices (h, k, l) is even, and zero when the sum is odd. That is, the (1,0,0) reflection is forbidden, and the (2,0,0) reflection is allowed and would be observed as a sharp peak in the scattering pattern. In Figure 2.10D, a few Bragg peaks are labeled for hexagonal $NaYF_4$ NCs.

The fwhm of the Bragg peaks is related to the crystal size.[152, 153] The peaks' widths narrow when the crystal size becomes larger. The relation between peak width and the crystallite size was found by Scherrer and is given by the Scherrer equation,

$$\beta_s = \frac{K\lambda}{D\cos\theta} \tag{2.8}$$

where β_s is a measure for the peak width (*e.g.*, fwhm), D the average size of the crystallites, θ the Bragg angle, and K the Scherrer constant, which value depends on the shape of the particle and the exact definition of β_s and D. K has a value close to one.[147] The Scherrer equation can be used to estimate the crystal size in the WAXS region. Nonetheless, the scattering pattern in the SAXS region is *directly* related to the crystallite size. In contrast, the peak width in WAXS is also affected by defects, disorder, or strain in the crystal.

The scattering intensity in a SAXS experiment of a dilute mixture is a function of the number density n, the square modulus of the form factor amplitude $F(\mathbf{q})$ denoted with $P(\mathbf{q})$, and the structure factor $S(\mathbf{q})$[149] :

$$I_{\mathrm{SAXS}} = nP(\mathbf{q})S(\mathbf{q}) \tag{2.9}$$

n is a measure for the concentration of the NCs, $P(\mathbf{q})$ depends on the shape and size of the NC and $S(\mathbf{q})$ is affected by the spatial distribution of NCs. The structure factor $S(\mathbf{q})$ is one when the distribution of the particles is random. In the case of ordered NC assemblies, additional features will be observed due to constructive and destructive interference. An example is the sharp peaks in the SAXS data for stacked NPLs in chapter 4.

The form factor amplitude of a geometric object is given by the volume integral over the electron density function $\Delta\rho(\mathbf{r})$ multiplied by a phase vector. For the nano-sized particles probed in the SAXS region, it can be assumed that the electron density is uniformly distributed in the particles. Consequently, it is sufficient to consider only the difference in scattering length density between the NC and the surroundings. This number is independent of r and can be placed in front of the integral. The form factor is then,

$$F(\mathbf{q}) = \Delta\rho \int_V e^{i(\mathbf{q})\cdot(\mathbf{r})} dV_{\mathrm{p}} \tag{2.10}$$

where $\Delta\rho$ is the scattering length density contrast between the particle and the solvent, and the integral is simply a function depending on the particle's morphology. Analytical Fourier transforms of many shapes are given in reference [154] and are used in chapters 4 and 5.

The form factor $P(q)$, which is solely dependent on the magnitude and not the direction of $\mathbf{q}$, is the average form factor, $\langle |F(\mathbf{r})|^2 \rangle$, of all possible orientations of the NC in solution. For spherical particles, the form factor $P(\mathbf{q})$ is equal to the orientationally averaged form factor, but this is not the case for most non-spherical particles. For many shapes, the form factor can only be evaluated numerically. Furthermore, also the size distribution needs to be considered in the form factor expression. For spherical particles with a Gaussian size distribution, an analytical expression can be given:

$$\langle P(q) \rangle_R = \frac{1}{\sqrt{2\pi}\sigma_R} \int_0^\infty e^{-\frac{1}{2}\left(\frac{R-R_0}{\sigma_R}\right)^2} 3V \left[\frac{\sin(qR) - \cos(qR)}{(qR)^3} \right]^2 dR \tag{2.11}$$

The scattering intensity for spherical particles of varying sizes with a polydispersity of 15% is shown in Figure 2.11A. The plot shows that the form factor of spheres contains minima. The position of the minima depends on the size of the spheres and shifts to smaller q for larger particles. When there is a large size distribution, the minima will smear out, *e.g.*, the minima in Figure 2.10D are more pronounced than in Figure 2.11A because the size distribution is smaller.

The concentration, size, and polydispersity of the particles can be extracted from the scattering data by fitting the data with a predefined model of a form as given in equation 2.9. Qualitatively, the dimensionality of a particle can be deduced from the behavior of the scattering intensity as a function of q. For example, the scattering curves of 2D particles (NPL) in Figure 2.11B show a different dependence on the scattering vector q than the scattering patterns in Figure 2.11A. The form factor scales with q^{-n} in the q-range comparable to the inverse

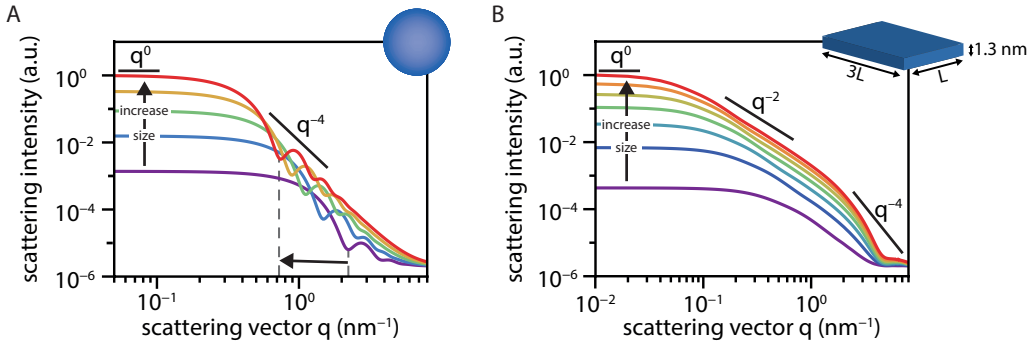

Figure 2.11 (A) Scattering pattern of spherical particles (QDs) with a radius of 2 – 6 nm (purple to red) and a polydispersity of 15%. The form factor of spherical particles contains minima, which shift to smaller q-values for larger spheres. The smaller the polydispersity, the more pronounced the minima will be. The scattering intensity of three-dimensional particles (spheres) contains a power law of q^{-4} at intermediate q-values and q^0 at small q-values ($qr \ll 1$). **(B)** The scattering pattern of two-dimensional particles (NPLs) with L is 2 – 14 nm (purple to red) and a thickness of 1.3 nm. The form factor of two-dimensional particles contains a range that scales with a power law of q^{-2}. At large q-values and small q-values, the scattering intensity scales with q^{-4} and q^0, similar compared to spherical particles. The q^0 region starts at smaller q-values because the dimensions of the NPLs are much larger. The intensity at small q scales with the NCs size, concentration, and $\Delta\rho$.

of the average particle size. The exponent n depends on the dimensionality of the particle. For spherical, two-dimensional, or rod-shaped particles, a power law of q^{-4}, q^{-2}, or q^{-1}, respectively, is observed for the form factor.[148, 155]

These power laws result from the dependency of the volume element for integration on r. For example, dV_{sphere} is equal to $4\pi r^2 dr$ and therefore the integral in equation 2.10 varies with r^2. Consequently, the form factor $\left(P(q) = \langle |F(\mathbf{r})|^2 \rangle\right)$ will scale with r^4, and a power law of q^{-4} is observed because the scattering vector is proportional to the inverse of r. A power law of q^{-4} is also present in the form factor of 2D particles at q values corresponding to sizes smaller than the thickness of the particles. A two-dimensional NC becomes three-dimensional for these q-values.

Although, in this thesis, the scattering patterns in the SAXS region will be qualitatively analyzed by determining the power law in specific q ranges and quantitatively by fitting the scattering patterns with a predefined model of the form $nP(\mathbf{q})S(\mathbf{q})$, there are a few more interesting regimes in a scattering pattern. At large q values, but still small compared to the WAXS region, the intensity scales with q^{-4}, as can be observed in Figures 2.11A and 2.11B. This region is the so-called Porod regime and can be used to calculate the surface area of a NC. In the Guinier regime, at small q values, the particle size (radius of gyration) can be extracted independently of the particle's shape with a linear fit of $\ln(I(x))$ versus q^2 plot. The constraint under which this approximation hold is $S(\mathbf{q}) = 1$, meaning that a diluted mixture without particle-particle interactions should be probed.

Lastly, at small q-values ($q \rightarrow 0$), $F(\mathbf{q})$ will be equal to $\Delta\rho V$ (eq. 10), and the scattering intensity in a dilute system will therefore scale with n, V^2, and $\Delta\rho^2$ (eq. 9). This means that at small q values, the intensity is independent of q. At these q values, distances are probed much larger than the dimensions of the NCs, effectively making the probed NCs zero-dimensional. This results in a power law of 0, that is, the intensity scales with q^0 for all particles at $qr \ll 1$. The q^0-dependent region occurs at larger q-values for the QDs compared to the NPLs, because the size of the QDs is much smaller than the NPLs. The onset of the q^0-dependent region can thus be used to distinguish between the two types of particles.

This section gave an overview of the theory behind SAXS and WAXS and methods to extract particle shape, size, concentration, etc. In chapters 4 and 5, SAXS and WAXS are used to elucidate the reaction mechanism of CdSe NPLs and $NaYF_4$ NPs. During both syntheses, multiple types of particles are present simultaneously. Additionally, the particles assemble even at high temperatures ($S(\mathbf{q}) \neq 1$). Consequently, elaborate models were used to fit the experimental data, as will be discussed in chapters 4 and 5.

References

1. Bayda, S.; Adeel, M.; Tuccinardi, T.; Cordani, M.; Rizzolio, F., The History of Nanoscience and Nanotechnology: From Chemical–Physical Applications to Nanomedicine. *Molecules* **2019,** *25* (1), 112.
2. Sciau, P., Nanoparticles in Ancient Materials: The Metallic Lustre Decorations of Medieval Ceramics. InTech: 2012.
3. Barber, D. J.; Freestone, I. C., An Investigation of The Origin of the Colour of the Lycurgus Cup by Analytical Transmission Electron Microscopy. *Archaeometry* **1990,** *32* (1), 33-45.
4. Reibold, M.; Paufler, P.; Levin, A. A.; Kochmann, W.; Pätzke, N.; Meyer, D. C., Carbon nanotubes in an ancient Damascus sabre. *Nature* **2006,** *444* (7117), 286-286.
5. Astruc, D., Introduction: Nanoparticles in Catalysis. *Chemical Reviews* **2020,** *120* (2), 461-463.
6. Geitenbeek, R. G.; Nieuwelink, A.-E.; Jacobs, T. S.; Salzmann, B. B. V.; Goetze, J.; Meijerink, A.; Weckhuysen, B. M., In Situ Luminescence Thermometry To Locally Measure Temperature Gradients during Catalytic Reactions. *ACS Catalysis* **2018,** *8* (3), 2397-2401.
7. Mangum, B. D.; Landes, T. S.; Theobald, B. R.; Kurtin, J. N., Exploring the bounds of narrow-band quantum dot downconverted LEDs. *Photonics Research* **2017,** *5* (2), A13-A22.
8. Yuan, Q.; Wang, T.; Yu, P.; Zhang, H.; Zhang, H.; Ji, W., A review on the electroluminescence properties of quantum-dot light-emitting diodes. *Organic Electronics* **2021,** *90*, 106086.
9. Estrada, D.; Shimizu, K.; Bohmer, M.; Gangwal, S.; Diederich, T.; Grabowski, S.; Tashjian, G.; Chamberlin, D.; Shchekin, O. B.; Bhardwaj, J., 32-1: On-chip Red Quantum Dots in White LEDs for General Illumination. *SID Symposium Digest of Technical Papers* **2018,** *49* (1), 405-408.
10. Kovalenko, M. V.; Manna, L.; Cabot, A.; Hens, Z.; Talapin, D. V.; Kagan, C. R.; Klimov, V. I.; Rogach, A. L.; Reiss, P.; Milliron, D. J.; Guyot-Sionnnest, P.; Konstantatos, G.; Parak, W. J.; Hyeon, T.; Korgel, B. A.; Murray, C. B.; Heiss, W., Prospects of Nanoscience with Nanocrystals. *ACS Nano* **2015,** *9* (2), 1012-1057.
11. Huang, X.; Jain, P. K.; El-Sayed, I. H.; El-Sayed, M. A., Gold nanoparticles: interesting optical properties and recent applications in cancer diagnostics and therapy. *Nanomedicine (Lond)* **2007,** *2* (5), 681-93.
12. Lee, K.-S.; El-Sayed, M. A., Gold and Silver Nanoparticles in Sensing and Imaging: Sensitivity of Plasmon Response to Size, Shape, and Metal Composition. *The Journal of Physical Chemistry B* **2006,** *110* (39), 19220-19225.
13. Issa, B.; Obaidat, I. M.; Albiss, B. A.; Haik, Y., Magnetic nanoparticles: surface effects and properties related to biomedicine applications. *Int J Mol Sci* **2013,** *14* (11), 21266-305.
14. Dave, S. R.; Gao, X., Monodisperse magnetic nanoparticles for biodetection, imaging, and drug delivery: a versatile and evolving technology. *WIREs Nanomedicine and Nanobiotechnology* **2009,** *1* (6), 583-609.

15. Wahajuddin; Arora, Superparamagnetic iron oxide nanoparticles: magnetic nanoplatforms as drug carriers. *International Journal of Nanomedicine* **2012**, 3445.
16. Vangijzegem, T.; Stanicki, D.; Laurent, S., Magnetic iron oxide nanoparticles for drug delivery: applications and characteristics. *Expert Opinion on Drug Delivery* **2019,** *16* (1), 69-78.
17. Filler, M. A., Semiconductors, Principles. In *Encyclopedia of Applied Electrochemistry*, Kreysa, G.; Ota, K.-i.; Savinell, R. F., Eds. Springer New York: New York, NY, 2014; pp 1953-1958.
18. Hofmann, P., *Solid state physics: an introduction*. John Wiley & Sons: 2022.
19. Benchamekh, R.; Gippius, N. A.; Even, J.; Nestoklon, M. O.; Jancu, J. M.; Ithurria, S.; Dubertret, B.; Efros, A. L.; Voisin, P., Tight-binding calculations of image-charge effects in colloidal nanoscale platelets of CdSe. *Physical Review B* **2014,** *89* (3), 035307.
20. Kittel, C., *Introduction to Solid State Physics*. 8th Edition ed.; John Wiley & Sons: New York, 2005.
21. Electrons in Solids. In *Foundations of Solid State Physics*, 2019; pp 173-223.
22. Ekimov, A. I.; Hache, F.; Schanne-Klein, M. C.; Ricard, D.; Flytzanis, C.; Kudryavtsev, I. A.; Yazeva, T. V.; Rodina, A. V.; Efros, A. L., Absorption and intensity-dependent photoluminescence measurements on CdSe quantum dots: assignment of the first electronic transitions. *J. Opt. Soc. Am. B* **1993,** *10* (1), 100-107.
23. Murphy, J. E.; Beard, M. C.; Norman, A. G.; Ahrenkiel, S. P.; Johnson, J. C.; Yu, P.; Mićić, O. I.; Ellingson, R. J.; Nozik, A. J., PbTe Colloidal Nanocrystals: Synthesis, Characterization, and Multiple Exciton Generation. *Journal of the American Chemical Society* **2006,** *128* (10), 3241-3247.
24. Ninomiya, S.; Adachi, S., Optical properties of cubic and hexagonal CdSe. *Journal of Applied Physics* **1995,** *78* (7), 4681-4689.
25. Rabouw, F. T.; De Mello Donega, C., Excited-State Dynamics in Colloidal Semiconductor Nanocrystals. *Topics in Current Chemistry* **2016,** *374* (5).
26. Efros, A. L.; Rosen, M., The Electronic Structure of Semiconductor Nanocrystals. *Annual Review of Materials Science* **2000,** *30* (1), 475-521.
27. Brus, L. E., Electron–electron and electron-hole interactions in small semiconductor crystallites: The size dependence of the lowest excited electronic state. *The Journal of Chemical Physics* **1984,** *80* (9), 4403-4409.
28. Ekimov, A. I.; Efros, A. L.; Onushchenko, A. A., Quantum size effect in semiconductor microcrystals. *Solid State Communications* **1985,** *56* (11), 921-924.
29. Ekimov, A. O., A. A. , Size quantization of the electron energy spectrum in a microscopic semiconductor crystal *JETP Letters* **1984,** *40*, 1136.
30. Murray, C. B.; Norris, D. J.; Bawendi, M. G., Synthesis and characterization of nearly monodisperse CdE (E = sulfur, selenium, tellurium) semiconductor nanocrystallites. *Journal of the American Chemical Society* **1993,** *115* (19), 8706-8715.
31. Ithurria, S.; Dubertret, B., Quasi 2D Colloidal CdSe Platelets with Thicknesses Controlled at the Atomic Level. **2008,** *130* (49), 16504-16505.
32. Peng, X.; Manna, L.; Yang, W.; Wickham, J.; Scher, E.; Kadavanich, A.; Alivisatos, A. P., Shape control of CdSe nanocrystals. *Nature* **2000,** *404* (6773), 59-61.
33. Alivisatos, A. P., Perspectives on the Physical Chemistry of Semiconductor Nanocrystals. *The Journal of Physical Chemistry* **1996,** *100* (31), 13226-13239.
34. Pokatilov, E. P.; Fonoberov, V. A.; Fomin, V. M.; Devreese, J. T., Development of an eight-band theory for quantum dot heterostructures. *Physical Review B* **2001,** *64* (24).
35. Efros, A. L.; Rosen, M., Quantum size level structure of narrow-gap semiconductor nanocrystals: Effect of band coupling. *Physical Review B* **1998,** *58* (11), 7120-7135.
36. Klimov, V. I., *Nanocrystal Quantum Dots, Second Edition*. CRC Press. : Boca Raton, 2017.
37. Norris, D. J.; Bawendi, M. G., Measurement and assignment of the size-dependent optical spectrum in CdSe quantum dots. *Physical Review B* **1996,** *53* (24), 16338-16346.
38. Ithurria, S.; Tessier, M. D.; Mahler, B.; Lobo, R. P. S. M.; Dubertret, B.; Efros, A. L., Colloidal nanoplatelets with two-dimensional electronic structure. *Nature Materials* **2011,** *10* (12), 936-941.
39. Pelant, I. V. J., *Luminescence spectroscopy of semiconductors*. Oxford University Press: Oxford, 2016.
40. Ji, B.; Rabani, E.; Efros, A. L.; Vaxenburg, R.; Ashkenazi, O.; Azulay, D.; Banin, U.; Millo, O., Dielectric Confinement and Excitonic Effects in Two-Dimensional Nanoplatelets. *ACS Nano* **2020,** *14* (7), 8257-8265.

41. Ithurria, S.; Bousquet, G.; Dubertret, B., Continuous Transition from 3D to 1D Confinement Observed during the Formation of CdSe Nanoplatelets. *Journal of the American Chemical Society* **2011,** *133* (9), 3070-3077.
42. Kumagai, M.; Takagahara, T., Excitonic and nonlinear-optical properties of dielectric quantum-well structures. *Physical Review B* **1989,** *40* (18), 12359-12381.
43. Tomar, R.; Kulkarni, A.; Chen, K.; Singh, S.; Van Thourhout, D.; Hodgkiss, J. M.; Siebbeles, L. D. A.; Hens, Z.; Geiregat, P., Charge Carrier Cooling Bottleneck Opens Up Nonexcitonic Gain Mechanisms in Colloidal CdSe Quantum Wells. *The Journal of Physical Chemistry C* **2019,** *123* (14), 9640-9650.
44. Guzelturk, B.; Martinez, P. L. H.; Zhang, Q.; Xiong, Q.; Sun, H.; Sun, X. W.; Govorov, A. O.; Demir, H. V., Excitonics of semiconductor quantum dots and wires for lighting and displays. *Laser & Photonics Reviews* **2014,** *8* (1), 73-93.
45. Geiregat, P.; Tomar, R.; Chen, K.; Singh, S.; Hodgkiss, J. M.; Hens, Z., Thermodynamic Equilibrium between Excitons and Excitonic Molecules Dictates Optical Gain in Colloidal CdSe Quantum Wells. *The Journal of Physical Chemistry Letters* **2019,** *10* (13), 3637-3644.
46. Anikeeva, P. O.; Halpert, J. E.; Bawendi, M. G.; Bulović, V., Quantum Dot Light-Emitting Devices with Electroluminescence Tunable over the Entire Visible Spectrum. *Nano Letters* **2009,** *9* (7), 2532-2536.
47. Kang, Y.; Song, Z.; Jiang, X.; Yin, X.; Fang, L.; Gao, J.; Su, Y.; Zhao, F., Quantum Dots for Wide Color Gamut Displays from Photoluminescence to Electroluminescence. *Nanoscale Research Letters* **2017,** *12* (1).
48. Purcell-Milton, F.; Gun'ko, Y. K., Quantum dots for Luminescent Solar Concentrators. *Journal of Materials Chemistry* **2012,** *22* (33), 16687-16697.
49. Bradshaw, L. R.; Knowles, K. E.; McDowall, S.; Gamelin, D. R., Nanocrystals for Luminescent Solar Concentrators. *Nano Letters* **2015,** *15* (2), 1315-1323.
50. Roh, J.; Park, Y.-S.; Lim, J.; Klimov, V. I., Optically pumped colloidal-quantum-dot lasing in LED-like devices with an integrated optical cavity. *Nature Communications* **2020,** *11* (1).
51. Lim, J.; Park, Y.-S.; Klimov, V. I., Optical gain in colloidal quantum dots achieved with direct-current electrical pumping. *Nature Materials* **2018,** *17* (1), 42-49.
52. Janjua, R. A.; Iqbal, O.; Ahmed, M. A.; Al-Kahtani, A. A.; Saeed, S.; Imran, M.; Wattoo, A. G., Homo–hetero/core–shell structure design strategy of NaYF4 nanocrystals for superior upconversion luminescence. *RSC Advances* **2021,** *11* (34), 20746-20751.
53. Vetrone, F.; Naccache, R.; Mahalingam, V.; Morgan, C. G.; Capobianco, J. A., The Active-Core/Active-Shell Approach: A Strategy to Enhance the Upconversion Luminescence in Lanthanide-Doped Nanoparticles. *Advanced Functional Materials* **2009,** *19* (18), 2924-2929.
54. Yi, G.-S.; Chow, G.-M., Water-Soluble NaYF4:Yb,Er(Tm)/NaYF4/Polymer Core/Shell/Shell Nanoparticles with Significant Enhancement of Upconversion Fluorescence. *Chemistry of Materials* **2007,** *19* (3), 341-343.
55. De Mello Donegá, C., Formation of nanoscale spatially indirect excitons: Evolution of the type-II optical character of CdTe/CdSe heteronanocrystals. *Physical Review B* **2010,** *81* (16).
56. Donegá, C. D. M., Synthesis and properties of colloidal heteronanocrystals. *Chem. Soc. Rev.* **2011,** *40* (3), 1512-1546.
57. Park, Y.-S.; Bae, W. K.; Pietryga, J. M.; Klimov, V. I., Auger Recombination of Biexcitons and Negative and Positive Trions in Individual Quantum Dots. *ACS Nano* **2014,** *8* (7), 7288-7296.
58. Vaxenburg, R.; Rodina, A.; Lifshitz, E.; Efros, A. L., Biexciton Auger Recombination in CdSe/CdS Core/Shell Semiconductor Nanocrystals. *Nano Letters* **2016,** *16* (4), 2503-2511.
59. Bae, W. K.; Park, Y.-S.; Lim, J.; Lee, D.; Padilha, L. A.; McDaniel, H.; Robel, I.; Lee, C.; Pietryga, J. M.; Klimov, V. I., Controlling the influence of Auger recombination on the performance of quantum-dot light-emitting diodes. *Nature Communications* **2013,** *4* (1).
60. Meinardi, F.; McDaniel, H.; Carulli, F.; Colombo, A.; Velizhanin, K. A.; Makarov, N. S.; Simonutti, R.; Klimov, V. I.; Brovelli, S., Highly efficient large-area colourless luminescent solar concentrators using heavy-metal-free colloidal quantum dots. *Nature Nanotechnology* **2015,** *10* (10), 878-885.
61. Ivanov, S. A.; Piryatinski, A.; Nanda, J.; Tretiak, S.; Zavadil, K. R.; Wallace, W. O.; Werder, D.; Klimov, V. I., Type-II Core/Shell CdS/ZnSe Nanocrystals: Synthesis, Electronic Structures, and Spectroscopic Properties. *Journal of the American Chemical Society* **2007,** *129* (38), 11708-11719.
62. Reiss, P.; Protière, M.; Li, L., Core/Shell Semiconductor Nanocrystals. *Small* **2009,** *5* (2), 154-168.

63. Lin, C.; Gong, K.; Kelley, D. F.; Kelley, A. M., Electron-Phonon Coupling in CdSe/CdS Core/Shell Quantum Dots. *ACS Nano* **2015,** *9* (8), 8131-41.
64. Achtstein, A. W.; Marquardt, O.; Scott, R.; Ibrahim, M.; Riedl, T.; Prudnikau, A. V.; Antanovich, A.; Owschimikow, N.; Lindner, J. K. N.; Artemyev, M.; Woggon, U., Impact of Shell Growth on Recombination Dynamics and Exciton–Phonon Interaction in CdSe–CdS Core–Shell Nanoplatelets. *ACS Nano* **2018,** *12* (9), 9476-9483.
65. Cui, J.; Beyler, A. P.; Coropceanu, I.; Cleary, L.; Avila, T. R.; Chen, Y.; Cordero, J. M.; Heathcote, S. L.; Harris, D. K.; Chen, O.; Cao, J.; Bawendi, M. G., Evolution of the Single-Nanocrystal Photoluminescence Linewidth with Size and Shell: Implications for Exciton–Phonon Coupling and the Optimization of Spectral Linewidths. *Nano Letters* **2016,** *16* (1), 289-296.
66. Krumer, Z.; Pera, S. J.; van Dijk-Moes, R. J. A.; Zhao, Y.; de Brouwer, A. F. P.; Groeneveld, E.; van Sark, W. G. J. H. M.; Schropp, R. E. I.; de Mello Donegá, C., Tackling self-absorption in luminescent solar concentrators with type-II colloidal quantum dots. *Solar Energy Materials and Solar Cells* **2013,** *111*, 57-65.
67. García-Santamaría, F.; Chen, Y.; Vela, J.; Schaller, R. D.; Hollingsworth, J. A.; Klimov, V. I., Suppressed Auger Recombination in "Giant" Nanocrystals Boosts Optical Gain Performance. *Nano Letters* **2009,** *9* (10), 3482-3488.
68. Lee, J. H., QD Display: A Game-Changing Technology for the Display Industry. *Information Display* **2020,** *36* (6), 9-13.
69. Tessier, M. D.; Javaux, C.; Maksimovic, I.; Loriette, V.; Dubertret, B., Spectroscopy of Single CdSe Nanoplatelets. *ACS Nano* **2012,** *6* (8), 6751-6758.
70. Gellen, T. A.; Lem, J.; Turner, D. B., Probing Homogeneous Line Broadening in CdSe Nanocrystals Using Multidimensional Electronic Spectroscopy. *Nano Letters* **2017,** *17* (5), 2809-2815.
71. Wong, C. Y.; Scholes, G. D., Biexcitonic Fine Structure of CdSe Nanocrystals Probed by Polarization-Dependent Two-Dimensional Photon Echo Spectroscopy. *The Journal of Physical Chemistry A* **2011,** *115* (16), 3797-3806.
72. Empedocles, S. A.; Bawendi, M. G., Quantum-Confined Stark Effect in Single CdSe Nanocrystallite Quantum Dots. *Science* **1997,** *278* (5346), 2114-2117.
73. Fernée, M. J.; Plakhotnik, T.; Louyer, Y.; Littleton, B. N.; Potzner, C.; Tamarat, P.; Mulvaney, P.; Lounis, B., Spontaneous Spectral Diffusion in CdSe Quantum Dots. *The Journal of Physical Chemistry Letters* **2012,** *3* (12), 1716-1720.
74. Klingshirn, C. F., *Semiconductor optics*. 1995.
75. Empedocles, S. A.; Norris, D. J.; Bawendi, M. G., Photoluminescence Spectroscopy of Single CdSe Nanocrystallite Quantum Dots. *Physical Review Letters* **1996,** *77* (18), 3873-3876.
76. Cui, J.; Beyler, A. P.; Marshall, L. F.; Chen, O.; Harris, D. K.; Wanger, D. D.; Brokmann, X.; Bawendi, M. G., Direct probe of spectral inhomogeneity reveals synthetic tunability of single-nanocrystal spectral linewidths. *Nature Chemistry* **2013,** *5* (7), 602-606.
77. Henderson, B.; Imbusch, G. F., *Optical Spectroscopy of Inorganic Solids*. Clarendon Press: 2006; p 199-238.
78. Brodu, A.; Ballottin, M. V.; Buhot, J.; Dupont, D.; Tessier, M.; Hens, Z.; Rabouw, F. T.; Christianen, P. C. M.; de Mello Donega, C.; Vanmaekelbergh, D., Exciton-phonon coupling in InP quantum dots with ZnS and (Zn, Cd) Se shells. *Physical Review B* **2020,** *101* (12), 125413.
79. Kelley, A. M., Exciton-optical phonon coupling in II-VI semiconductor nanocrystals. *J Chem Phys* **2019,** *151* (14), 140901.
80. Lin, C.; Gong, K.; Kelley, D. F.; Kelley, A. M., Size-Dependent Exciton–Phonon Coupling in CdSe Nanocrystals through Resonance Raman Excitation Profile Analysis. *The Journal of Physical Chemistry C* **2015,** *119* (13), 7491-7498.
81. Takagahara, T., theory of exciton dephasing in QDs. *Physical Review B* **1999,** *60* (4), 2639 – 2652.
82. Takagahara, T., Electron—phonon interactions in semiconductor nanocrystals. *Journal of Luminescence* **1996,** *70* (1-6), 129-143.
83. Salvador, M. R.; Graham, M. W.; Scholes, G. D., Exciton-phonon coupling and disorder in the excited states of CdSe colloidal quantum dots. *The Journal of Chemical Physics* **2006,** *125* (18), 184709.
84. Soloviev, V. N.; Eichhöfer, A.; Fenske, D.; Banin, U., Size-Dependent Optical Spectroscopy of a Homologous Series of CdSe Cluster Molecules. *Journal of the American Chemical Society* **2001,** *123* (10), 2354-2364.

85. Voznyy, O.; Mokkath, J. H.; Jain, A.; Sargent, E. H.; Schwingenschlögl, U., Computational Study of Magic-Size CdSe Clusters with Complementary Passivation by Carboxylic and Amine Ligands. *The Journal of Physical Chemistry C* **2016,** *120* (18), 10015-10019.
86. Muckel, F.; Lorenz, S.; Yang, J.; Nugraha, T. A.; Scalise, E.; Hyeon, T.; Wippermann, S.; Bacher, G., Exciton-driven change of phonon modes causes strong temperature dependent bandgap shift in nanoclusters. *Nat Commun* **2020,** *11* (1), 4127.
87. Liu, S.; Shu, Y.; Zhu, M.; Qin, H.; Peng, X., Anomalous Emission Shift of CdSe/CdS/ZnS Quantum Dots at Cryogenic Temperatures. *Nano Letters* **2022,** *22* (7), 3011-3017.
88. Mittleman, D. M.; Schoenlein, R. W.; Shiang, J. J.; Colvin, V. L.; Alivisatos, A. P.; Shank, C. V., Quantum size dependence of femtosecond electronic dephasing and vibrational dynamics in CdSe nanocrystals. *Physical Review B* **1994,** *49* (20), 14435-14447.
89. Salvador, M. R.; Hines, M. A.; Scholes, G. D., Exciton–bath coupling and inhomogeneous broadening in the optical spectroscopy of semiconductor quantum dots. *The Journal of Chemical Physics* **2003,** *118* (20), 9380-9388.
90. Shim, M.; Guyot-Sionnest, P., Intraband hole burning of colloidal quantum dots. *Physical Review B* **2001,** *64* (24), 245342.
91. Takagahara, T., Theory of Exciton Dephasing in Semiconductor Quantum Dots. Springer Berlin Heidelberg: 2002; pp 353-388.
92. Li, J. J.; Wang, Y. A.; Guo, W.; Keay, J. C.; Mishima, T. D.; Johnson, M. B.; Peng, X., Large-Scale Synthesis of Nearly Monodisperse CdSe/CdS Core/Shell Nanocrystals Using Air-Stable Reagents via Successive Ion Layer Adsorption and Reaction. *Journal of the American Chemical Society* **2003,** *125* (41), 12567-12575.
93. Kovalenko, M. V.; Bodnarchuk, M. I.; Zaumseil, J.; Lee, J.-S.; Talapin, D. V., Expanding the Chemical Versatility of Colloidal Nanocrystals Capped with Molecular Metal Chalcogenide Ligands. *Journal of the American Chemical Society* **2010,** *132* (29), 10085-10092.
94. Dubois, F.; Mahler, B.; Dubertret, B.; Doris, E.; Mioskowski, C., A Versatile Strategy for Quantum Dot Ligand Exchange. *Journal of the American Chemical Society* **2007,** *129* (3), 482-483.
95. Owen, J. S.; Chan, E. M.; Liu, H.; Alivisatos, A. P., Precursor Conversion Kinetics and the Nucleation of Cadmium Selenide Nanocrystals. *Journal of the American Chemical Society* **2010,** *132* (51), 18206-18213.
96. Rempel, J. Y.; Bawendi, M. G.; Jensen, K. F., Insights into the Kinetics of Semiconductor Nanocrystal Nucleation and Growth. **2009,** *131* (12), 4479-4489.
97. De Mello Donegá, C.; Liljeroth, P.; Vanmaekelbergh, D., Physicochemical Evaluation of the Hot-Injection Method, a Synthesis Route for Monodisperse Nanocrystals. *Small* **2005,** *1* (12), 1152-1162.
98. Rinkel, T.; Nordmann, J.; Raj, A. N.; Haase, M., Ostwald-ripening and particle size focussing of sub-10 nm NaYF(4) upconversion nanocrystals. *Nanoscale* **2014,** *6* (23), 14523-30.
99. Liu, C.; Wang, H.; Li, X.; Chen, D., Monodisperse, size-tunable and highly efficient β-NaYF4:Yb,Er(Tm) up-conversion luminescent nanospheres: controllable synthesis and their surface modifications. *Journal of Materials Chemistry* **2009,** *19*, 3546-3553.
100. Rinkel, T.; Raj, A. N.; Duhnen, S.; Haase, M., Synthesis of 10 nm beta-NaYF4:Yb,Er/NaYF4 Core/Shell Upconversion Nanocrystals with 5 nm Particle Cores. *Angew Chem Int Ed Engl* **2016,** *55* (3), 1164-7.
101. Karthika, S.; Radhakrishnan, T. K.; Kalaichelvi, P., A Review of Classical and Nonclassical Nucleation Theories. *Crystal Growth & Design* **2016,** *16* (11), 6663-6681.
102. Strey, R.; Wagner, P. E.; Viisanen, Y., The Problem of Measuring Homogeneous Nucleation Rates and the Molecular Contents of Nuclei: Progress in the Form of Nucleation Pulse Measurements. *The Journal of Physical Chemistry* **1994,** *98* (32), 7748-7758.
103. Whitehead, C. B.; Özkar, S.; Finke, R. G., LaMer's 1950 Model for Particle Formation of Instantaneous Nucleation and Diffusion-Controlled Growth: A Historical Look at the Model's Origins, Assumptions, Equations, and Underlying Sulfur Sol Formation Kinetics Data. *Chemistry of Materials* **2019,** *31* (18), 7116-7132.
104. Groeneveld, E.; de Mello Donegá, C., The Challenge of Colloidal Nanoparticle Synthesis. In *Nanoparticles: Workhorses of Nanoscience*, de Mello Donegá, C., Ed. Springer Berlin Heidelberg: Berlin, Heidelberg, 2014; pp 145-189.
105. Kwon, S. G.; Hyeon, T., Formation Mechanisms of Uniform Nanocrystals via Hot-Injection and Heat-Up Methods. *Small* **2011,** *7* (19), 2685-2702.

106. Peng, X.; Wickham, J.; Alivisatos, A. P., Kinetics of II-VI and III-V Colloidal Semiconductor Nanocrystal Growth: "Focusing" of Size Distributions. *Journal of the American Chemical Society* **1998,** *120* (21), 5343-5344.
107. Lamer, V. K.; Dinegar, R. H., Theory, Production and Mechanism of Formation of Monodispersed Hydrosols. *Journal of the American Chemical Society* **1950,** *72* (11), 4847-4854.
108. Whitehead, C. B.; Özkar, S.; Finke, R. G., LaMer's 1950 model of particle formation: a review and critical analysis of its classical nucleation and fluctuation theory basis, of competing models and mechanisms for phase-changes and particle formation, and then of its application to silver halide, s. *Materials Advances* **2021,** *2* (1), 186-235.
109. Watzky, M. A.; Finke, R. G., Transition Metal Nanocluster Formation Kinetic and Mechanistic Studies. A New Mechanism When Hydrogen Is the Reductant: Slow, Continuous Nucleation and Fast Autocatalytic Surface Growth. *Journal of the American Chemical Society* **1997,** *119* (43), 10382-10400.
110. Finney, E. E.; Finke, R. G., Nanocluster nucleation and growth kinetic and mechanistic studies: A review emphasizing transition-metal nanoclusters. *Journal of Colloid and Interface Science* **2008,** *317* (2), 351-374.
111. Prins, P. T.; Montanarella, F.; Dümbgen, K.; Justo, Y.; Van Der Bok, J. C.; Hinterding, S. O. M.; Geuchies, J. J.; Maes, J.; De Nolf, K.; Deelen, S.; Meijer, H.; Zinn, T.; Petukhov, A. V.; Rabouw, F. T.; De Mello Donega, C.; Vanmaekelbergh, D.; Hens, Z., Extended Nucleation and Superfocusing in Colloidal Semiconductor Nanocrystal Synthesis. *Nano Letters* **2021,** *21* (6), 2487-2496.
112. Van Embden, J.; Chesman, A. S. R.; Jasieniak, J. J., The Heat-Up Synthesis of Colloidal Nanocrystals. *Chemistry of Materials* **2015,** *27* (7), 2246-2285.
113. Wang, F.; Tang, R.; Buhro, W. E., The Trouble with TOPO; Identification of Adventitious Impurities Beneficial to the Growth of Cadmium Selenide Quantum Dots, Rods, and Wires. *Nano Letters* **2008,** *8* (10), 3521-3524.
114. Evans, C. M.; Evans, M. E.; Krauss, T. D., Mysteries of TOPSe revealed: insights into quantum dot nucleation. *Journal of the American Chemical Society* **2010,** *132* (32), 10973-10975.
115. Lyashchova, A.; Dmytruk, A.; Dmitruk, I.; Klimusheva, G.; Mirnaya, T.; Asaula, V., Optical absorption, induced bleaching, and photoluminescence of CdSe nanoplatelets grown in cadmium octanoate matrix. *Nanoscale Research Letters* **2014,** *9* (1), 88.
116. Chen, Y.; Chen, D.; Li, Z.; Peng, X., Symmetry-Breaking for Formation of Rectangular CdSe Two-Dimensional Nanocrystals in Zinc-Blende Structure. *Journal of the American Chemical Society* **2017,** *139* (29), 10009-10019.
117. Riedinger, A.; Ott, F. D.; Mule, A.; Mazzotti, S.; Knüsel, P. N.; Stephan; Prins, F.; Erwin, S. C.; Norris, D. J., An intrinsic growth instability in isotropic materials leads to quasi-two-dimensional nanoplatelets. *Nature Materials* **2017,** *16* (7), 743-748.
118. Van Der Stam, W.; Rabouw, F. T.; Geuchies, J. J.; Berends, A. C.; Hinterding, S. O. M.; Geitenbeek, R. G.; Van Der Lit, J.; Prévost, S.; Petukhov, A. V.; De Mello Donega, C., In Situ Probing of Stack-Templated Growth of Ultrathin Cu2–xS Nanosheets. *Chemistry of Materials* **2016,** *28* (17), 6381-6389.
119. Castro, N.; Bouet, C.; Ithurria, S.; Lequeux, N.; Constantin, D.; Levitz, P.; Pontoni, D.; Abecassis, B., Insights into the Formation Mechanism of CdSe Nanoplatelets Using in Situ X-ray Scattering. *Nano Lett* **2019,** *19* (9), 6466-6474.
120. Morrison, P. J.; Loomis, R. A.; Buhro, W. E., Synthesis and Growth Mechanism of Lead Sulfide Quantum Platelets in Lamellar Mesophase Templates. *Chemistry of Materials* **2014,** *26* (17), 5012-5019.
121. Liu, Y.-H.; Wang, F.; Wang, Y.; Gibbons, P. C.; Buhro, W. E., Lamellar Assembly of Cadmium Selenide Nanoclusters into Quantum Belts. *Journal of the American Chemical Society* **2011,** *133* (42), 17005-17013.
122. Cho, K.-S.; Talapin, D. V.; Gaschler, W.; Murray, C. B., Designing PbSe Nanowires and Nanorings through Oriented Attachment of Nanoparticles. *Journal of the American Chemical Society* **2005,** *127* (19), 7140-7147.
123. Berends, A. C.; De Mello Donega, C., Ultrathin One- and Two-Dimensional Colloidal Semiconductor Nanocrystals: Pushing Quantum Confinement to the Limit. *The Journal of Physical Chemistry Letters* **2017,** *8* (17), 4077-4090.
124. Wang, F.; Wang, Y.; Liu, Y.-H.; Morrison, P. J.; Loomis, R. A.; Buhro, W. E., Two-Dimensional Semiconductor Nanocrystals: Properties, Templated Formation, and Magic-Size Nanocluster Intermediates. *Accounts of Chemical Research* **2015,** *48* (1), 13-21.

125. Schliehe, C.; Juarez, B. H.; Pelletier, M.; Jander, S.; Greshnykh, D.; Nagel, M.; Meyer, A.; Foerster, S.; Kornowski, A.; Klinke, C.; Weller, H., Ultrathin PbS Sheets by Two-Dimensional Oriented Attachment. *Science* **2010,** *329* (5991), 550-553.
126. Salzmann, B. B. V.; van der Sluijs, M. M.; Soligno, G.; Vanmaekelbergh, D., Oriented Attachment: From Natural Crystal Growth to a Materials Engineering Tool. *Accounts of Chemical Research* **2021,** *54* (4), 787-797.
127. Bouet, C.; Mahler, B.; Nadal, B.; Abecassis, B.; Tessier, M. D.; Ithurria, S.; Xu, X.; Dubertret, B., Two-Dimensional Growth of CdSe Nanocrystals, from Nanoplatelets to Nanosheets. *Chemistry of Materials* **2013,** *25* (4), 639-645.
128. Jiang, Y.; Ojo, W.-S.; Mahler, B.; Xu, X.; Abécassis, B.; Dubertret, B., Synthesis of CdSe Nanoplatelets without Short-Chain Ligands: Implication for Their Growth Mechanisms. *ACS Omega* **2018,** *3* (6), 6199-6205.
129. Suter, J. D.; Pekas, N. J.; Berry, M. T.; May, P. S., Real-Time-Monitoring of the Synthesis of β-NaYF4:17% Yb,3% Er Nanocrystals Using NIR-to-Visible Upconversion Luminescence. *The Journal of Physical Chemistry C* **2014,** *118* (24), 13238-13247.
130. Liu, S.; De, G.; Xu, Y.; Wang, X.; Liu, Y.; Cheng, C.; Wang, J., Size, phase-controlled synthesis, the nucleation and growth mechanisms of NaYF4:Yb/Er nanocrystals. *Journal of Rare Earths* **2018,** *36* (10), 1060-1066.
131. Radunz, S.; Schavkan, A.; Wahl, S.; Würth, C.; Tschiche, H. R.; Krumrey, M.; Resch-Genger, U., Evolution of Size and Optical Properties of Upconverting Nanoparticles during High-Temperature Synthesis. *The Journal of Physical Chemistry C* **2018,** *122* (50), 28958-28967.
132. Naduviledathu Raj, A.; Rinkel, T.; Haase, M., Ostwald Ripening, Particle Size Focusing, and Decomposition of Sub-10 nm NaREF4 (RE = La, Ce, Pr, Nd) Nanocrystals. *Chemistry of Materials* **2014,** *26* (19), 5689-5694.
133. Voss, B.; Haase, M., Intrinsic Focusing of the Particle Size Distribution in Colloids Containing Nanocrystals of Two Different Crystal Phases. *ACS Nano* **2013,** *7* (12), 11242-11254.
134. May, P. B.; Suter, J. D.; May, P. S.; Berry, M. T., The Dynamics of Nanoparticle Growth and Phase Change During Synthesis of β-NaYF4. *The Journal of Physical Chemistry C* **2016,** *120* (17), 9482-9489.
135. Sui, Y.; Tao, K.; Tian, Q.; Sun, K., Interaction Between Y3+ and Oleate Ions for the Cubic-to-Hexagonal Phase Transformation of NaYF4 Nanocrystals. *The Journal of Physical Chemistry C* **2012,** *116* (2), 1732-1739.
136. Rastogi, C. K.; Lu, E.; Tam, J.; Pichaandi, J. M.; Howe, J.; Winnik, M. A., Influence of the Sodium Precursor on the Cubic-to-Hexagonal Phase Transformation and Controlled Preparation of Uniform NaNdF4 Nanoparticles. *Langmuir* **2021,** *37* (6), 2146-2152.
137. Geuchies, J. J.; Van Overbeek, C.; Evers, W. H.; Goris, B.; De Backer, A.; Gantapara, A. P.; Rabouw, F. T.; Hilhorst, J.; Peters, J. L.; Konovalov, O.; Petukhov, A. V.; Dijkstra, M.; Siebbeles, L. D. A.; Van Aert, S.; Bals, S.; Vanmaekelbergh, D., In situ study of the formation mechanism of two-dimensional superlattices from PbSe nanocrystals. *Nature Materials* **2016,** *15* (12), 1248-1254.
138. Van Aert, S.; Verbeeck, J.; Erni, R.; Bals, S.; Luysberg, M.; Dyck, D. V.; Tendeloo, G. V., Quantitative atomic resolution mapping using high-angle annular dark field scanning transmission electron microscopy. *Ultramicroscopy* **2009,** *109* (10), 1236-1244.
139. Abel, K. A.; Boyer, J.-C.; Andrei, C. M.; Van Veggel, F. C. J. M., Analysis of the Shell Thickness Distribution on NaYF4/NaGdF4 Core/Shell Nanocrystals by EELS and EDS. *The Journal of Physical Chemistry Letters* **2011,** *2* (3), 185-189.
140. Van Der Stam, W.; Berends, A. C.; Rabouw, F. T.; Willhammar, T.; Ke, X.; Meeldijk, J. D.; Bals, S.; De Mello Donega, C., Luminescent CuInS₂ Quantum Dots by Partial Cation Exchange in Cu_{2–x}S Nanocrystals. *Chemistry of Materials* **2015,** *27* (2), 621-628.
141. De Mello Donegá, C.; Koole, R., Size Dependence of the Spontaneous Emission Rate and Absorption Cross Section of CdSe and CdTe Quantum Dots. *The Journal of Physical Chemistry C* **2009,** *113* (16), 6511-6520.
142. Maes, J.; Castro, N.; De Nolf, K.; Walravens, W.; Abécassis, B.; Hens, Z., Size and Concentration Determination of Colloidal Nanocrystals by Small-Angle X-ray Scattering. *Chemistry of Materials* **2018,** *30* (12), 3952-3962.
143. Peters, J. L.; De Wit, J.; Vanmaekelbergh, D., Sizing Curve, Absorption Coefficient, Surface Chemistry, and Aliphatic Chain Structure of PbTe Nanocrystals. *Chemistry of Materials* **2019,** *31* (5), 1672-1680.
144. Yu, W. W.; Qu, L.; Guo, W.; Peng, X., Experimental Determination of the Extinction Coefficient of CdTe, CdSe, and CdS Nanocrystals. *Chemistry of Materials* **2003,** *15* (14), 2854-2860.
145. Cademartiri, L.; Montanari, E.; Calestani, G.; Migliori, A.; Guagliardi, A.; Ozin, G. A., Size-Dependent Extinction Coefficients of PbS Quantum Dots. *Journal of the American Chemical Society* **2006,** *128* (31), 10337-10346.

146. Craievich, A. F., Small-Angle X-ray Scattering by Nanostructured Materials. Springer International Publishing: 2018; pp 1185-1230.
147. Lamas, D. G.; De Oliveira Neto, M.; Kellermann, G.; Craievich, A. F., X-Ray Diffraction and Scattering by Nanomaterials. Elsevier: 2017; pp 111-182.
148. Li, T.; Senesi, A. J.; Lee, B., Small Angle X-ray Scattering for Nanoparticle Research. *Chemical Reviews* **2016,** *116* (18), 11128-11180.
149. Als-Nielsen, J., Mcmorrow, D. , *Elements of Modern X-ray Physics*. John Wiley & Sons, Inc.: 2011.
150. Kostiv, U.; Engstova, H.; Krajnik, B.; Slouf, M.; Proks, V.; Podhorodecki, A.; Jezek, P.; Horak, D., Monodisperse Core-Shell NaYF(4):Yb(3+)/Er(3+)@NaYF(4):Nd(3+)-PEG-GGGRGDSGGGY-NH(2) Nanoparticles Excitable at 808 and 980 nm: Design, Surface Engineering, and Application in Life Sciences. *Front Chem* **2020,** *8* (497), 497.
151. Perera, S. S.; Amarasinghe, D. K.; Dissanayake, K. T.; Rabuffetti, F. A., Average and Local Crystal Structure of β-Er:Yb:NaYF4 Upconverting Nanocrystals Probed by X-ray Total Scattering. *Chemistry of Materials* **2017,** *29* (15), 6289-6297.
152. Patterson, A. L., The Scherrer Formula for X-Ray Particle Size Determination. *Physical Review* **1939,** *56* (10), 978-982.
153. Langford, J. I.; Wilson, A. J. C., Scherrer after sixty years: A survey and some new results in the determination of crystallite size. *Journal of Applied Crystallography* **1978,** *11* (2), 102-113.
154. Renaud, G.; Lazzari, R.; Leroy, F., Probing surface and interface morphology with Grazing Incidence Small Angle X-Ray Scattering. *Surface Science Reports* **2009,** *64* (8), 255-380.
155. Beaucage, G., Approximations Leading to a Unified Exponential/Power-Law Approach to Small-Angle Scattering. *Journal of Applied Crystallography* **1995,** *28* (6), 717-728.

I would like to thank M.L.J. Peerlings and D.M. Dekker for performing the low temperature measurement under my supervision, and B.B.V. Salzmann for providing the NPL samples.

Chapter 3

Luminescence Line Broadening of CdSe Nanoplatelets and Quantum Dots for Application in w-LEDs

Bases on:

Johanna C. van der Bok, Daphne M. Dekker, Matt L. J. Peerlings, Bastiaan B. V. Salzmann, and Andries Meijerink, J. Phys. Chem. C 2020, 124, 22, 12153–12160.

Abstract

Nanoplatelets (NPLs) of CdSe are an emerging class of luminescent materials, combining tunable and narrow emission bands with high quantum yields. This is promising for application in white light LEDs (w-LEDs) and displays. The origin of the narrow spectral width of exciton emission in core NPL compared to core-shell NPL and quantum dot (QD) emission is not fully understood. Here we investigate and compare temperature-dependent emission spectra of core and core-shell CdSe NPLs and QDs. A wide temperature range, 4 – 423 K, is chosen to gain insight into contributions from homogeneous and inhomogeneous broadening and also to extend measurements into a temperature regime that is relevant for operating conditions in w-LEDs (T ≈ 423 K). The results show that temperature-induced homogeneous broadening does not strongly vary between the various CdSe nanostructures ($\Delta E_{hom} \approx 60 - 80$ meV at 423 K), indicating that electron-phonon coupling strengths are similar. Only for the smallest QDs is stronger exciton-phonon coupling observed. The origin of the narrow bandwidth reported at 300 K for core CdSe NPLs is attributed to the absence of inhomogeneous broadening. At 423 K, the spectral width of NPL exciton emission is still narrower than that of QDs. A comparison with traditional w-LED phosphors is made to outline advantages (tunability, narrow bandwidth, high efficiency) and disadvantages (color shift, stability issues) of NPLs for application in w-LEDs.

3.1 Introduction

In the past decade, a revolution in lighting has transformed the lighting market to a market dominated by w-LEDs. The ban on incandescent lamps has contributed to this rapid transition. In addition, the high efficacy of w-LEDs (>100 lm/W), compactness, and long life time (>30 000 h) make w-LEDs an attractive and flexible form of lighting in homes, offices and for outdoor illumination. The first generation of w-LEDs relied on generating white light from an efficient blue (In,Ga)N LED and partial blue-to-yellow conversion by the YAG:Ce phosphor. However, this design results in cold white light due to the lack of orange/red emission.[1] A remedy for the unpleasant cold color temperature was found by combining YAG:Ce with orange/red emitting phosphors. The most widely used phosphors nowadays rely on d–f emission from the lanthanide ions Eu^{2+} or Ce^{3+} and are characterized by relatively broad emission bands in the green, yellow, orange, or red spectral region.[1] There is, however, a need for narrower band emitters to increase the efficacy of w-LEDs and improve the color gamut of LCD displays with w-LED backlights. Especially for the traditional red emitting phosphors, the broad emission band has a significant part of the emitted light in the wavelength region beyond 630 nm.[2] The sensitivity of the human eye drops sharply between 630 and 700 nm, thus making displays and w-LEDs less efficient (reduced lumen/W efficacy). Hence, there is a need for narrow-band red emitters. This can be achieved by using semiconductor nanoparticles (NPs) such as CdSe or InP quantum QDs.[3, 4] The success of these NPs has already been demonstrated in the QLED displays of Samsung.[5] The use of both a narrow band green and red emitter increases the efficiency and widens the color gamut of these displays significantly. Still, there is a need for further reducing the spectral width.

A promising subclass of the semiconductor nanomaterials are CdSe NPLs which exhibit an even narrower emission bandwidth compared to zero-dimensional (0D) QDs.[6] The charge carriers in 2D NPLs are only confined in one dimension. Recent publications have reported on efficient visible emission from CdSe NPLs of only a few monolayers thick. The atomically

well-defined nature of the thickness (typically 3.5 or 4.5 monolayers) minimizes inhomogeneous broadening, giving rise to narrow emission bands around 460 nm (3.5 monolayers) or 510 nm (4.5 monolayers).[6] Full width at half maximum (fwhm) as narrow as ~40 meV[7] has been reported at room temperature compared to ~70-120 meV for CdSe quantum dots.[8-10] In order to increase the quantum yield and stability and to tune the photoluminescence (PL) towards the red, a CdS shell is grown around NPLs. However, upon introducing a shell, the characteristic narrow bandwidth of CdSe NPLs is lost.[11] Contradictory explanations have been proposed for this increase in broadening. The broadening is either ascribed to stronger exciton phonon-coupling due to the CdS shell[12] or ascribed to an increase in inhomogeneous broadening caused by a no longer atomically well-defined NPL.[13]

Temperature-dependent studies can help to distinguish between the contributions of homogeneous and inhomogeneous broadening. Studies on thermal line broadening of CdSe NPL emission are typically limited to measurements up to room temperature.[14, 15] However, temperatures relevant for application in lamps and displays are much higher, even exceeding 150 °C in high power w-LEDs. At elevated temperatures, homogeneous broadening due to exciton-phonon coupling dominates over inhomogeneous broadening. It is therefore important to extend the temperature range and investigate the broadening of CdSe NPL and QD emission over a wide range of temperatures, up to 150 °C. The wider temperature range is not only relevant for practical applications but also extends the range in which thermal broadening can be investigated and compared to gain insight into differences between thermal broadening and exciton-phonon coupling in the different CdSe nanostructures. Finally, high-temperature measurements will allow for the comparison of spectral widths for NPL emission and other luminescent materials used in w-LEDs (QDs, Mn^{4+}- or Eu^{2+}-phosphors) under relevant operation conditions to evaluate if NPLs still have better performance at the elevated temperatures in w-LEDs.

In this report, we investigate and compare thermal exciton luminescence line broadening in a variety of CdSe nanostructures, *viz.*, CdSe QDs and NPLs and CdSe/CdS core/shell QDs and NPLs. PL spectra were recorded, and the PL bandwidths of QDs and NPLs of different sizes and shell thicknesses were determined in a wide temperature regime, from 4 to 423 K (150 °C). The results show that homogeneous broadening is rather similar for the different types of CdSe nanomaterials and that the reduced emission bandwidth for core CdSe NPLs is caused by strongly reduced inhomogeneous broadening. Shell growth on NPLs gives rise to more inhomogeneous broadening and explains the increased broadening of core-shell NPLs in comparison to core-only NPLs.

3.2 Results and discussion

The spectral line width of emission from an ensemble of emitters is affected by inhomogeneous and homogeneous broadening. Inhomogeneous broadening is caused by a variation in emission wavelength between different emitters, for example, due to size variations in the NPs. Inhomogeneous broadening is not strongly temperature dependent. Homogeneous broadening for exciton emission in QDs and NPLs is dominated by lifetime broadening. The Heisenberg uncertainty principle dictates that a shorter coherence lifetime of the excited and ground state gives rise to a larger uncertainty in the transition energy (emission wavelength). The main cause for a rapidly decreasing coherence lifetime upon heating is interaction with phonons (lattice vibrations). Phonon absorption, emission, and phonon scattering (Raman) processes contribute to a shortening of the coherence lifetime (dephasing time). The phonon-induced exciton

dephasing processes are strongly temperature dependent and are responsible for homogeneous line broadening of the exciton emission with temperature as the phonon population increases. The temperature dependence is complex as different types of phonon dephasing processes have a different temperature dependence.[16]

Interaction with phonons also affects the position of the PL maximum. The shift of the PL maximum is influenced by various mechanisms, including phonon coupling and thermal expansion of the lattice. A phenomenological relation between the PL maximum and temperature was proposed by Varshni, including a T^2 dependent term.[17] In order to extract a value for the exciton-phonon coupling strength and the effective phonon energy, the PL maximum as a function of the temperature can also be fitted with a semiempirical expression by Cardona *et al*.[18] The relation between the PL maximum and temperature is however not well understood. For example, the PL maxima of PbSe QDs as a function of the temperature can shift to lower energies, stay constant or even shift to higher energies depending on the size of the QDs.[19] This makes the temperature shift of the PL maximum a less reliable probe for differences in exciton-phonon coupling strengths. Therefore, here we first evaluate differences in exciton-phonon coupling as well as the broadening at high temperatures by extracting the fwhm of the emission spectra over a broad range of temperatures.

The investigated systems are QDs of different sizes: green (510QDs), orange (580QDs), and red (620QDs) emitting QDs. The number in the naming represents the emission wavelength at room temperature; 580QDs passivated with two monolayers of CdS. In the text, these are referred to as core-shell QDs; NPLs with a thickness of 3.5 monolayers (460NPLs) and 4.5 monolayers (510NPLs); and 510NPLs passivated with a shell of 1 monolayer CdS (1ML core-shell NPLs) or 6 monolayers (6ML core-shell NPLs). Details on the synthesis methods are given in the supporting information.

The PL spectra of the investigated systems at temperatures ranging from 4 K (violet) to 423 K (red) are shown in Figure 3.1A–D and Figure S3.4A–D. An extra peak appeared on the low energy side upon cooling for the core NPLs (Figure 3.1C, Figure S3.4C, and Figure S3.5). The origin of this low energy peak has been assigned to trion emission,[20] a phonon replica,[21] or excited state luminescence of a *p*-state.[22, 23] The higher energy peak is assigned to "normal" exciton emission, and from the PL spectra the fwhm of this higher energy peak was determined and used to investigate the exciton-phonon coupling strength. The splitting in two separate peaks is not observed for core-shell NPLs with one and six monolayers CdS, probably because of the larger inhomogeneous broadening. Interestingly, the PL spectra of the core-shell NPLs do become more asymmetric at low temperatures suggesting that also here, the PL spectrum not only displays exciton emission below ~200 K, similar to what is observed for core NPLs. Recently, additional evidence supporting trion emission in core-shell NPLs has been reported.[24, 25]

The expected spectral line shape is Gaussian for inhomogeneous broadening and Lorentzian for homogeneous broadening.[16] The experimentally measured spectra could not be fitted well by either a Lorentzian or Gaussian over the entire temperature range. A product of a Lorentzian and Gaussian (approximation of a Voigt function[26]) could be used to fit the data, but no trend was observed for the relative contribution of the Lorentzian component as a function of temperature. Therefore, the fwhm was determined directly by measuring the spectral width at half the peak intensity, except for the low-temperature spectra of the core and core-shell NPLs. To reduce interference by the lower energy emission, described in the previous paragraph, the

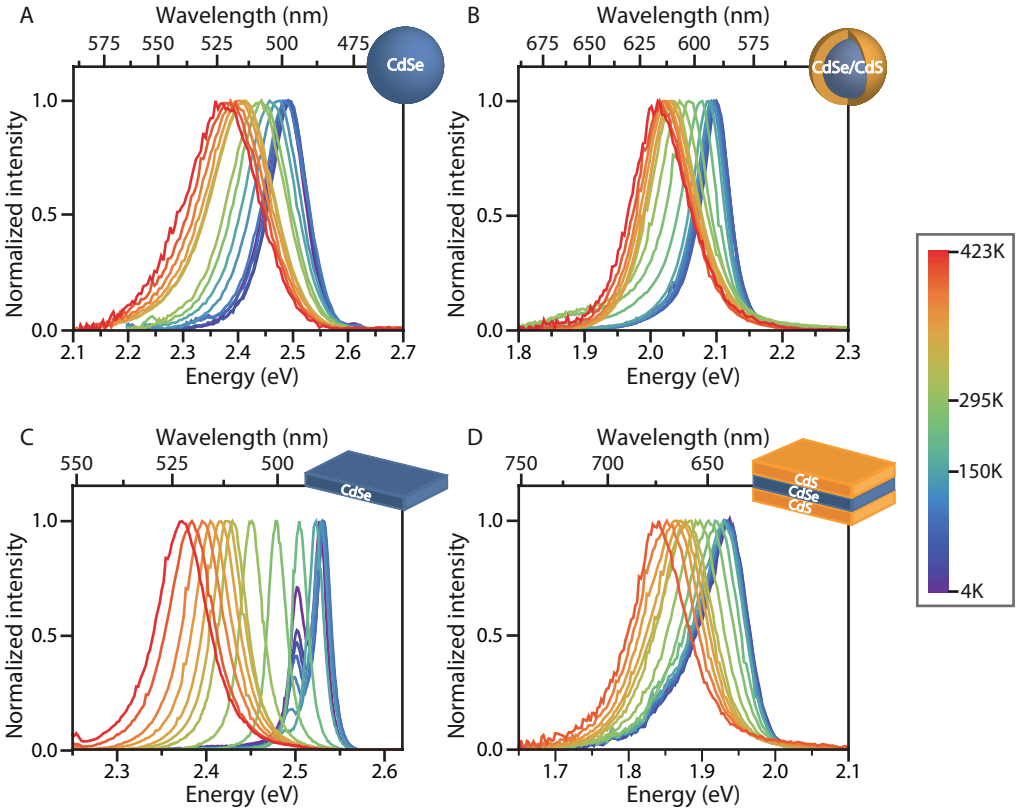

Figure 3.1 Normalized temperature-dependent spectra of **(A)** 510QDs, **(B)** core-shell QDs, **(C)** 510NPLs, and **(D)** 6ML core-shell NPLs. Temperature ranges from 4 K (violet) to 423 K (red). At a temperature of 150 K and lower, a second peak is observed in C and a more asymmetric PL spectrum in D.

width on the higher energy side was determined and taken as the hwhm for spectra recorded below 150 K and used to determine the fwhm.

The fwhm's obtained from the spectra in Figure 3.1, and Figure S3.4 are shown in Figure 3.2. The left-hand panel of Figure 3.2 shows the data for the NPLs, and the right-hand panel shows the data for the QDs. Note that the temperature is plotted from high to low temperature for the QDs in order to enable a better comparison of the fwhm at temperatures relevant for applications (423 K, where the two plots meet in the middle). Also, note that the spectra at 423 K of the 6 ML core-shell NPLs were not taken into account because the PL was irreversibly quenched (Figure S3.6).

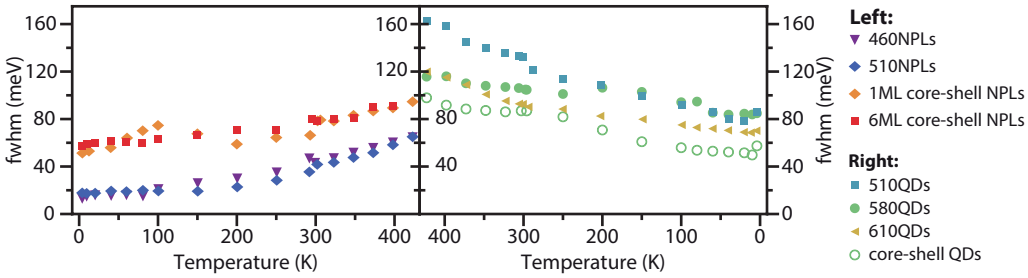

Figure 3.2 Temperature dependence of fwhm obtained from PL spectra in Figure 3.1 and Figure S3.4 (see text for details). Left panel, data NPLs: 460NPLs (purple triangles), 510NPLs (blue diamonds), 1ML core-shell NPLs (orange diamonds), and 6ML core-shell NPLs (red squares). Right panel, data QDs: 510QDS (light blue squares), 580 QDs (green circles), 610QDs (yellow triangles), and core-shell QDs (open green circles). Data in the right panel is plotted from high to low temperature to allow for comparison of fwhm's at the operating temperature of w-LEDs at 423 K in the middle where the two plots meet.

3.2.1 Inhomogeneous broadening

At 4 K, almost all phonons are frozen out, and phonon-induced dephasing processes are minimized. Therefore, the observed spectral width for ensemble measurements reflects the inhomogeneous broadening. The data in Figure 3.2 show that the inhomogeneous broadening for core NPLs of different thicknesses (3.5 or 4.5 monolayers) is similar and quite narrow (~18 meV). This reflects that the thickness of the core NPLs is indeed well-defined and the same within an ensemble of NPLs. The fwhm at 4 K significantly increases for the core-shell NPLs compared to the core-only NPLs, to ~60 meV. This suggests that the larger bandwidth for core-shell NPLs emission previously reported at room temperature is due to increased inhomogeneous broadening. This inhomogeneous broadening can be caused by inhomogeneities in shell thickness or defects at the core/shell interface. In addition, a clear red shift is observed upon CdS shell growth. The red shift is explained by electron delocalization over the core and shell, thus reducing the electron confinement energy. A larger (local) shell thickness on the NPL can lower the exciton energy and cause a redshift of the emission that depends on local variations in shell thickness.

The inhomogeneous broadening of the core QDs is larger than for the core NPLs and varies between 70 and 90 meV. No clear trend with size is observed. Inhomogeneous broadening is expected to become smaller when the particle size increases because a smaller size distribution is easier to achieve for larger particles, and size variations affect the emission energy less for larger QDs (weaker confinement effects). Indeed, less inhomogeneous broadening is observed for 610QDs, but 510QD and 580QD do not follow this trend and have a similar inhomogeneous line width. Variation in size distribution during synthesis may be the reason for not observing the expected trend. An interesting observation can be made when the 580QDs and core-shell QDs are compared. The core-shell particles are synthesized using the 580QDs but have a smaller fwhm at 4 K. The reduction in fwhm could be due to annealing of the core QDs when the mixture is heated up during the SILAR shell growth procedure. A smaller fwhm at room temperature upon shell growth was also observed by Bawendi *et al.*, although a different synthesis method was used.[8]

3.2.2 Homogeneous broadening

Upon raising the temperature, occupation of phonon modes reduces the coherence lifetime of the excited state through exciton-phonon coupling processes. This causes homogeneous broadening and, therefore, an increase of the line width as can be seen in Figure 3.2. At low temperatures, line broadening will be dominated by dephasing processes induced by coupling to low-energy acoustic phonon modes. At higher temperatures, when the thermal occupation of higher energy optical phonon modes occurs, additional dephasing channels are opened, including higher-order, two-phonon processes (*e.g.*, resonant and nonresonant Raman scattering). This can explain the steeper temperature dependence observed above 100 K.

The overall line width is a convolution of homogeneous and inhomogeneous broadening. Therefore, it is incorrect to take the increase in fwhm for all NPs in Figure 3.2 as a measure of the exciton-phonon coupling strength. This is only possible when the inhomogeneous broadening is similar, as is, for example, the case for 460NPLs and 510NPLs. The increase in fwhm as a function of the temperature is similar for these two systems, indicating similar exciton-phonon coupling in these systems. Typically, a stronger electron-phonon coupling is expected for stronger confinement, and this would give rise to a stronger coupling in the thinner 460NPLs.[27, 28] The fact that this is not observed may be related to the larger lateral dimensions of the 460NPLs compared to the 510NPLs, *i.e.*, the 460NPLs do not have a smaller volume than the 510NPLs (Figure S3.2A,B). To confirm the influence of the lateral size on electron-phonon coupling, it will be interesting to conduct careful studies on line broadening in NPLs of the same thickness but with different lateral dimensions.

The exciton-phonon coupling strength can also be compared for the 580QDs and 510QDs, which also show a similar inhomogeneous broadening. Figure 3.2 shows that the exciton-phonon coupling is stronger in the smaller 510QDs. This is in agreement with the expectation that stronger confinement enhances the electron-phonon coupling strength.[28]

To be able to compare the homogeneous broadening in all the different CdSe NPs (QDs and NPLs), deconvolution of the homogeneous and inhomogeneous broadening is needed. The experimentally measured fwhm (Γ_{total}) is a convolution of the homogeneous broadening, which has a Lorentzian line shape, and the inhomogeneous broadening, which has a Gaussian line shape. The contribution of both line shapes results in a total broadening given by equation 3.1.[29] The inhomogeneous component ($\Gamma_{Gaus/inhom}$) is approximately the fwhm at 4 K.

$$\Gamma_{total} = \frac{\Gamma_{Lor/hom}}{2} + \sqrt{\frac{\Gamma_{Lor/hom}^{2}}{4} + \Gamma_{Gaus/inhom}^{2}} \tag{3.1}$$

Using equation 3.1 and the inhomogeneous line widths determined from the emission spectra at 4 K, the temperature dependence of the homogeneous line width was determined for the various CdSe core and core-shell nanostructures. The results are plotted in Figure 3.3 and show that the homogeneous broadening is similar for the different CdSe nanostructures and increases to about 60 – 80 meV at 423 K. Only the 510 QDs show a stronger broadening (~120 meV at 423 K). Comparing the slopes for the homogeneous temperature broadening for the core-shell NPLs (red) and core NPLs (violet) reveals that the exciton-phonon coupling is not stronger in core-shell NPLs as was previously claimed. The same conclusion was also obtained by Achtstein *et al.* based on fitting the shift of the PL maximum.[13] Nonetheless, no reduction in exci-

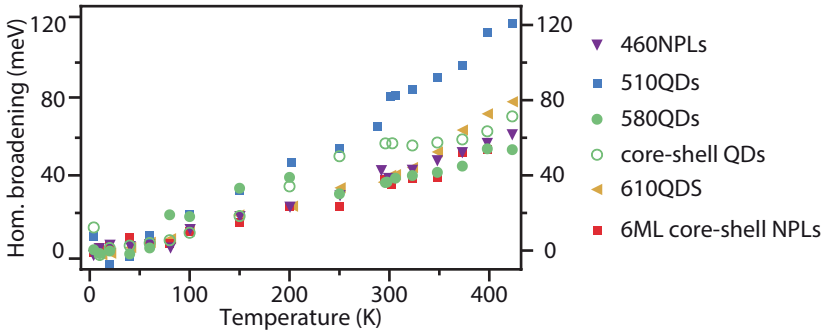

Figure 3.3 Temperature dependence of the homogeneous broadening for QDs and NPLs. The plot shows stronger homogeneous broadening for small NPs (510QDs, blue squares), but similar homogeneous broadening for the other investigated NPs at w-LED operating temperatures (423K).

ton-phonon coupling in core-shell NPLs is observed either, which deviates from results based on a shift of the PL maximum. The present measurements on fwhm over a wide temperature range allow for a better comparison of the homogeneous line broadening than previous reports, which included measurements only up to 300 K[13] or only from 300 to 370 K.[30] It is evident that especially between 300 and 423 K there is significant homogeneous broadening in a temperature regime where homogeneous broadening starts to dominate over inhomogeneous broadening. Within the experimental uncertainty, there is not a strong difference between the thermal broadening for the various QDs and NPLs investigated. The origin of the narrow bandwidth in core-only NPLs is clearly the extremely small inhomogeneous line width and not a weak electron-phonon coupling.

The exciton-phonon coupling strength can also be investigated by considering the temperature-induced shift of the PL maximum. As discussed above, the peak shift is not only affected by exciton-phonon coupling, and this makes it a less reliable method to probe phonon-coupling strengths. Still, for the materials investigated, the position of the PL maximum was determined for temperatures between 4 and 423 K, as shown in Figure 3.4. The shift of the PL maximum in meV is given as well as the relative shift. Larger temperature shifts are observed for the exciton emission in NPLs in comparison to QDs. Shell growth reduces the temperature-induced shift of the exciton emission in the NPLs. For the QDs, a larger shift is observed for the smallest 510QDs.

As discussed above, exciton-phonon coupling can alter the band structure, resulting in a shift of the PL maximum. Also lattice contraction upon lowering the temperature results in stronger confinement and gives rise to a blue shift of the PL maximum. The effect of the contraction of the lattice on the confinement is expected to be larger for more strongly confined systems resulting in a larger shift of the PL maximum. This is consistent with the observations in Figure 3.4, which shows a larger absolute temperature shift for 460NPLs than for the 510NPLs. When the relative shift is considered (see Table 3.1), both systems show a similar shift of ~6.2%. The temperature-induced shift for core-shell NPLs is weaker, with relative shifts of the exciton emission energy of ~3.8% and ~5.2% between 4 and 423 K. The relative shifts for exciton emission in QDs is smaller and varies between 2 and 5%, with larger shifts observed

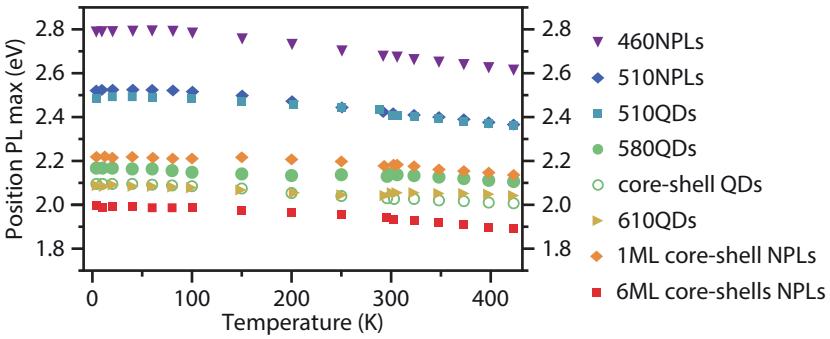

Figure 3.4 Temperature-dependent position PL maximum. Larger shifts of PL maximum are observed for NPLs compared to QDs.

Table 3.1 absolute and relative shift PL maximum from 4 K to 423 K

Material	Absolute shift (meV)	Relative shift (%)
▼ 460NPLs	175	6.2
◆ 510NPLs	157	6.2
■ 510QDs	127	5.1
● 580QDs	61	2.8
○ core-shell QDs	88	4.2
▶ 610QDs	47	2.3
◆ 1ML core-shell NPLs	81	3.8
■ 6ML core-shells NPLs	100	5.2

Absolute shift (meV) and relative shift (%) of PL maximum over a temperature range of 4-423 K for materials shown in **Figure 3.4**.

for smaller QDs. One can speculate that the larger shifts observed in NPLs are connected with strong confinement in one direction that changes upon lattice expansion in this direction. It can be intuitively understood that this effect is stronger than expansion in all directions in a QD, but further (theoretical) investigations are needed to provide a full understanding of the temperature dependence of the exciton energy in NPLs and QDs and the role of lattice contraction and coupling to optical and acoustic phonon modes.

3.2.3 Line width and line shift at 423K

Narrow band emission from CdSe NPLs has been suggested as a promising narrow band alternative for replacing CdSe and InP QDs in w-LEDs and displays. For color purity and widening the color gamut, a narrow band emission is desired, while for color point stability, temperature-induced shifts should be minimized.[4] Most studies related to the application of semiconductor NPLs and QDs as spectral converters in w-LEDs rely on measurements at room temperature.[14, 31] However, for on-chip application luminescent materials in w-LEDs, temperatures as high as 150 °C are reached. It is therefore important to consider spectral line widths and

temperature-induced shifts at 150 °C for QDs and NPLs and compare these with traditional phosphors based on microcrystalline insulator materials doped with Eu^{2+}, Ce^{3+}, or Mn^{4+}. Here we have extended the temperature range to this relevant temperature regime. When comparing the fwhm at 150 °C (423 K), it becomes evident that the core NPLs still outperform core-shell NPLs, QDs, and core-shell QDs for applications due to the smaller fwhm of ~65 meV compared to 100 – 120 meV for core-shell NPLs and QDs. Especially when comparing the green emitting particles (510QDs and 510NPLs), it is evident that NPLs have a fwhm that is a factor two smaller, making NPLs a superior candidate for a narrow green emitter in w-LEDs.

Core-shell NPLs, which emit in the red, have a slightly smaller or similar fwhm compared to the red-emitting 610QDs (~120 meV at 423 K) and core-shell QDs (~100 meV at 423 K). In terms of fwhm, the core-shell NPLs do not underperform compared to QDs emitting in the red. Nevertheless, the spectral width of core-shell NPLs is larger compared to core-only NPLs and is related to the larger inhomogeneous width, as discussed above. Reducing the inhomogeneous broadening for core-shell NPLs is feasible by improving the synthesis procedure in order to obtain a better-defined and homogeneous shell thickness throughout the NPLs or a better-defined interface between the core and the shell. This will reduce the inhomogeneous broadening and make core-shell NPLs a better candidate for narrow red emitters. Rossinelli *et al.* have recently reported core-shell nanoplatelets with a narrower emission bandwidth.[32, 33] For application of red-emitting NPLs in w-LEDs, the synthesis of stable NPLs with a high quantum yield and narrow band emission is crucial, and improved shell-growth methods will be highly beneficial.

Finally, it is interesting to compare the performance at 423 K with traditional microcrystalline phosphors that are presently applied in w-LEDs such as $(Ca,Sr)AlSiN_3:Eu^{2+}$ (CASN), $SrLiAl_3N_4:Eu^{2+}$ (SLA), and $K_2SiF_6:Mn^{4+}$ (KSF). The spectral width at low temperatures is much larger for the Eu^{2+} emission. Rather than a narrow zero-phonon line (which characterizes low-temperature exciton emission in NPLs and QDs), a vibrationally broadened spectrum over typically 40 – 80 nm (120 – 235 meV) is observed, even for a single Eu^{2+} ion at 4 K. The thermal broadening is however less pronounced than for exciton emission and has a weak $\sqrt{\coth\left(\frac{\hbar\omega}{kT}\right)}$ temperature dependence.[16, 34] Typical line widths for the red Eu^{2+} emission in CASN increase from 237 meV at 300 K to 251 meV at 423 K[35] and from 182 meV (300 K) to 198 meV (423 K) for Eu^{2+} in SLA.[36] Despite the weaker temperature dependence, it is evident that even at high temperatures, the spectral widths of semiconductor nanostructures outperform that of traditional Eu^{2+} phosphors. The line emission of Mn^{4+} phosphors is narrower and concentrated in a number of sharp emission lines between 610 and 640 nm, spreading over a spectral region of only 90 meV, corresponding to an effective fwhm below 60 meV and thus competing with the narrow red emission of NPLs.[37]

Temperature stability is an important characteristic of w-LED phosphors. Temperature-induced color shifts are undesired as a small shift of the emission maximum with temperature can give rise to noticeable color variations in w-LEDs. Color stability is therefore important to keep the color temperature of a w-LED independent of temperature fluctuations due to variations in the external temperature or operating conditions. The temperature shift of the emission maximum of NPL emission is relatively large. Between 300 and 423 K, a close to linear temperature shift is observed of 0.50 meV/K for 460NPLs and 0.44 meV/K for 510NPLs. For core-shell NPLs and QDs, the temperature shift of the emission maximum is smaller but still significant

(between 0.2 and 0.4 meV/K). In this respect, the shift of the emission maximum of traditional phosphors is much better (*e.g.*, <0.1 meV/K for SLA) and gives rise to better color temperature stability in response to external temperature variations. In addition to the thermal drift of the emission color, the stability, toxicity, and chemical integrity of CdSe NPs at the operating temperature in w-LEDs for on-chip application of QDs are a concern. Recently, coating strategies have been developed that allow for on-chip application in mid-power LEDs[3, 38, 39] and give hope that the stability of CdSe NPLs can be improved in a similar way to enable on-chip application in w-LEDs.

3.3 Conclusion

The spectral width and thermal broadening of exciton emission in core and core-shell CdSe NPLs has been investigated and compared with the temperature behavior of CdSe QDs in a wide temperature range (4 – 423 K), extending to temperatures relevant for application as spectral converters in w-LEDs. Measurements at cryogenic temperatures show that exciton emission of NPLs is characterized by a very narrow inhomogeneous line width (18 meV versus ~60 – 80 meV for QDs and core-shell NPLs). The narrow inhomogeneous broadening is attributed to the highly homogeneous (atomically precise) thickness of the NPLs of 3.5 (460 nm emission) or 4.5 monolayers (510 nm emission) of CdSe. Homogeneous (Heisenberg) broadening of exciton emission in NPLs and QDs is due to phonon-assisted dephasing processes and increases strongly with temperature. At 4 K, homogeneous broadening is negligible as phonons are frozen out. The homogeneous linewidth increases rapidly with temperature, reaching widths varying between 60 and 80 meV at 423 K for different sizes of core and core-shell NPLs and QDs. Stronger phonon coupling seems to be observed for stronger confinement (smaller NPs), but the variation in homogeneous broadening is not large. Therefore, the size dependence of exciton phonon coupling cannot explain the much narrower bandwidth observed for CdSe NPLs. The narrow bandwidth for NPL exciton emission is therefore attributed to the narrow inhomogeneous line width and not to stronger exciton-phonon coupling in core-shell NPLs compared to core NPLs as previously suggested. In addition to line broadening, the temperature-induced shift of the exciton peak maximum was investigated. The thermal shift of the emission maximum for both NPLs and QDs is significantly larger than for traditional w-LED phosphors and may give rise to undesired fluctuations in the color temperature of w-LEDs. In spite of the large thermal shift and thermal stability issues at the operating temperature in w-LEDs, the favorable spectral properties make CdSe NPLs a promising class of materials for application in w-LEDs and displays.

3.4 Methods

CdSe Quantum dots were synthesized based on a method described by Li et al. using a reaction time of several seconds up to 10 minutes for the green (510QDs), orange (580QDs), and red (620QDs) emitting QDs, respectively.[40] 580QDs were passivated with two monolayers of CdS using the SILAR method.[40] NPLs with a thickness of 3.5 monolayers (460NPLs) and 4.5 monolayers (510NPLs) were synthesized as published by Dubertret *et al.*[41] The 510NPLs were passivated with a shell of 1 monolayer CdS using the c-ALD-method (1ML core-shell NPLs) or 6 monolayers using a method developed by Rossinelli *et al.* (6ML core-shell NPLs).[32, 42] Further details on the synthesis methods and transmission electron microscopy images are given in the supporting information.

The temperature-dependent measurements ranging from 4 to 423 K were performed in an Oxford Instruments liquid helium cryostat (up to 300 K) and a Linkam high-temperature stage (above 300 K) placed inside an Edinburgh FLS920 spectrometer equipped with a Hamamatsu R928 PMT detector and a 450 W xenon lamp as the excitation source. The excitation power used during the measurements was low, and an upper limit was estimated at ~100 mW/cm^2. At these low excitation powers, the line width is not affected by multiexciton emission. Emission of biexcitons is, for example, observed at an excitation power above 100 W/cm^2.[43] To confirm this, emission spectra at higher excitation powers also were recorded, and no effect on the line width was observed (Figure S3.3).

The low-temperature measurements were performed in toluene or hexane for the QDs and NPLs, respectively. The particles were dispersed in the high-boiling solvent 1-octadecene for high-temperature measurements. Emission spectra were corrected for the sensitivity of the detection system (emission monochromator throughput and detector response), and the intensity was converted to a photon flux per energy interval when the x-axis was converted to energy scale (from nm to eV).[44]

S3 Supporting information

S3.1 Experimental methods and characterization

S3.1.1 Chemicals

1-butanol (anhydrous, 99.8%), 1-octadecene (ODE, 90%), 1-octanethiol (98.5%), 2-propanol (99.5%), cadmium acetate dihydrate (98%), cadmium nitrate tetrahydrate (99,99%, trace metal basis), hexane (anhydrous, 95%), methanol (anhydrous, 99,8%), N-methylformamide (NMF, 99.8%), octadecylamine (ODA, 90%), oleic acid (OA, 90%), oleylamine (70%), sodium hydrosulfide hydrate, Sodium myristate (≥99%), Sulfur (S, 99.998%), trioctylphosphine (90%), toluene (anhydrous, 95%), triethylamine (≥99%), trifluoroacetic acid (99%), trifluoroacetic anhydride (99%), trioctylphosphine oxide (90%) were all purchased from Sigma Aldrich. Sodium acetate (99.999% pure on trace metal basis) was purchased from Merck. Selenium powder (200 mesh, 99.999%) was purchased from Brunschwig Chemie.

S3.1.2 Synthesis CdSe QDs and CdSe/CdS core-shell QDs based on Li *et al.*[40]

Precursors

A 0.065 M cadmium oleate precursor was prepared by degassing a mixture of 0.64 g cadmium acetate dihydrate, 25.9 g 1-octadecene (ODE) and 3.73 g oleic acid (OA) for 2 hours at 120 °C under vacuum. A 0.74 M TOP-Se solution was made by dissolving 1.4 g elemental selenium in 7.5 g trioctylphosphine at 80 °C. After the selenium was dissolved 11.9 g ODE was added.

For the shell growth a 0.1 M cadmium precursor was prepared by degassing 1.07 g cadmium acetate dihydrate, 23.6 g ODE, and 9.05 g OA at 120 °C under vacuum for 2 hours. To obtain a 0.1 M sulfur precursor, 48 mg elemental sulfur was dissolved in 11.8 g ODE at 180 °C.

Synthesis of CdSe QDs

A mixture of 1.11 g trioctylphosphine oxide (TOPO), 3.2 g octadecylamine (ODA) and 5.2 g TOP-Se precursor was heated to 300°C. 4.9 g of the 0.065M cadmium precursor was rapidly injected. After the injection the temperature was kept at 280–290°C. QDs of different sizes were made by varying the reaction time from seconds up to 10 minutes. Particles were purified twice with 1 equivalent toluene, 1 equivalent methanol and 2 equivalent butanol and centrifuged at 2500 rpm (700 RCF) for 10 min. The QDs were dispersed in 10 mL toluene.

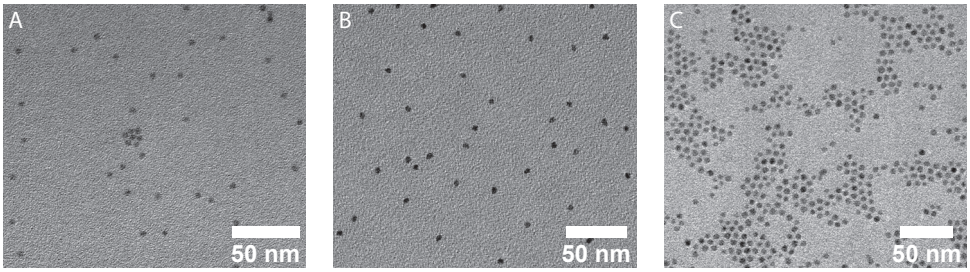

Figure S3.1 TEM images of CdSe QDs: 580QDs (A, diameter 3.6 nm ± 0.3 nm) and 610QDs (B, diameter 4.4 nm ± 0.3 nm). TEM image of CdSe/CdS core-shell QDs (C, diameter 5.0 nm ± 0.4 nm).

Synthesis CdSe/CdS core-shell QDs

0.820 mL of a 0.122mM CdSe QD solution in toluene (diameter particle: 3.6 nm), 1 gram ODA and 3 mL ODE was heated to 150°C. After all toluene was evaporated, the mixture was heated to 240°C. Alternately a 0.1 M cadmium precursor or a 0.1 M sulfur precursor was added dropwise with intervals of 10 min. For the first and second CdS layer 0.180 mL and 0.225 mL of the precursor solutions was added respectively. Core-shell particles were purified as described above.

Transmission electron microscopy (TEM) images of core QDs of different sizes and core-shell QDs are shown in **Figure S3.1**.

S3.1.3 Synthesis of CdSe nanoplatelets based on Ithurria *et al.*[41]

NPLs emitting at 460 nm (460NPLs)

A 1M TOP-Se precursor was prepared by dissolving 157.6 mg elemental selenium in 2 mL TOP under inert atmosphere. 278 mg cadmium acetate dihydrate, 285 µL OA and 15 mL ODE was mixed and degassed under vacuum for 1 hour at room temperature. This mixture was heated to 200 °C under nitrogen atmosphere and 150 µL of 1M TOPSe was injected. After 1 hour at 200 °C, the mixture was cooled down to room temperature. The product was purified twice by addition of 40 mL methanol/butanol mixture (1:3 ratio) and centrifuged at 2500 rpm (700 RCF) for 10 minutes. NPLs were dispersed in 4 mL hexane.

NPLs emitting at 510 nm (510NPLs)

First, a cadmium myristate precursor was synthesized by dissolving 1.23 g cadmium nitrate tetrahydrate in 40 ml methanol and 3.13 g sodium myristate in 250 mL methanol. The cadmium nitrate solution was added to the sodium myristate solution while stirring. A white precipitate was visible. The precipitate was vacuum filtrated using a Buchner flask and rinsed with 1L of methanol. The cadmium myristate was dried overnight under vacuum to remove methanol.

For the synthesis of the nanoplatelets (NPLs) 170 mg cadmium myristate, 15 mL ODE and 12 mg elemental selenium was heated to 240 °C under nitrogen atmosphere. At 195 °C, when the mixture turned orange, 40 mg cadmium acetate and 20 mg sodium acetate was added to the reaction mixture. The synthesis was quenched by addition of 15 mL hexane after 5 min at 240 °C (first 5 mL was added with cation, due to low boiling point of hexane). At 95 °C 1mL OA was added. NPLs were purified twice by addition of 30 mL methanol/butanol mixture (1:2) and centrifuged at 3000 rpm (~1000 RCF). The NPLs were dispersed in 10 mL hexane.

S3.1.4 Synthesis of CdSe/CdS core-shell NPLs based on Kelestemur *et al.*[45] and Rossinelli *et al.*[46]

1 ML core-shell NPLs

A 0.4M cadmium acetate solution and 0.2M sulfide solution were prepared under inert atmosphere by dissolving 150.6 mg hydrosulfide hydrate in 10 mL N-methylformamide (NMF) and 1066 mg cadmium acetate dihydrate in 9.75 mL NMF. 1 mL of the sulfide solution and 1 mL of the 510NPLs solution were mixed. In 5 to 10 minutes the NPLs transferred to the NMF phase. The hexane (upper phase) was removed. 1.5 mL hexane was added, mixed by shaking, and removed. This was repeated once more. The NPLs were further purified by adding 3 mL toluene and 1mL acetonitrile and centrifuged at 3000 rpm (1000 RCF) for 10 min. This was repeated one more time. The product was dispersed in 1 mL NMF.

The cadmium layer was grown by adding 1 mL 0.4M cadmium acetate solution to the NPLs in NMF. The mixture was stirred for 5 min at 600 RPM. The NPLs were purified twice with 12 mL toluene and 4 mL acetonitrile and centrifuged at 3000 rpm for 10 minutes. The NPLs were dispersed in 1.5 mL hexane.

6 ML core-shell NPLs

5.75 g CdO and 20 mL acetonitrile were added to a 100 mL roundbottom flask. The mixture was stirred and cooled with an ice bath. First, 0.7 mL trifluoroacetic acid was added followed by 6.2 mL trifluoroacetic anhydride. After 10 minutes the mixture was heated to 50°C until a the solution became white. 28.6 mL OA, 180 mL 2-propanol and 14 mL triethylamine where mixed and stirred in a 500 mL Erlenmeyer flask.

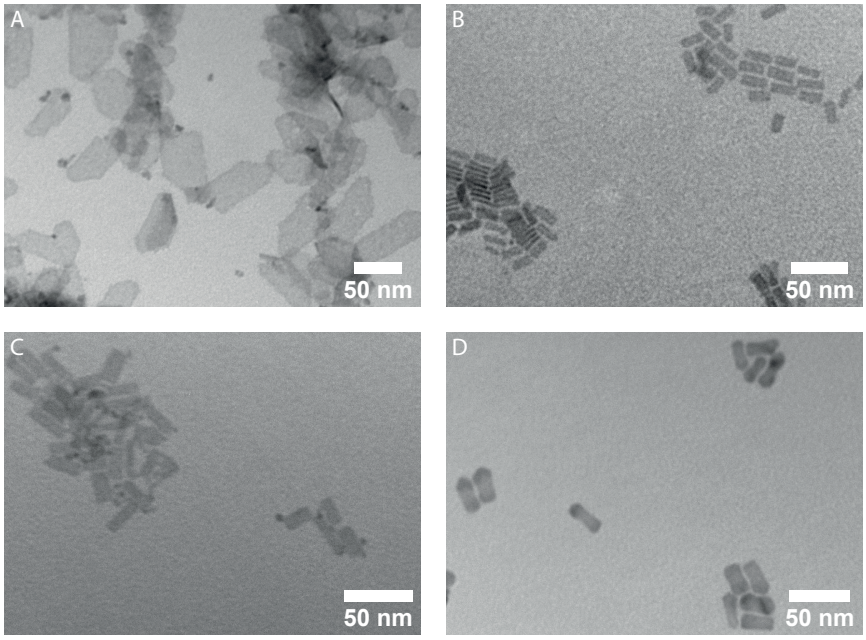

Figure S3.2 TEM images of CdSe NPLs of 3.5 ML (**A**, 460NPLs) with large lateral dimensions (length: 76 nm ± 18 nm, width: 34 nm ± 10 nm) and NPLs of 4.5 ML (**B**, 510NPLs) with small lateral dimensions (length: 19 nm ± 2.1 nm, width: 7.1 nm ± 1.3 nm). In **C** and **D** TEM images of core-shell NPLs with 1 ML CdS (length: 22 nm ± 4.2 nm, width: 7.7 nm ± 1.3 nm) and 6 ML CdS (length: 24 nm ± 3.5 nm, width: 9.7 nm ± 1.4 nm) are shown respectively.

The cadmium trifluoroacetate solution was added to the OA solution while stirring. The white precipitate was vacuum filtrated using a Buchner flask and rinsed several times with methanol. The product was dried under vacuum overnight.

140 mg cadmium oleate, 5 mL ODE and 1.6 mL 510NPLs were mixed and put under a nitrogen atmosphere. The hexane was evaporated by running a nitrogen flow through a needle over the mixture for 1 hour. 1mL oleylamine was added and the mixture was heated to 300 °C. When a temperature of 180 °C was reached, 7mL/L 1-octanethiol in ODE was added with a rate of 3mL/h using a syringe pump. After 75 minutes the reaction mixture was cooled down to room temperature using an air flow. 5 mL hexane was added and the mixture was centrifuged at 3000 rpm (~1000 RCF) for 10 min. The NPLs were dispersed in 5 mL hexane and 100 µL oleylamine was added. The mixture was centrifuged twice at 3000 rpm for 10 min. After discarding the supernatant, 5 mL hexane was added in between the centrifuge cycles. The final product was dispersed in 5 mL hexane.

The thickness of the CdS shell is estimated to be 6 monolayers (ML), based on the position of the PL spectrum at room temperature (658 nm) compared to the spectra of 4 ML thick shell (~650 nm) and 7 ML thick shell (~662 nm).[42]

TEM image of core and core-shell NPLs of the synthesis described above are shown in Figure S3.2.

S3.2 Additional experimental data

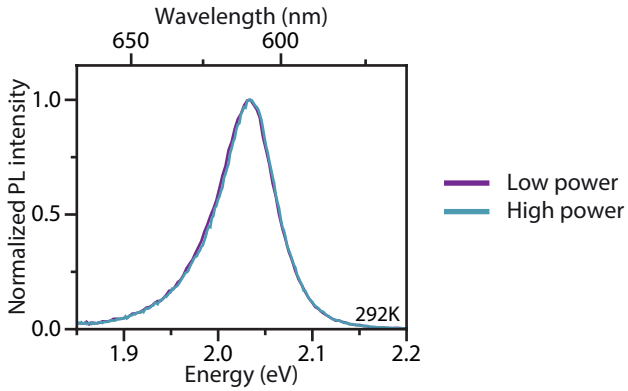

Figure S3.3 Comparison PL spectra with a typical excitation power used during measurements (upper limit ~100 mW/cm^2, violet) and a spectrum recorded at twice the excitation power (blue). No change in the line width was observed.

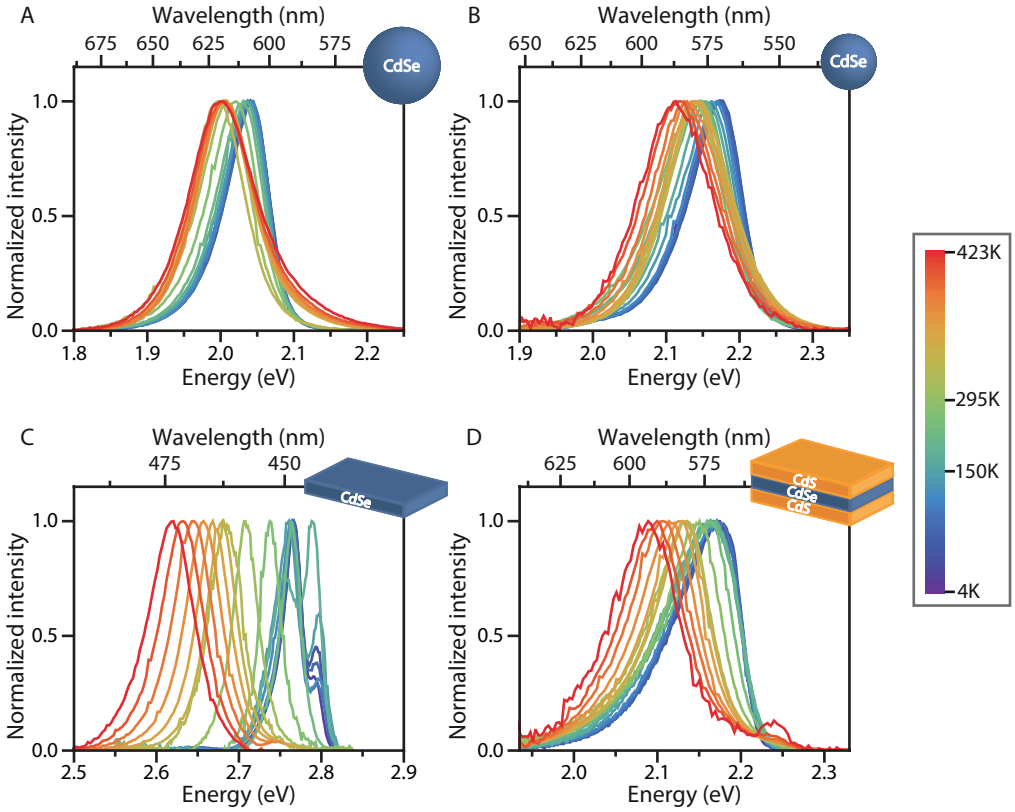

Figure S3.4 Normalized temperature dependent spectra of (A) 610QDs, (B) 580QDs, (C) 460NPLs and (D) 1ML core-shell NPLs. Temperature ranges from 4K (violet) to 423K (red). At a temperature of 150 K and lower a second peak is observed in C and a more asymmetric PL spectrum in D.

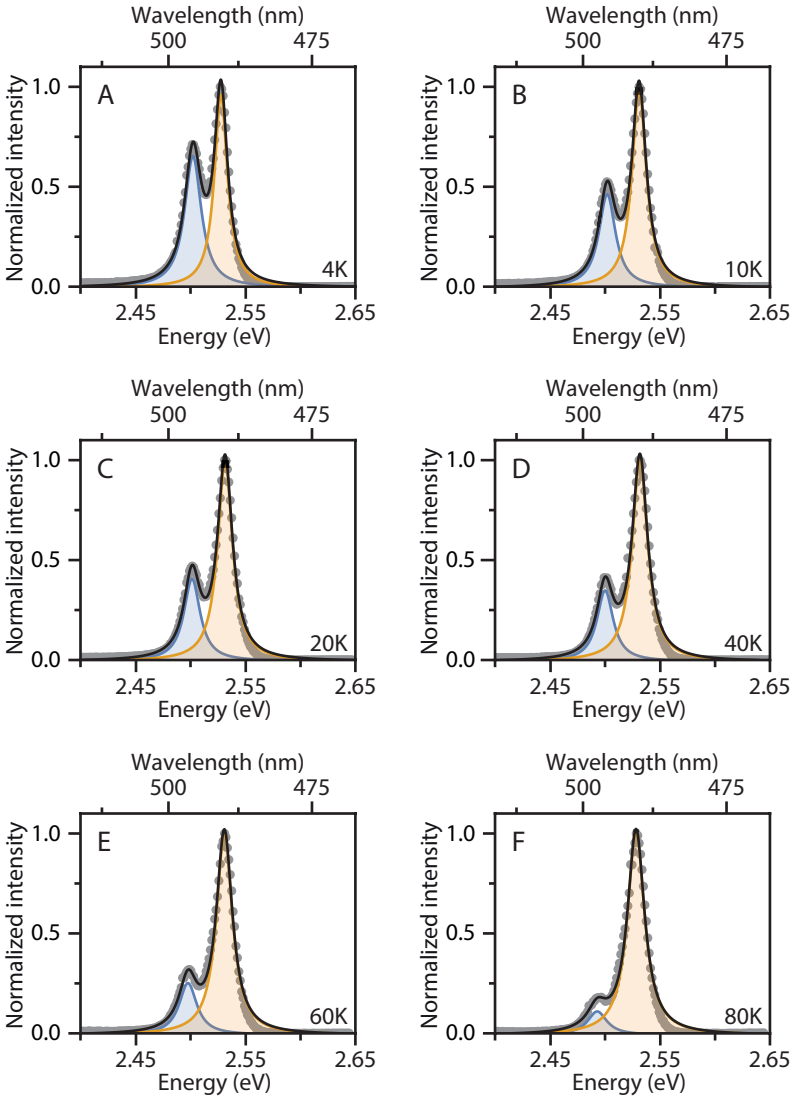

Figure S3.5 Data PL spectra 510NPLs at low temperatures (gray dots). Splitting of the PL spectra can be observed at low temperatures. Intensity of peak at lower energy increases with decreasing temperature. Data is fitted with sum of two Lorentzian functions (black). Contributions of both Lorentzian functions are shown in blue and orange. The wings of the Lorentzian fit deviates from the data. This results in an incorrect determination of the fwhm when the intensity of the low energy peak is high.

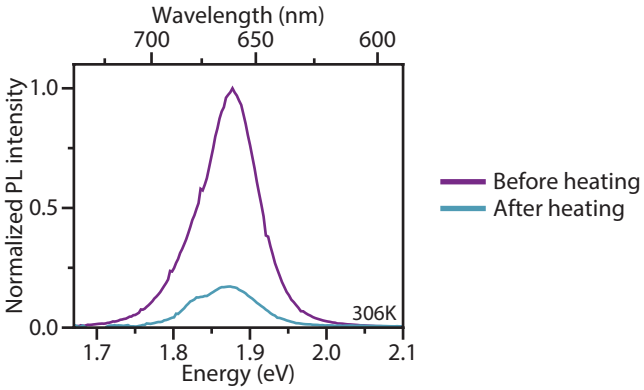

Figure S3.6 PL spectra of 6ML core-shell NPLs at 306K before and after heating to 423K. PL is irreversible quenched due to heating at high temperatures.

References

1. Chen, L.; Lin, C.-C.; Yeh, C.-W.; Liu, R.-S., Light Converting Inorganic Phosphors for White Light-Emitting Diodes. *Materials* **2010,** *3* (3), 2172-2195.
2. Stockman, A.; Sharpe, L. T., The spectral sensitivities of the middle- and long-wavelength-sensitive cones derived from measurements in observers of known genotype. **2000,** *40* (13), 1711-1737.
3. Estrada, D.; Shimizu, K.; Bohmer, M.; Gangwal, S.; Diederich, T.; Grabowski, S.; Tashjian, G.; Chamberlin, D.; Shchekin, O. B.; Bhardwaj, J., 32-1: On-chip Red Quantum Dots in White LEDs for General Illumination. *SID Symposium Digest of Technical Papers* **2018,** *49* (1), 405-408.
4. Mangum, B. D.; Landes, T. S.; Theobald, B. R.; Kurtin, J. N., Exploring the bounds of narrow-band quantum dot downconverted LEDs. *Photonics Research* **2017,** *5* (2), A13-A22.
5. Jang, E.; Jang, H.; Kang, H. A.; Cho, O., 67-1: Invited Paper : Environmentally Friendly Quantum Dots for Display Applications. *SID Symposium Digest of Technical Papers* **2017,** *48* (1), 980-983.
6. Ithurria, S.; Dubertret, B., Quasi 2D Colloidal CdSe Platelets with Thicknesses Controlled at the Atomic Level. *Journal of the American Chemical Society* **2008,** *130* (49), 16504-16505.
7. Tessier, M. D.; Javaux, C.; Maksimovic, I.; Loriette, V.; Dubertret, B., Spectroscopy of Single CdSe Nanoplatelets. *ACS Nano* **2012,** *6* (8), 6751-6758.
8. Chen, O.; Zhao, J.; Chauhan, V. P.; Cui, J.; Wong, C.; Harris, D. K.; Wei, H.; Han, H.-S.; Fukumura, D.; Jain, R. K.; Bawendi, M. G., Compact High-Quality CdSe–CdS Core–Shell Nanocrystals with Narrow Emission Linewidths and Suppressed Blinking. *Nature Materials* **2013,** *12* (5), 445-451.
9. Reiss, P.; Carayon, S.; Bleuse, J.; Pron, A., Low polydispersity core/shell nanocrystals of CdSe/ZnSe and CdSe/ZnSe/ZnS type: preparation and optical studies. *Synthetic Metals* **2003,** *139* (3), 649-652.
10. Cui, J.; Beyler, A. P.; Marshall, L. F.; Chen, O.; Harris, D. K.; Wanger, D. D.; Brokmann, X.; Bawendi, M. G., Direct probe of spectral inhomogeneity reveals synthetic tunability of single-nanocrystal spectral linewidths. *Nature Chemistry* **2013,** *5* (7), 602-606.
11. Mahler, B.; Nadal, B.; Bouet, C.; Patriarche, G.; Dubertret, B., Core/Shell Colloidal Semiconductor Nanoplatelets. **2012,** *134* (45), 18591-18598.
12. Tessier, M. D.; Mahler, B.; Nadal, B.; Heuclin, H.; Pedetti, S.; Dubertret, B., Spectroscopy of Colloidal Semiconductor Core/Shell Nanoplatelets with High Quantum Yield. *Nano Letters* **2013,** *13* (7), 3321-3328.
13. Achtstein, A. W.; Marquardt, O.; Scott, R.; Ibrahim, M.; Riedl, T.; Prudnikau, A. V.; Antanovich, A.; Owschimikow, N.; Lindner, J. K. N.; Artemyev, M.; Woggon, U., Impact of Shell Growth on Recombination Dynamics and Exciton–Phonon Interaction in CdSe–CdS Core–Shell Nanoplatelets. *ACS Nano* **2018,** *12* (9), 9476-9483.
14. Scott, R.; Prudnikau, A. V.; Antanovich, A.; Christodoulou, S.; Riedl, T.; Bertrand, G. H. V.; Owschimikow, N.; Lindner, J. K. N.; Hens, Z.; Moreels, I.; Artemyev, M.; Woggon, U.; Achtstein, A. W., A comparative

study demonstrates strong size tunability of carrier-phonon coupling in CdSe-based 2D and 0D nanocrystals. *Nanoscale* **2019,** *11* (9), 3958-3967.

15. Achtstein, A. W.; Schliwa, A.; Prudnikau, A.; Hardzei, M.; Artemyev, M. V.; Thomsen, C.; Woggon, U., Electronic structure and exciton-phonon interaction in two-dimensional colloidal CdSe nanosheets. *Nano Lett* **2012,** *12* (6), 3151-3157.
16. Henderson, B.; Imbusch, G. F., *Optical Spectroscopy of Inorganic Solids*. Clarendon Press: 2006; p 199-238.
17. Varshni, Y. P., Temperature dependence of the energy gap in semiconductors. *Physica* **1967,** *34* (1), 149-154.
18. Logothetidis, S.; Cardona, M.; Lautenschlager, P.; Garriga, M., Temperature dependence of the dielectric function and the interband critical points of CdSe. **1986,** *34* (4), 2458-2469.
19. Dey, P.; Paul, J.; Bylsma, J.; Karaiskaj, D.; Luther, J. M.; Beard, M. C.; Romero, A. H., Origin of the temperature dependence of the band gap of PbS and PbSe quantum dots. **2013,** *165*, 49-54.
20. Shornikova, E. V.; Biadala, L.; Yakovlev, D. R.; Sapega, V. F.; Kusrayev, Y. G.; Mitioglu, A. A.; Ballottin, M. V.; Christianen, P. C. M.; Belykh, V. V.; Kochiev, M. V.; Sibeldin, N. N.; Golovatenko, A. A.; Rodina, A. V.; Gippius, N. A.; Kuntzmann, A.; Jiang, Y.; Nasilowski, M.; Dubertret, B.; Bayer, M., Addressing the exciton fine structure in colloidal nanocrystals: the case of CdSe nanoplatelets. *Nanoscale* **2018,** *10* (2), 646-656.
21. Biadala, L.; Liu, F.; Tessier, M. D.; Yakovlev, D. R.; Dubertret, B.; Bayer, M., Recombination Dynamics of Band Edge Excitons in Quasi-Two-Dimensional CdSe Nanoplatelets. **2014,** *14* (3), 1134-1139.
22. Achtstein, A. W.; Scott, R.; Kickhöfel, S.; Jagsch, S. T.; Christodoulou, S.; Bertrand, G. H. V.; Prudnikau, A. V.; Antanovich, A.; Artemyev, M.; Moreels, I.; Schliwa, A.; Woggon, U., p-State Luminescence in CdSe Nanoplatelets: Role of Lateral Confinement and a Longitudinal Optical Phonon Bottleneck. *Physical Review Letters* **2016,** *116* (11).
23. Specht, J. F.; Scott, R.; Corona Castro, M.; Christodoulou, S.; Bertrand, G. H. V.; Prudnikau, A. V.; Antanovich, A.; Siebbeles, L. D. A.; Owschimikow, N.; Moreels, I.; Artemyev, M.; Woggon, U.; Achtstein, A. W.; Richter, M., Size-dependent exciton substructure in CdSe nanoplatelets and its relation to photoluminescence dynamics. *Nanoscale* **2019,** *11* (25), 12230-12241.
24. Antolinez, F. V.; Rabouw, F. T.; Rossinelli, A. A.; Cui, J.; Norris, D. J., Observation of Electron Shakeup in CdSe/CdS Core/Shell Nanoplatelets. *Nano Letters* **2019**, 8495-8502.
25. Shornikova, E. V.; Biadala, L.; Yakovlev, D. R.; Feng, D.; Sapega, V. F.; Flipo, N.; Golovatenko, A. A.; Semina, M. A.; Rodina, A. V.; Mitioglu, A. A.; Ballottin, M. V.; Christianen, P. C. M.; Kusrayev, Y. G.; Nasilowski, M.; Dubertret, B.; Bayer, M., Electron and Hole g-Factors and Spin Dynamics of Negatively Charged Excitons in CdSe/CdS Colloidal Nanoplatelets with Thick Shells. *Nano Lett* **2018,** *18* (1), 373-380.
26. Jain, V.; Biesinger, M. C.; Linford, M. R., The Gaussian-Lorentzian Sum, Product, and Convolution (Voigt) functions in the context of peak fitting X-ray photoelectron spectroscopy (XPS) narrow scans. *Applied Surface Science* **2018,** *447*, 548-553.
27. Mittleman, D. M.; Schoenlein, R. W.; Shiang, J. J.; Colvin, V. L.; Alivisatos, A. P.; Shank, C. V., Quantum size dependence of femtosecond electronic dephasing and vibrational dynamics in CdSe nanocrystals. *Physical Review B* **1994,** *49* (20), 14435-14447.
28. Takagahara, T., Electron-Phonon Interactions in Semiconductor Quantum Dots. Springer Berlin Heidelberg: 2002; pp 115-147.
29. Olivero, J. J.; Longbothum, R. L., Empirical fits to the Voigt line width: A brief review. *Journal of Quantitative Spectroscopy and Radiative Transfer* **1977,** *17* (2), 233-236.
30. Bose, S.; Shendre, S.; Song, Z.; Sharma, V. K.; Zhang, D. H.; Dang, C.; Fan, W.; Demir, H. V., Temperature-dependent optoelectronic properties of quasi-2D colloidal cadmium selenide nanoplatelets. *Nanoscale* **2017,** *9* (19), 6595-6605.
31. Osinkski, J.; Kurtin, J. N.; Mangum, B. D.; Nelson, R. Multiple quantum dot (QD) device. US 9,423,083 B2, mar. 7, 2014.
32. Rossinelli, A. A.; Riedinger, A.; Marqués-Gallego, P.; Knüsel, P. N.; Antolinez, F. V.; Norris, D. J., High-temperature growth of thick-shell CdSe/CdS core/shell nanoplatelets. *Chemical Communications* **2017,** *53* (71), 9938-9941.
33. Rossinelli, A. A.; Rojo, H.; Mule, A. S.; Aellen, M.; Cocina, A.; De Leo, E.; Schaublin, R.; Norris, D. J., Compositional Grading for Efficient and Narrowband Emission in CdSe-Based Core/Shell Nanoplatelets. *Chemistry of Materials* **2019,** *31* (22), 9567-9578.

34. ten Kate, O. M.; Zhang, Z.; van Ommen, J. R.; Hintzen, H. T., Dependence of the photoluminescence properties of Eu2+ doped M–Si–N (M = alkali, alkaline earth or rare earth metal) nitridosilicates on their structure and composition. *Journal of Materials Chemistry C* **2018,** *6* (21), 5671-5683.
35. Tian, J.; Zhuang, W.; Liu, R.; Wang, L.; Liu, Y.; Yan, C.; Chen, G.; Xu, H.; Chen, M.; Jiang, Z.; Zhang, X., Enhanced thermal quenching characteristic via carbon doping in red-emitting CaAlSiN 3 :Eu 2+ phosphors. *Journal of the American Ceramic Society* **2019,** *102* (12), 7336-7346.
36. Zhang, X.; Tsai, Y. T.; Wu, S. M.; Lin, Y. C.; Lee, J. F.; Sheu, H. S.; Cheng, B. M.; Liu, R. S., Facile Atmospheric Pressure Synthesis of High Thermal Stability and Narrow-Band Red-Emitting SrLiAl3N4:Eu(2+) Phosphor for High Color Rendering Index White Light-Emitting Diodes. *ACS Appl Mater Interfaces* **2016,** *8* (30), 19612-19617.
37. Senden, T.; Van Harten, E. J.; Meijerink, A., Synthesis and narrow red luminescence of Cs2HfF6:Mn4+, a new phosphor for warm white LEDs. *Journal of Luminescence* **2018,** *194*, 131-138.
38. Haley, K. N.; Mangum, B. D.; Zhao, W.; Stott, N. E.; Kurtin, J. N. Quantum dot (QD) polymer composites for on-chip light emitting diode (LED) applications. US2018/0006195 A1, Sep. 19, 2017.
39. Zhao, W.; Kurtin, J. N. Composition of, and method for forming, a semiconductor structure with multiple insulator coatings. US 10,266,760 B2, Apr. 23, 2019.
40. Li, J. J.; Wang, Y. A.; Guo, W.; Keay, J. C.; Mishima, T. D.; Johnson, M. B.; Peng, X., Large-Scale Synthesis of Nearly Monodisperse CdSe/CdS Core/Shell Nanocrystals Using Air-Stable Reagents via Successive Ion Layer Adsorption and Reaction. *Journal of the American Chemical Society* **2003,** *125* (41), 12567-12575.
41. Ithurria, S.; Bousquet, G.; Dubertret, B., Continuous Transition from 3D to 1D Confinement Observed during the Formation of CdSe Nanoplatelets. *Journal of the American Chemical Society* **2011,** *133* (9), 3070-3077.
42. Ithurria, S.; Talapin, D. V., Colloidal Atomic Layer Deposition (c-ALD) using Self-Limiting Reactions at Nanocrystal Surface Coupled to Phase Transfer between Polar and Nonpolar Media. **2012,** *134* (45), 18585-18590.
43. Htoon, H.; Malko, A. V.; Bussian, D.; Vela, J.; Chen, Y.; Hollingsworth, J. A.; Klimov, V. I., Highly Emissive Multiexcitons in Steady-State Photoluminescence of Individual "Giant" CdSe/CdS Core/Shell Nanocrystals. *Nano Letters* **2010,** *10* (7), 2401-2407.
44. Mooney, J.; Kambhampati, P., Get the Basics Right: Jacobian Conversion of Wavelength and Energy Scales for Quantitative Analysis of Emission Spectra. *The Journal of Physical Chemistry Letters* **2013,** *4* (19), 3316-3318.
45. Kelestemur, Y.; Guzelturk, B.; Erdem, O.; Olutas, M.; Gungor, K.; Demir, H. V., Platelet-in-Box Colloidal Quantum Wells: CdSe/CdS@CdS Core/Crown@Shell Heteronanoplatelets. *Advanced Functional Materials* **2016,** *26* (21), 3570-3579.
46. Rossinelli, A. A.; Riedinger, A.; Marques-Gallego, P.; Knusel, P. N.; Antolinez, F. V.; Norris, D. J., High-temperature growth of thick-shell CdSe/CdS core/shell nanoplatelets. *Chem Commun (Camb)* **2017,** *53* (71), 9938-9941.

* Authors contributed to this work equally by writing the proposal and conducting synchrotron experiments together. They intensely collaborated in the data analysis of the scattering data in chapter 4 and 5. J. C. van der Bok had the main responsibility for the analysis of scattering data analysis in this chapter. D. N. Maaskant and F. A. Brzesowsky performed the *in situ* absorption and ICP measurements under supervision of J. C. van der Bok. All authors are gratefully acknowledged for their contribution to the experiments, discussion and manuscript.

Chapter 4

In situ optical and X-ray spectroscopy reveal evolution towards mature CdSe nanoplatelets by synergetic action of myristate and acetate ligands

Bases on:

J. C. van der Bok*, P. T. Prins*, F. Montanarella, D. N. Maaskant, F. A. Brzesowsky, M. M. van der Sluijs, B. B. V. Salzmann, F. T. Rabouw, A. V. Petukhov, C. De Mello Donega, D. Vanmaekelbergh, and A. Meijerink, *J. Am. Chem. Soc.* **2022**, *144*, (18), 8096–8105.

Abstract

The growth of two-dimensional platelets of the CdX family (X=S, Se, or Te) in an organic solvent requires the presence of both long- and short-chain ligands. This results in nanoplatelets of atomically precise thickness and long-chain ligand-stabilized Cd top and bottom surfaces. The platelets show a bright and spectrally pure luminescence. Despite the enormous interest in CdX platelets for optoelectronics, the growth mechanism is not fully understood. Riedinger *et al.* studied the reaction without a solvent and showed the favorable role for short-chain carboxylates for growth in two dimensions. Their model, based on the total energy of island nucleation, shows favored side facets growth versus growth on the top and bottom surfaces. However, several aspects of the synthesis under realistic conditions are not yet understood: Why are both short- and long-chain ligands required to obtain platelets? Why does the synthesis result in both isotropic nanocrystals and platelets? At which stage of the reaction is there bifurcation between isotropic and 2D growth? In this chapter, an *in situ* study of the CdSe nanoplatelet reaction under practical synthesis conditions is reported. The study shows that without short-chain ligands, both isotropic and mini-nanoplatelets form in the early stage of the process. However, most remaining precursors are consumed in isotropic growth. The addition of acetate induces a dramatic shift toward nearly exclusive 2D growth of already existing mini-nanoplatelets. Hence, although myristate stabilizes mini-nanoplatelets, mature nanoplatelets only grow by a subtle interplay between myristate and acetate, the latter catalyzes fast lateral growth of the side facets of the mini-nanoplatelets.

4.1 Introduction

Over the past decades, CdSe nanoparticles with a wide variety of shapes have been synthesized, for instance quantum dots (QDs),[1] nanorods,[2] and nanoplatelets (NPLs). The latter family is of particular interest because CdSe NPLs exhibit by far the narrowest-band emission of them all.[3] This remarkable property makes CdSe NPLs of interest for implementation in displays, as narrow-band emitters are needed to achieve higher energy efficiency and a wider color gamut.[4,5] The narrow band emission arises from the atomically accurate thickness of these quasi-two-dimensional nanoparticles resulting in strongly reduced inhomogeneous broadening of the emission spectra compared to QDs and nanorods.[6-8]

Implementation of NPLs in applications is only viable if high-quality NPLs are synthesized with high yield and post-synthesis purification steps are minimized. This can only be achieved if the formation of NPLs proceeds with a higher yield than is currently obtained with state-of-the-art synthesis protocols. The synthesis protocol typically used for CdSe NPLs is a solution-based method, similar to the first reported method,[9] where cadmium myristate and elemental selenium are heated in octadecene, and cadmium acetate is introduced in the reaction mixture at elevated temperature. Both CdSe QDs and NPLs form and must be separated by size-selective precipitation of the NPLs at a later stage.[10-15] This is often not clear from reports on the synthesis and optical properties of CdSe NPLs. The NPL yield, if reported, is low; Moreels *et al.* reported an increase in yield for 3.5 ML NPLs using an alternative propionic acid-based method, while the authors reported a chemical yield of 40% when they used the standard method of Ithuria.[15] Moreover, we find that, with the standard CdSe NPL synthesis, the concentration of NPLs formed is far below that of QDs. Platelets are thus formed as a side product, and the low reaction yield and necessity of a purification step form a severe drawback for commercial application.

An improved synthesis method can resolve these issues but requires a better understanding of the reaction mechanism. Even though the first reports on the syntheses of zinc blende CdSe NPLs date from 2008,[9, 16] the formation mechanism of these NPLs is still under debate. Mechanisms proposed for zinc blende CdSe NPL formation include oriented attachment,[17-19] templated growth,[20] and continuous lateral growth.[10, 12, 21] Because experimental data on nanocrystal nucleation and the evolution of (an)isotropic growth under realistic synthesis conditions are lacking, consensus on the formation mechanism has not yet been established. In addition, it is not clear why both long-chain and short-chain ligands are imperative for NPL formation, what controls the growth of both isotropic QDs and 2D NPLs, and how acetate catalyzes the formation of large NPLs in the widely used CdSe NPL synthesis method pioneered by Itthuria and Dubertret.[9] In this study, we provide answers to these questions by studying CdSe QD and NPL nucleation and growth under realistic synthesis conditions.

It is challenging to study nanocrystal growth under reaction conditions that mimic the standard laboratory synthesis, and this has, so far, never been reported for CdSe NPLs. Previous studies on the growth of NPLs have either used *ex situ* analysis of aliquots taken during the reaction or *in situ* probing of the synthesis performed in capillaries.[12, 17, 21] The pitfalls of the first approach are the low temporal resolution and disturbance of the reaction by taking aliquots. Furthermore, aliquots are not fully representative of the reaction mixture, and collecting quantitative aliquots is challenging. The second approach suffers from higher size polydispersity than for a synthesis performed in a flask due to insufficient mixing of reagents and temperature inhomogeneity. Additionally, the difference in reaction volume and diffusion rates in a capillary compared to a reaction flask can influence the reaction. Moreover, and this is crucial for the CdSe NPL synthesis, no additional reactants can be introduced during the reaction when using capillaries.

To resolve these issues and to allow *in situ* probing of the NPL growth, we used a specially designed three-neck flask adapted from a design in the literature with an indentation in the glass (Figure 4.1A).[22, 23] This indentation enables *in situ* UV/Vis absorption spectroscopy and small-angle X-ray scattering (SAXS) studies because it reduces the pathlength from the entire flask (leading to saturation of absorption) to a few millimeters. Hence, the intensity of transmitted light and X-rays is sufficient to conduct meaningful spectroscopy and scattering experiments. The use of this adapted three-neck flask also enables studies under standard reaction conditions, that is, inert atmosphere, high temperatures, and sufficient stirring, identical to the conditions used in the practical synthesis of CdSe NPLs. Moreover, a powder or liquid injector can be installed on top of the flask to remotely add other precursors during the synthesis. Therefore, no adaptions need to be made to the synthesis method for CdSe NPLs, where cadmium acetate is added at elevated temperatures. The growth of high-quality CdSe QDs has previously been investigated for a hot-injection synthesis demonstrating the unique capabilities of this home-built setup for *in situ* monitoring of nanocrystal formation.[24]

Here, we first follow and quantify the formation of CdSe NPLs and QDs and show that the currently used synthesis method yields CdSe NPLs in a much lower concentration with respect to CdSe QDs. A separation step is required to obtain nearly homogeneous solutions of NPLs, and the chemical yield is low, typically less than 50%. Then, we report on *in situ* UV/Vis absorption spectroscopy and SAXS measurements to monitor and quantify the formation of CdSe NPLs and QDs under different synthesis conditions with and without addition of acetate.

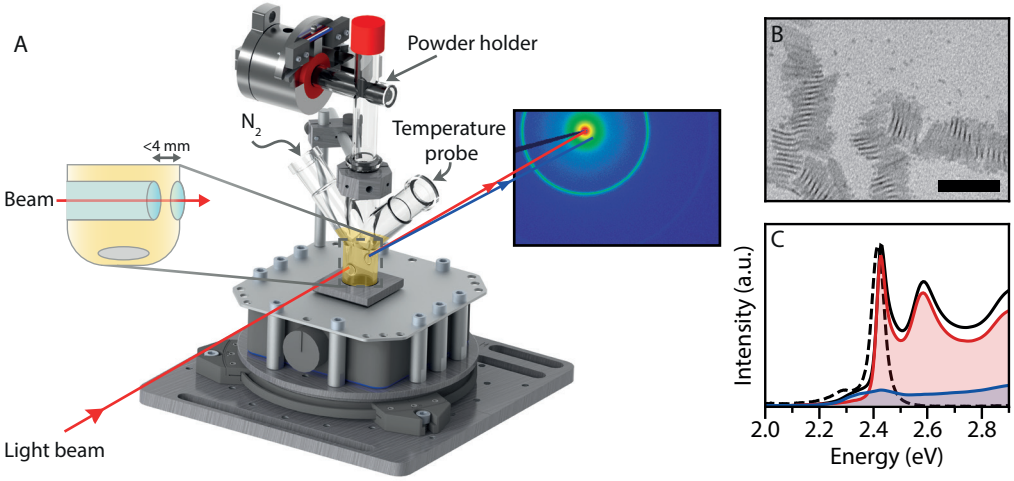

Figure 4.1 (A) Schematic of the experimental setup for *in situ* absorption spectroscopy and X-ray scattering experiments, containing a magnetic stirrer, a custom-made flask, and a powder injector. A protective container and heating ribbon are omitted from the image for clarity. A Teflon™ rod a with small cavity functions as a powder holder. This rod can be rotated remotely, upon which the powder falls into the reaction mixture. The flask can be connected to a nitrogen outlet. The reaction mixture is probed with either a collimated X-ray beam or UV/Vis light beam. An indentation in the reaction flask reduces the pathlength to less than 4 mm. **(B)** TEM image of the product obtained during the *in situ* SAXS experiment with the addition of cadmium acetate at 220 °C. Both NPLs and QDs are formed. The NPLs agglomerate into long stacks. The scalebar represents 50 nm. **(C)** Room-temperature absorption (solid) and emission (dashed) spectra of the same product confirm that both NPLs (2.43 eV) and QDs (~2.3 eV) are formed during the reaction. The contribution of the NPLs and QDs is shown in red and blue respectively. These spectra of the separate contributions were obtained after size-selective precipitation.

By combining the results from both techniques, insights into the growth mechanism and the role of the ligands are obtained. Oriented attachment and lateral extension at the expense of QDs could be excluded as a formation mechanism. Our results show that both myristate and acetate play a pivotal role in the formation of NPLs. In the presence of long myristate ligands, a small concentration of mini-CdSe NPLs nucleates in addition to QDs, even without addition of acetate. In the continued absence of acetate, isotropic growth of QDs dominates. However, the addition of cadmium acetate triggers fast anisotropic growth of the mini-NPLs along the side facets which almost completely outcompetes further QD growth. The results are explained by a subtle interplay between long-chain myristate and short-chain acetate ligands in the formation and growth of QDs and NPLs. These insights can help adapt the synthesis to better control the interplay between ligands and favor the nucleation and growth of 2D NPLs to improve the yield of CdSe NPLs.

4.2 Results and Discussion

The formation of NPLs was followed *ex situ* and *in situ* for the widely used synthesis method[9] for CdSe NPLs which is described in detail in the Methods section. Briefly, it involves a solution-based reaction by heating Cd myristate and elemental Se in octadecene (ODE) typically to

240 °C with the addition of Cd acetate at a specific temperature. The home-built experimental setup for *in situ* measurements is depicted in Figure 4.1. The setup allows for the addition of cadmium acetate at any time and temperature during the synthesis without opening the reaction vessel. First, the optimal addition temperature was determined by adding cadmium acetate at 190, 220, or 240 °C. All experiments were performed in duplicate to verify reproducibility (Figure S4.1). The addition of cadmium acetate at 220 °C resulted in the formation of QDs (3.4 nm diameter[25]) and monodisperse 4.5 monolayer (ML) NPLs. Other temperatures yielded more than one NPL population or a higher fraction of QDs, as can be deduced from the *ex situ* absorption (Supporting Information S4.1.3). For this reason, we focus here on the CdSe NPL synthesis with the addition of cadmium acetate at 220 °C.

A transmission electron microscopy (TEM) image of the product using these reaction conditions (Figure 4.1B) shows the presence of both NPLs and QDs in the final product. The NPLs have a rectangular shape, typical for when anhydrous cadmium acetate is used,[26] with lateral dimensions of 27 ± 2.2 nm by 7.5 ± 1.2 nm (Figures 4.1B and S4.3B). The NPLs tend to form large stacks. *Ex situ* absorption and emission spectra at room temperature are shown in Figure 4.1C. The contribution of the NPLs is highlighted in red and features the characteristic heavy- and light-hole transitions of 4.5 ML NPLs at ~2.4 eV (~510 nm) and ~2.6 eV (~480 nm).[9] The QDs produce a relatively weak absorption and emission feature near 2.3 eV. The contribution of the QDs to the total absorption is indicated in blue.

The fractions of QDs and NPLs in the absorption spectrum were determined with the absorption spectra obtained after size-selective precipitation. From this, we estimated (Supporting Information, Section S4.1.4) concentrations of QDs and NPLs in the reaction mixture of 2.9 µM and 0.35 µM, respectively. This is a rough estimate because the QD fraction still contains residual NPL absorption. Furthermore, the QD concentration is underestimated by the scattering of stacked NPLs at 2.35 eV. This scattering also affects the absorbance at 300 nm. Nevertheless, this rough estimate reveals that the NPL concentration is an order of magnitude lower than the QD concentration. This may seem surprising considering the weak absorption feature of the QDs in Figure 4.1C but it is a consequence of the much lower QD extinction coefficient due to the difference in the volume (21 nm^3 for the QDs compared to 263 nm^3 for the NPLs) and intrinsic absorption coefficient μ_i ($2 \cdot 10^5$ cm^{-1} compared to $6 \cdot 10^5$ cm^{-1}) at a wavelength of 300 nm.[13, 27, 28] Note that even though the concentration of NPLs is about ten times lower, the CdSe yield for the QDs and NPLs is similar due to the large volume difference. The difficulty in extracting the absolute concentrations and the relatively low NPL concentration stresses the importance of exploring the reaction mechanism using *in situ* studies.

4.2.1 In situ study of the evolution of the reaction

The temperature and time evolution of the absorption spectra and SAXS data of the *in situ* measurements are shown in Figures 4.2A,B. The colors reflect the time relative to the cadmium acetate addition at $t = 0$ min, as is specified by the legend on the left. Both data sets show the formation of QDs starting from ~170 °C (dark blue) by the increase in UV absorption and scattering. The q^0 slope extending to 1 nm^{-1} and shape of the early X-ray scattering patterns match the form factor of spherical particles (Figure S4.8), that is, the QDs. These QDs grow over time shifting the absorption maximum to lower energies and slightly shifting the scattering minimum to smaller q values (compare the dark blue and dashed scattering pattern around

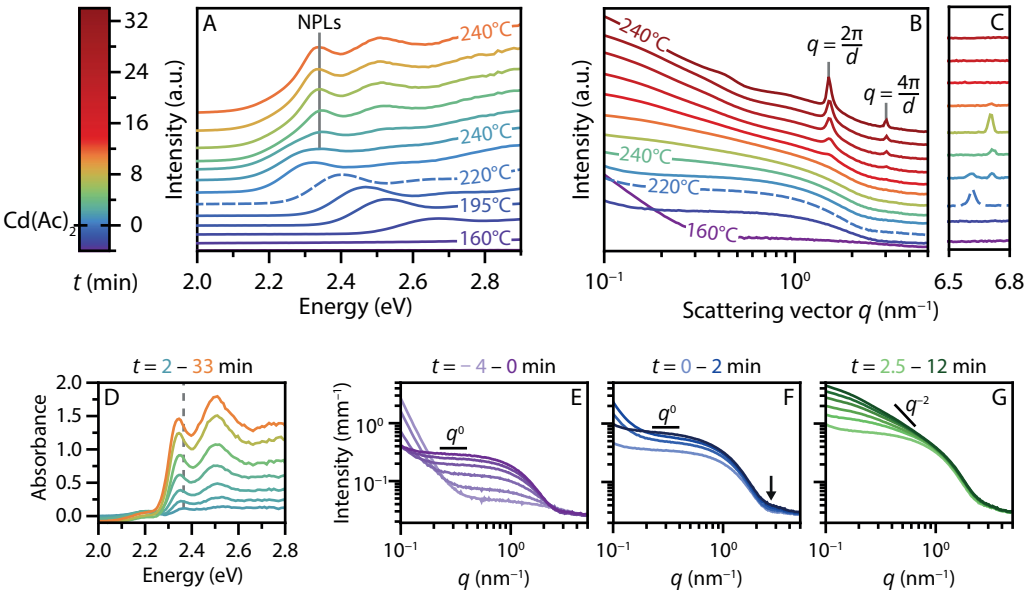

Figure 4.2 Absorption spectra **(A)** and scattering patterns **(B and C)**, shifted for clarity, obtained *in situ* during the synthesis of CdSe NPLs. The colors of all curves correspond to the times indicated in the legend. Temperature increases from ~160 to 240 °C and is then kept at 240 °C. Cadmium acetate is added at 220 °C (dashed line, t = 0 min). Blue to cyan absorption spectra show growth of QDs. The absorption features of the NPLs (2.35 eV) become visible shortly after addition of the acetate. The SAXS data also indicate growth of isotropic particles (purple to blue, scattering intensity scaling as q^0), followed by growth of NPLs after addition of acetate (blue to red, q^0 regime disappears). Structure factor peaks are observed, due to stacking of the formed NPLs ($d = 2\pi/q$ = 4.2 nm). In C, the atomic scattering peak of solid cadmium acetate can be observed. The peak shifts around 230 °C , probably due to a change in the crystal structure. After ~10 min at 240 °C the acetate is completely dissolved. **(D)** The QD absorbance (a spectrum at 230 °C) is subtracted from the data in A. The resulting spectra show the heavy- and light-hole transition of 4.5 ML NPLs at 2.35 and 2.52 eV, respectively, shifted to lower energies compared to room temperature due to temperature effects (see main text). A dashed gray line is added to emphasize the shift of the absorption maximum in the first few frames due to quantum confinement in the lateral dimensions. **(E)** SAXS patterns until addition of the acetate. **(F)** SAXS patterns shortly after addition of acetate. The scattering increases at q = 2 – 3 nm^{-1}, but still, a q^0 regime is observed. **(G)** SAXS patterns 2.5 – 12 min after the acetate addition, reflecting particle growth at 240 °C. The slope at q < 1 nm^{-1} becomes steeper than the previous q^0 scaling, indicating growth of anisotropic particles.

q = 3 nm^{-1}). These features are consistent with the theoretical scattering patterns for growing QDs but a minor contribution of small anisotropic nanostructures cannot be excluded.

The evolution of the QD growth in the scattering patterns is shown in more detail in Figure 4.2E. A shallow minimum is visible at q ~ 3 nm^{-1} and shifts to ~2.8 nm^{-1} over time. The minimum is shallow because of the polydispersity in size. The intense scattering at q < 0.2 nm^{-1} in the first few frames is caused by the scattering of undissolved µm-large selenium particles (Figure S4.6E). The additional scattering reduces when the selenium dissolves and is not significant anymore at t ~ 0 min. No lamellar phase is observed in the SAXS data when nanoparticles

start to form. The cadmium myristate dissolves around 100 °C (Figure S4.6A), well before the onset of nucleation. This rules out templated NPL growth on a lamellar Cd myristate phase and is consistent with other reports.[10, 21, 29]

The absorption spectra in Figure 4.2A show that after the addition of cadmium acetate at 220 °C (dashed), the existing QDs continue to increase in size over the first minute (*i.e.,* the absorption feature shifts to lower energy). Within one minute after the acetate addition, a new absorption feature appears at 2.35 eV, quickly outgrowing the QD absorption. In the scattering data, the growth of small particles is apparent from the increase in intensity at q = 2–3 nm^{-1} (Figure 4.2F, arrow). The slope at q < 1 nm^{-1} still scales with q^0, typical for isotropic particles. After several minutes (Figure 4.2B, yellow and orange), the slope starts to deviate from q^0 which shows that anisotropic particles have formed. The slope is not equal to a q^{-2} slope expected for 2D materials (Figure 4.2G) because the scattering pattern originates from QD and NPL scattering resulting in a slope between q^0 and q^{-2}.

To monitor the growth of the NPLs, the QD contribution was subtracted from the absorption spectra. The resulting spectra are shown in Figure 4.2D and clearly contain the heavy- and light-hole transitions characteristic of 4.5 ML NPLs (at 2.35 and 2.52 eV, respectively). Note that at elevated temperatures, the peak position shifts to lower energies, and the peak width increases compared to room temperature (Figure 4.1C). The peak maximum shifted from 2.43 eV at room temperature to 2.35 eV at 240 °C, corresponding to a shift of 0.37 meV/°C, which matches values of 0.31 – 0.44 meV/°C reported and obtained in Chapter 3 for the emission of 4.5 ML NPLs.[30, 31]

The intensity of the NPL absorption in Figure 4.2D increases over time. In addition, the absorption maximum shifts noticeably between the first few displayed spectra (light blue to green), more than expected from temperature effects. Both the intensity increase and the shift in position are evidence of the growth in the NPL lateral dimensions.[32] At first, the still laterally small NPL dimensions lead to three-dimensional confinement of the exciton. As the NPLs grow, the lateral dimensions quickly exceed the confinement regime, and consequently, the peak does not shift any further. The small fluctuations of the absorption maxima (green to orange) are caused by temperature fluctuations, varying between 235 and 245 °C.

Overall, the evolution of absorption spectra in the different synthesis stages is consistent with the scattering data. Additionally, the scattering data show the stacking of NPLs after ~12 minutes as structure factor peaks begin to appear at q = 1.5 nm^{-1} and q = 3.0 nm^{-1}.[33] These q-values are consistent with linear stacks of NPLs with a center-to-center distance of $d = 2\pi n/q$ = 4.2 nm (with n = 1 or 2). This distance is set by twice the length of the myristate ligand plus the thickness of a 4.5 ML NPL (1.3 nm).[34] Thus, the length determined for the myristate ligands is 1.45 nm, slightly shorter than the 1.7 nm expected for myristate with a fully extended carbon chain.[35] This means that the ligands are not fully extended, or they slightly interpenetrate.

The scattering data further reveal the presence and slow dissolution of solid cadmium acetate crystallites. The reappearance of strong scattering at q < 0.2 nm^{-1} at t = 0 min in Figure 4.2F and the appearance of a peak in the scattering pattern at q = 6.63 nm^{-1} (Figure 4.2C) indicate the presence of undissolved cadmium acetate crystallites (Figure S4.6F). The peak's intensity decreases at 230 °C, and a new peak appears at q = 6.71 nm^{-1}. This shift is probably caused by a change of the cadmium acetate crystal structure.[36, 37] The signal disappears completely after ~10 min at 240 °C. Similar behavior is observed when cadmium myristate and cadmium acetate are heated without the presence of selenium (Figure S4.6D). When cadmium acetate is

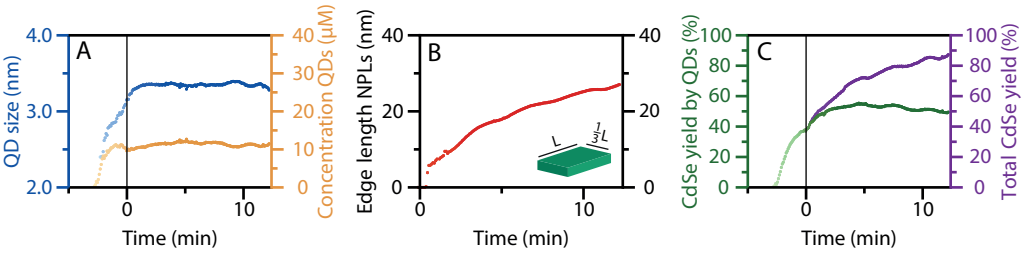

Figure 4.3 Fit results extracted from the SAXS patterns in Figure 4.2B. **(A)** QD diameter (blue) and QD concentration (orange). **(B)** Length *L* of the longest edge of the NPLs. The aspect ratio of the lateral dimensions is 1:3. *L* could be underestimated in the first few minutes because the concentration of the NPLs was kept at a constant value of 0.6 μM during the fitting procedure. **(C)** Percentage of CdSe consumed by the formed QDs in green (CdSe yield by QDs) and by the QDs and NPLs in purple (Total CdSe yield).

heated in the absence of cadmium myristate, the peak in Figure 4.2C does not disappear until a temperature of 255 °C (Figure S4.6F), that is, the melting temperature of cadmium acetate.[36] We conclude that the dissolution of cadmium acetate is assisted by reaction with cadmium myristate forming $Cd(Ac)_{2-x}(Myr)_x$. These results show that NPLs start forming when cadmium acetate is still, at least partly, present as a solid (compare lemon-colored lines in Figures 4.2A,D with that in Figure 4.2C).

The size, aspect ratio, and concentration of the QDs and NPLs can be extracted by fitting the SAXS data in Figure 4.2B, this makes it possible to follow the formation of QDs and NPLs over time. The scattering patterns were carefully corrected for background effects and analyzed to obtain information on the size and shape evolution of nanostructures in the reaction mixture, as described in detail in the Supporting Information. This analysis gave a NPL aspect ratio of 1:3 and a concentration of 0.6 μM. The evolution of size and concentration for the QDs is shown in Figure 4.3A in blue and orange, respectively. The length of the largest lateral dimension *L* of the NPLs is shown in Figure 4.3B in red. The scattering patterns were fitted until the NPLs started to stack at $t = 12$ min. The oscillation in the data is caused by a temperature fluctuation during the synthesis.

Figure 4.3A shows that the QD concentration quickly increases to ~11 μM during the heat-up from 170 to 220 °C and remains constant afterward. The QD diameter increases during this period as well. In the first 1.5 min following cadmium acetate addition, the QDs continue growing from 3.16 to 3.36 nm, consistent with the analysis of the absorption spectra discussed earlier. After 1.5 min, the QD growth stops.

Immediately after the cadmium acetate addition, the lateral dimensions of the NPLs grow, as shown in Figure 4.3B. Within half a minute after the addition of cadmium acetate, NPLs with lateral dimensions of 5.0 by 1.7 nm are visible. This indicates that small NPLs are present before the acetate addition (*vide infra*) but not easily observed because the scattering is negligible compared to the QD scattering (Figure S4.9B). The edge lengths rapidly increase after acetate addition to 26 by 8.7 nm after 12 min, just before the NPLs start to stack. TEM analysis gives lateral dimensions of 27 ± 2.2 by 7.5 ± 1.2 nm (Figure 4.1B and S4.3B), which matches the SAXS results and confirms the reliability of the fitting procedure. The constant concentration of QDs after the cadmium acetate addition indicates that NPL formation is not due to attachment of seed QDs.

Moreover, the diameter of the QDs is already 3.16 nm when cadmium acetate is added, by far exceeding the NPL thickness of 1.3 nm. The constant QD radius and concentration show that the growing NPLs do not consume existing QDs, but the CdSe monomers that are still present in the reaction mixture. The CdSe yield of the reaction, calculated from the incorporated amount of selenium in the nanoparticles (S4.4.1) with respect to the selenium added in the reaction mixture, as shown in Figure 4.3C supports this; The available CdSe units are far from depleted at $t = 0$ min: the total yield (purple) is only 40%. Over the 12 min following cadmium acetate addition, an additional 10% of the available CdSe is incorporated in the QDs. Simultaneously, 40% of the CdSe is incorporated in the NPLs. Hence, the growth of the NPLs is much faster than that of the QDs after the addition of cadmium acetate.

Additionally, the 10% increase in yield due to QD growth indicates that the QDs do not dissolve in favor of NPL growth. The QDs are an undesired by-product of the reaction and consume roughly half of the available precursors. The concentration of QDs (~11 μM) is much higher than the NPL concentration (0.6 μM), as was also estimated from the *ex situ* absorption spectrum. Although most QDs formed before cadmium acetate addition induces the growth of NPLs, they still form when cadmium acetate is added much earlier (Figure S4.3A), and such procedures produce 3.5 ML NPLs instead of 4.5 ML NPLs.

4.2.2 *In situ* study without cadmium acetate

To study the role of cadmium acetate further, we compare the results discussed above with a synthesis using the same reaction conditions but without the addition of cadmium acetate. The *in situ* absorption spectra and SAXS patterns are shown in Figures 4.4A,B, respectively. They show, up until 220 °C, a similar QD evolution compared to the results in Figures 4.2A,B. In contrast to the experiment of Figure 4.2, we add no acetate at 220 °C at $t = 0$. Nevertheless, a new absorption feature still arises around $t = 2$ min. The feature, labeled with "NPLs" in Figure 4.4A, is first visible at 2.34 eV (light blue) and later shifts to 2.28 eV (green). Clearly, a mixture of two types of nanoparticles still forms in the absence of acetate (see also S4.3).

The presence of two populations of nanoparticles is evident in the *ex situ* absorption and emission spectra as well (Figure 4.4C). The luminescence and absorption spectra at room temperature show, in addition to the QD absorption and emission, a peak of a second population of nanoparticles at 2.47 eV. These two populations could be separated with size-selective precipitation. The high-angle annular dark-field scanning transmission electron microscopy (HAADF-STEM) image in Figure 4.4D reveals that the two species of nanoparticles are spherical QDs and small anisotropic nanoparticles. The anisotropic nanoparticles appear as rod-like structures in the HAADF-STEM image with the largest lateral dimension equal to ~5 nm.

These nanoparticles stack during the synthesis, and give rise to the structure factor peaks in the SAXS data at $q = 1.5$ nm^{-1} and $q = 3$ nm^{-1}. These q-values are due to stacking at a center-to-center distance of 4.5 nm, which is larger than the center-to-center distance found above for the stacked 4.5 ML NPLs (Figure 4.2B) by 0.3 nm. This difference matches the thickness of one CdSe monolayer, that is, half a unit cell. The anisotropic nanoparticles are thus likely "mini-NPLs" of 5.5 ML thickness. They appear as rod-like structures on (S)TEM images and in a HDAAF-STEM tilt series (Figure S4.4) because the shortest lateral dimension is not much larger than the thickness of the mini-NPLs, when assuming a similar aspect ratio as that of the large NPLs (3:1).

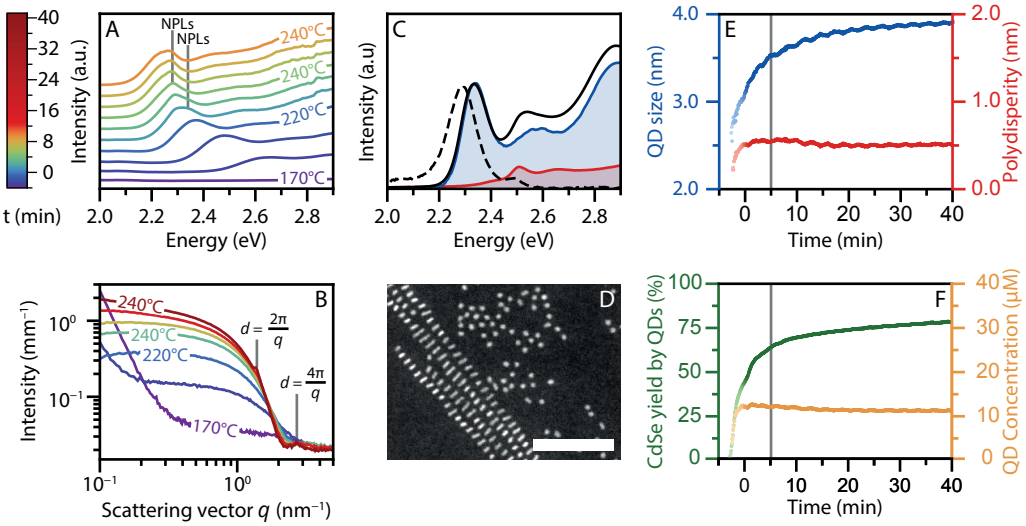

Figure 4.4 Absorption spectra **(A)** and scattering patterns **(B)** of *in situ* experiments when no acetate is added to the reaction mixture. In A, the spectra are shifted in intensity for clarity. The weak absorption features of 4.5 mini-NPLs at 2.34 eV and 5.5 ML mini-NPLs at 2.28 eV are labeled with NPLs for clarity. Features shift to lower energies compared to room temperature due to temperature effects. The structure factor peaks of the stacked 5.5 ML mini-NPLs are labeled in B (d = 4.5 nm). **(C)** Absorption (solid) and emission (dashed) spectra at room temperature of the product obtained during the *in situ* SAXS experiment. Next to QD absorption and emission (2.3 eV), also a second population of nanoparticles is present: mini-NPLs (2.47 eV). The blue and red curves represent contributions from the supernatant (QDs, blue) and precipitate (predominantly mini-NPLs, red) after selective precipitation. **(D)** HDAAF-STEM image of the reaction product showing stacked mini-NPLs and QDs, scalebar 50 nm. **(E)** Diameter (blue) and polydispersity (red) of the QDs extracted from fitting the SAXS data in B. **(F)** QD concentration during the reaction (orange) and the reaction yield (green). This yield only accounts for the CdSe consumed by the QDs. The total yield, including the mini-NPLs, is ~3% higher than the yield in F. The gray line in E and F at ~5 min indicates when the stacking of the mini-NPLs starts to contribute to the total scattering.

Heating the reaction mixture to 240 °C results in the formation of 5.5 ML mini-NPLs. Mini-NPLs with a thickness of 4.5 ML can also be synthesized by lowering the final reaction temperature to 190 °C instead of 240 °C. Structure factor peaks at the same position as in Figure 4.2B were observed in SAXS data obtained using these reaction conditions (Figure S4.13). In the reaction with acetate, the 4.5 ML mini-NPLs rapidly grow to form 4.5 ML NPLs. Without acetate, 5.5 ML mini-NPLs form upon heating to 240 °C. This temperature dependence suggests that the two absorption features in Figure 4.4A, labeled with NPLs, correspond to mini-NPLs with a thickness of 4.5 ML formed below 240 °C (2.34 eV, slightly higher energy than that of large 4.5 ML NPLs) and 5.5 ML mini-NPLs formed after a temperature of 240 °C is reached (2.28 eV). Note that the stronger confinement for the small lateral dimension of the 5.5 ML mini-NPLs results in stronger temperature dependence of the absorption maximum, shifting it to a higher energy (2.47 eV) at room temperature compared to the thinner but larger 4.5 ML NPLs (2.43 eV).

The size, polydispersity, and concentration of the QDs and mini-NPLs and the reaction yield were extracted from the SAXS data as well.[38] The method is discussed in detail in the SI (S4.2.3). The form factor of a disk was used to approximate the mini-NPLs shape. An average radius for the mini-NPLs of 3.5 nm was obtained with 4.5% polydispersity and a concentration of ~0.25 μM. The fit results for the QDs are shown in Figures 4.4E and 4.4F. The evolution of the QD concentration in the cases with and without cadmium acetate is very similar, (orange, Figures 4.3A and 4.4F). The polydispersities are also similar, reaching a value of ~0.5 nm after an initial increase. However, the increase in QD size over time is strikingly different between the experiments. While acetate addition leads to stagnating QD growth shortly after t = 0 (Figure 4.2), the growth continues until a final size of 3.8 nm at t = 10 min in the absence of acetate. The 0.4 nm difference in final size shows that without cadmium acetate, more CdSe precursor is available for QD growth. In other words, the presence of cadmium acetate results in precursor consumption by the growth of the second population of nanocrystals, that is, the NPLs.

The same conclusion can be drawn by comparing the reaction yields with and without the addition of cadmium acetate. The yield of the reaction without cadmium acetate is given in Figure 4.4F in green. The yield in Figure 4.4F accounts only for the CdSe incorporated in the QDs and can therefore directly be compared to the corresponding results of the experiment with acetate (green in Figure 4.3C). Similar values for the yield are obtained until t = 0 min (38%). However, without the addition of cadmium acetate, the final CdSe consumption by QDs is much higher (70% compared to 50% after 12 min). Without acetate, the anisotropic particles (mini-NPLs) take up 3% of the total CdSe content (S4.4.2), compared to 40% CdSe incorporated in NPLs in the experiment with acetate. We verified the yield derived from the SAXS results by ICP-OES analysis. Yields of 47 ± 1.5 and 75 ± 1% were obtained with ICP at reaction times corresponding to t = 10 minutes and t = 30 minutes in Figure 4.4F, respectively. This matches well with the SAXS results. The results from optical absorption, SAXS, and ICP-OES are consistent and show that the contribution of the stacked and individual mini-NPLs to the total yield for the synthesis without acetate is low.

We learn from these experiments that the addition of the acetate strongly enhances the growth rate of already existing anisotropic particles (mini-NPLs) but not the growth rate of the QDs. The presence of acetate promotes the lateral growth of already existing NPLs so strongly that almost no reactants are used in the further growth of the QDs. The question rises if acetate also affects the nucleation of mini-NPLs versus small QDs in the initial stage of the reaction. From the fit, we estimate a mini-NPL concentration of 0.25 μM without and a NPL concentration of 0.6 μM with acetate. The 0.25 μM is a lower limit as only the stacked mini-NPLs contribute, while the 0.6 μM is a more reliable estimate of the total concentration of NPLs. Both concentrations of (mini)-NPLs are very small compared to the QD concentration. Hence, acetate does not strongly affect the initial ratio between QDs and mini-NPLs, but its role is to favor very strongly the lateral growth of already existing mini-NPLs.

4.2.3 Growth mechanism of CdSe NPLs

Figure 4.5 gives a schematic overview of the reaction mechanism based on the data discussed in this work. In the early stage of the reaction, both QDs and mini-NPLs with small lateral dimensions form. The mini-NPLs have an order of magnitude lower concentration than the QDs. Once formed, the mini-NPLs are likely stabilized by strong Van der Waals interactions between the long alkyl chains of the ligand layers on the top and bottom facets. The stability of

the myristate layers on the large facets is evidenced by the center-to-center distances observed for (mini-)NPL stacks by *in situ* SAXS. Even at high temperature, these distances are consistent with spacing by slightly interpretating myristate layers. Furthermore, a higher concentration of long-chain ligands results in increased NPL absorption relative to QD absorption.[29]

When solid cadmium acetate crystallites are added to the reaction mixture, the solution concentration of cadmium acetate is initially low as the crystallites dissolve slowly. As the solution concentration of acetate increases, the monomer consumption by the small facets of the NPL starts to outcompete the monomer consumption by the QDs. Importantly, our work demonstrates that the conditions under which NPLs grow are not required to make NPLs nucleate. Indeed, we observe mini-NPLs even if we do not add acetate to the reaction and at approximately the same final concentration as for the large NPLs. On the other hand, the formation of mini-NPLs seems to be disrupted if too much acetate is available too early in the reaction. For example, when cesium acetate (melting point 195 °C) instead of cadmium acetate is added at 190 °C while heating to 240 °C, only 3D particles are formed (Figure S4.5A). Under these conditions, the concentration of acetate in solution is too high immediately after addition. On the other hand, NPLs are formed when cesium acetate is added at 190 °C without further heating to 240 °C (Figure S4.5B). The results are in line with previous reports on acetates catalyzing NPL growth.[9] All reported acetates have melting points well above 190 °C (see SI Section S4.1.9). Note that the addition of different acetates also affects the lateral shape of the NPLs. Likely other factors next to the melting point, such as the reactivity of the cation acetate, also affect the growth of the NPLs.

The model proposed by Norris *et al.*[10,39] explains anisotropic 2D growth of (mini-)NPLs by a lower activation energy for island nucleation on side facets compared to top and bottom facets. This activation energy is determined by the volume, area, and line energies of zinc blende CdSe. The synthesis condition used to construct the model, *i.e.*, NPLs formed in a melt of cadmium acetate and selenium, deviates significantly from the solution-based synthesis studied here. Furthermore, the work of Norris *et al.* considers constant reaction conditions, while in our and standard experiments, the conditions are changed midway by addition of cadmium acetate. The presence of acetate affecting the CdSe monomer consumption stresses the importance of including the effect of the surfactants on anisotropic growth.

The effect of cadmium acetate addition can be included in a NPL growth model as a drop in the values for area, line, and volume energies. Lowering any of these energies results in a decrease in the activation energy for "island nucleation", *i.e.*, the formation of a new monolayer on an existing facet, and hence an acceleration of crystal growth. With the right combination of energy values, island nucleation rates on the narrow facets outpaces that on the top and bottom facets. The fastest growing facets can consume available monomers so quickly that growth on other facets effectively stops. Interestingly, further lowering area, line, and volume energies decreases the difference in the activation energies between narrow and large facets. This explains why the addition of too much acetate early in the reaction results in isotropic growth, as it decreases the anisotropy in growth rates.

The middle part of Figure 4.5 gives a molecular picture of the potential effects of cadmium acetate on the volume, surface, and line energies. The volume energy may become more negative when cadmium acetate is present in the reaction mixture by lowering the solubility of the cadmium precursor. The surface and line energies decrease due to changes in the ligand cov-

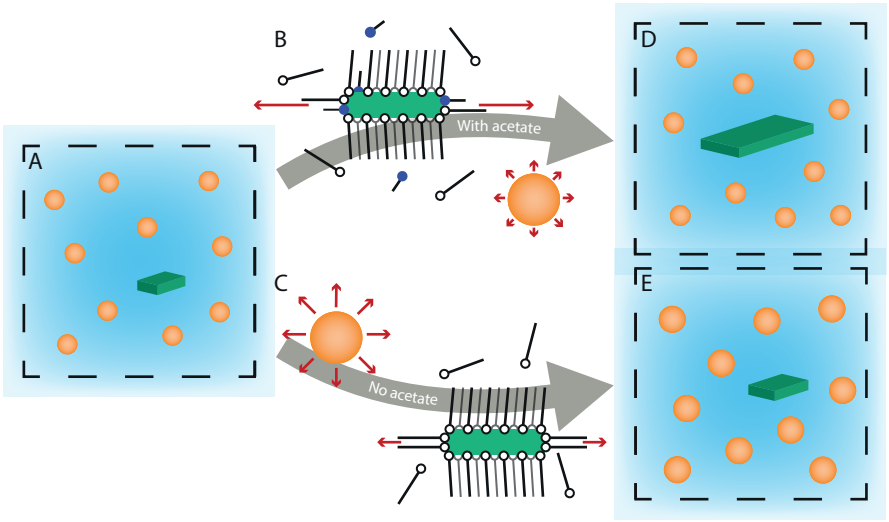

Figure 4.5 Schematic overview of the CdSe NPL growth mechanism. **(A)** Nanoparticles nucleate and grow. An order of magnitude more QDs are formed than NPLs. Middle **(B)**: The addition of acetate results in faster monomer consumption. With the reaction conditions used here, most monomers are consumed by growth of the small facets of the NPL (red arrows). As a result, the NPLs grow laterally, and the QDs do not grow much **(D)**. The concentration of QDs and NPLs is unaffected by the addition of an acetate. Middle **(C)**: If no acetate is added, both QDs and mini-NPLs grow with a comparable monomer consumption (red arrows). This way the NPLs remain small, and slightly larger QDs are obtained compared to with the addition of acetate **(E)**.

erage of the NPL by exchanges of myristate ligands with acetate. The reaction rate for all NPL and QD facets will likely increase. However, as the activation energy for island nucleation on narrow NPL facets is the lowest, the effective monomer consumption by the narrow facets of the NPL will outcompete the monomer consumption by the QDs and large facets (red arrows). A higher ligand exchange of the side facets by short acetate ligands, due to weaker binding sites at the edges,[11] may further enhance the 2D growth by lowering the steric barrier for monomer attachment on side facets.

The formation of large NPLs, using the standard CdSe NPL reaction protocol, thus ultimately relies on the synergy between cadmium myristate and cadmium acetate ligands, where the cadmium myristate reduces isotropic growth by stabilizing mini-NPLs at the early stages of the reaction, and addition of cadmium acetate results in faster growth on the small side facets. The molecular picture that we present is in line with the model of Norris, which emphasizes that an appropriate balance of surface and line energies is required for two-dimensional growth. When no acetate is added, both the QDs and mini-NPLs grow with a comparable monomer consumption (Figure 4.5C). This can be deduced from the similar ratio between the concentrations and contributions to the total yield (11 μM compared to 0.25 μM, and 75% yield and 3% yield after 12 min). The presence of acetate favors lateral growth of the platelets and, by precursor consumption, impedes further growth of the QDs. Acetate addition determines the sizes but not the final concentrations of the two types of particles (Figure 4.5D and 4.5E).

4.3 Conclusions

With our home-built setup, we were able to probe *in situ* the formation of CdSe NPLs with (or without) the addition of cadmium acetate for the standard NPL synthesis under realistic reaction conditions. Analysis of *in situ* absorption and scattering experiments shows that both isotropic and anisotropic particles form at an early stage of the reaction even without short-chain ligands. NPLs with large lateral dimensions (~27 by 7.5 nm) are formed due to a synergy between the long myristate ligands stabilizing top/bottom facets of the 2D structures and short acetate ligands that promote fast growth of the NPL side facets but do not affect the NPL concentration. The concentration of NPLs (~0.6 μM) is low compared to the QDs (~11 μM), which are always formed as a prominent and undesired side product. These QDs are responsible for a low NPL reaction yield and have to be removed using size-selective precipitation. The new insights in the mechanism of CdSe NPL formation can help improve the synthesis conditions (such as type and concentration of ligands, reaction temperature, etc.) to optimize the mini-NPL *versus* QD formation and NPL growth to improve the NPL yield.

4.4 Methods

4.5 ML CdSe NPLs were synthesized as reported by Ithurria *et al.*[12] For the *in situ* measurements, the synthesis was scaled down by a factor of two. 85 mg of cadmium myristate (0.15 mmol, see SI), 6.0 mg of elemental selenium (0.075 mmol) and 7.5 mL of ODE were loaded in a specially designed three-neck flask and degassed under vacuum at room temperature for 1 h. After degassing, the mixture was put under a nitrogen atmosphere, and the powder injector (Figure 3.1A) was connected with 26 mg of cadmium (0.11 mmol) acetate in the powder holder. The system was flushed three times by applying a vacuum or nitrogen flow. Then, the mixture was heated to 240 °C with a rate of 15 °C/min using a heating ribbon around the flask. For the *in situ* absorption measurements, a transparent medium was needed to align the flask with the UV/Vis light beam. Therefore, an additional heating step to ~110 °C, before heating to 240 °C, was implemented to melt and dissolve the cadmium myristate.

A series of experiments was conducted to investigate the role of acetate in the formation of CdSe NPLs. In the various experiments, the flask with the reaction mixture was heated to 240 °C. Cadmium acetate was added at 190 °C, 220 °C or 240 °C by rotating the powder holder. Furthermore, an experiment without the addition of acetate was performed. During the reaction, UV/Vis absorption spectra or X-ray scattering patterns were recorded. After heating up and a reaction time of 10 – 45 min at 240 °C the mixture was let to cool down to room temperature. 0.5 mL of oleic acid was added at 70 °C and 7 mL hexane at room temperature. The product was purified twice by adding 45 mL of methanol/butanol mixture (1:2) and centrifuged at 3000 rpm (~1000 RCF). Special care was taken to precipitate all the product to ensure that the absorption spectra give a reliable view of the ratio QDs-to-NPLs. If the supernatant was not transparent, more methanol was added. Finally, the product was redispersed in 4 mL of hexane.

The SAXS experiments were conducted at the SWING beamline of synchrotron Soleil at an energy of 16 keV and a sample-to-detector distance of 1.83 m. This allowed us to probe a $\boldsymbol{q}$-range of 0.05 nm^{-1} – 8 nm^{-1}. 2D scattering patterns were recorded every 5 s with an exposure time of 3 s. The background scattering of the solvent, reactants and flask was subtracted from the azimuthally integrated 2D scattering patterns (S4.2.1 and S4.2.2). Models for the fitting of the scattering patterns are discussed in the Supporting Information (S4.2.3).

The *in situ* absorption experiments were performed using a DH-2000-BAL lamp as the excitation source, 200 µm core solarization resistant fibers and a USB4000 spectrometer all from Ocean Insight. To obtain a collimated light beam with a diameter smaller than 5 mm, the diameter of the indentation in the glass, the following optics was used: 14 mm focal point (f14) Vis achromatic lens, 350 nm long pass filter, f30 Vis aspherical achromatic lens, 200 µm pinhole, and f14 Vis aspherical, achromatic lens. The light bundle after the sample was coupled into a fiber using a f14 Vis aspherical, achromatic lens. The lenses and filter were obtained from Edmund Optics. Spectra were recorded with an integration time of 100 ms. The absorbance was calculated afterward, taking an I_0-spectrum just before nanoparticles started to form.

S4 Supporting Information

S4.1 Experimental methods and characterization

S4.1.1 Materials

1-butanol (anhydrous, 99.8%), 1-octadecene (ODE, 90%), cadmium(II) acetate anhydrous (99.995%), cadmium(II) nitrate tetrahydrate (99,99%, trace metal basis), cesium(I) acetate (99.999%, trace metal basis), hexane (anhydrous, 95%), methanol (anhydrous, 99,8%), methanol (100%), oleic acid (OA, 90%), sodium myristate (≥99%), toluene (anhydrous, 95%) were all purchased from Sigma Aldrich. Selenium powder (200 mesh, 99.999%) was purchased from Brunschwig Chemie. ODE and OA were degassed at 100 °C under vacuum for 3h and other chemicals were used without further purification.

S4.1.2 Cadmium myristate precursor

Cadmium myristate precursor was prepared by dissolving 1.23 g cadmium nitrate tetrahydrate (4 mmol) in 40 mL methanol and 3.13 g sodium myristate (12.5 mmol) in 250 mL methanol. The cadmium nitrate solution was added to the sodium myristate solution while stirring. A white precipitate was visible. The precipitate was vacuum filtrated using a Buchner flask and rinsed with 1 L of methanol (hydrous). The cadmium myristate was dried overnight under vacuum to remove methanol and water.

S4.1.3 Absorption spectra products *in situ* SAXS experiments in homebuilt setup

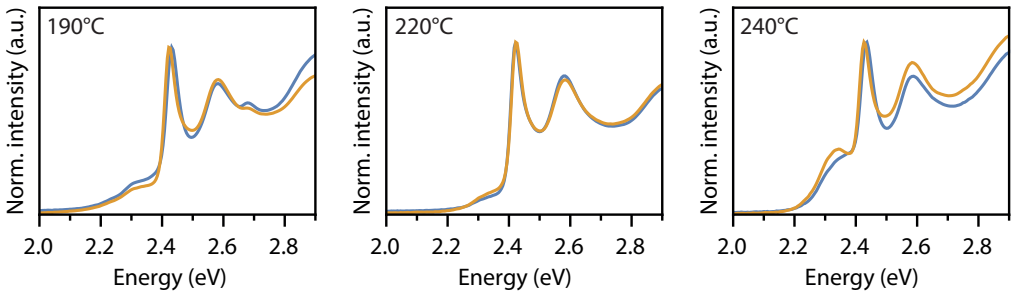

Figure S4.1 *Ex situ* absorption spectra of the product from *in situ* SAXS experiments where cadmium acetate is added at 190 °C, 220 °C, and 240 °C. Experiments were performed in duplicate (orange and blue). These *ex situ* results verify that synthesis is reproducible in our homebuilt setup. NPLs emitting at 2.7 eV (460 nm) are obtained next to NPLs emitting at 2.45 eV (510 nm) and QDs at ~2.3 eV (~540 nm) when acetate is added at 190 °C. When cadmium acetate is added at 240 °C, more QDs compared to NPLs are formed. Addition at 220 °C results in the formation of only one population of NPLs and a smaller amount of QDs. For these reasons, 220 °C was used for the procedure in the main text.

S4.1.4 Concentration QDs and NPLs from *ex situ* absorption spectra

The NPL and QD concentration were estimated from the *ex situ* spectra in Figure 4.1C (S4.2A) and Figure 4.4C (S4.2B) using Lambert-Beers law. The contribution of the NPLs- or QDs absorbance to the total absorbance at 300 nm (4.13 eV) was determined by fitting the spectra with the QD and NPL fractions obtained with size-selective precipitation. The absorption coefficients well above the band edge absorption were calculated for the NPLs and QDs as described in literature.[25, 27, 40] For these calculations, the QD volume was extracted from the absorption spectra using the sizing curve by Hens *et al.*[25] and the volume of the NPLs was obtained from TEM analysis. The resulting concentrations of the product dispersions were scaled to match the volume during the synthesis at 240 °C, *i.e.*, scaled to a total volume of 9.4 mL (7.5 mL ODE and a volume expansion of 25% at 240 °C.[41]) This ensures that the calculated concentrations

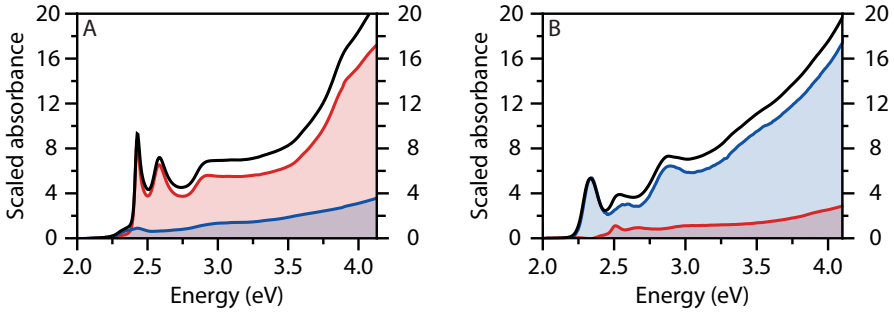

Figure S4.2 Absorption spectra from main text with absorbance at high energy for determination of the QD and NPL concentration. The absorbance is scaled to match the absorbance of the reaction mixture in the reaction flask at 240 °C. **(A)** Synthesis with addition of cadmium acetate. NPLs (red) and QD (blue) contributions were extracted using size-selective precipitation. **(B)** Synthesis without addition of cadmium acetate, mini-NPLs and QD contribution are shown in red and blue, respectively. No pure mini-NPL fraction could be extracted, the spectrum in red therefore contains some QD absorption.

can directly be compared to the concentrations obtained from the *in situ* SAXS analysis. A QD and NPL concentration of 2.9 µM and 0.35 µM were obtained for the synthesis with addition of cadmium acetate. A QD concentration of 11.2 µM was extracted for the synthesis without addition cadmium acetate.

S4.1.5 TEM-images of 3.5 ML NPLs, 4.5 ML NPLs and 5.5 ML mini-NPLs

The TEM-images and HDAAF-STEM images in the SI or main text were either recorded on a FEI Technai 20 operating at 80 keV or a Talos F200X operating at 200 keV. Samples were made by drop-casting a dilute dispersion of nanoparticles on a TEM-grid.

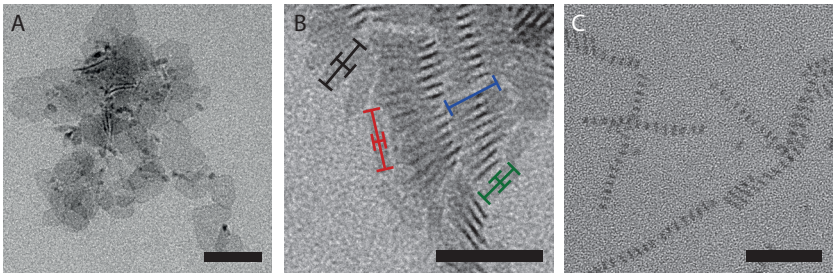

Figure S4.3 (A) TEM-image displaying 3.5 ML NPLs and QDs obtained when cadmium acetate is added at room temperature and the reaction mixture is heated to 240 °C for 10 minutes in a standard three-neck flask. **(B)** TEM-image of 4.5 ML NPLs obtained during SAXS experiment in homebuilt setup with addition of cadmium acetate at 220 °C. The lateral dimensions of a few NPLs are indicated in the image. The average lateral dimensions, 27 ± 2.2 nm by 7.5 ± 1.2 nm, were determined by measuring >100 NPLs. **(C)** Bright-field TEM image 5.5 ML mini-NPLs obtained when no cadmium acetate is added. Synthesis performed in homebuilt setup. Scalebars correspond to 50 nm.

S4.1.6 Tilt series HDAAF-STEM 5.5 ML mini-NPLs

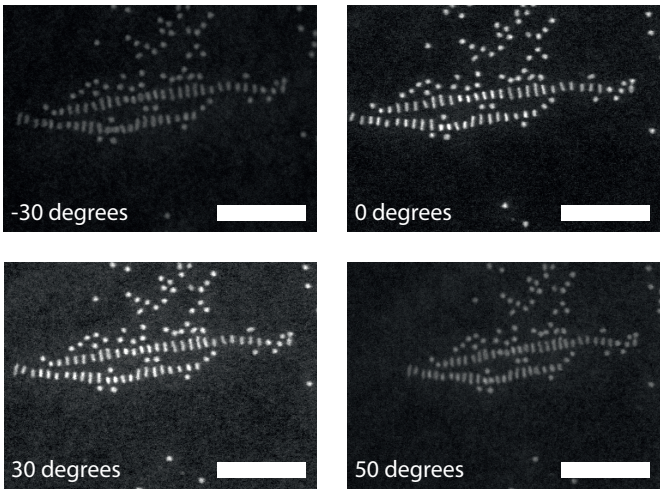

Figure S4.4 Tilt series of reaction product without addition of cadmium acetate. The HDAAF-STEM images were measured for the reaction product without size-selective precipitation and show the presence of both mini-NPLs and QDs.

S4.1.7 NPLs synthesis with cesium acetate

The synthesis method for NPLs with the addition of cesium acetate is similar to the method reported in the main text. The amounts were not halved for these experiments and were performed in a standard 100 mL three-neck round-bottom flask. 86 mg cesium acetate (0.44 mmol) was added at 190 °C. A twice as high amount in mmol of cesium(I)acetate compared to cadmium(II)acetate was added to ensure that an equal amount of acetate was present during the reaction.

S4.1.8 TEM images and absorption spectra cesium acetate experiments

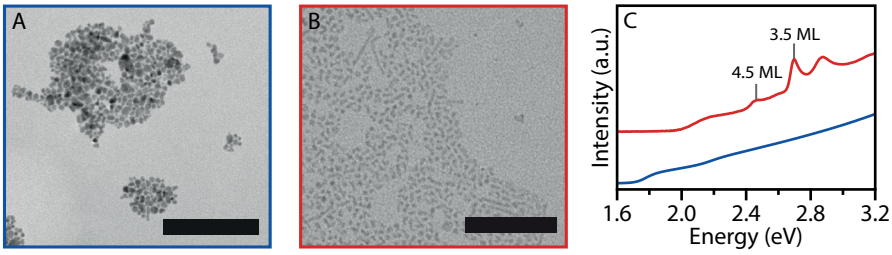

Figure S4.5 TEM-images of the synthesis product when cesium acetate is added at 190 °C and temperature is increased to 240 °C, scale bar 200 nm **(A)** or cesium acetate is added at 190 °C without increasing the temperature, scale bar 100 nm **(B)**. The absorption spectra are shown in blue and red, respectively **(C)**. NPLs are only observed on TEM images and in absorption spectra when the temperature is not increased above the melting temperature of cesium acetate (195 °C).

S4.1.9 Melting point other acetate salts

In the literature other acetate salts have been reported, including $Mn(Ac)_2.4H_2O$, $Zn(Ac)_2$, $Mg(Ac)2.4H_2O$, $Co(Ac)_2.4H_2O$, and Na(Ac), to promote formation of CdSe NPLs.[9] All these mentioned acetates resulted in the formation of NPLs in our own experiments as well (addition temperature of 190 °C). The melting temperature of all these acetates is higher than 190 °C: $Co(Ac)_2$ (298 °C), $Mn(Ac)_2$ (210 °C), $Zn(Ac)_2$ (257 °C), $Na(Ac)_2$ (324 °C). For $Mg(Ac)_2.4H_2O$, a melting point of 90 °C is often reported. However, $Mg(Ac)_2$ dissolves in the water incorporated in the crystal at this temperature, giving a seemingly lower melting temperature. A melting temperature of ~230 °C is reported by Yu Jiang *et al.* for $Mg(Ac)_2$.[42] In this respect, it is worth noting that we only observe anhydrous cadmium acetate in the scattering patterns (peak at $q = 6.63\ nm^{-1}$) when we either add anhydrous or hydrous cadmium acetate. The water incorporated in the crystal is apparently quickly lost. Therefore, we consider the melting points of the anhydrous salt even if the hydrous version is added.

S4.2 Backgrounds, data correction and analysis of SAXS patterns

S4.2.1 SAXS patterns of the precursors

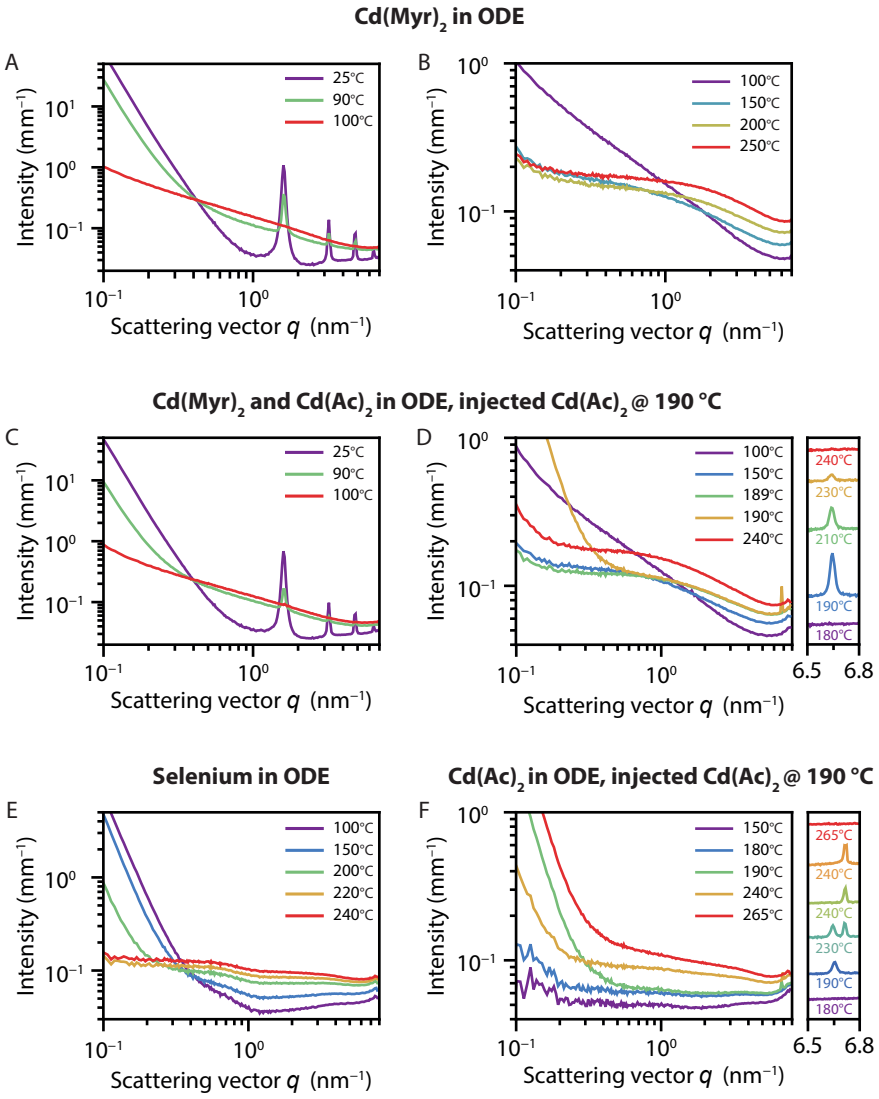

Figure S4.6 Top: Scattering patterns of cadmium myristate in ODE at low **(A)** and high **(B)** temperatures. At low temperatures a lamellar phase is observed, which melts around 100 °C. The scattering patterns of experiments discussed in the main text were corrected using these scattering patterns. **(C,D)** scattering patterns of cadmium myristate in ODE with the addition of cadmium acetate at 190 °C. The addition of cadmium acetate can be observed by the increase in scattering at small q-values ($q < 0.2$ nm^{-1}) and by a peak at ~6.7 nm^{-1} (orange, D). The scattering peak is plotted more clearly next to the figure. These scattering patterns are shifted for clarity. The increase in intensity at $q < 0.2$ nm^{-1} and the peak at ~6.7 nm^{-1}

disappear upon heating the mixture to 230 °C. Note: This temperature is lower compared to when the acetate is injected at 220 °C (experiment in the main text) because the acetate is introduced earlier. **(E)** Scattering patterns at different temperatures of selenium in ODE (selenium added at room temperature). The presence of large selenium clumps results in scattering at small q-values. Selenium starts to dissolve after reaching 150 °C. Selenium in ODE gives an almost constant background at 220 °C and higher. **(F)** Scattering patterns of cadmium acetate in ODE at different temperatures (acetate injected at 190 °C). The increase in scattering at small q and the appearance of a peak at ~6.7 nm^{-1} upon addition of the acetate is also observed here. Around 230 °C, the peak shifts to higher q-values, similar to what was observed during the experiment in the main text. The cadmium acetate salt does not melt/dissolve at temperatures lower than its melting temperature (255 °C) without the presence of cadmium myristate in the mixture. In the right panel, where the cadmium acetate peak is shown, the peak is still observed after prolonged heating at 240 °C. The two plots at 240 °C are 20 min apart. This indicates that the cadmium acetate reacts with cadmium myristate when both are present in the reaction mixture.

S4.2.2 SAXS data processing

We obtained the 1D scattering curves of the growing nanocrystals by azimuthal integration of the patterns recorded on the 2D detector. The curves were processed by subtracting the temperature-dependent scattering of a cadmium myristate precursor solution in the reaction flask (Figure S4.6, left) and the scattering of the empty flask:

$$I_{\text{proc}}(T) = I_{\text{raw}}(T) - aI_{\text{flask}} - b\left[I_{\text{Cd(Myr)}_2\text{ in ODE}}(T) - I_{\text{flask}}\right] \tag{S4.1}$$

The values for a varied between 0.95 and 1.05. A constant value of ~0.8 was used for b for all temperatures. This value was determined at 240 °C. After this processing, $I_{\text{proc}}(T)$ still contained some residual cadmium myristate scattering before the temperature reached 240 °C because less myristate precursor had reacted. This additional scattering was accounted for during the fit by approximating the scattering, arbitrarily, with the form factor of a sphere with a radius of ~0.7 nm ($P_{\text{sphere,myr}}$ in follwing sections). Figure S4.7 shows that the scattering of cadmium myristate resembles that of a sphere (red) for $q > 1$ nm^{-1}. At these q-values, cadmium myristate background is the dominant contribution to the scattering signal in the initial stages of our in situ synthesis experiments. The strength of this background signal decreases as the reaction mixture is heated and is negligible when the temperature hits 240 °C. Selenium does not produce any significant background at intermediate q-values, and it fully dissolves in ODE at the temperatures of interest.

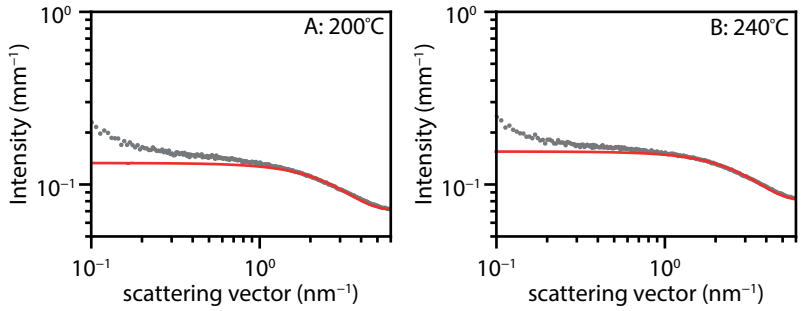

Figure S4.7 The scattering of cadmium myristate (gray) at 200 °C **(A)** and 240 °C **(B)** can be approximated with the scattering pattern of a spherical particle with a radius of 0.7 nm (red). This calculated scattering curve was used during the fitting procedure to fit the initially higher scattering of cadmium myristate, which was underestimated by the correction described above.

The absolute scattering intensity was corrected for the pathlength of X-rays through the reaction flask, which ranged from 3.4 mm to 3.8 mm, and was determined by measuring the scattering intensity of water for each of the different flasks used during our experiments. The scattering intensity could then be calibrated using the known absolute scattering cross-section of water ($1.65 \cdot 10^{-3}$ mm^{-1} at 16 keV).[43]

S4.2.3 Qualitative analysis and models for the weighted least-square fitting procedure

Qualitative analysis SAXS scattering pattern QDs and NPLs

The scattering patterns can be analyse qualitatively by inspecting the q-dependence of the scattering. Figure S4.8 displays some theoretical scattering patterns for spherical (QDs) and rectangular (NPLs) shaped particles of different sizes.

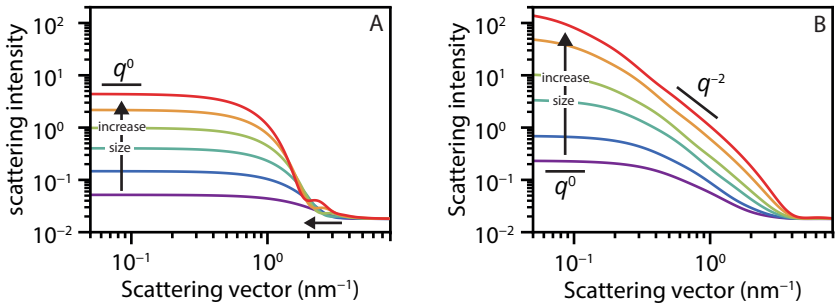

Figure S4.8 Theoretical form factor of **(A)** spheres and **(B)** rectangular 2D particles with a thickness of 1.3 nm. A similar polydispersity of the particles and amount of background scattering are used as in the experiments. The number density of the rectangular particles is one order of magnitude lower than the QDs. QD diameters considered in the panel range from 2 to 4.5 nm. For larger QDs, the minima shift to smaller q values (horizontal arrow). The lateral dimensions of the NPLs in panel B range from 1.5 nm by 4.5 nm to 8 nm by 24 nm. Qualitatively, NPLs and QDs can easily be distinguished in SAXS; both have a regime where the scattering is independent of q (indicated with q^0), but the NPLs also have a range where the slope scales with q^{-2}. Additionally, the minima for rectangular particles are less pronounced due to rotational averaging.

Quantum dots

CdSe quantum dots (QDs) have a quasi-spherical shape. Good fit results can be obtained from SAXS data of CdSe QDs by assuming spheres with a Gaussian size distribution. The scattering intensity of spherical particles with a Gaussian distribution of radii is given by

$$I(q) = n_1 \Delta\rho^2 \left\langle P_{\text{sphere}}(q) \right\rangle_R S_{\text{spheres}}(q), \tag{S4.2}$$

where n_1 is the number density, $\Delta\rho$ the scattering length density (SLD) contrast, $\left\langle P_{\text{sphere}}(q) \right\rangle_R$ the average form factor for spherical particles with average radius R_0 and standard deviation σ_R. $S_{\text{spheres}}(q)$ is the structure factor due to positional order between the particles. In our experiments, the QD density remains low and the inter-QD interactions are weak, so $S_{\text{spheres}}(q) = 1$. The form factor of a sphere of radius R is

$$P_{\text{sphere}}(q) = 36\pi\Delta\rho^2 V_{\text{sphere}}^2 \frac{(\sin qR - qR\cos qR)^2}{(qR)^6}. \tag{S4.3}$$

Averaging over a Gaussian size distribution is described by

$$\left\langle P_{\text{sphere}}(q) \right\rangle_R = 36\pi\Delta\rho^2 \frac{1}{\sqrt{2\pi}\sigma_R} \int_0^\infty e^{-\frac{1}{2}\left(\frac{R-R_0}{\sigma_R}\right)^2} V_{\text{sphere}}^2 \frac{(\sin qR - qR\cos qR)^2}{(qR)^6} \mathrm{d}R, \tag{S4.4}$$

where V_{sphere} is the volume of a sphere with radius R. $\Delta\rho$ is calculated by subtracting the SLD of the reaction mixture from that of CdSe: $\Delta\rho = \rho_{CdSe} - \rho_{reaction\ mixture}$. Using the SLD calculator provided by the National Institute of Standards and Technology (NIST, https://www.ncnr.nist.gov/resourses/activation/) we obtained $\rho_{CdSe} = 40.6 \times 10^{-6}$ Å^{-1} for CdSe at 16 keV. For the organic reaction mixture, we considered a mass density of 0.63 g cm^{-3} at 240 °C[41] due to thermal expansion. With this density, we obtain $\rho_{reaction\ mixture} = 6.1 \times 10^{-6}$ Å^{-1} at 16 keV.

Experiments without acetate addition: stacked mini NPLs

The scattering intensity of a stack of NPLs can be approximated by[44]

$$I(q) = n_2 \Delta\rho^2 \langle P_{NPLs}(q) \rangle_R F_{stacking}(q), \tag{S4.5}$$

where n_2 is the number density of the NPLs, $\Delta\rho$ the SLD contrast between the NPL and the reaction mixture (see model for QDs), $\langle P_{NPLs}(q) \rangle_R$ the average form factor of the lateral shape of the NPLs and $F_{stacking}$(q) the shape factor for the structure in the perpendicular direction. The mini-NPLs were, for simplicity, fitted with the form factor of a disk with radius R:

$$P_{mini\text{-}NPL}(q) = 16\pi\Delta\rho^2 A_{NPL}^2 \frac{2J_1(qR)^2}{(qR)^2} \tag{S4.6}$$

With a Gaussian distribution in the radii of the disk, this becomes

$$\langle P_{mini\text{-}NPL}(q) \rangle_R = 16\pi\Delta\rho^2 \frac{1}{\sqrt{2\pi}\sigma_R} \int_0^\infty e^{-\frac{1}{2}\left(\frac{R-R_0}{\sigma_R}\right)^2} A_{NPL}^2 \frac{2J_1(qR)^2}{(qR)^2} \mathrm{d}R, \tag{S4.7}$$

with A_{NPL} the area of a disk with radius R, $J_1(qR)$ the first-order Bessel function, R_0 the average radius and σ_R the standard deviation in R.

The shape factor $F_{stacking}(q)$ is the Fourier transform of the electron density profile in the stacking direction and is given by[38]

$$F_{stacking}(q) = NL^2 \frac{\sin(qL/2)}{qL/2} \frac{\sin(qNd/2)}{\sin(qd/2)}, \tag{S4.8}$$

where L is the thickness of the 5.5 ML mini-NPLs which is 1.6 nm, d the spacing between two NPLs which could be determined by the position of the structure factor peaks (d = 4.5 nm), N is the number of NPLs in a stack. A Gaussian distribution was also used for the number of NPLs in a stack:

$$\langle F_{stacking}(q) \rangle_N = \frac{L^2}{\sqrt{2\pi}\sigma_N} \int_0^\infty e^{-\frac{1}{2}\left(\frac{N-N_0}{\sigma_N}\right)^2} N \frac{\sin(qL/2)}{qL/2} \frac{\sin(qNd/2)}{\sin(qd/2)} \mathrm{d}N \tag{S4.9}$$

The complete model, used for the synthesis where no acetate is added, is:

$$I(q) = B + n_0 P_{sphere,myr}(q) + n_1 \Delta\rho^2 \langle P_{sphere}(q) \rangle_R + n_2 \Delta\rho^2 \langle P_{mini\text{-}NPL}(q) \rangle_R \langle F_{stacking}(q) \rangle_N \tag{S4.10}$$

The first term is the background scattering and the second accounts for the additional scattering of cadmium myristate during the heat-up. The scattering patterns were fitted using this model, with B, n_0, n_1, n_2, $R_{mini\text{-}NPLs}$, R_{QDs}, $\sigma_{R,mini\text{-}NPLs}$, $\sigma_{R,QDs}$, N and σ_N as free fit parameters. An example of a fit with the contribution of the QDs and stacked NPLs is shown in Figure S4.9

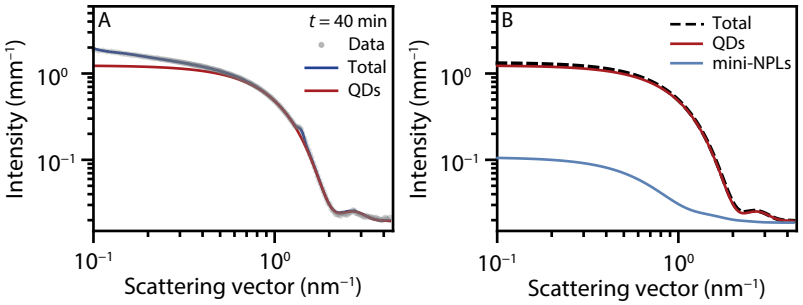

Figure S4.9 (A) Fit (blue) of scattering pattern 40 min after reaching a temperature of 220 °C using a the discussed models for scattering of QDs and stacked 5.5 ML mini-NPLs. The contribution of the QDs is shown in red. **(B)** Scattering intensity of unstacked 5.5 ML mini-NPLs compared to the fitted QD-scattering in A. In blue the scattering of 5.5 ML mini-NPLs with a 3.5 nm radius, thickness of 1.6 nm, and a concentration of 0.25 μM. These values were extracted from the fit in A. The effect of unstacked mini-NPLs on the total scattering (black dashed) is neglectable. The same holds for NPLs with small lateral dimensions in a synthesis with addition of cadmium acetate. The increase in scattering at small q in A is mainly caused by the stacks of mini-NPLs, not by the scattering of individual mini-NPLs.

Experiments with acetate addition: large rectangular 4.5 ML NPLs

The large 4.5 ML NPLs obtained when cadmium acetate is added during the reaction could not be fitted well with the form factor of a disk (in contrast to the 5.5 ML mini-NPLs). These scattering patterns were fitted using the form factor of a rectangular-shaped particle with a thickness of 1.3 nm, corresponding to 4.5 ML NPLs. The form factor, averaged over all orientations, for this anisotropic particle is given by[45]

$$P_{\mathrm{NPL}}(q) = \int_0^{2\pi}\int_0^{\pi}\left|4RWd\frac{\sin(q_xR)}{q_xR}\frac{\sin(q_yW)}{q_yW}\frac{\sin(q_zd/2)}{q_zd/2}\right|^2 \sin\theta\,\mathrm{d}\theta\,\mathrm{d}\phi \qquad \text{(S4.11)}$$

$$q_x = q\sin\theta\cos\phi$$
$$q_y = q\sin\theta\sin\phi$$
$$q_z = q\cos\theta$$

where R, W, and d are the half-length, half-width and thickness of the particles, respectively. Best fits were obtained with W equal to 3R. Again, a Gaussian distribution in R was used.

The complete model to fit the scattering data for experiments with acetate addition is

$$I(q) = B + n_0P_{\mathrm{sphere,myr}}(q) + n_1\Delta\rho^2\left\langle P_{\mathrm{sphere}}(q)\right\rangle_R + n_2\Delta\rho^2\left\langle P_{\mathrm{NPLs}}(q)\right\rangle_R + aI_{\mathrm{Cd(Ac)_2\ in\ ODE}} \qquad \text{(S4.12)}$$

The first term accounts for background scattering and the second for the additional myristate scattering during the heat-up. The last term accounts for the scattering of the cadmium acetate crystallites in the reaction mixture. The ratio between the lateral dimension, W/R = 3, and the NPL concentration, $n_2/N_A = c_{\mathrm{NPL}}$ = 0.6 μM, were determined from a fit to the scattering curve at an experiment time where the cadmium acetate has melted, *i.e.*, t = 9 min. The values were fixed for the fits to the curves at all other times.

Both experiments (with or without acetate addition) saw the polydispersity of the QDs ($\sigma_{R,QDs}$) increase to a value of 0.5 nm during the heat-up to 220 °C. Background scattering from cadmium acetate, following addition at 220 °C, complicated reliable fitting of the scattering contribution from QDs. We therefore fixed the QD polydispersity at $\sigma_{R,QDs}$ = 0.5 nm for the analysis of all scattering curves following acetate addition. Examples of fitted data before and after cadmium acetate dissolution are shown in Figure S4.10.

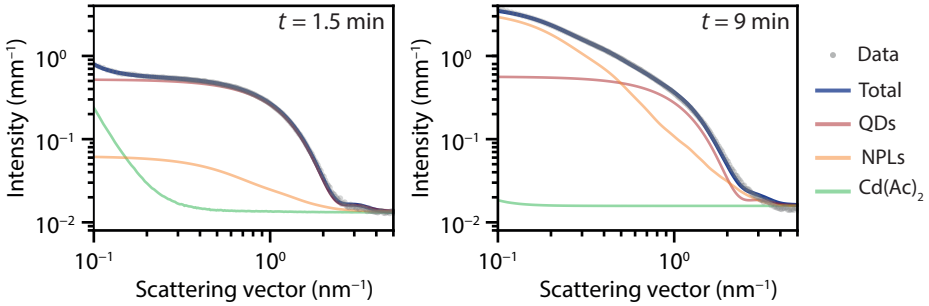

Figure S4.10 Fitted scattering patterns at t = 1.5 min (left) and t = 9 min (right) with the contribution of QD-, NPL- and cadmium acetate scattering to the total scattering. The fitted intensity of the flat background scattering B (~0.015 mm^{-1}) is added to the fits shown in blue, red, orange, and green.

S4.2.4 Fit results SAXS with and without cadmium acetate addition

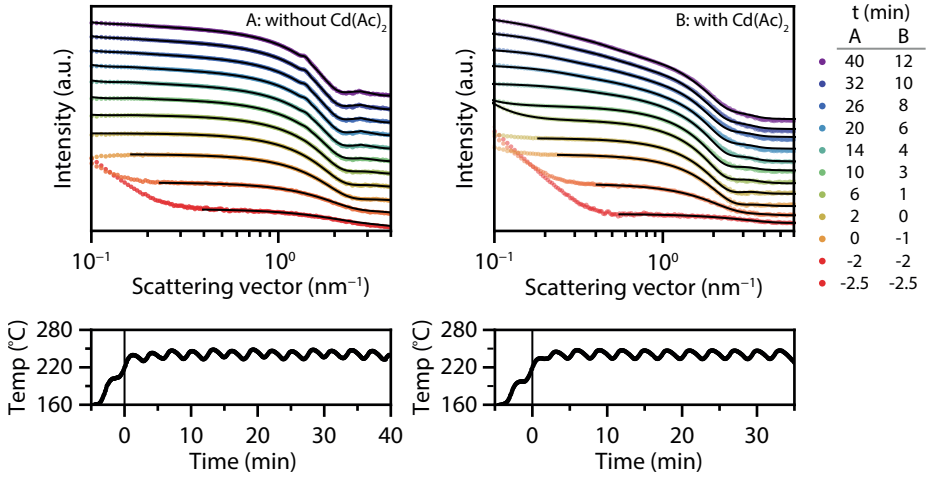

Figure S4.11 Selection of scattering patterns with fit (black) obtained using the models described above. Synthesis **(A)** without and **(B)** with the addition of cadmium acetate at t = 0. Scattering patterns are shifted in intensity for clarity. Below the temperature profiles are given of the respective experiments.

S4.2.5 Variations fitting procedure SAXS data with cadmium acetate addition

In Figure S4.12, we check that our fit results are robust to slight variations of the model used. We compare the fit results obtained with a fixed time-independent NPL concentration c_{NPL} to those obtained when c_{NPL} is a free parameter, and the results obtained with and without the inclusion of a background contribution due to cadmium acetate. The estimated lateral dimensions are similar at t > 7.5 min for three variations considered to the model (blue, red, and green). The variation where both the NPLs concentration and cadmium acetate background was fitted (orange) gives slightly smaller values because it overestimates the

cadmium acetate background. However, if no cadmium acetate background is included in the model, the NPL concentration shows an unrealistic peak in the NPL concentration around t = 2 min and the lateral dimensions are very large at t < 2.5 min (Figure S4.12, green). This is likely an artifact due to the false assignment of the sloping background scattering of cadmium acetate to NPLs. We resolve this difficulty by fixing c_{NPL} = 0.6 μM, which is the constant value extracted for t > 5 min (Figure S4.12B). This might give rise to a slight overestimation of the lateral dimension in the first minutes after the addition of cadmium acetate. The value of 0.6 μM is similar to the concentration of mini-NPLs obtained when no acetate is added and therefore is likely a good estimate of the NPL concentration around t = 0 – 5 min.

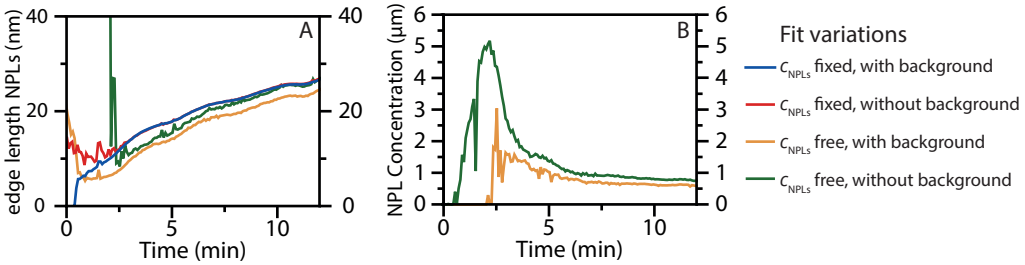

Figure S4.12 Fit results of the synthesis with cadmium acetate addition (Figure S4.11B) using four variations to the model described for scattering of NPLs with a rectangular shape: **(A)** the NPL size, expressed in terms of the longest edge length while the aspect ratio is fixed at 3:1, and **(B)** NPL concentration. We kept the NPL concentration fixed at c_{NPL} = 0.6 μM (blue and red) or used it as a free fit parameter (orange and green). We did (blue and orange) or did not (red and green) include a background contribution of cadmium acetate.

S4.2.6 SAXS data formation mini-NPLs at 190 °C followed with addition cadmium acetate

The data in the main text shows that 5.5 ML mini-NPLs form when the reaction mixture is heated to 240 °C without adding cadmium acetate at 190 °C. Thinner mini-NPLs can be synthesized when the reaction temperature is kept at 190 °C instead. The structure factor peaks in Figure S4.13A show that 4.5 ML mini-NPLs form after prolonged heating at 190 °C. Large 4.5 ML NPLs can still be formed when cadmium acetate is added after 35 min at 190 °C. The reaction temperature is also increased to 240 °C as for a standard 4.5ML NPLs synthesis (Figure S4.13B).

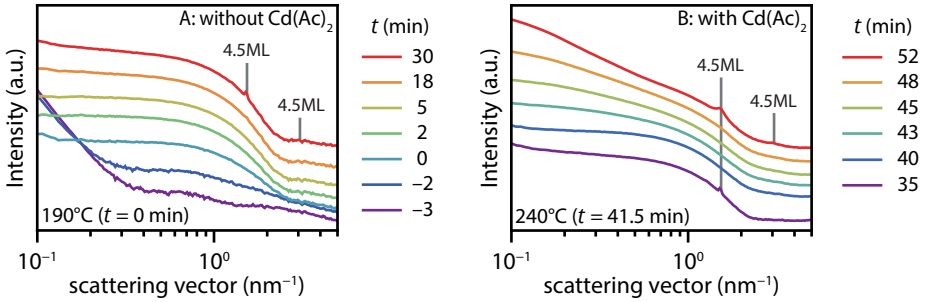

Figure S4.13 (A) Scattering data without adding cadmium acetate with a reaction temperature of 190 °C instead of 240 °C as in the main text. The scattering data corresponds to the form factor of spherical NCs, but after prolonged heating, structure factor peaks appear corresponding to 4.5ML mini-NPLs (red). **(B)** Upon addition of cadmium acetate (t = 35 min), the mini-NPLs first unstack (purple to blue scattering pattern), and the lateral dimension of the NPLs increase (green–orange), which can be deduced from the change in slope for q < 1 nm^{-1}. At the end of the reaction, the large NPLs also form stacks, indicated by the structure factor peaks. The peaks' positions correspond to 4.5 ML NPLs.

S4.3 Fit *In situ* absorption synthesis without addition acetate

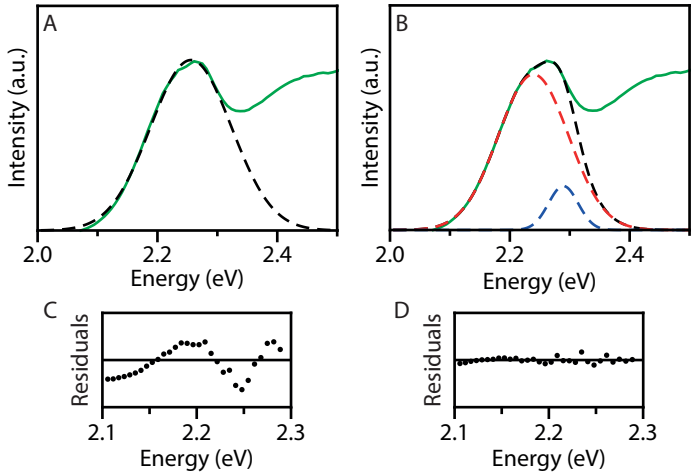

Figure S4.14 Single gaussian **(A)** and double Gaussian **(B)** fit of first exciton transition in the *in situ* absorption spectrum at t = 10 min and T = 240 °C for the synthesis without addition of cadmium acetate (orange spectrum Figure 4.4A). The fit and the fit residuals of the single Gaussian fit (**A** and **C**) show a systematic deviation and reveal an additional feature on the high energy side. The double Gaussian fits the data well (see fit residuals, **D**) and reveals a small extra absorption peak at the position of the 5.5 ML mini-NPLs (at ~2.28 eV).

S4.4 Comparison SAXS and ICP-OES results

S4.4.1 Calculation yield from SAXS data

The yields of the reaction displayed in Figures 4.3C and 4.4F were determined from the SAXS data by calculating the amount of selenium incorporated into the QDs and (mini-)NPLs and the amount of selenium added at the start of the reaction (6 mg) because selenium is the element in deficit. From the SAXS scattering patterns, we extracted the molar concentration ($n_{NP}/N_A = c_{NP}$) and average volume $\langle V_{NP} \rangle_R$ of the nanoparticles (NPs), where R are the radii (QDs and mini-NPLs) or edge lengths (NPLs). The yield can be obtained by calculating the average amount of selenium in a NP

$$N_{Se} = \frac{4 \langle V_{NP} \rangle_R}{a^3}, \tag{S4.13}$$

where $a^3 = 0.22$ nm^3 is the volume of the cubic unit cell of zinc blende CdSe. The factor 4 comes in because a unit cell contains four Se atoms. The yield can then be expressed as:

$$\text{Yield}(\%) = c_{NC} \frac{N_{Se}}{c_0} \cdot 100\%, \tag{S4.14}$$

where c_0 is the initial concentration of selenium ($8.2 \cdot 10^{-3}$ M), *i.e.*, 6 mg in a total reaction volume of 9.4 mL, taking the thermal expansion of the reaction mixture into account.

Note that for the volume of the NPLs and mini-NPLs a thickness of 1.2 nm and 1.5 nm is used instead of the actual thickness (1.3 nm and 1.6 nm) to account for the additional cadmium layer. The number of selenium atoms in a (mini-)NPL would be overestimated without this adjustment.

S4.4.2 Yield and concentration synthesis without addition $Cd(Ac)_2$

Figure 4.4F of the main text shows the CdSe consumption by the QDs (CdSe yield by QDs) when no cadmium acetate is added. For the total yield of the synthesis also the CdSe consumption by the mini-NPLs should be considered. The concentration and size of the mini-NPLs could be extracted from the SAXS data when the mini-NPLs started to stack. The reaction yield as a function of reaction time was then calculated as

$$\text{Yield}(\%) = \frac{4\langle V_{\text{mini-NPL}}\rangle_R}{a^3}\frac{c_{\text{mini-NPLs}}}{c_0}\cdot 100\%, \qquad \text{(S4.15)}$$

where $\langle V_{\text{mini-NPL}}\rangle_R$ is the NPL volume averaged over the fitted distribution of disk radii, $a^3 = 0.22\ \text{nm}^3$ is the volume of the cubic unit cell of zinc blende CdSe, and c_0 is the initial concentration of Se (the element in deficit) in the reaction mixture. The factor four comes in because a unit cell contains four Se atoms. For the calculated the volume, relevant for Se consumption, a thickness of 1.5 nm instead of 1.6 nm was used to compensate for the additional cadmium layer as both top and bottom facets are Cd-terminated.

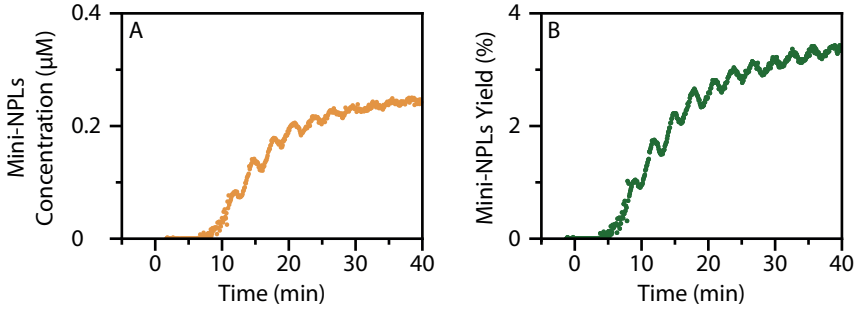

Table 1: Yield ICP-OES and SAXS without addition $Cd(Ac)_2$

ICP-OES		SAXS			
t (min)	Total Yield (%)	*t* (min)	Total Yield (%)	QD Yield (%)	mini-NPL Yield (%)
13	52 ± 0.8	13	71.5 – 73	70	1.5 – 3
13	44 ± 0.8	30	79	76	3
13	42 ± 2.7	40	81	78	3
13	49 ± 0.9				
30	74 ± 1.0				
30	75 ± 0.9				

Figure S4.15 Concentration **(A)** and yield **(B)** of 5.5 ML mini-NPLs as a function of reaction time for synthesis without addition cadmium acetate. The oscillations are caused by temperature oscillation (S4.2.4) affecting the expansion of the reaction flask and reaction volume. The concentration and yield plotted are underestimated values because only the scattering of stacking mini-NPLs is visible over scattering of QDs, while scattering of individual mini-NPLs is too weak. The growth of mini-NPL concentration and yield between t = 5 min and 30 min reflect that more and longer stacks are formed. Starting from t = 30 min, the NPL concentration levels off to a constant value of 0.25 µM. **Table 1** shows the total yield determined with ICP-OES and SAXS for reactions without addition of cadmium acetate. The values represent the selenium consumption by QD and mini-NPLs. At 13 min, there is not much stacking of the mini-NPLs yet. The yield is estimated to be between 1.5% and 3%.

The concentration and yield of the stacked mini-NPLs are shown in Figure S4.15. After 30 – 40 min, the concentration was ~0.25 µM and the yield ~3%. This results in a total yield, QD and mini-NPLs CdSe consumption of 81% after a reaction time of 40 min.

The concentration and yield of the mini-NPLs could be underestimated because only the concentration of the stacked mini-NPLs could be extracted from the SAXS data. Therefore, the total reaction yield was also determined *ex situ* with ICP-OES. The selenium concentration (element in deficit) in a sample cannot be determined directly with ICP because sample preparation with an acid results in the formation of H_2Se, which escapes. Instead, the cadmium concentration was measured and a molar ratio of Se:Cd = 1 in the QDs and mini-NPLs was assumed to determine the yield of the reaction. The sample preparation is discussed in the following section. The yields obtained after a reaction time of 10 min and 30 min are shown in Table 1 in Figure S4.15.

The yield obtained via ICP-OES is similar to the SAXS results. After 30 min, the total yield is ~75% and ~79%, respectively. After 13 min, the yield is a bit lower in the ICP analysis (~47% compared to ~72%), which is likely due to the heat-up difference in a standard three-neck flask compared to the flask used for SAXS analysis. Overall, the comparison of ICP and SAXS results shows that the mini-NPL concentration and yield are not heavily underestimated with only probing the stacked mini-NPLs.

S4.4.3 Yield synthesis with addition $Cd(Ac)_2$

The SAXS yield was also verified with ICP-OES for the synthesis with addition of cadmium acetate. The comparison is shown below in Table 2. The ICP yield was measured thrice. For the ICP results, a molar ratio of Se:Cd = 1 in the QDs and NPLs was used. Due to the additional cadmium layer, this ratio will deviate for the NPLs. Also here, the yield around 13 minutes is slightly lower, likely due the heat-up difference in a standard three-neck flask compared to the flask used for SAXS analysis. Both the SAXS and ICP results show that at 13 min a higher total reaction yield is obtained when cadmium acetate is added to the reaction mixture.

Table 2: Yield ICP-OES and SAXS with addition $Cd(Ac)_2$

ICP-OES		SAXS			
t (min)	Total Yield (%)	*t* (min)	Total Yield (%)	QD Yield (%)	NPL Yield (%)
13	63 ± 1.4	12	88	50	38
13	76 ± 1.5				
13	70 ± 1.0				

S4.4.4 Preparation and measurement method ICP-OES

To prepare the ICP samples, first, the unreacted precursors were removed after a synthesis using the standard washing method discussed in the experimental section. The total mass of the product in hexane was weighted (~10 g). 2 grams of the whole product was taken and put under vacuum to remove hexane. 2 mL 65% nitric acid was added to dissolve the CdSe nanoparticles. After the solution was clear, it was diluted with Milli-Q water to a total volume of 10 mL. The samples were diluted at least 500 times with a 5% nitric acid in milli-Q water solution to obtain a cadmium concentration of ~0.5 ppm. The exact cadmium concentration was determined with a 0 – 1 ppm cadmium in a 5% nitric acid calibration curve made using standard solution 3 of PerkinElmer. Measurements were conducted with a PerkinElmer ICP-OES Optima 8300. The cadmium concentration was measured using the emission lines at 228.8 nm, 214.4 nm, and 226.5 nm. The yield was calculated using the average ppm values obtained with measurements on these three emission lines.

References

1. Murray, C. B.; Norris, D. J.; Bawendi, M. G., Synthesis and characterization of nearly monodisperse CdE (E = sulfur, selenium, tellurium) semiconductor nanocrystallites. *Journal of the American Chemical Society* **1993,** *115* (19), 8706-8715.
2. Peng, X.; Manna, L.; Yang, W.; Wickham, J.; Scher, E.; Kadavanich, A.; Alivisatos, A. P., Shape control of CdSe nanocrystals. *Nature* **2000,** *404* (6773), 59-61.
3. Chen, Z.; Nadal, B.; Mahler, B.; Aubin, H.; Dubertret, B., Quasi-2D Colloidal Semiconductor Nanoplatelets for Narrow Electroluminescence. *Advanced Functional Materials* **2014,** *24* (3), 295-302.
4. Estrada, D.; Shimizu, K.; Bohmer, M.; Gangwal, S.; Diederich, T.; Grabowski, S.; Tashjian, G.; Chamberlin, D.; Shchekin, O. B.; Bhardwaj, J., 32-1: On-chip Red Quantum Dots in White LEDs for General Illumination. *SID Symposium Digest of Technical Papers* **2018,** *49* (1), 405-408.
5. Mangum, B. D.; Landes, T. S.; Theobald, B. R.; Kurtin, J. N., Exploring the bounds of narrow-band quantum dot downconverted LEDs. *Photonics Research* **2017,** *5* (2), A13-A22.
6. Tessier, M. D.; Javaux, C.; Maksimovic, I.; Loriette, V.; Dubertret, B., Spectroscopy of Single CdSe Nanoplatelets. *ACS Nano* **2012,** *6* (8), 6751-6758.
7. Reiss, P.; Carayon, S.; Bleuse, J.; Pron, A., Low polydispersity core/shell nanocrystals of CdSe/ZnSe and CdSe/ZnSe/ZnS type: preparation and optical studies. *Synthetic Metals* **2003,** *139* (3), 649-652.
8. Cui, J.; Beyler, A. P.; Marshall, L. F.; Chen, O.; Harris, D. K.; Wanger, D. D.; Brokmann, X.; Bawendi, M. G., Direct probe of spectral inhomogeneity reveals synthetic tunability of single-nanocrystal spectral linewidths. *Nature Chemistry* **2013,** *5* (7), 602-606.
9. Ithurria, S.; Dubertret, B., Quasi 2D colloidal CdSe platelets with thicknesses controlled at the atomic level. *J Am Chem Soc* **2008,** *130* (49), 16504-5.
10. Riedinger, A.; Ott, F. D.; Mule, A.; Mazzotti, S.; Knüsel, P. N.; Stephan; Prins, F.; Erwin, S. C.; Norris, D. J., An intrinsic growth instability in isotropic materials leads to quasi-two-dimensional nanoplatelets. *Nature Materials* **2017,** *16* (7), 743-748.
11. Singh, S.; Tomar, R.; Ten Brinck, S.; De Roo, J.; Geiregat, P.; Martins, J. C.; Infante, I.; Hens, Z., Colloidal CdSe Nanoplatelets, A Model for Surface Chemistry/Optoelectronic Property Relations in Semiconductor Nanocrystals. *Journal of the American Chemical Society* **2018,** *140* (41), 13292-13300.
12. Ithurria, S.; Bousquet, G.; Dubertret, B., Continuous Transition from 3D to 1D Confinement Observed during the Formation of CdSe Nanoplatelets. *Journal of the American Chemical Society* **2011,** *133* (9), 3070-3077.
13. Yeltik, A.; Delikanli, S.; Olutas, M.; Kelestemur, Y.; Guzelturk, B.; Demir, H. V., Experimental Determination of the Absorption Cross-Section and Molar Extinction Coefficient of Colloidal CdSe Nanoplatelets. *The Journal of Physical Chemistry C* **2015,** *119* (47), 26768-26775.
14. Geiregat, P.; Roda, C.; Tanghe, I.; Singh, S.; Di Giacomo, A.; Lebrun, D.; Grimaldi, G.; Maes, J.; Van Thourhout, D.; Moreels, I.; Houtepen, A. J.; Hens, Z., Localization-limited exciton oscillator strength in colloidal CdSe nanoplatelets revealed by the optically induced stark effect. *Light Sci Appl* **2021,** *10* (1), 112.
15. Di Giacomo, A.; Rodà, C.; Khan, A. H.; Moreels, I., Colloidal Synthesis of Laterally Confined Blue-Emitting 3.5 Monolayer CdSe Nanoplatelets. *Chemistry of Materials* **2020,** *32* (21), 9260-9267.
16. Ouyang, J.; Zaman, M. B.; Yan, F. J.; Johnston, D.; Li, G.; Wu, X.; Leek, D.; Ratcliffe, C. I.; Ripmeester, J. A.; Yu, K., Multiple Families of Magic-Sized CdSe Nanocrystals with Strong Bandgap Photoluminescence via Noninjection One-Pot Syntheses. *The Journal of Physical Chemistry C* **2008,** *112* (36), 13805-13811.
17. Chen, Y.; Chen, D.; Li, Z.; Peng, X., Symmetry-Breaking for Formation of Rectangular CdSe Two-Dimensional Nanocrystals in Zinc-Blende Structure. *Journal of the American Chemical Society* **2017,** *139* (29), 10009-10019.
18. Liu, Y.; Rowell, N.; Willis, M.; Zhang, M.; Wang, S.; Fan, H.; Huang, W.; Chen, X.; Yu, K., Photoluminescent Colloidal Nanohelices Self-Assembled from CdSe Magic-Size Clusters via Nanoplatelets. *The Journal of Physical Chemistry Letters* **2019,** *10* (11), 2794-2801.
19. Liu, Y.; Zhang, B.; Fan, H.; Rowell, N.; Willis, M.; Zheng, X.; Che, R.; Han, S.; Yu, K., Colloidal CdSe 0-Dimension Nanocrystals and Their Self-Assembled 2-Dimension Structures. *Chemistry of Materials* **2018,** *30* (5), 1575-1584.
20. Lyashchova, A.; Dmytruk, A.; Dmitruk, I.; Klimusheva, G.; Mirnaya, T.; Asaula, V., Optical absorption, induced bleaching, and photoluminescence of CdSe nanoplatelets grown in cadmium octanoate matrix. *Nanoscale Research Letters* **2014,** *9* (1), 88.

21. Castro, N.; Bouet, C.; Ithurria, S.; Lequeux, N.; Constantin, D.; Levitz, P.; Pontoni, D.; Abecassis, B., Insights into the Formation Mechanism of CdSe Nanoplatelets Using in Situ X-ray Scattering. *Nano Lett* **2019,** *19* (9), 6466-6474.
22. Wu, L.; Fournier, A. P.; Willis, J. J.; Cargnello, M.; Tassone, C. J., In SituX-ray Scattering Guides the Synthesis of Uniform PtSn Nanocrystals. *Nano Letters* **2018,** *18* (6), 4053-4057.
23. Wu, L.; Willis, J. J.; McKay, I. S.; Diroll, B. T.; Qin, J.; Cargnello, M.; Tassone, C. J., High-temperature crystallization of nanocrystals into three-dimensional superlattices. *Nature* **2017,** *548* (7666), 197-201.
24. Prins, P. T.; Montanarella, F.; Dümbgen, K.; Justo, Y.; Van Der Bok, J. C.; Hinterding, S. O. M.; Geuchies, J. J.; Maes, J.; De Nolf, K.; Deelen, S.; Meijer, H.; Zinn, T.; Petukhov, A. V.; Rabouw, F. T.; De Mello Donega, C.; Vanmaekelbergh, D.; Hens, Z., Extended Nucleation and Superfocusing in Colloidal Semiconductor Nanocrystal Synthesis. *Nano Letters* **2021,** *21* (6), 2487-2496.
25. Maes, J.; Castro, N.; De Nolf, K.; Walravens, W.; Abécassis, B.; Hens, Z., Size and Concentration Determination of Colloidal Nanocrystals by Small-Angle X-ray Scattering. *Chemistry of Materials* **2018,** *30* (12), 3952-3962.
26. Bertrand, G. H. V.; Polovitsyn, A.; Christodoulou, S.; Khan, A. H.; Moreels, I., Shape control of zincblende CdSe nanoplatelets. *Chemical Communications* **2016,** *52* (80), 11975-11978.
27. Achtstein, A. W.; Antanovich, A.; Prudnikau, A.; Scott, R.; Woggon, U.; Artemyev, M., Linear Absorption in CdSe Nanoplates: Thickness and Lateral Size Dependency of the Intrinsic Absorption. *The Journal of Physical Chemistry C* **2015,** *119* (34), 20156-20161.
28. Geiregat, P.; Tomar, R.; Chen, K.; Singh, S.; Hodgkiss, J. M.; Hens, Z., Thermodynamic Equilibrium between Excitons and Excitonic Molecules Dictates Optical Gain in Colloidal CdSe Quantum Wells. *The Journal of Physical Chemistry Letters* **2019,** *10* (13), 3637-3644.
29. Jiang, Y.; Ojo, W.-S.; Mahler, B.; Xu, X.; Abécassis, B.; Dubertret, B., Synthesis of CdSe Nanoplatelets without Short-Chain Ligands: Implication for Their Growth Mechanisms. *ACS Omega* **2018,** *3* (6), 6199-6205.
30. Scott, R.; Prudnikau, A. V.; Antanovich, A.; Christodoulou, S.; Riedl, T.; Bertrand, G. H. V.; Owschimikow, N.; Lindner, J. K. N.; Hens, Z.; Moreels, I.; Artemyev, M.; Woggon, U.; Achtstein, A. W., A comparative study demonstrates strong size tunability of carrier-phonon coupling in CdSe-based 2D and 0D nanocrystals. *Nanoscale* **2019,** *11* (9), 3958-3967.
31. Van Der Bok, J. C.; Dekker, D. M.; Peerlings, M. L. J.; Salzmann, B. B. V.; Meijerink, A., Luminescence Line Broadening of CdSe Nanoplatelets and Quantum Dots for Application in w-LEDs. *The Journal of Physical Chemistry C* **2020,** *124* (22), 12153-12160.
32. Failla, M.; García Flórez, F.; Salzmann, B. B. V.; Vanmaekelbergh, D.; Stoof, H. T. C.; Siebbeles, L. D. A., Observation of the quantized motion of excitons in CdSe nanoplatelets. *Physical Review B* **2020,** *102* (19), 195405-195410.
33. Jana, S.; Phan, T. N. T.; Bouet, C.; Tessier, M. D.; Davidson, P.; Dubertret, B.; Abécassis, B., Stacking and Colloidal Stability of CdSe Nanoplatelets. *Langmuir* **2015,** *31* (38), 10532-10539.
34. She, C.; Fedin, I.; Dolzhnikov, D. S.; Demortière, A.; Schaller, R. D.; Pelton, M.; Talapin, D. V., Low-Threshold Stimulated Emission Using Colloidal Quantum Wells. *Nano Letters* **2014,** *14* (5), 2772-2777.
35. Tanford, C., Micelle shape and size. *The Journal of Physical Chemistry* **1972,** *76* (21), 3020-3024.
36. Małecka, B., Thermal decomposition of Cd(CH3COO)2·2H2O studied by a coupled TG-DTA-MS method. *Journal of Thermal Analysis and Calorimetry* **2004,** *78* (2), 535-544.
37. Martínez-Casado, F. J.; Ramos-Riesco, M.; Rodríguez-Cheda, J. A.; Cucinotta, F.; Matesanz, E.; Miletto, I.; Gianotti, E.; Marchese, L.; Matěj, Z., Unraveling the Decomposition Process of Lead(II) Acetate: Anhydrous Polymorphs, Hydrates, and Byproducts and Room Temperature Phosphorescence. *Inorganic Chemistry* **2016,** *55* (17), 8576-8586.
38. Van Der Stam, W.; Rabouw, F. T.; Geuchies, J. J.; Berends, A. C.; Hinterding, S. O. M.; Geitenbeek, R. G.; Van Der Lit, J.; Prévost, S.; Petukhov, A. V.; De Mello Donega, C., In Situ Probing of Stack-Templated Growth of Ultrathin Cu2–xS Nanosheets. *Chemistry of Materials* **2016,** *28* (17), 6381-6389.
39. Knüsel, P. N.; Riedinger, A.; Rossinelli, A. A.; Ott, F. D.; Mule, A. S.; Norris, D. J., Experimental Evidence for Two-Dimensional Ostwald Ripening in Semiconductor Nanoplatelets. *Chemistry of Materials* **2020,** *32* (7), 3312-3319.
40. Hens, Z.; Moreels, I., Light absorption by colloidal semiconductor quantum dots. *Journal of Materials Chemistry* **2012,** *22* (21), 10406-10415.

41. Huang, D.; Simon, S. L.; McKenna, G. B., Chain length dependence of the thermodynamic properties of linear and cyclic alkanes and polymers. *The Journal of Chemical Physics* **2005,** *122* (8), 084907.
42. Jiang, Y.; Chen, H.; Mu, X.; He, Z., Thermal decomposition of magnesium acetate in nitrogen. *Journal of Physics: Conference Series* **2020,** *1653* (1), 012057.
43. Dreiss, C. A.; Jack, K. S.; Parker, A. P., On the absolute calibration of bench-top small-angle X-ray scattering instruments: a comparison of different standard methods. *Journal of Applied Crystallography* **2006,** *39* (1), 32-38.
44. Platz, G., P. Lindner, Th. Zemb (Eds.): Neutron, X-Ray and Light-Scattering: Introduction to an Investigative Tool for Colloidal and Polymer Systems, North Holland, Amsterdam, 1991, ISBN 0-444-88946-9, 375 Seiten, Preis: Dfl. 175. *Berichte der Bunsengesellschaft für physikalische Chemie* **1992,** *96* (6), 839-839.
45. Renaud, G.; Lazzari, R.; Leroy, F., Probing surface and interface morphology with Grazing Incidence Small Angle X-Ray Scattering. *Surface Science Reports* **2009,** *64* (8), 255-380.

* Authors contributed to this work equally by writing the proposal and conducting synchrotron experiments together. They intensely collaborated in the data analysis of the scattering data in chapter 4 and 5. P. T. Prins had the main responsibility for the analysis of scattering data analysis in this chapter. All authors are gratefully acknowledged for their contribution to the experiments, discussion and manuscript, especially F. T. Rabouw for the simulations. J. D. Meeldijk is acknowledged for the HR-TEM measurements at the Electron Microscopy Centre Utrecht.

Chapter 5

The formation of $NaYF_4:Er^{3+},Yb^{3+}$ nanocrystals studied by *in situ* x-ray scattering: phase transition and size focussing

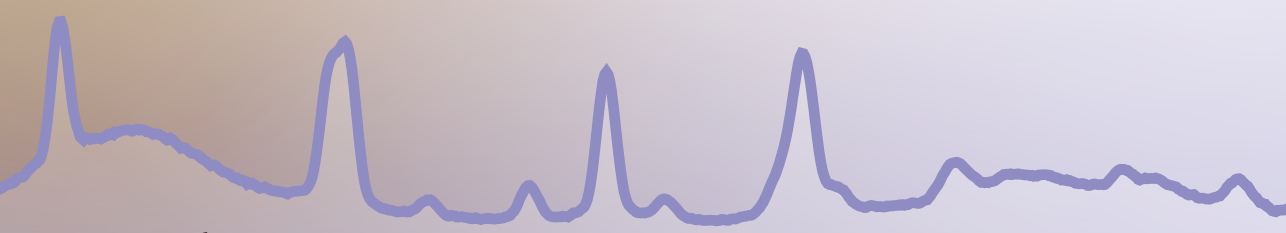

Based on:

P. T. Prins*, J. C. van der Bok*, T. P. van Swieten, S. O. M. Hinterding, A. J. Smith, A. V. Petukhov, A. Meijerink, F. T. Rabouw, *Angew. Chem. Int. Ed.* **2023**, *Accepted*.

Abstract

$NaYF_4$ nanocrystals (NCs) are popular as host material for trivalent lanthanide ions and co-doped with Yb^{3+} and Er^{3+} they are efficient upconversion materials. Both cubic α-phase and hexagonal β-phase $NaYF_4$ NCs can be synthesized, where the β-phase has a higher upconversion efficiency. β-$NaYF_4$ NCs are synthesized using small α-phase $NaYF_4$ NCs as precursor particles. These α-$NaYF_4$ precursor particles can have a large size distribution, yet yielding a monodisperse batch of β-$NaYF_4$ NCs. Multiple studies have investigated this intriguing synthesis. Contradicting models for the formation mechanism have been proposed, which include phase transition in only a small subset of the precursor particles, or nucleation of β-$NaYF_4$ NCs from monomers released by dissolving α-$NaYF_4$ NCs. We show that neither of these models are consistent with the high-time resolution *in situ* x-ray scattering data we obtained using a setup that closely resembled laboratory conditions. Small-angle x-rays scattering reveals that the particle size distribution evolves from initially unimodal ~2 nm, to bimodal midway in the reaction, and finally returns to a unimodal distribution of larger ~6 nm NCs. Surprisingly, wide-angle x-rays scattering shows that the phase transition is not the cause of the bimodal distribution, as it mostly occurs later during the reaction. This is supported by *ex situ* high-resolution TEM-analysis, which unveils that both large α-$NaYF_4$ and β-$NaYF_4$ NCs are present midway through the reaction. Supported by population-balancing simulations, we show that a distribution of surface reaction rates of the α-$NaYF_4$ precursor particles can lead to the observed progression in size distribution. These variations in reactivity are likely related to the Na/RE stoichiometry.

5.1 Introduction

Lanthanide ions are used for their light-emitting properties in a variety of applications. They are attractive because of their many options for color conversion, producing narrow-band emissions with long excited-state lifetimes. In particular, upconversion of light is possible with lanthanide ions, *i.e.*, the conversion of low-energy into high-energy photons. This phenomenon is useful for background-free imaging,[1-3] security inks,[4, 5] solar-energy conversion,[6, 7] and other applications.[8] It often relies on energy-transfer processes between lanthanide dopants in a crystalline host material. The most popular host material for this purpose is β-phase $NaREF_4$, with RE = Y, Gd, or Lu, because it makes high upconversion efficiencies possible and reproducible synthesis procedures for high-quality nano[9, 10] and bulk materials[11] are available. Where bulk materials are usually superior in terms of quantum efficiency,[9, 10, 12] colloidal nanocrystals (NCs) are non-scattering and solvent-dispersible, which makes them preferable for various applications[8] and processing methods.[13, 14]

$NaYF_4$ NCs of the cubic α-phase were first reported in 2004.[15] A synthesis procedure for NCs of the hexagonal β-phase followed in 2006.[16] The latter procedure did not use molecular precursors but small α-$NaYF_4$ precursor particles for the nucleation and growth of β-$NaYF_4$ NCs. This peculiar strategy has since been further developed to produce bright and highly monodisperse batches of β-$NaREF_4$ NCs for a wide variety of compositions.[17, 18] It has also been employed for the synthesis of core–shell or core–multi-shell geometries with improved properties due to a designed dopant distribution.[9, 19-24]

The intriguing formation of large monodisperse β-$NaREF_4$ NCs from smaller α-$NaREF_4$ precursor particles has triggered studies into the growth mechanism. The studies involve, for example, *ex situ* electron microscopy and X-ray scattering/diffraction on aliquots taken during

synthesis.[25-28] Such techniques provide insight into the intermediate stages of the reaction, but they offer limited time resolution and limited possibilities for quantitative analysis. Other studies have used *in situ* photoluminescence to study the growth mechanism from α-$NaREF_4$ to β-$NaREF_4$ NCs,[26, 27] which enhances the time resolution but still only enables qualitative analysis. Besides, the models reported are sometimes directly contradictory. For example, one model proposes that α-$NaREF_4$ precursor particles dissolve, after which β-$NaREF_4$ NCs nucleate and grow,[25] while an alternative model proposes that α-$NaREF_4$ particles grow, after which an α-to-β phase transition occurs at a specific size.[29] One of the most thorough studies, using a combination of *in situ* photoluminescence and multiple *ex situ* techniques, concludes: "It is still not completely clear where the β-phase seeds originate from."[27]

In this work, we follow the formation of β-$NaYF_4$ NCs from α-$NaYF_4$ precursor particles using *in situ* X-ray scattering. A home-built adaptation of a three-neck flask ensures similar reaction conditions—temperature, volume, stirring—to common lab-based syntheses, while allowing X-ray accessibility.[30] Small-angle X-ray scattering (SAXS) reveals the size distribution of NCs, while wide-angle X-ray scattering (WAXS) on crystal planes shows the α-to-β phase transition.[31]

Surprisingly, we observe a small subensemble of rapidly growing α-$NaYF_4$ precursor particles, while the rest remains small and eventually dissolves. This produces a striking bimodal particle size distribution midway during the reaction. The α-to-β phase transition does not occur until the growing particles are >4 nm radius. This disproves earlier models of dissolution of α-$NaYF_4$ particles followed by nucleation of β-$NaYF_4$ NCs, as well as the idea that the phase transformation triggers rapid growth.[25, 29] We hypothesize that variations in surface reaction rate of the α-$NaYF_4$ precursor particles trigger faster growth of a small subensemble, which eventually transforms into β-$NaYF_4$ NCs. This idea is corroborated by population-balancing simulations. We propose that the distribution of surface reaction rates of the α-$NaYF_4$ precursor particles is critical and controllable by tuning the Na/RE stoichiometry which is known to strongly affect the growth kinetics of $NaYF_4$ NCs.[32] These insights could lead to new synthesis strategies for bright NCs or intricate core–shell geometries.

5.2 Results and discussion

We study the state-of-the-art synthesis procedure for upconversion NCs of β-$NaYF_4$ doped with 2% Er^{3+} and 18% Yb^{3+}presented in reference [32], which is schematically visualized in Figure 5.1A For brevity, the specification of dopant content will be omitted in the rest of the text. The used method is hydroxide-free and thereby avoids the incorporation of OH^- at F^- positions in the lattice, significantly improving the upconversion quantum efficiency.[9, 33] The first step of the procedure is the formation of cubic α-$NaYF_4$ particles at 200 °C from a solution of oleate salts and NH_4F in oleic acid and 1-octadecene (see Methods section). Transmission electron microscopy (TEM; Figure 5.1C) shows small particles with ill-defined shapes. The SAXS pattern of our α-$NaYF_4$ particles (Figure 5.1B; left) matches spherical particles with a volume-weighted radius 2.2 ± 0.5 nm (mean ± standard deviation) and the WAXS pattern (Figure 5.1B; right) confirms the cubic crystal phase. In the second step, the purified α-$NaYF_4$ precursor particles are heated with a ramp of 10 °C/min to 300 °C in a mixture of oleic acid and 1-octadecene, transforming into β-$NaYF_4$ NCs over the course of 90 minutes. The SAXS pattern of our final NCs (Figure 5.1D; left) shows that they are 5.7 ± 0.3 nm in volume-weighted radius, while the WAXS pattern (Figure 5.1D; right) matches the hexagonal crystal phase. Indeed, TEM (Figure

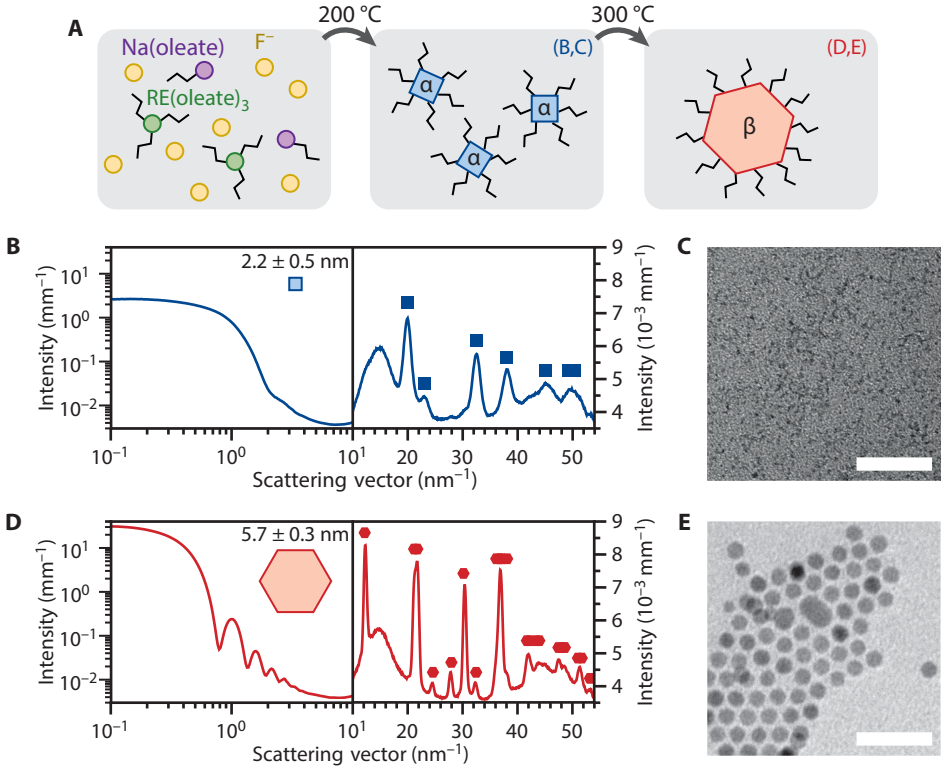

Figure 5.1 Synthesis of β-$NaYF_4$:Er^{3+},Yb^{3+} NCs from α-$NaYF_4$:Er^{3+},Yb^{3+} precursor particles. **(A)** Schematic of the synthesis procedure. Step 1: Na(oleate), F^- and $RE(oleate)_3$ (with RE = Y, Er, Yb) form small α-$NaYF_4$ precursor particles. Step 2: The precursor particles transform into larger β-$NaYF_4$ NCs. **(B)** SAXS and WAXS patterns of the α-$NaYF_4$ particles at 300 °C. Diffraction peaks expected for α-$NaYF_4$ are indicated with blue squares.[34] **(C)** Transmission electron micrograph on the α-$NaYF_4$ particles before heating. **(D)** Same as in panel B but for the β-$NaYF_4$ product NCs measured after 60 min at 300 °C. The reference for β-$NaYF_4$ in WAXS is shown with red hexagons.[35] **(E)** Transmission electron micrograph on the final β-$NaYF_4$ NCs after heating for 90 min. TEM scale bars are 50 nm.

5.1E) shows larger, monodisperse, and well-defined NCs with a number-weighted radius of 5.5 ± 0.4 nm (Figure S5.3A)

We followed the second step of the synthesis *in situ*, *i.e.*, the transformation from α-$NaYF_4$ to β-$NaYF_4$, using SAXS and WAXS at beamline I22 of Diamond Light Source, United Kingdom (see Methods section).[37] The high X-ray photon flux enabled scattering measurements through ~4 mm of reaction mixture in our custom three-neck flask at an integration time as short as 1 second. Scattering patterns were recorded continuously every five seconds while the dispersion of purified α-$NaYF_4$ particles was heated from room temperature to 300 °C. The moment the reaction mixture reached 300 °C is defined as $t = 0$ (Figure 5.2A). We discuss the scattering patterns after $t = 0$. The early patterns at 300 °C are already somewhat different from the pat-

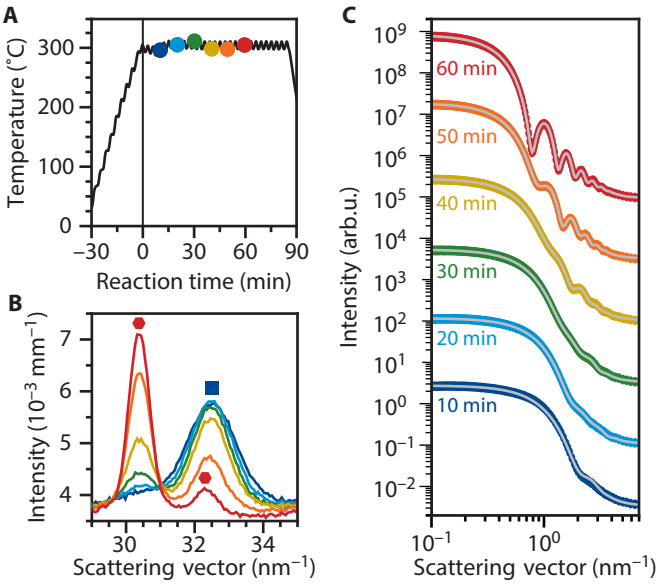

Figure 5.2 *In situ* measurements of phase transformation and growth. **(A)** The temperature recorded by a thermocouple during the synthesis procedure as a function of reaction time. Colored dots highlight moments of the recordings shown in panels B and C. **(B)** Waxs patterns recorded at different times (see panel A), showing the phase transition from α- to β-$NaYF_4$. Diffraction peaks due to the α- and β-phases are indicated with a blue square and red hexagons, respectively: the 220 (32.53 nm^{-1}) reflection of α-$NaYF_4$ and the 201 (30.38 nm^{-1}) and 210 (32.35 nm^{-1}) reflections of β-$NaYF_4$. Nanocrystal growth is evident from the peak narrowing. **(C)** Saxs patterns recorded at the same times as the data in panel B. The NCs are more monodisperse and larger at later times, as evidenced by the sharper dips in the pattern occurring at lower scattering vector. The gray lines are fits to a model of spherical particles with a distribution of radii, optimized using McSAS.[36] See Figure S5.4 for full-range WAXS and unshifted SAXS patterns.

terns at room temperature (Figure S5.5), most likely reflecting a slight increase in crystallinity and/or size of the α-$NaYF_4$ seed particles upon heating.

Figure 5.2B and 5.2C shows the scattering pattern recorded *in situ* at different times during the synthesis. In the WAXS pattern (Figure 5.2B), a narrow peak at 30.38 nm^{-1} due to β-$NaYF_4$ appears, while a broader peak at 32.53 nm^{-1} due to α-$NaYF_4$ goes down. This shows the formation of large β-$NaYF_4$ NCs with narrow diffraction peaks from smaller α-$NaYF_4$ precursor particles with broader diffraction peaks. The SAXS patterns (Figure 5.2C) show a shift of the first dip from 2 nm^{-1} at t = 10 min to 0.7 nm^{-1} at t = 60 min, confirming the growth of particles. Simultaneously, multiple pronounced minima are evident at t > 40 min. This highlights the narrowing of the size distribution of the particles. These results are qualitatively consistent with the *ex situ* TEM data of Figure 5.1.

For a quantitative analysis of the *in situ* scattering, we first focus on the SAXS data. We fit the patterns with t > 5 min to an ensemble of polydisperse spherical particles with a distribution of radii using the open-source program McSAS.[36, 38] This program can retrieve size distributions using a Monte Carlo rejection sampling approach (see S5.1 in SI). The patterns at t < 5 min are

very complex because of particle aggregation (Figure S5.5) and are therefore disregarded in our quantitative analysis. The gray lines in Figure 5.2C show best fits to the SAXS patterns at six different reaction times, as found by McSAS. The fitted size distributions as a function of reaction time are presented in the color map of Figure 5.3A. The initially unimodal size distribution with radii of 2.2 ± 0.5 nm (volume-weighted; mean ± standard deviation) splits into two peaks at t = 17 min. The mean radius in both peaks increases with time and the small-particle peak disappears around t = 57 min. The final distribution is again unimodal, with radii 5.7 ± 0.3 nm (volume-weighted). Our fitting procedure thus shows that the absolute size dispersity decreases during the reaction from 0.5 to 0.3 nm. Such size focusing has been known but a decrease in absolute values for size dispersion is remarkable, especially considering that a crystal phase transition occurs simultaneously.

Figure 5.3B–F are different visualizations of the particle size distributions during the reaction. The size distributions in terms of volume fraction (Figure 5.3B) show that the total volume of $NaYF_4$ material (*i.e.*, the area under the curves) remains approximately constant during the transition from a unimodal to a bimodal distribution and back. The size distributions in terms of number of particles (Figure 5.3C) show that, meanwhile, the particle concentration decreases by a factor 25. This is a necessary consequence of particle growth at a constant amount of material. We distinguish between the kinetics of "small" and "large" particles by integrating the size distributions using a threshold radius of 3.5 nm (Figure 5.3D). Evaluating the particle concentration as a function of time (Figure 5.3F) shows that the number of large particles grows until t = 35 min and then remains constant. Meanwhile, the reaction yield as a function of time (Figure 5.3E) shows that the transfer of material from small to large particles is quantitative and complete at t = 55 min. This is the moment when the small particles have completely disappeared (Figure 5.3F). The gray area in Figure 5.3E are particles smaller than 1 nm and are likely a by-product of the reaction.

It is tempting to interpret the bimodal size distribution from the SAXS analysis (Figure 5.3A–F) as due to small α-$NaYF_4$ precursor particles and large β-$NaYF_4$ NCs. Indeed, we know from *ex situ* analysis (Figure 5.1) that the initial precursor particles are small and α-$NaYF_4$, while the product NCs are larger and β-$NaYF_4$. The SAXS data suggest a mechanism where some precursor particles undergo an α-to-β phase transition that triggers their further growth at the expense of the dissolution of remaining precursor particles. This simple and attractive model, previously suggested in the literature,[29] is however inconsistent with the kinetics in the WAXS data. We see that at moments when the size distribution is already distinctly bimodal (*e.g.*, green line in Figure 5.3B; t = 30 min), the corresponding *in situ* diffraction (green line Figure 5.2B) shows only a minor reflection from β-$NaYF_4$. If the large particles were β-$NaYF_4$ already at t = 20 – 40 min, we should observe strong β-$NaYF_4$ reflections in WAXS, even more so because diffraction intensity scales with the square of a crystallite's volume. Instead, we observe that the amplitude of the β-$NaYF_4$ WAXS peak (Figure 5.3G) grows more slowly than the amount of material in large particles (Figure 5.3F). A significant portion of the large particles must be α-phase particles. We thus have to conclude that splitting of the size distribution is *not* triggered by an α-to-β phase transition in a subset of particles but is instead due to differences in growth rate among the α-phase particles.

To confirm that some of the large particles midway during the reaction are α-phase, we turn to *ex situ* high-resolution TEM. Figure 5.4 shows TEM images of aliquots taken midway during

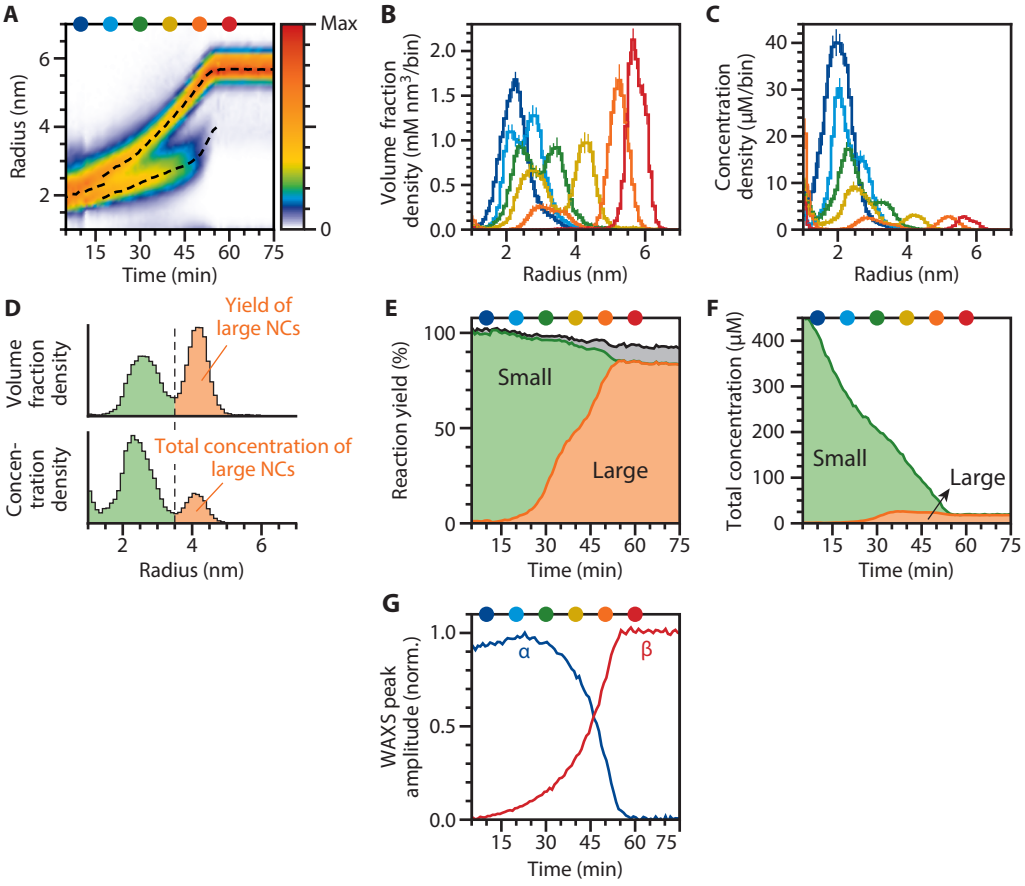

Figure 5.3 Growth dynamics from *in situ* scattering. **(A)** Size distribution as a function of reaction time. The color scale shows the size distribution in terms of volume fraction density per unit of radius. The dashed lines correspond to the modes of the distributions, which are unimodal in the initial ($t < 17$ min) and final ($t > 57$ min) stages of the reaction, and bimodal midway. **(B)** Six size distributions on a one-dimensional scale. The *y*-axis shows volume fraction density, *i.e.*, the particle volume per unit of volume of reaction mixture per unit of radius. Colors correspond to the same times as in Figure 5.2C and those highlighted by colored disks in panel A. The bin width on the *x*-axis is 0.1 nm. **(C)** The same size distributions as in panel B, with the *y*-axis showing concentration density, *i.e.*, number of particles per unit of volume of reaction mixture per unit of radius. **(D)** Schematic of our procedure to obtain total concentrations and yields, using the distributions at $t = 40$ min (yellow in panels B,C) as an example. Integrating volume fraction density (top), we obtain the reaction yield while integrating concentration density (bottom), we obtain the total concentration. Setting the upper (lower) integration bound at a radius of 3.5 nm yields the reaction yield of small (large) NCs or the total concentration of small (large) NCs. **(E)** The cumulative total reaction yield (black line), reaction yield of small NCs (green area), and reaction yield of large NCs (orange area) as a function of time, where we set the threshold between small and large at 3.5 nm (panel D). The gray area is small material with a fitted radius of < 1 nm (Figure S5.6). The yield is defined with respect to the total amount of α-$NaYF_4$ precursor material at $t = 0$. **(F)** Same as in E but in terms of concentration. **(G)** Amplitude of the WAXS peaks at 19.92 nm^{-1} (blue; α-$NaYF_4$, 111 reflection) and 30.38 nm^{-1} (red; β-$NaYF_4$, 201 reflection) as a function of reaction time.

the synthesis of β-$NaLuF_4$ NCs. We were able to obtain high-resolution TEM of $NaLuF_4$ particles but not of $NaYF_4$. The two materials are chemically similar, but $NaLuF_4$ contains the heavy element Lu (atomic number $Z = 71$ vs. $Z = 39$ for Y), which provides the critical advantage of strong interaction with the electron beam. *In situ* SAXS and WAXS (Figure S5.7 – S5.9) and *ex situ* TEM analysis (Figure S5.10C,D) show that the synthesis mechanism of β-$NaLuF_4$ NCs is the same as for β-$NaYF_4$ NCs, except that full conversion takes ~30 minutes longer and the final size is larger (15.7 ± 1.0 nm). Quantitative analysis of the SAXS patterns of $NaLuF_4$ particles is more challenging because of aggregation resulting in additional scattering.

The TEM images (Figure 5.4A) of an aliquot taken midway during the reaction confirm that it contains a mixture of small and large particles. This is explicitly visible in the particle size distribution obtained from the TEM analysis (Figure S5.10A,B). In Figure 5.4B,C we magnify two regions of the TEM image and highlight four larger particles with radii of 4–5 nm. The atomic lattice planes of these particles are visible. Fast Fourier transforming the images (Figure 5.4D,E) helps us determine the lattice spacings of the particles. Based on this, we can identify one large α-phase and one large β-phase particle in each image. More examples of large α-phase and β-phase particle are given in Figure S5.11. The simultaneous presence of large α- and β-phase particles supports our interpretation of the *in situ* SAXS and WAXS data: a subset of the α-phase particles grows *before* they transform into the β-phase. Growth of α-phase particles is also consisted with the narrowing of the diffraction peak of the cubic phase in Figure 5.2B; compare dark blue, cyan and green diffraction patterns.

Now the question arises what causes the differences in reaction rate among initial α-phase precursor particles that triggers the splitting of the size distribution? First, the α-phase precursor particles differ in terms of surface faceting and ligand coverage. This is however not a likely cause for the differences in reaction rate because the surface of NCs is highly dynamic, and fluctuations average out the reaction rates of any particular surface structure. Instead, we propose that differences in stoichiometry determine which α-phase precursor particles grow faster than others. Indeed, the Na/RE ratio has been used as an important parameter to control the reaction kinetics and final size in synthesis procedures.[32] Our results suggest that variations in—rather than the average—Na/RE ratio among particles is a hidden but key aspect enabling this size control. The small materials produced during the synthesis (<1 nm diameter, gray area in Figure 5.3E) might be left-over NaF from the conversion of partially off-stoichiometric α-$NaYF_4$ to stoichiometric β-$NaYF_4$.

On the ensemble scale, the average stoichiometry of α-phase particles can vary continuously between a RE excess (Na/RE = 0.6) and a Na excess (Na/RE = 1.2), which affect the reaction kinetics.[32] Stoichiometries likely vary continuously on the single-particle scale as well. Yet the size distribution midway during the synthesis is distinctly bimodal (Figure 5.3A – C). To reconcile the seeming contradiction between a continuous stoichiometry distribution and bimodal growth, we constructed a simple mathematical model for nanoparticle growth with a continuous distribution of growth rates. This model and its results are presented below. It produces an evolution from a unimodal to a bimodal and back to a unimodal size distribution, in qualitative agreement with the experiment, and helps us explain these unusual size dynamics.

Our model simulates the evolution of the radii of spherical α-$NaYF_4$ particles as they exchange monomers with the surrounding solution. It thus focuses on the surprising evolution of the size distribution of α-$NaYF_4$ particles rather than on the transformation into the β-phase.

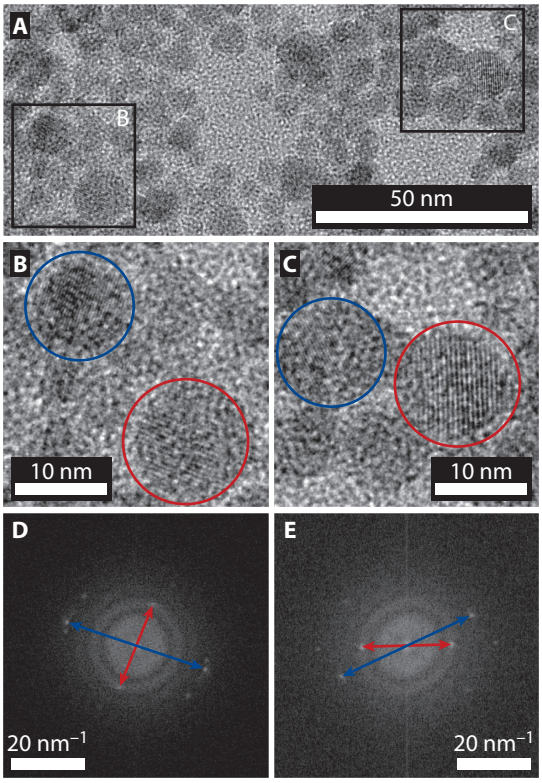

Figure 5.4 *Ex situ* electron microscopy of an aliquot taken midway during the reaction. These experiments were performed on $NaLuF_4$ particles, which are chemically similar to $NaYF_4$. **(A)** TEM of an aliquot taken 30 min after the reaction mixture reached 300 °C. **(B,C)** Zooms of the areas highlighted with black squares in panel A. Blue and red circles highlight α- and β-phase particles, respectively. **(D,E)** Fast Fourier transforms of panels B and C, respectively. The spots highlighted with blue arrows are at a distance of $2\pi/d = 20$ nm^{-1} from the origin, matching the {111} lattice spacing, $d_{111} = 0.32$ nm, of α-$NaLuF_4$.[34] The red arrows highlight spots matching the {100} lattice spacing, $d_{100} = 0.51$ nm, of β-$NaLuF_4$.[35] Comparing the orientation of the lattice planes in panels B,C with the angle of the spots in panels D,E, we identify the particles circled in blue as α-phase and those circled in red as β-phase. The additional peaks in the patterns, not indicated by arrows, are likely due to some small particles in the same region shown in panels B,C.

Release of monomers results in particle shrinking, while uptake results in growth. The growth rate of a particle of radius r is

$$\frac{dr}{dt} = f(r)\left(S - e^{\frac{2\gamma}{k_B T \rho r}}\right) \tag{5.1}$$

The factor between brackets describes how the growth rate depends on monomer concentration. It contains the surface energy γ and number density ρ of the particles, the thermal energy $k_B T$, and the supersaturation S, defined as the monomer concentration normalized to the concentration of a solution in equilibrium with bulk α-$NaYF_4$. The prefactor $f(r)$ describes the

radius dependence of the reaction rate. We take $f(r) = A/r^2$, which reflects a size-dependent rate constant for monomer uptake/release[39] and allows for straightforward tuning of a particle's reaction rate through the value of A. Slightly different expressions for $f(r)$ have been used for the cases of diffusion- or reaction-limited growth with size-independent rate constants.

We model the simultaneous growth of particles with uniformly distributed rate constants A. This tests whether α-$NaYF_4$ particles with a continuous distribution of reaction rates can evolve from a unimodal to a bimodal and back to a unimodal size distribution (Figure 5.5A). We approximate the continuous distribution with 80 different types of particles, having values of A of $\{A_{max}/80, 2A_{max}/80, 3A_{max}/80, \ldots, A_{max}\}$. At the start of the simulation, each type of particle is equally abundant (Figure 5.5B; top) and has a Gaussian radius distribution with mean 2 nm and standard deviation 0.25 nm (Figure 5.5C; top). We discretize the radius distributions and make the radii evolve according to equation 5.1. The time dependence of S is tracked simultaneously, as it changes because of monomer uptake and release by the particles. The value of S is initiated such that at $t = 0$ the monomers are in equilibrium with particles of the mean radius (2 nm). This means that particles smaller than the mean tend to dissolve, while larger particles grow. The SI provides more details on the algorithm of this simplified reaction model, while the text below presents the results and interpretation.

Figure 5.5B – E show the simulation results. Midway during the reaction, half of the particles with a fast reaction rate have dissolved (Figure 5.5B; mid, purple) while the other half have significantly grown (Figure 5.5C; mid, purple). Meanwhile, particles with an intermediate reaction rate dissolved more (Figure 5.5B; mid, blue) and grew less (Figure 5.5C; mid, blue) than the fast-reacting particles. Slowly reacting particles hardly dissolved (Figure 5.5B; mid, green) nor changed size (Figure 5.5C; mid, green). At late stages of the reaction, particles of intermediate and slow reaction rates have dissolved nearly completely, while the fast-reacting particles survive (Figures 5.5B,C; bottom). This evolution of number of particles is summarized in **Figure 5.5D**. It produces an overall particle size distribution that is unimodal initially, is bimodal midway during the reaction, and then returns to unimodal (Figure 5.5E). Hence, a continuous distribution of reaction rates (through parameter A) can naturally produce a bimodal size distribution of particles coupled through monomer exchange.

The simulation results of Figure 5.5B – E help us explain the evolution of the particle size distribution intuitively. The size distribution is bimodal midway during the reaction because: (1) particles with fast reaction rates grow rapidly, (2) particles with slow reaction rates have not had sufficient time to change size, (3) particles with intermediate reaction rates are too slow to keep up with the growth of the fastest particles, but sufficiently fast to dissolve as the few growing particles reduce the monomer concentration. The distinct minimum in the growth rate distribution (Figure 5.5B; mid) results in the bimodal size distribution in the simulation (Figure 5.5E), which we also observe experimentally (Figure 5.3B).

5.3 Conclusion

Our combined *in situ* scattering experiments, *ex situ* electron microscopy, and kinetic modeling provide a new mechanistic picture of the synthesis of β-$NaYF_4$ NCs. As the reaction temperature is reached, a subensemble of the α-$NaYF_4$ precursor particles with higher reactivity starts growing. Whether or not an α-$NaYF_4$ precursor particle grows may be determined by its stoichiometry. While stoichiometry likely varies continuously across the ensemble of particles, this

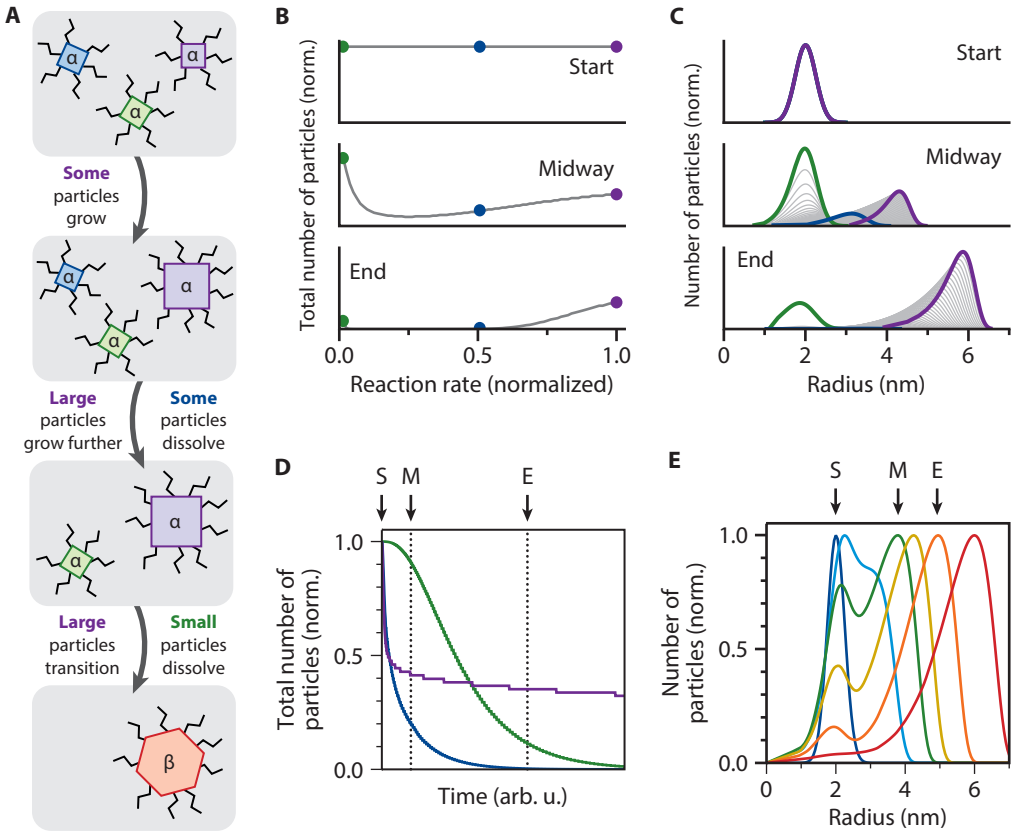

Figure 5.5 Simulation of the splitting size distribution of α-phase particles. **(A)** Schematic of the proposed synthesis mechanism, based on *in situ* SAXS and WAXS. Some of the initial α-phase precursor particles grow, while the others remain small, producing a bimodal size distribution midway during the reaction. The large particles transform into β-phase while the small particles dissolve eventually. **(B)** Our rate equation model couples particles of different reaction rates through uptake and release of monomers in the solution. From top to bottom: the number of particles at different reaction rates at different stages of the reaction. In our model, particles can grow or dissolve, while the reaction rate constant *A* (see main text) is fixed. **(C)** From top to bottom: size distributions of particles of 80 different reaction rates (gray lines) at different stages of the reaction. Highlighted are the size distributions of the particles reacting most slowly (in green), at the mean rate (in blue), and fastest (in purple). **(D)** Time evolution of the number of particles reacting most slowly (green), at the mean rate (blue), and fastest (purple). The times denoted "Start" (S), "Midway" (M), and "End" (E) in panels B,C are indicated. **(E)** Total simulated size distribution at increasing reaction time, going from blue to red.

can nevertheless, as verified with the simulation, produce the bimodal size distribution that we observe midway during the reaction. The subensemble of α-$NaYF_4$ particles largest in size then transforms into β-$NaYF_4$, likely because of a size-dependent balance between surface and bulk free energies of the two phases.[40] Meanwhile, the smaller α-$NaYF_4$ particles dissolve as larger particles (α- or β-phase) consume monomers from solution. The consumption of smaller

α-$NaYF_4$ particles might accelerate as the larger particles transition into the thermodynamically more stable β-phase. Our experiments show that, if this happened, it would be *after* the bimodal size distribution appears (Figure 5.2).[41] The simulation does not include this phase transformation and its potential effect on growth rates explicitly, because it aims to test the origin of the bimodal size distribution conceptually.

The sequence of events we uncovered here is markedly different from commonly considered reaction mechanisms for NC synthesis. In particular, a mechanism of dissolution of α-phase and simultaneous nucleation of β-phase particles is excluded by the observation of growing α-$NaYF_4$ particles (Figure 5.3E,G). The proposed role of stoichiometry variations offers a new handle to optimize synthesis outcomes. Indeed, existing synthesis procedures have used of the overall stoichiometry in a reaction mixture to, for example, tune particle size[32] or prevent secondary nucleation.[17] Clever strategies with intentional stoichiometry variations among precursor particles might enable the one-pot synthesis of core–shell or gradient-composition NCs. In addition, stoichiometry-dependent reaction rates could be key in the synthesis mechanisms of various material classes with loose stoichiometries, including $NaREF_4$, hybrid organic/inorganic perovskites, Cu- and Ag-containing semiconductors, or metal alloys.

5.4 Methods

Synthesis of α-$NaYF_4$:Yb^{3+},Er^{3+} and α-$NaLuF_4$:Yb^{3+},Er^{3+} nanocrystals

α-$NaYF_4$:Yb^{3+},Er^{3+}nanocrystals were synthesized using the protocol by Haase *et al*., eventually leading to β-$NaYF_4$:Yb^{3+},Er^{3+} nanocrystals with an average diameter of 11 nm.[9] For the first step, the synthesis of the α-$NaYF_4$:Yb^{3+},Er^{3+} nanocrystals, 4.06 g (12 mmol) yttrium acetate tetrahydrate, 1.14 g (2.7 mmol) ytterbium acetate tetrahydrate, and 0.126 g (0.3 mmol) erbium acetate tetrahydrate were combined with 150 mL oleic acid and 150 mL 1-octadecene in a 1L flask. The mixture was kept under vacuum for 1 h at RT followed by 2 h at 100 °C to degas and remove the acetic acid. Next, 13.7 g (45 mmol) sodium oleate was added under a nitrogen flow, and the vacuum was reapplied while the sodium oleate dissolved. Afterward, 3.33 g (90 mmol) ammonium fluoride was added under nitrogen flow, and subsequently, the reaction vessel was flushed three times to eliminate oxygen by alternating a short vacuum and refilling with nitrogen. The mixture was heated to 200 °C under a nitrogen atmosphere and kept at this temperature for 1h. After letting the reaction mixture cool down to room temperature, the nanoparticles were extracted from the reaction mixture by a few purification steps. First, ethanol was added with a ratio 1:2 reaction mixture:ethanol, and the mixture was centrifuged at 2750 rpm (840 RCF) for 5 min. The precipitate was redispersed in 100 mL hexane and centrifuged at 1000 rpm for 10 min. The sediment, the byproduct NaF, was discarded. The nanocrystal dispersion was washed once more with a 1:2 reaction mixture: ethanol ratio and centrifuged at 3000 rpm. The precipitate was redispersed in 10 g hexane. Thermal gravimetric analysis (TGA) measurements showed a weight loss of 40% due to the ligands, giving a dispersion of 17.4 wt% α-$NaYF_4$:Yb^{3+},Er^{3+} nanoparticles in hexane.

$NaLuF_4$:Yb^{3+},Er^{3+} nanocrystals were synthesized using the method described above with 3.66 g (8.64 mmol) lutetium acetate tetrahydrate, 0.820 g (1.94 mmol) ytterbium acetate tetrahydrate, 0.090 mg (0.22 mmol) erbium acetate tetrahydrate, 108 mL oleic acid and 108 mL 1-octadecene. The mixture was degassed overnight at 120 °C. In the subsequent steps, 9.84 g (32.4 mmol) sodium oleate and 2.40 g (64.8 mmol) ammonium fluoride were added. Weight

loss due to ligand loss in the TGA measurements was 22.6%, and a final dispersion of 14.1 wt% α-$NaLuF_4$:Yb^{3+},Er^{3+} nanoparticles in hexane was obtained.

Formation of β-$NaYF_4$:Yb^{3+},Er^{3+} and β-$NaLuF_4$:Yb^{3+},Er^{3+} nanocrystals

The β-$NaYF_4$:Yb^{3+},Er^{3+} nanocrystals were synthesized *in situ* at the beamline in a custom designed flask[30, 39] with a reduced volume compared to the protocol by Haase *et al.*[9] Therefore, the synthesis was down-scaled to three-tenth of the standard reaction volume. 1.78 g (1.5 mmol) of the α-$NaYF_4$:Yb^{3+},Er^{3+} nanoparticles dispersed in hexane, 3 mL OA, and 3 mL 1-octadecene were combined in this flask and put under vacuum for 30 min at RT and at least 1 h at 50 °C to degas the mixture and remove the hexane. The mixture was then put under a nitrogen atmosphere and heated to 300 °C with a ramp rate of 10 °C/min. After 90 min, the mixture was cooled down to RT. The reaction mixture was purified twice with EtOH (1:4, reaction mixture: EtOH, 3000 rpm) and redispersed in 6 g hexane.

For the β-$NaLuF_4$:Yb^{3+},Er^{3+} synthesis at the beamline, 2.42 g (1.25 mmol) of the α-$NaLuF_4$:Yb^{3+},Er^{3+} nanoparticles dispersed in hexane was combined with 2.5 mL oleic acid and 2.5 mL 1-octadecene. The same procedure was used as for the synthesis of β-$NaYF_4$:Yb^{3+},Er^{3+} nanoparticles. Reaction time at 300 °C was 180 min.

2.92 g (1.5 mmol) of the α-$NaLuF_4$:Yb^{3+},Er^{3+} nanoparticles dispersed in hexane was combined with 3 mL oleic acid and 3 mL 1-octadecene for the β-$NaLuF_4$:Yb^{3+},Er^{3+} with aliquots synthesis. The reaction time for this synthesis was 120 min at 300 °C. The aliquot discussed in the text was taken at 60 min at 300 °C.

Small- and wide-angle X-ray scattering

The SAXS and WAXS experiments were performed at I22 of synchrotron Diamond at an energy of 20 keV± 2.3 eV using a Pilatus P3-2M SAXS detector and a P3-2M-DLS L-shaped WAXS detector. The sample-to-detector distance to the SAXS and WAXS detectors was 21.6 cm and 977.6 cm, respectively. This enabled us to probe a q-range of 0.023 nm^{-1} – 3.1 nm^{-1} for SAXS and a range of 2.4 nm^{-1} – 61 nm^{-1} for WAXS. The scattering patterns were collected with an exposure time of 1 s followed by a waiting time of 4 s. The beamline setup and data acquisition of I22 are discussed in ref. [37].

The SAXS and WAXS experiments were conducted under nitrogen flow in a custom-made three-neck flask and setup discussed in detail in refs. [30, 39]. In these experiments, a Vigreux was added on top of the flask instead of an injector.

TEM measurements

TEM samples were prepared by drop-casting a diluted (100–1000 times) dispersion of NCs onto a copper TEM grid. The TEM-grids of the $NaLuF_4$:Yb^{3+},Er^{3+} aliquots, which were not purified, were treated with a mixture of EtOH and activated carbon as described in ref. [42] to reduce contamination by hydrocarbons during imaging. The measurements on $NaLuF_4$:Yb^{3+},Er^{3+} were performed on a Fei Talos F200X operating at 200 keV, and other TEM measurements were performed on a Fei T20 operating at 200 keV.

S5 Supporting Information – Chapter 5

S5.1 Data analysis

S5.1.1 Data preparation for fitting

The SAXS and WAXS patterns contain the scattering of the NCs but also from additional components. This background scattering needs to be removed before the data can be analyzed. Background scattering originates from the setup, flask, and the mixture of oleic acid and 1-octadecene (OA/ODE). The isolated scattering of these components is respectively obtained by measuring an empty beam path, an empty flask, and a flask with OA/ODE inside. The SAXS/WAXS patterns of the empty beam and empty flask are shown in **Figure S5.1**. The scattering of OA/ODE is temperature dependent and was for that reason measured as function of temperature. The temperature-dependent patterns are shown in **Figure S5.2**.

When measuring the temperature dependent SAXS and WAXS of the reaction mixture without any nanoparticles, *i.e.*, 3 mL OA and 3 mL ODE, we observed that part of the SAXS did not depend on temperature alone but also on time. Additional scattering, noticeable from $q = 0.03\ \text{nm}^{-1} - 0.5\ \text{nm}^{-1}$, appears after ~260 °C, increases with time, and remains when cooling down to room temperature. We could isolate the additional scattering by comparing the scattering before and after heating and subtracting the temperature-dependent contribution. The time-dependent scattering pattern, shown in **Figure S5.2C**, has a slope of q^{-2} in the Guinier regime and q^{-4} in the Porod regime. This indicates Gaussian polymer chains or randomly oriented two-dimensional structures (lamellae or platelets). When performing a least square fitting with the shape specific model from ref. [43], we obtain a radius of gyration of 4.5 nm. We hypothesize that the scattering originates from polymerized 1-octadecene, as discussed in ref. [44].

At small q, the *in situ* scattering should be independent of q since we are measuring a non-clustered dispersion of spherical particles. Therefore, the contribution over time of scattering due to polymer formation could be determined by fitting the additional scattering at low q as a function of time. The data was then corrected using this contribution factor and the scattering of the polymer as a function of q.

To summarize, in total we consider five contributions to the *in situ* SAXS/WAXS patterns, the nanocrystals, the setup, the flask, the OA/ODE, and the polymer:

$$I(q,t,T) = I_{\text{NC}}(q,t,T) + I_{\text{setup}}(q) + a_1 I_{\text{flask}}(q) + a_2 I_{\text{OA+ODE}}(q,T) + a_3(t) I_{\text{polymer}}(q). \qquad \text{(S5.1)}$$

Values of 0.9 and 0.65 were obtained for the prefactors a_1 and a_2, respectively. These values are independent of time and temperature. The prefactor a_3 is determined by a least square fitting method for every scattering pattern. To be specific, we determined the scattering that should be subtracted from our data to obtain q-independent scattering at low q as discussed above. Since we now know all factors involved, we can obtain $I_{\text{NC}}(q, t, T)$.

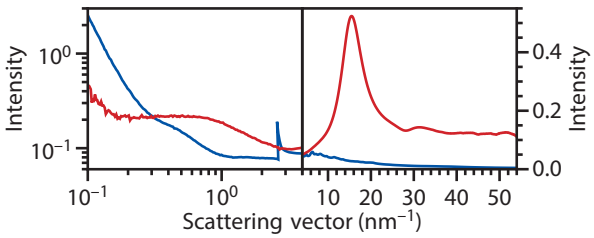

Figure S5.1 SAXS and WAXS from the empty beam (blue) and an empty reaction flask (red).

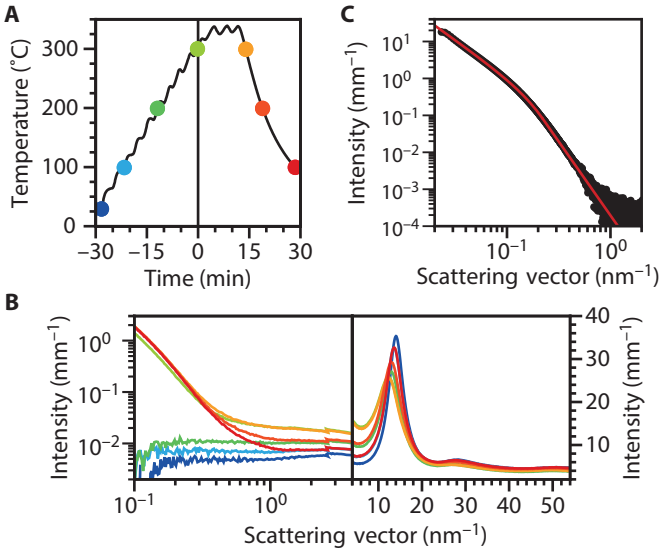

Figure S5.2 Temperature dependence of the SAXS and WAXS from a mixture of 3 mL oleic acid and 3 mL octadecene. **(A)** Temperature recorded with a thermocouple during the heating of the reaction mixture with particles as function of reaction time. Colored dots highlight moments of the recordings shown in panel B. **(B)** SAXS and WAXS patterns recorded at times defined in panel A. The scattering intensity at $q < 1$ nm^{-1} is not reversible when cooling down. **(C)** Time-dependent SAXS pattern extracted from the patterns shown in panel B. The red line is a fit with a general model for the Guinier and Porod regime. The best fit is obtained with radius of gyration of 4.5 nm. The WAXS was fully reversible and only dependents on temperature.

To minimize the amount of data points, thereby speeding up the fitting process in the next step, we rebinned the data to 162 data points ranging from $q = 0.1$ nm^{-1} – 7 nm^{-1}.

Lastly, we have to correct the intensity for the path length of the flask to obtain the intensity in the unit of mm^{-1}. The pathlength of the flasks was acquired by measuring the transmission through the flask with and without chloroform. Using the attenuation length of chloroform at 20 keV, 1.01 mm, we obtained a pathlength of 4.5 mm and 4.1 mm for the $NaYF_4$:Yb^{3+},Er^{3+} and $NaLuF_4$:Yb^{3+},Er^{3+} synthesis, respectively.

The curve of $I_{NC}(q, t, T)$ corrected for pathlength was provided to the McSAS program for further analysis of particle size distributions.

S5.1.2 Thermal expansion

The amount of starting material in the synthesis is 1.5 mmol of α-$NaYF_4$:Yb^{3+},Er^{3+} as discussed above. At room temperature the volume is 3 mL OA and 3 mL ODE. However, at 300 °C this volume will expand due to thermal expansion of OA and ODE, following:

$$V_2 = V_1 \exp\left[\int_{T_1}^{T_2} \alpha_V(T)\mathrm{d}T\right], \tag{S5.2}$$

With V_1 and V_2 the volume at 20 °C (T_1) and 300 °C (T_2), respectively. $\alpha_V(T)$ is the temperature-dependent volume-expansion coefficient obtained from Yaws.[45] The obtained volumes are 3.9 mL OA and 4.1 mL ODE at 300 °C. With a total volume of 8 mL, we obtain a concentration of α-$NaYF_4$:Yb^{3+},Er^{3+} units at $t = 0$ of $c_{NaYF_4} = 0.19$ mol L^{-1}.

The thermal expansion of α-$NaYF_4$:Yb^{3+},Er^{3+} is less compared to the reaction mixture but was still taken into account. The unit cell volume increases from 0.551 nm^3 at 20 °C to 0.555 nm^3 at 300 °C using a volume thermal expansion coefficient of 81.68×10^{-6} K^{-1}.[46]

In relation to the volume changes calculated above, the densities of OA, ODE, and α-$NaYF_4$:Yb^{3+},Er^{3+} decrease due to thermal expansion from 0.888, 0.785 and 4.062 g/cm^3 at 20 °C to 0.570, 0.690 and 3.970 g/cm^3 at 300 °C respectively. These values were used to calculate the theoretical scattering length density (SLD).

S5.1.3 Data fitting with McSAS

The particles investigated here are quasi-spherical, and for that reason, we used a model for spheres with a distribution of radii. The scattering intensity for spheres with a discrete distribution of radii is:

$$I(q) = \Delta\rho^2 \sum_{k=R_{\min}}^{R_{\max}} \frac{\phi_k}{V_k}\left[\frac{3V_k(\sin(qR_k) - qR_k\cos(qR_k))}{(qR_k)^3}\right]^2 + B, \tag{S5.3}$$

Where $\Delta\rho$ is the SLD difference between the spheres and the medium, R_{min} and R_{max} are the radius of the smallest (0.05 nm) and largest (7.95 nm) bin respectively, φ_k is the volume fraction of nanocrystals in bin k, V_k is the volume of particles in bin k, and B is a constant background contribution. When optimizing the model, the McSAS code, discussed in Ref [36], adjusts φ_k and B to obtain a good fit. We used the following settings: 50,000 as maximum number of iterations, 2000 as number of contributions, 2/3 as compensation component, 20 as number of reps, and a convergence criterion of 3.5. This convergence criterion was too low for the early scattering patterns; a successful fit was not obtained within the maximum number of iterations. Thus, the convergence criterion was slightly increased to still obtain fitting results for the first few patterns.

S5.1.4 Scattering length densities

When taking the limit $q \to 0$ of the equation above we obtain

$$\lim_{q\to0} I(q) = \Delta\rho^2 \sum_{k=R_{\min}}^{R_{\max}} \phi_k V_k + B. \tag{S5.4}$$

Given that at $t = 0$, the amount of α-$NaYF_4$:Yb^{3+},Er^{3+} is expected to be equal to the amount added, we get

$$\sum_{k=R_{\min}}^{R_{\max}} \phi_k = \frac{c_{NaYF_4} N_A V_{\text{unit cell}}}{z_{\text{unit cell}}}. \tag{S5.5}$$

By inserting the number of units in a unit cell $z_{\text{unit cell}} = 2$, c_{NaYF_4}, and $V_{\text{unit cell}}$ as discussed in thermal expansion section, we obtain $\Delta\rho = 22.8$ $Å^{-2}$. To obtain this value we used the first 15 scattering patterns after $t = 0$, a time period in which the yield does not change. This calculated value for $\Delta\rho$ corresponds well to the theoretical $\Delta\rho = 24.5$ $Å^{-2}$, calculated on the NIST website (https://www.ncnr.nist.gov/resources/activation/) using the densities of OA, ODE and α-$NaYF_4$ at 300 °C specified earlier. For the reaction mixture, we used the volume weighted SLD using 6.58 $Å^{-2}$ for OA and 5.55 $Å^{-2}$ for ODE resulting in 6.05 $Å^{-2}$. The calculated SLD for α-$NaYF_4$ is 30.58 $Å^{-2}$.

We used $\Delta\rho = 22.8$ $Å^{-2}$ as an input parameter in the McSAS fitting procedure. Thereby, the fitting resulted in absolute volume fractions and NC concentrations. These results are shown and discussed in the main text.

S5.2 Supporting Figures

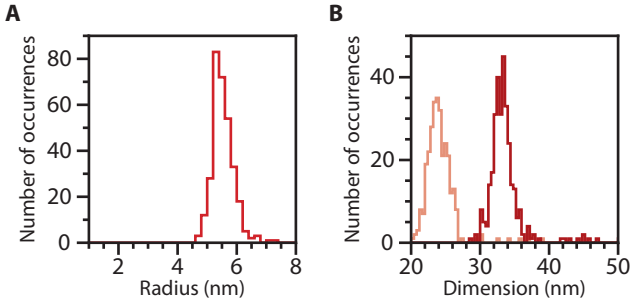

Figure S5.3 (A) TEM analysis on the final β-$NaYF_4$:Er^{3+},Yb^{3+} NCs synthesized while collecting the SAXS and WAXS discussed in the main text. Representative TEM image is shown in Figure 5.1E in the main text. The number-weighted mean radius is 5.5 ± 0.4 nm. **(B)** TEM analysis on the aliquot taken while measuring *in situ* SAXS and WAXS during the formation of β-$NaLuF_4$:Er^{3+},Yb^{3+} NCs. Representative TEM image is shown in Figure S5.7E. The number-weighted mean dimensions are 24.2 ± 2.2 nm and 33.5 ± 2.5 nm. *In situ* SAXS and WAXS results are shown in the Figures S5.8 and S5.9.

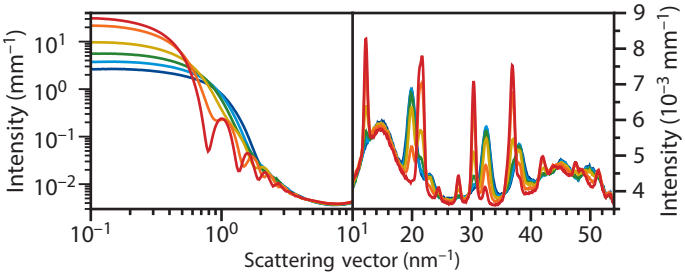

Figure S5.4 Unshifted SAXS patterns and full-range WAXS patterns on the formation of β-$NaYF_4$:Er^{3+},Yb^{3+} NCs at the same times as the data in the main text in Figure 5.2 in panels B and C. See main text for the discussion of the data.

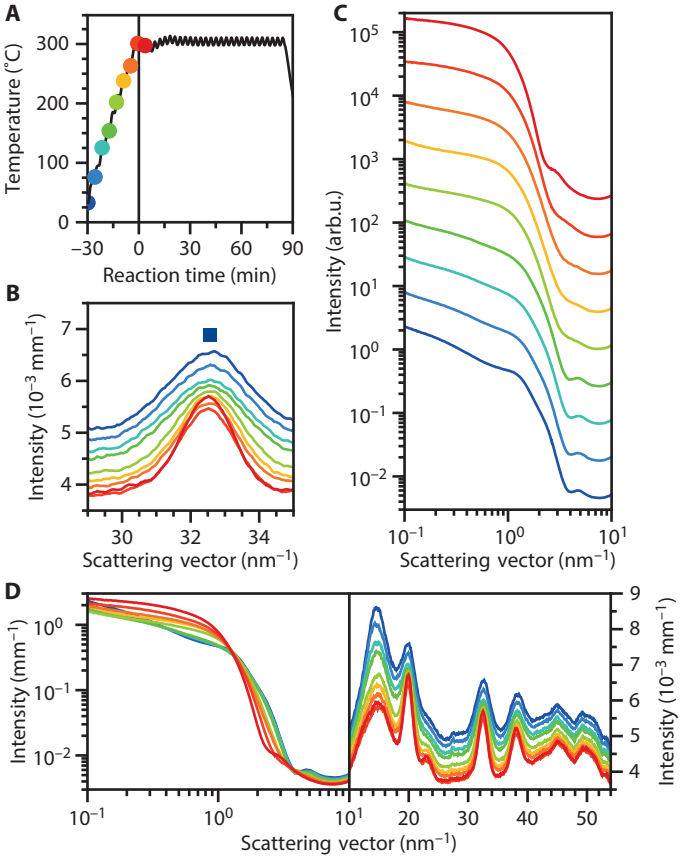

Figure S5.5 *In situ* measurements on the formation of β-$NaYF_4$:Er^{3+},Yb^{3+} NCs during heat-up to 300 °C until t = 5 min. **(A)** The temperature recorded by a thermocouple during the synthesis procedure as a function of reaction time. Colored dots highlight moments of the recordings shown in panels B, C, and D. **(B)** WAXS patterns recorded at times defined in panel a. The diffraction peak due to the α-phase is indicated with a blue square.[34] Although less evident due to changing background scattering, the peak narrows indicating some particle growth and/or increase in crystallinity during heat-up. **(C)** SAXS patterns recorded at the same times as the data in panel B. **(D)** Unshifted SAXS patterns and full-range WAXS patterns same times as the data in panels B and C. Initially, the SAXS patterns do not match the form factor scattering as expected for isolated spherical particles; the particles are clustered, resulting in structure factor scattering. The presence of structure factor scattering is especially clear at low scattering vectors where the scattering pattern is not flat and at q = 1 nm^{-1} where there is a structure factor peak. After reaching 300 °C around t = 5 min, the scattering patterns become flat at low scattering vectors, and it is possible to fit the patterns with a model of spherical particles with a distribution of radii, as discussed in the main text.

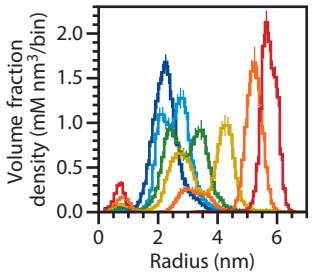

Figure S5.6 Six size distributions on a one-dimensional scale. The *y*-axis shows volume fraction density, *i.e.,* the particle volume per unit of reaction mixture volume per unit of radius. Colors correspond to the same times as in Figure 5.2C in the main text and those highlighted by colored disks in panel Figure 5.2A and Figure 5.3. The bin width on the *x*-axis is 0.1 nm. This plot includes the material < 1 nm, the gray area in Figure 5.3E.

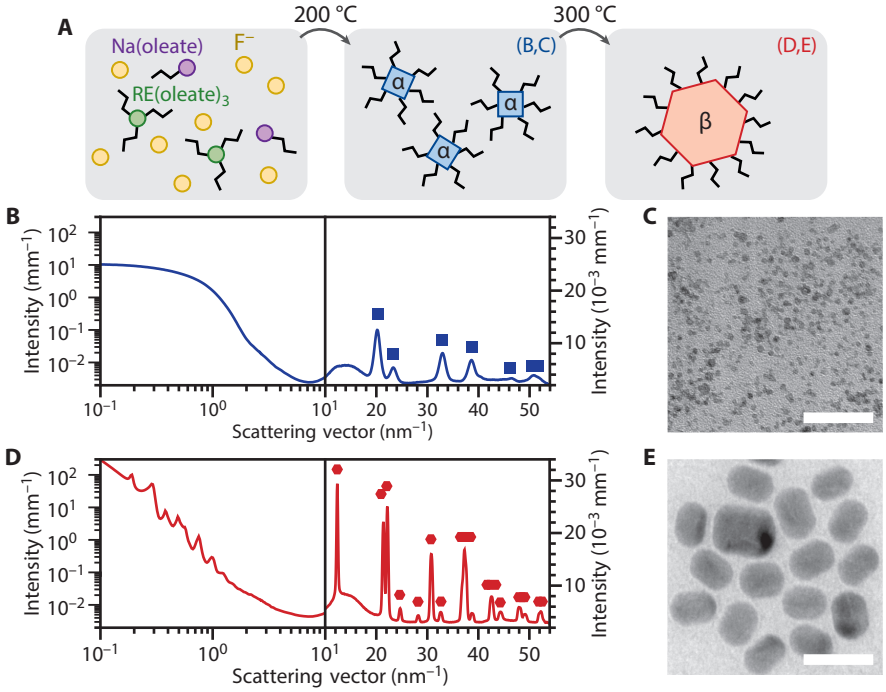

Figure S5.7 Synthesis of β-$NaLuF_4$:Er^{3+},Yb^{3+} NCs from β-$NaLuF_4$:Er^{3+},Yb^{3+} precursor particles. **(A)** Schematic of the synthesis procedure. Step 1: Na(oleate), F^- and $RE(oleate)_3$ (with RE = Lu, Er, Yb) form small α-$NaLuF_4$:Er^{3+},Yb^{3+} precursor particles. Step 2: The precursor particles transform into larger β-$NaLuF_4$:Er^{3+},Yb^{3+} NCs. **(B)** SAXS and WAXS patterns of the α-$NaLuF_4$:Er^{3+},Yb^{3+} particles at 300 °C. Diffraction peaks expected for α-$NaLuF_4$ are indicated with blue squares.[34] A fit of the SAXS pattern with the McSAS method described earlier, gives a radius of 2.5 ± 0.9 nm. **(C)** Transmission electron micrograph on the α-$NaYF_4$:Er^{3+},Yb^{3+} particles before heating to 300 °C. **(D)** Same as in panel B but for the β-$NaLuF_4$:Er^{3+},Yb^{3+} product NCs measured after 131 min at 300 °C. The reference for β-$NaLuF_4$ in WAXS is shown with red hexagons.[35] (E) Transmission electron micrograph on an aliquot taken at 150 min. The β-$NaLuF_4$:Er^{3+},Yb^{3+} NCs are anisotropic with dimensions 24.2 ± 2.2 nm and 33.5 ± 2.5 nm (Figure S5.3B). TEM scale bars are 50 nm.

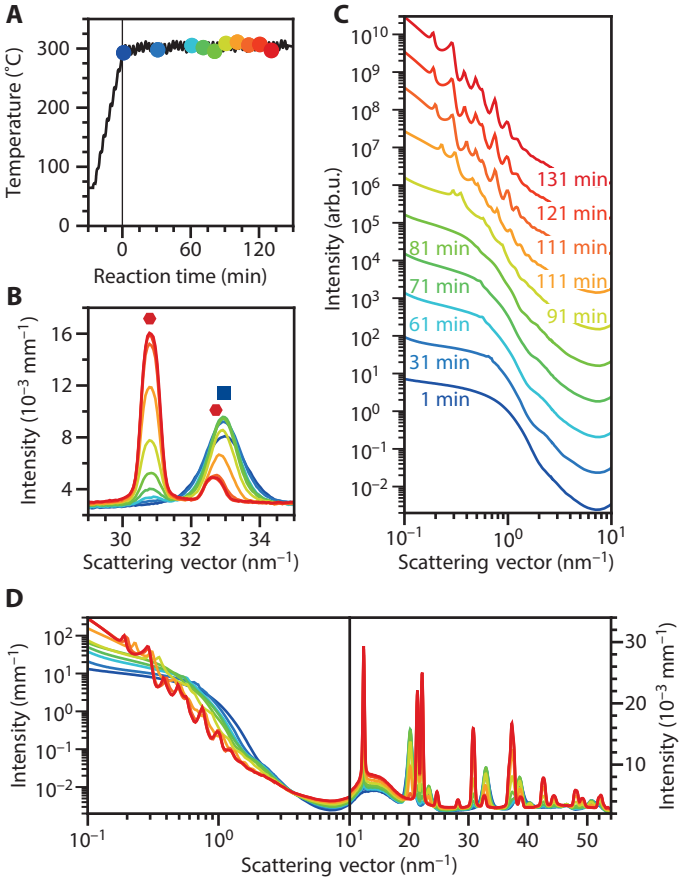

Figure S5.8 *In situ* measurements of phase transformation and growth during the formation of β-$NaLuF_4$:Er^{3+},Yb^{3+} NCs. **(A)** The temperature recorded by a thermocouple during the synthesis procedure as a function of reaction time. Colored dots highlight moments of the recordings shown in panels B, C, and D. **(B)** WAXS patterns recorded at different times (see panel A), showing the phase transition from α- to β-$NaLuF_4$:Er^{3+},Yb^{3+}. Diffraction peaks due to the α- and β-phases are indicated with a blue square and red hexagons, respectively: the 220 (32.96 nm^{-1}) reflection of α-$NaLuF_4$ and the 201 (30.81 nm^{-1}) and 210 (32.66 nm^{-1}) reflections of β-$NaLuF_4$. Nanocrystal growth is evident from the peak narrowing. **(C)** SAXS patterns recorded at the same times as the data in panel B. **(D)** Unshifted SAXS patterns and full-range WAXS patterns at the same times as the data in panels B and C. Early in the synthesis, sharp features arise in the SAXS patterns around 0.6 nm^{-1}, indicative of structure factor scattering due to clustering of the NCs. The slope at lower scattering vectors also indicates the presence of clusters; the clusters have sizes larger than the NCs resulting in scattering at lower scattering vectors. At the end of the synthesis, the features shift and become more apparent, most likely due to both NC growth and cluster size growth. The peak positions indicate hexagonally packed columns of stacked NCs with a stacking distance of 33 nm and an intercolumn separation of 22 nm. These dimensions correspond well to the sizes obtained from the TEM analysis in Figure 5.3B, 33.5 ± 2.5 nm and 24.2 ± 2.2 nm, respectively.

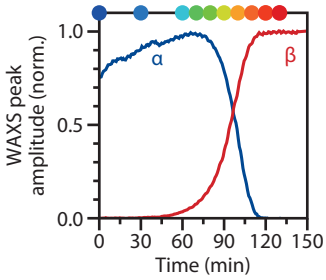

Figure S5.9 Amplitude of the WAXS peaks at 20.19 nm^{-1} (blue; α-$NaLuF_4$,111 reflection) and 30.81 nm^{-1} (red; β-$NaLuF_4$,201 reflection) as a function of reaction time. Colors correspond to the same times as in Figure S5.8. The conversion takes longer for $NaLuF_4$ than for $NaYF_4$, as discussed in the main text.

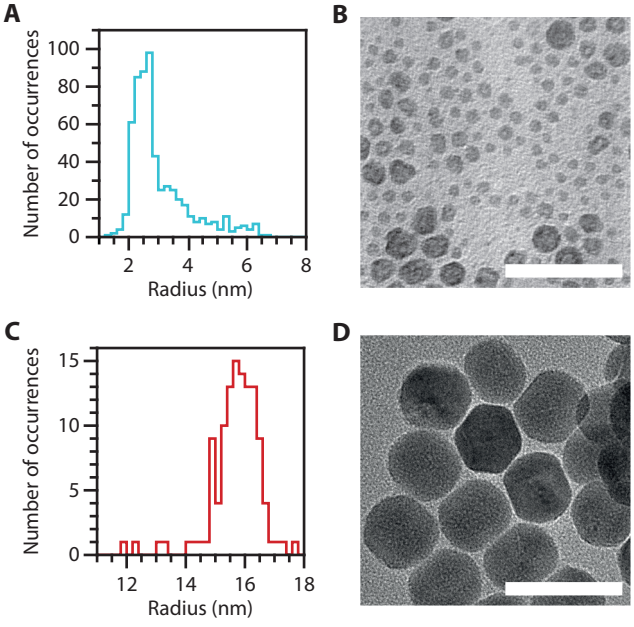

Figure S5.10 TEM analysis on the β-$NaLuF_4$:Er^{3+},Yb^{3+} NCs synthesis with aliquots. **(A,B)** Histogram and TEM image of aliquot taken after 60 min at 300 °C. The sample is highly polydisperse with a number-weighted mean radius of 3.0 ± 1.0 nm. **(C,D)** Histogram and TEM of product obtained after heating for 2h at 300 °C. The number-weighted mean radius is 15.7 ± 1.0 nm. TEM Scale bars corresponds to 50 nm.

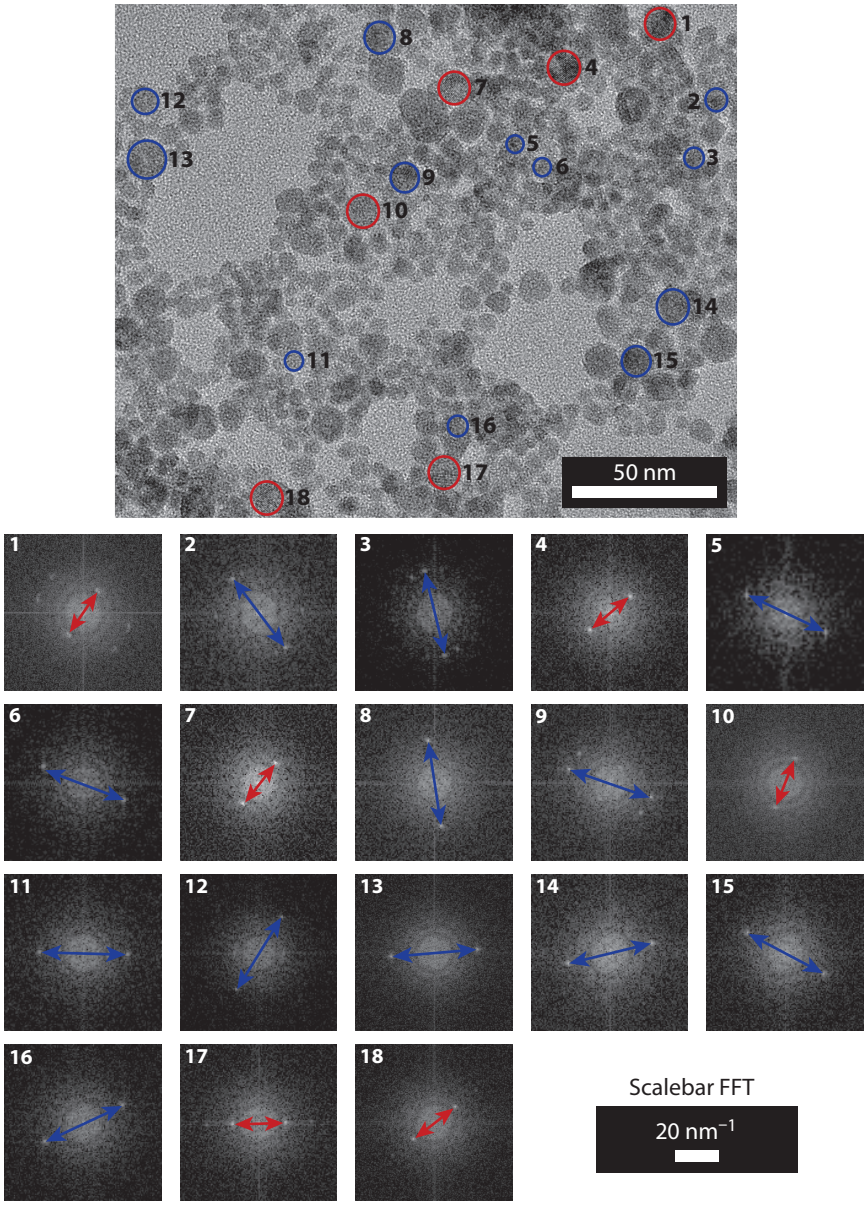

Figure S5.11 *Ex situ* electron microscopy of an aliquot taken midway during the reaction during the formation of β-$NaLuF_4$:Er^{3+},Yb^{3+} NCs. Panels display an extended analysis of sample discussed in the main text (Figure 5.4). Below Fast Fourier transforms of the circled and numbered areas in the TEM image are given. The particles highlighted in blue are identified as α-phase particles and in red as β-phase. As in the main text, the spots highlighted with blue arrows are at a distance of $2\pi/d = 20$ nm^{-1} from the origin, matching the {111} lattice spacing, $d_{111} = 0.31$ nm, of α-$NaLuF_4$. The red arrows highlight spots matching the {100} lattice spacing, $d_{100} = 0.51$ nm, of β-$NaLuF_4$.

S5.3 Simulation of particle growth

We simulate particles that change their radius r in time t according to

$$\frac{\mathrm{d}r}{\mathrm{d}t} = f(r)\left(S - \mathrm{e}^{2\gamma/k_\mathrm{B}T\rho r}\right), \tag{S5.6}$$

where γ and ρ are the surface energy and density of the particles, and $k_\mathrm{B}T$ is the thermal energy. The supersaturation S is the monomer concentration in solution normalized to the monomer concentration of a solution in equilibrium with a macroscopic crystal. We choose

$$f(r) = \frac{A}{r^2}. \tag{S5.7}$$

This describes growth with a stronger size dependence than expected for diffusion- or reaction-limited growth with a size-independent rate constant. Such stronger size dependence is necessary to produce absolute size focusing in a synthesis where particles nucleate over a prolonged period.[39] The continuous distribution of reaction rate constants in our model makes size-dependent rate constants necessary to keep a narrow size distribution.

We initiate the model with a flat distribution of reaction rate constants A uncorrelated with a Gaussian distribution of particle radii. To solve the evolution of sizes from equation S5.6, we discretize the distribution of rate constants, the distribution of radii, and time. More precisely, we consider M types of particles with reaction rate constants

$$A_j = \frac{j+1}{M}A_\mathrm{max}, \tag{S5.8}$$

where $j \in \{0, 1, 2, \ldots M-1\}$. For each type j of particle, we initiate the number of particles $n_{i,j}$ of radius $r_{i,j,0}$ (where 0 denotes start of the simulation; time $t = 0$) according to a Gaussian size distribution:

$$n_{i,j} = \frac{8n_\mathrm{tot}}{\sqrt{2\pi}MN}\exp\left[-\frac{1}{2}\left(\frac{i-N/2}{N/8}\right)^2\right], \tag{S5.9}$$

where N is the number of discrete radii considered and n_0 is the total number of particles in the system:

$$n_\mathrm{tot} = \sum_{j=0}^{M-1}\sum_{i=0}^{N-1} n_{i,j}. \tag{S5.10}$$

The initial radii are uniformly distributed between r_min and r_max:

$$r_{i,j,0} = r_\mathrm{min} + \frac{i}{N-1}(r_\mathrm{max} - r_\mathrm{min}) \tag{S5.11}$$

with $i \in \{0, 1, 2, \ldots, N-1\}$. We see that the initial radii are independent of particle type j. We initiate the supersaturation at a value of

$$S_0 = \exp\left(\frac{2\gamma}{k_\mathrm{B}T\rho r_{N/2,M/2,0}}\right), \tag{S5.12}$$

where again the subscript 0 denotes the start of the simulation ($t = 0$). The value of S_0 is such that particles at the peak of the size distribution, *i.e.*, those with radius $r_{N/2,j,0}$ (for any j), are stable at $t = 0$. Indeed, equation S5.6 shows that $\mathrm{d}r/\mathrm{d}t = 0$ for these particles at $t = 0$.

Next, we let the particle radii evolve in discrete time steps:

$$r_{i,j,t+1} = r_{i,j,t} + \frac{A}{r_{i,j,t}^2}\left(S_t - e^{2\gamma/k_B T \rho r_{i,j,t}}\right) \tag{S5.13}$$

for all i and all j. We update the supersaturation using

$$S_{t+1} = S_t + \frac{4\pi}{3}\rho \sum_{j=0}^{M-1}\sum_{i=0}^{N-1} n_{i,j}\left(r_{i,j,t}^3 - r_{i,j,t+1}^3\right). \tag{S5.14}$$

If any of the radii $r_{i,j,t}$ ever drops below a threshold value r_{th} we immediately dissolve these particles ($n_{i,j} \to 0$) and no longer track this subset (i, j). This step minimizes numerical errors as the radii of shrinking particles could otherwise go below zero.

From the simulation output we calculate particle size distributions as a function of time. The number $n_{i,j}$ of particles of type j at time t is converted into a `density' $x_{i,j,t}$ of particles of type j per unit of radius:

$$x_{i,j,t} = \frac{n_{i,j}}{r_{i+1,j,t} - r_{i-1,j,t}}. \tag{S5.15}$$

This conversion is necessary because the radii become nonuniformly distributed as time progresses. We assign the value of density $x_{i,j,t}$ to a radius value of $r_{i,j,t}$. The particle size distributions presented in the main text (Figure 5.5C and 5.5E) show these densities of particles per unit of radius.

For the simulation results in Figure 5.5 of the main text, we used the following input values: $M = 80$, $N = 200$, $A_{max} = 8 \times 10^{-5}$, $n_{tot} = 0.31$, $r_{min} = 1$, $r_{max} = 3$, $r_{th} = 0.1$, $\gamma/k_B T = 10$, and $\rho = 10$.

References

1. Vetrone, F.; Naccache, R.; Juarranz de la Fuente, A.; Sanz-Rodríguez, F.; Blazquez-Castro, A.; Rodriguez, E. M.; Jaque, D.; Solé, J. G.; Capobianco, J. A., Intracellular imaging of HeLa cells by non-functionalized NaYF4:Er3+, Yb3+ upconverting nanoparticles. *Nanoscale* **2010,** *2* (4), 495-498.
2. Gargas, D. J.; Chan, E. M.; Ostrowski, A. D.; Aloni, S.; Altoe, M. V. P.; Barnard, E. S.; Sanii, B.; Urban, J. J.; Milliron, D. J.; Cohen, B. E.; Schuck, P. J., Engineering bright sub-10-nm upconverting nanocrystals for single-molecule imaging. *Nature Nanotechnology* **2014,** *9* (4), 300-305.
3. Yang, Y.; Sun, Y.; Cao, T.; Peng, J.; Liu, Y.; Wu, Y.; Feng, W.; Zhang, Y.; Li, F., Hydrothermal synthesis of NaLuF4:153Sm,Yb,Tm nanoparticles and their application in dual-modality upconversion luminescence and SPECT bioimaging. *Biomaterials* **2013,** *34* (3), 774-783.
4. Kim, W. J.; Nyk, M.; Prasad, P. N., Color-coded multilayer photopatterned microstructures using lanthanide (III) ion co-doped NaYF4 nanoparticles with upconversion luminescence for possible applications in security. *Nanotechnology* **2009,** *20* (18), 185301.
5. Lu, Y.; Zhao, J.; Zhang, R.; Liu, Y.; Liu, D.; Goldys, E. M.; Yang, X.; Xi, P.; Sunna, A.; Lu, J.; Shi, Y.; Leif, R. C.; Huo, Y.; Shen, J.; Piper, J. A.; Robinson, J. P.; Jin, D., Tunable lifetime multiplexing using luminescent nanocrystals. *Nature Photonics* **2014,** *8* (1), 32-36.
6. Zou, W.; Visser, C.; Maduro, J. A.; Pshenichnikov, M. S.; Hummelen, J. C., Broadband dye-sensitized upconversion of near-infrared light. *Nature Photonics* **2012,** *6* (8), 560-564.
7. Wang, J.; Ming, T.; Jin, Z.; Wang, J.; Sun, L.-D.; Yan, C.-H., Photon energy upconversion through thermal radiation with the power efficiency reaching 16%. *Nature Communications* **2014,** *5* (1), 5669.
8. Zhou, B.; Shi, B.; Jin, D.; Liu, X., Controlling upconversion nanocrystals for emerging applications. *Nature Nanotechnology* **2015,** *10* (11), 924-936.

9. Homann, C.; Krukewitt, L.; Frenzel, F.; Grauel, B.; Würth, C.; Resch-Genger, U.; Haase, M., NaYF 4 :Yb,Er/NaYF 4 Core/Shell Nanocrystals with High Upconversion Luminescence Quantum Yield. *Angewandte Chemie International Edition* **2018,** *57* (28), 8765-8769.
10. Würth, C.; Fischer, S.; Grauel, B.; Alivisatos, A. P.; Resch-Genger, U., Quantum Yields, Surface Quenching, and Passivation Efficiency for Ultrasmall Core/Shell Upconverting Nanoparticles. *Journal of the American Chemical Society* **2018,** *140* (14), 4922-4928.
11. Krämer, K. W.; Biner, D.; Frei, G.; Güdel, H. U.; Hehlen, M. P.; Lüthi, S. R., Hexagonal Sodium Yttrium Fluoride Based Green and Blue Emitting Upconversion Phosphors. *Chemistry of Materials* **2004,** *16* (7), 1244-1251.
12. Boyer, J.-C.; van Veggel, F. C. J. M., Absolute quantum yield measurements of colloidal NaYF4: Er3+, Yb3+ upconverting nanoparticles. *Nanoscale* **2010,** *2* (8), 1417-1419.
13. Brechbühler, R.; Rabouw, F. T.; Rohner, P.; le Feber, B.; Poulikakos, D.; Norris, D. J., Two-Dimensional Drexhage Experiment for Electric- and Magnetic-Dipole Sources on Plasmonic Interfaces. *Physical Review Letters* **2018,** *121* (11), 113601.
14. Zhang, Z.; Chen, Y.; Zhang, Y., Self-Assembly of Upconversion Nanoparticles Based Materials and Their Emerging Applications. *Small* **2022,** *18* (9), 2103241.
15. Heer, S.; Kömpe, K.; Güdel, H.-U.; Haase, M., Highly Efficient Multicolour Upconversion Emission in Transparent Colloids of Lanthanide-Doped NaYF4 Nanocrystals. *Advanced Materials* **2004,** *16* (23-24), 2102-2105.
16. Mai, H. X.; Zhang, Y. W.; Si, R.; Yan, Z. G.; Sun, L. D.; You, L. P.; Yan, C. H., High-quality sodium rare-earth fluoride nanocrystals: controlled synthesis and optical properties. *J Am Chem Soc* **2006**, *128* (19), 6426-36.
17. Rinkel, T.; Raj, A. N.; Duhnen, S.; Haase, M., Synthesis of 10 nm beta-NaYF4:Yb,Er/NaYF4 Core/Shell Upconversion Nanocrystals with 5 nm Particle Cores. *Angew Chem Int Ed Engl* **2016,** *55* (3), 1164-1167.
18. Voß, B.; Nordmann, J.; Uhl, A.; Komban, R.; Haase, M., Effect of the crystal structure of small precursor particles on the growth of β-NaREF4 (RE = Sm, Eu, Gd, Tb) nanocrystals. *Nanoscale* **2013,** *5* (2), 806-812.
19. Deng, R.; Qin, F.; Chen, R.; Huang, W.; Hong, M.; Liu, X., Temporal full-colour tuning through non-steady-state upconversion. *Nature Nanotechnology* **2015,** *10* (3), 237-242.
20. Wang, F.; Liu, X., Upconversion Multicolor Fine-Tuning: Visible to Near-Infrared Emission from Lanthanide-Doped NaYF4 Nanoparticles. *Journal of the American Chemical Society* **2008,** *130* (17), 5642-5643.
21. Johnson, N. J.; Korinek, A.; Dong, C.; van Veggel, F. C., Self-focusing by Ostwald ripening: a strategy for layer-by-layer epitaxial growth on upconverting nanocrystals. *J Am Chem Soc* **2012,** *134* (27), 11068-11071.
22. Fischer, S.; Bronstein, N. D.; Swabeck, J. K.; Chan, E. M.; Alivisatos, A. P., Precise Tuning of Surface Quenching for Luminescence Enhancement in Core–Shell Lanthanide-Doped Nanocrystals. *Nano Letters* **2016,** *16* (11), 7241-7247.
23. Bastian, P. U.; Nacak, S.; Roddatis, V.; Kumke, M. U., Tracking the Motion of Lanthanide Ions within Core–Shell–Shell NaYF4 Nanocrystals via Resonance Energy Transfer. *The Journal of Physical Chemistry C* **2020,** *124* (20), 11229-11238.
24. Liu, L.; Li, X.; Fan, Y.; Wang, C.; El-Toni, A. M.; Alhoshan, M. S.; Zhao, D.; Zhang, F., Elemental Migration in Core/Shell Structured Lanthanide Doped Nanoparticles. *Chemistry of Materials* **2019,** *31* (15), 5608-5615.
25. Voss, B.; Haase, M., Intrinsic Focusing of the Particle Size Distribution in Colloids Containing Nanocrystals of Two Different Crystal Phases. *ACS Nano* **2013,** *7* (12), 11242-11254.
26. Suter, J. D.; Pekas, N. J.; Berry, M. T.; May, P. S., Real-Time-Monitoring of the Synthesis of β-NaYF4:17% Yb,3% Er Nanocrystals Using NIR-to-Visible Upconversion Luminescence. *The Journal of Physical Chemistry C* **2014,** *118* (24), 13238-13247.
27. Radunz, S.; Schavkan, A.; Wahl, S.; Würth, C.; Tschiche, H. R.; Krumrey, M.; Resch-Genger, U., Evolution of Size and Optical Properties of Upconverting Nanoparticles during High-Temperature Synthesis. *The Journal of Physical Chemistry C* **2018,** *122* (50), 28958-28967.
28. Zhao, M. L.; Hao, L. N.; Zhang, J.; Zhang, C. Y.; Lu, Y.; Qian, H. S., Sequential Growth of High Quality Sub-10 nm Core-Shell Nanocrystals: Understanding the Nucleation and Growth Process Using Dynamic Light Scattering. *Langmuir* **2019,** *35* (2), 489-494.
29. May, P. B.; Suter, J. D.; May, P. S.; Berry, M. T., The Dynamics of Nanoparticle Growth and Phase Change During Synthesis of β-NaYF4. *The Journal of Physical Chemistry C* **2016,** *120* (17), 9482-9489.
30. van der Bok, J. C.; Prins, P. T.; Montanarella, F.; Maaskant, D. N.; Brzesowsky, F. A.; van der Sluijs, M. M.; Salzmann, B. B. V.; Rabouw, F. T.; Petukhov, A. V.; De Mello Donega, C.; Vanmaekelbergh, D.; Meijerink, A., In Situ Optical and X-ray Spectroscopy Reveals Evolution toward Mature CdSe Nanoplatelets by Synergetic Action of Myristate and Acetate Ligands. *Journal of the American Chemical Society* **2022,** *144* (18), 8096-8105.

31. Homann, C.; Bolze, J.; Haase, M., Colloidal Crystals of NaYF4 Upconversion Nanocrystals Studied by Small-Angle X-Ray Scattering (SAXS). *Particle & Particle Systems Characterization* **2019,** *36* (2), 1800391.
32. Rinkel, T.; Nordmann, J.; Raj, A. N.; Haase, M., Ostwald-ripening and particle size focussing of sub-10 nm NaYF(4) upconversion nanocrystals. *Nanoscale* **2014,** *6* (23), 14523-14530.
33. Rabouw, F. T.; Prins, P. T.; Villanueva-Delgado, P.; Castelijns, M.; Geitenbeek, R. G.; Meijerink, A., Quenching Pathways in NaYF4:Er3+,Yb3+ Upconversion Nanocrystals. *ACS Nano* **2018,** *12* (5), 4812-4823.
34. Roy, D. M.; Roy, R., Controlled massively defective crystalline solutions with the fluorite structure. *Journal of The Electrochemical Society* **1964,** *111* (4), 421.
35. Perera, S. S.; Amarasinghe, D. K.; Dissanayake, K. T.; Rabuffetti, F. A., Average and Local Crystal Structure of β-Er:Yb:NaYF4 Upconverting Nanocrystals Probed by X-ray Total Scattering. *Chemistry of Materials* **2017,** *29* (15), 6289-6297.
36. Bressler, I.; Pauw, B. R.; Thunemann, A. F., McSAS: software for the retrieval of model parameter distributions from scattering patterns. *Journal of Applied Crystallography* **2015,** *48* (3), 962-969.
37. Smith, A. J.; Alcock, S. G.; Davidson, L. S.; Emmins, J. H.; Hiller Bardsley, J. C.; Holloway, P.; Malfois, M.; Marshall, A. R.; Pizzey, C. L.; Rogers, S. E.; Shebanova, O.; Snow, T.; Sutter, J. P.; Williams, E. P.; Terrill, N. J., I22: SAXS/WAXS beamline at Diamond Light Source - an overview of 10 years operation. *Journal of Synchrotron Radiation* **2021,** *28* (3), 939-947.
38. Bressler, I.; Pauw, B. R. McSAS. https://github.com/bamresearch/mcsas.
39. Prins, P. T.; Montanarella, F.; Dümbgen, K.; Justo, Y.; Van Der Bok, J. C.; Hinterding, S. O. M.; Geuchies, J. J.; Maes, J.; De Nolf, K.; Deelen, S.; Meijer, H.; Zinn, T.; Petukhov, A. V.; Rabouw, F. T.; De Mello Donega, C.; Vanmaekelbergh, D.; Hens, Z., Extended Nucleation and Superfocusing in Colloidal Semiconductor Nanocrystal Synthesis. *Nano Letters* **2021,** *21* (6), 2487-2496.
40. Garvie, R. C., Stabilization of the tetragonal structure in zirconia microcrystals. *The Journal of Physical Chemistry* **1978,** *82* (2), 218-224.
41. Thoma, R. E.; Insley, H.; Hebert, G. M., The Sodium Fluoride-Lanthanide Trifluoride Systems. *Inorganic Chemistry* **1966,** *5* (7), 1222-1229.
42. Li, C.; Tardajos, A. P.; Wang, D.; Choukroun, D.; Van Daele, K.; Breugelmans, T.; Bals, S., A simple method to clean ligand contamination on TEM grids. *Ultramicroscopy* **2021,** *221*, 113195.
43. Hammouda, B., A new Guinier–Porod model. *Journal of Applied Crystallography* **2010,** *43* (4), 716-719.
44. Dhaene, E.; Billet, J.; Bennett, E.; Van Driessche, I.; De Roo, J., The Trouble with ODE: Polymerization during Nanocrystal Synthesis. *Nano Letters* **2019,** *19* (10), 7411-7417.
45. Yaws, C. L., *Yaws' Handbook of Thermodynamic and Physical Properties of Chemical Compounds*. Knovel: 2003.
46. Mathews, M. D.; Ambekar, B. R.; Tyagi, A. K.; Köhler, J., High temperature X-ray diffraction studies on sodium yttrium fluoride. *Journal of Alloys and Compounds* **2004,** *377* (1), 162-166.

Chapter 6

Conclusion and outlook

6.1 Introduction

Nanomaterials have become an increasingly important class of materials in the past decades due to their size-tunable optical, electronic, and magnetic properties. Nanomaterials are not only of great scientific interest, but their versatility has also resulted in a wide range of applications. This thesis focuses on two types of luminescent (light-emitting) nanomaterials, cadmium chalcogenide nanocrystals (NCs) and $NaYF_4$ NCs doped with rare earth ions (lanthanides, *e.g.*, erbium and ytterbium). Both the optical properties and nanocrystal growth mechanisms are investigated.

Semiconductor NCs, especially CdSe nanoplatelets (NPLs), exhibit narrow emission bands in the visible part of the spectrum, a property needed for more efficient white light LEDs (w-LEDs) and vibrant displays. In these applications, the luminescent materials operate at elevated temperatures, which affects the emission linewidth. Insight into this thermal broadening is important for application in w-LEDs but has so far not been investigated over a temperature range that is relevant for this application. In this thesis, I report on the temperature-dependent spectral linewidth of cadmium chalcogenide NPLs and quantum dots (QDs).

$NaYF_4$ NCs doped with lanthanide ions are efficient upconversion materials that can convert two low-energy infrared photons to one high-energy visible photon. These materials can be used in deep-tissue imaging and to enhance the efficiency of solar cells. The formation mechanism of both $NaYF_4$ NCs and CdSe NPLs is still debated. Control over the NC growth is essential to adjust the NC properties. In this thesis, I report on the mechanisms of their nucleation and growth, monitored using *in situ* absorption and small- and wide-angle x-ray scattering techniques (SAXS and WAXS). Below, a summary of the results and outlook on these three topics is given.

6.2.1 Luminescence line broadening in cadmium chalcogenide QDs and NPLs

Chapter 3 focuses on the spectral width of emission from CdSe NPLs and QDs. First, the origin of the narrow emission linewidth of core NPLs compared to core-shell NPLs is discussed. Core-only NPLs exhibit exceptionally narrow emission spectra, but this feature is lost upon passivating the NPL surface with a CdS shell to enhance the quantum yield. In the literature, this is attributed to either an increase in inhomogeneous broadening or stronger homogenous broadening.[1, 2] The first can be caused by a thickness variation in the shell or inhomogeneities at the core-shell interface. The latter is induced by faster coherence loss due to stronger coupling with phonons, which is strongly temperature dependent. To investigate the origin of the broadening, temperature-dependent emission spectra of core and core-shell CdSe NPLs and QDs were recorded and compared. A wide temperature range, 4–423 K, was chosen to gain insight into contributions from homogeneous and inhomogeneous broadening and also to extend measurements into a temperature regime that is relevant for operating conditions in w-LEDs ($T \approx 423$ K).

Measurements at cryogenic temperatures, when the phonons are frozen out and homogeneous broadening is negligible, show that exciton emission of NPLs is characterized by a very narrow inhomogeneous line width (18 meV vs. ~60–80 meV for QDs and core–shell NPLs). The temperature-induced homogeneous broadening does not strongly vary between the various CdSe nanostructures ($\Delta E_{hom} \approx$ 60–80 meV at 423 K), indicating that electron–phonon coupling strengths are similar. Stronger coupling is only observed for the smallest QDs. The similar ho-

mogeneous broadening in NPLs and core-shell NPLs implies that the broader emission spectra of core-shell NPLs can be attributed to inhomogeneous broadening and not a difference in homogeneous broadening. The inhomogeneous broadening extracted at 4 K is indeed much larger for core-shell NPLs compared to core NPLs.

6.2.2 Comparison to conventional materials and outlook

Not only is the emission linewidth important for using NCs in w-LEDs and displays, but other properties should also be considered. A comparison with traditional microcrystalline w-LED phosphors was made to outline the advantages (tunability, narrow bandwidth, high efficiency) and disadvantages (temperature-induced color shift, toxicity, and stability issues) of NPLs for application in w-LEDs.

First, the spectral width of core-NPLs at room temperature and 423 K outperforms that of QDs and conventional phosphors. However, the temperature-induced shift of the exciton peak maximum is larger in NCs compared to phosphors and even stronger in core-NPLs compared to QDs, likely due to the stronger confinement in the thickness dimension of the NPLs. The spectral shift gives rise to a lower color temperature stability with variations in the external temperature, and it is a drawback when using NPLs in w-LEDs and displays.

Secondly, irreversible thermal quenching of the core-shell NPLs luminescence occurred at high temperatures. In general, the thermal stability of QDs and other NCs is one of the concerns for implementation in w-LEDs. Recent advances in coating strategies for the on-chip application of QDs show improved stability at high temperatures. Additionally, a new synthesis method for core-shell NPLs at high temperatures also results in narrower spectral width at room temperature; this is explained by a more uniform shell and, thus, less inhomogeneous broadening.[3] It would be interesting to investigate the photoluminescence stability at high temperatures for these improved core-shell NPLs.

Temperature-induced color shift and NC stability must be considered when implementing NPLs in w-LEDs. Still, the spectral tunability, high quantum yields, strong absorption, and narrow bandwidth are considerable advantages of semiconductor NPLs over conventional luminescent materials. After enhancing the CdS shell uniformity, both narrow-band green and red emitters can be realized with core and core-shell NPLs, making them exciting candidates for lighting devices and displays.

It should be remarked here that the use of Cd in consumer products is restricted, especially in the EU. New legislation may completely prevent the use of Cd-containing materials. However, the findings presented in this thesis can inspire the research and development of Cd-free nanocrystalline materials, such as InP and Cu_2InS quantum dots and platelets.

6.3.1 *In situ* studies on CdSe NPL growth mechanism

The formation mechanisms of NCs are challenging to study because *in situ* measurements are required that do not interfere with the NC formation and do not affect the syntheses results. At the same time, often a high time resolution is needed. So far, studies of the CdSe NPL formation and growth mechanism involved analyzing aliquots extracted from the reaction vessel or following the reaction in capillaries that do not represent typical synthesis conditions. With a specially designed homemade setup, the formation of CdSe NPLs could be probed *in situ* under realistic reaction conditions. In Chapter 4, the growth mechanism of CdSe NPLs is investigated

using *in situ* optical absorption and SAXS. The anisotropic growth is unexpected because of the cubic crystal structure. Additionally, both QDs and NPLs form during the reaction. This results in a low NPL yield and necessitates an additional size-selective purification step to separate the QDs from the NPLs. A better understanding of the growth mechanism of zinc blende CdSe NPLs is thus needed.

The growth mechanism for the standard reaction protocol is studied, where cadmium myristate and selenium are heated in 1-octadecene, and cadmium acetate is added during the heat-up.[4] The results show that at an early stage in the reaction, both isotropic and anisotropic particles form (QDs and mini-NPLs). The concentration of QDs (~11 μM) and mini-NPLs (~0.6 μM) is independent of whether cadmium acetate is added or not. However, anisotropic particles (NPLs) with much larger lateral dimensions (~27 by 7.5 nm) form when cadmium acetate is added and the QDs remain smaller (diameter of 3.4 nm vs. 3.8 nm without acetate).

The formation of large NPLs, using the standard reaction protocol, relies on the presence of both cadmium myristate and cadmium acetate. Cadmium myristate likely stabilizes the small mini-NPLs at an early stage of the reaction by passivating the top and bottom facets. A high concentration of cadmium acetate in the early stages of the reaction results in three-dimensional growth, but low concentrations in at least the early stages results in faster growth of the small side facets of the (mini-)NPLs. The rapid consumption of CdSe monomers by growth on the small side facets by the fast 2D growth hampers further growth of the QDs present in the reaction mixture. Without acetate, no rapid 2D growth of NPL is observed, allowing QDs to continue to grow. The addition of cadmium acetate thus enhanced the NPL reaction yield (~3% vs. 40%) but left the concentration of NPLs versus QDs unaltered. The nucleation of an order of magnitude more QDs than NPLs results in an overall low NPL yield of 40% with the standard solution-based synthesis method.

The *in situ* measurements show that NPLs form via continuous addition of monomers, while alternative growth mechanisms like oriented attachment and templated growth could be excluded. Norris *et al*. proposed a model for the anisotropic 2D growth of zinc blende NPLs. In this model, the activation energy for island nucleation on the side facets is lower than on the top and bottom facets. The activation energy depends on the volume, area, and line energies. This model does not explicitly include the effect of ligands on the NPL growth, mainly because the model is based on NPL growth in a melt of precursor where adding a short-chain ligand is unnecessary. The experiments in Chapter 4 show that the ligands influence the 2D growth in a solution-based synthesis and their role should be included in the growth model.

6.3.2 Implications for the mechanism of NPL growth and outlook

The effect of cadmium acetate can be included in the growth model of Norris *et al.*[5] by lowering the values for the area, line, and volume energies. Reducing any of these energies results in a decrease in the activation energy for forming a new monolayer on existing facets, thus accelerating crystal growth. Only with the right combination of energies will the growth on the small side facets outpace the growth on the larger facets. Lowering the energies too much will diminish the favored two-dimensional growth resulting in 3D growth as observed for high acetate concentrations.

The results in Chapter 4 show that possibilities to improve the low reaction yield of the NPL synthesis lie in the early stages of the reaction, where the concentration of QDs and NPLs is de-

termined. With the standard reaction method, an order of magnitude fewer mini-NPLs nucleate than QDs. The nucleation of mini-NPLs should be enhanced or the three-dimensional QD growth rate reduced to improve the NPLs yield. Increasing the acetate concentration at early stages does not have the desired effect, but the impact of the cadmium myristate concentration on the concentration of mini-NPLs versus QDs could affect the NPL nucleation and is worth investigating. Higher concentrations of myristate might enhance the formation and stabilization of mini-NPLs, and higher concentrations of long-chain ligands will likely slow down the overall growth rate, ensuring that fewer CdSe monomers are consumed by QD growth. Besides varying the concentration of the precursors and ligands used in the standard synthesis method, other types of precursors or ligands could also be introduced to the reaction mixture. For example, the addition of $CdCl_2$ made it possible to synthesize NPLs with a thickness above 5.5 MLs,[6] which could not be achieved with the standard synthesis method. This illustrates how ligands can affect the area, line, and volume energies and thereby influence the outcome of the synthesis.

6.4.1 *In situ* studies on hexagonal $NaYF_4$ growth mechanism

The formation of hexagonal β-phase particles is intriguing because they form via cubic α-phase particles with a large size distribution, yet a small distribution of β-phase particles is obtained at the final stage of the reaction. The formation mechanism of these particles is still unknown. The hypotheses are that the β-phase particles either nucleate from monomers released by the α-phase particles or a phase transition occurs for a subset of the α-phase particles.[7,8]

In Chapter 5, the formation of hexagonal β-phase particles was studied with SAXS and WAXS combined with TEM analysis. For the experiments, first α-phase particles were synthesized, purified, and then heated to 300 °C in a mixture of ODE and oleic acid. The scattering data were recorded *in situ* using the homebuilt setup to mimic realistic reaction conditions.

The α-particles cluster at room temperature, but after 10 min at 300 °C a homogeneous dispersion is obtained and a radius of 2.2 nm and a polydispersity of ~20% could be extracted. The size distribution splits in two after 17 minutes at 300 °C. The WAXS data shows that the signal of the β-phase is almost negligible compared to the α-phase at 17 minutes. Thus, the splitting of the size distribution is not related to a phase transition from the α- to β-phase. Fourier transforms of high-resolution TEM images also show that both larger α-particles and β-particles are present in the reaction mixture when the splitting occurs. The small particles visible on the TEM images seem to be exclusively α-phase particles.

The average size of the two distributions increases in size over time, but the concentration of particles with a size smaller than 3.5 nm decreases from 250 μM to zero over a period of one hour. One of the size distributions thus completely dissolves within one hour, leaving particles with a final radius of 5.7 nm and a polydispersity of ~5%. These particles have the hexagonal crystal structure. The signal of the cubic α-phase particles starts to decrease more rapidly after ~40 min, while the signal of the hexagonal β-phase increases at a similar rate.

The model to explain the bimodal distribution should not focus on the change in the crystal structure because this occurs in the last 15 – 20 min of the reaction while splitting of the size distributions already starts after ~17 min. A simulation in chapter 5 shows that a bimodal distribution and, finally, one size distribution with a low polydispersity can be obtained with a distribution of many reaction (dissolution/growth) rates for the initially formed NCs. In this

simulation, the NCs with the fastest growth/dissolution rate increase in size, and some of them dissolve. The NCs with an intermediate growth/dissolution rate grow less and dissolve more because the fast-growing particles decrease the supersaturation level. The NCs with a slow growth/dissolution rate hardly dissolve or grow due to the slow rate. The NCs with intermediate growth rates are thus consumed first, while the NCs with a slow growth/dissolution rate will survive longer because they dissolve more slowly. This results in a bimodal distribution in sizes during the reaction and, eventually, one distribution of particle sizes with a low polydispersity, in agreement with the experimental observations.

6.4.2 Implications for preexisting models on hexagonal $NaYF_4$ NC growth and outlook

The models discussed in the literature[7,8] to explain the growth of hexagonal β-phase NCs focus on the change in crystal structure to explain the formation of hexagonal NCs with a small size distribution. Our measurements show that this is not the cause for the bimodal distributions and that a distribution of growth/dissolution rates can explain the observations. The underlying reason for the distribution of growth/dissolution rates could be differences in ligand density at the surface or the ratio between sodium and rare earth ions. Previous studies have shown that both influence the speed of the reaction and the final size of the hexagonal NCs.[9-11] At high temperatures, differences in stoichiometry are more likely to affect the reaction rate than ligand density. The slow growing and dissolving NCs are then the most sodium-deficient NCs. The *in situ* measurements have thus given new insight into the reaction mechanism and provide quantitative information on the evaluation of concentration, size, and phase transformation of $NaYF_4$ NCs during growth under the widely used synthesis conditions. The model to explain the experimental results suggests a difference between the slow and fast growing NCs, which should be investigated further, for example, by similar *in situ* measurements for different sodium/rare earth ion ratios in the reaction mixture. The new insights can also help to improve the synthesis methods for core-shell NCs, which are difficult to obtain without secondary nucleation.

References

1. Tessier, M. D.; Mahler, B.; Nadal, B.; Heuclin, H.; Pedetti, S.; Dubertret, B., Spectroscopy of Colloidal Semiconductor Core/Shell Nanoplatelets with High Quantum Yield. *Nano Letters* **2013**, *13* (7), 3321-3328.
2. Achtstein, A. W.; Marquardt, O.; Scott, R.; Ibrahim, M.; Riedl, T.; Prudnikau, A. V.; Antanovich, A.; Owschimikow, N.; Lindner, J. K. N.; Artemyev, M.; Woggon, U., Impact of Shell Growth on Recombination Dynamics and Exciton–Phonon Interaction in CdSe–CdS Core–Shell Nanoplatelets. *ACS Nano* **2018**, *12* (9), 9476-9483.
3. Rossinelli, A. A.; Rojo, H.; Mule, A. S.; Aellen, M.; Cocina, A.; De Leo, E.; Schaublin, R.; Norris, D. J., Compositional Grading for Efficient and Narrowband Emission in CdSe-Based Core/Shell Nanoplatelets. *Chemistry of Materials* **2019**, *31* (22), 9567-9578.
4. Ithurria, S.; Bousquet, G.; Dubertret, B., Continuous Transition from 3D to 1D Confinement Observed during the Formation of CdSe Nanoplatelets. *Journal of the American Chemical Society* **2011**, *133* (9), 3070-3077.
5. Riedinger, A.; Ott, F. D.; Mule, A.; Mazzotti, S.; Knüsel, P. N.; Stephan; Prins, F.; Erwin, S. C.; Norris, D. J., An intrinsic growth instability in isotropic materials leads to quasi-two-dimensional nanoplatelets. *Nature Materials* **2017**, *16* (7), 743-748.
6. Christodoulou, S.; Climente, J. I.; Planelles, J.; Brescia, R.; Prato, M.; Martín-García, B.; Khan, A. H.; Moreels, I., Chloride-Induced Thickness Control in CdSe Nanoplatelets. *Nano Letters* **2018**, *18* (10), 6248-6254.
7. May, P. B.; Suter, J. D.; May, P. S.; Berry, M. T., The Dynamics of Nanoparticle Growth and Phase Change During Synthesis of β-NaYF4. *The Journal of Physical Chemistry C* **2016**, *120* (17), 9482-9489.
8. Voss, B.; Haase, M., Intrinsic Focusing of the Particle Size Distribution in Colloids Containing Nanocrystals of Two Different Crystal Phases. *ACS Nano* **2013**, *7* (12), 11242-11254.

9. Rastogi, C. K.; Lu, E.; Tam, J.; Pichaandi, J. M.; Howe, J.; Winnik, M. A., Influence of the Sodium Precursor on the Cubic-to-Hexagonal Phase Transformation and Controlled Preparation of Uniform NaNdF4 Nanoparticles. *Langmuir* **2021**, *37* (6), 2146-2152.
10. Sui, Y.; Tao, K.; Tian, Q.; Sun, K., Interaction Between Y3+ and Oleate Ions for the Cubic-to-Hexagonal Phase Transformation of NaYF4 Nanocrystals. *The Journal of Physical Chemistry C* **2012**, *116* (2), 1732-1739.
11. Rinkel, T.; Nordmann, J.; Raj, A. N.; Haase, M., Ostwald-ripening and particle size focussing of sub-10 nm NaYF(4) upconversion nanocrystals. *Nanoscale* **2014**, *6* (23), 14523-30.

Samenvatting in het Nederlands

Introductie

Nanomaterialen trekken al enkele decennia de aandacht omdat materialen op nanometer schaal zich anders kunnen gedragen dan grotere kristallen (micrometerschaal en daarboven). De optische, elektronische en magnetische eigenschappen kunnen worden aangepast door simpelweg de grootte van de nanokristallen te variëren. Zo worden kristalletjes met variërende grootte in het 1-10 nm gebied, specifiek "quantum dots" genoemd, gebruikt voor het maken van verschillende kleuren licht in lcd-beeldschermen (QLED van Samsung). Ook worden nanodeeltjes gebruikt als katalysator in de chemische sector om reacties te versnellen. Chemische reacties vinden namelijk plaats aan het oppervlak van een katalysator en kleinere deeltjes bevatten meer oppervlak dan grotere brokken voor dezelfde hoeveelheid materiaal.

Nanomaterialen worden gedefinieerd als materialen met minstens een dimensie kleiner dan 100 nm (nanometer is een miljoenste van een millimeter). Dit is een heel ruime definitie en het is dus ook niet verwonderlijk dat nanomaterialen onderling zeer verschillende eigenschappen hebben, afhankelijk van de chemische samenstelling, afmetingen en vorm. Vooral de aanpasbaarheid van de eigenschappen maakt nanomaterialen aantrekkelijk om te gebruiken in een breed scala aan toepassingen door de mogelijkheid eigenschappen te optimaliseren voor bestaande of nieuwe toepassingen. Er wordt bijvoorbeeld onderzoek gedaan naar het gebruik van nanodeeltjes in batterijen. De onderzochte nanodeeltjes zijn beter bestand tegen expansie van het materiaal tijdens het opladen en verder zou het ook mogelijk worden om natrium te gebruiken in batterijen in plaats van lithium.[1] Natrium is in tegenstelling tot lithium in overvloed aanwezig. Ander onderzoek kijkt of nanodeeltjes gebruikt kunnen worden om doorzichtige zonnecellen te maken, zodat ook ramen gebruikt kunnen worden om zonne-energie te absorberen en om te zetten in elektriciteit.[2] Ook in het medische veld zijn er al toepassingen waarin nanodeeltjes gebruikt worden om medicijnen lokaal in het lichaam af te leveren.[3]

Nanomaterialen is dus een heel ruim begrip en er zijn veel verschillende soorten nanodeeltjes met andere eigenschappen die we willen begrijpen en manipuleren. Dit proefschrift focust op twee verschillende nanomaterialen met bijzondere optische eigenschappen, namelijk cadmium selenide (CdSe) en natrium yttrium fluoride ($NaYF_4$) nanodeeltjes waarbij een gedeelte van de yttrium ionen is vervangen door lanthaniden, bijvoorbeeld erbium (Er) en ytterbium (Yb) ionen ($NaYF_4$:Yb^{3+},Er^{3+}). Het introduceren van "vreemde" ionen in een kristalrooster met een bepaalde samenstelling wordt doteren genoemd.

Nanodeeltjes zijn zo klein dat ze niet met een lichtmicroscoop zichtbaar gemaakt kunnen worden. Om de nanodeeltjes te kunnen bekijken, wordt een elektronenmicroscoop gebruikt. Hierbij worden de nanodeeltjes op een rooster met een dunne laag polymeer overgebracht en beschenen met een elektronenbundel. De elektronen ondergaan interacties met het kristal (rooster) en worden bijvoorbeeld afgebogen. Dit zorgt ervoor dat er op de plaats waar nanodeeltjes liggen, minder elektronen doorgelaten worden. Transmissie elektron spectroscopie (TEM) geeft daarom plaatjes waarop de nanodeeltjes er donkerder uitzien. Twee TEM-plaatjes, van de nanodeeltjes die worden bestudeerd in dit proefschrift, worden weergeven in Figuur 1.

In Figuur 1A zijn de CdSe nanodeeltjes zichtbaar. Tijdens de synthese die bestudeerd wordt in hoofdstuk 4 vormen zich twee soorten deeltjes, namelijk bolvormige quantum dots (QDs) en platte nanoplatelets (NPLs). De QDs zijn de bolvormig deeltjes met een diameter van 3.4 nm en de NPLs zijn dunne plaatjes met een dikte van 1.3 nm en een lengte en breedte van ongeveer 10 bij 30 nm. Op het TEM plaatjes liggen de meeste NPLs op hun kant en is de lange zijde van de

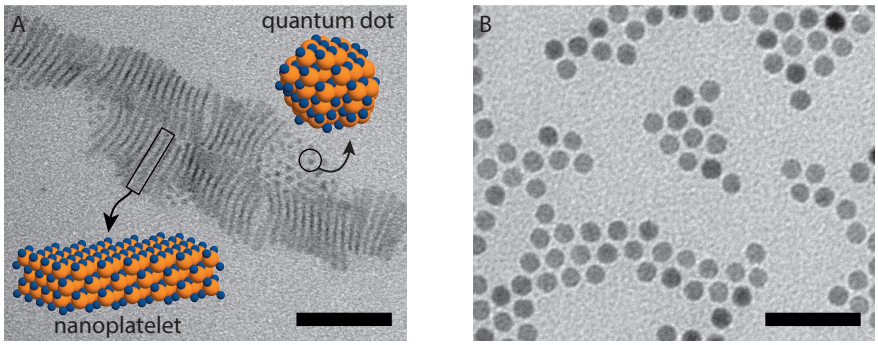

Figuur 1 Transmissie elektronenmicroscopie (TEM) plaatjes van de nanodeeltjes die bestudeerd worden in dit proefschrift. **(A)** CdSe QDs en NPLs. **(B)** Gedoteerde nanodeeltjes $NaYF_4$:Er^{3+},Yb^{3+}. In het linker figuur worden ook schematische afbeeldingen weergeven van een QD en een NPL. Hierbij zijn de oranje bollen selenium atomen en de blauwe bollen cadmium atomen. De NPLs hebben een goed gedefinieerde dikte van enkele lagen cadmium en selenium. Schaalbalk rechtsonder komt overeen met 50 nm in beide TEM plaatjes.

rechthoeken zichtbaar. De schematische representaties van deze twee deeltjes zijn ook weergegeven in Figuur 1A. De blauwe bollen zijn cadmium atomen en de oranje bollen zijn selenium atomen. De NPLs hebben een goed gedefinieerde dikte van enkele monolagen waarvan de boven- en onderlaag beide bestaan uit cadmium atomen. De NPLs op dit TEM plaatje zijn vier monolagen CdSe dik plus een extra cadmium laag. In dit proefschrift worden deze deeltjes 4.5 monolaag (ML) NPLs genoemd, het is ook mogelijk om NPLs te maken die één of meer monolagen CdSe dikker of dunner zijn.

Figuur 1B is een TEM-plaatje van de gedoteerde nanodeeltjes $NaYF_4$:Er^{3+},Yb^{3+}. Ook deze deeltjes zijn bolvorming, maar worden geen quantum dots genoemd. De naam QDs wordt specifiek gebruikt voor materialen waar de optische eigenschap veranderd kunnen worden door de dimensies van het materiaal te veranderen. Dat is voor $NaYF_4$ nanodeeltjes niet het geval, maar het zijn juist de ionen zoals erbium en ytterbium die verspreid in het nanodeeltje aanwezig zijn, die zorgen voor de interessante optische eigenschappen. De twee plaatjes in Figuur 1 hebben dezelfde schaal en laten dus zien dat de $NaYF_4$ nanodeeltjes veel groter zijn dan de CdSe QDs (12 nm vs. 3.4 nm).

De CdSe en gedoteerde $NaYF_4$ nanodeeltjes hebben interessante, maar totaal verschillende optische eigenschappen. Zo kan de kleur licht die CdSe nanodeeltjes absorberen of uitzenden gevarieerd worden door de grootte van de deeltjes aan te passen. CdSe QDs zenden bijvoorbeeld blauw licht uit als ze een diameter van 2 nm hebben en rood licht wanneer de diameter 6 nm is. Dit wordt het kwantum confinement (kwantum opsluiting) effect genoemd en is typerend voor halfgeleidermaterialen op de nanoschaal. $NaYF_4$ nanodeeltjes hebben geen grootte afhankelijke optische eigenschappen, maar lanthaniden kunnen makkelijk worden ingebouwd in het kristalrooster op de plaats van yttrium. De lanthaniden hebben de bijzondere eigenschap dat ze twee of meer lichtdeeltjes (fotonen) met een lage energie om kunnen zetten in één lichtdeeltje met een hogere energie. Dit proces wordt upconversion genoemd.

Door de verschillende optische eigenschappen zijn de (beoogde) applicaties voor deze deeltjes ook verschillend. CdSe nanodeeltjes worden gebruikt in lcd-beeldschermen voor een hogere efficiëntie en betere kleurweergave. Ze kunnen ook toegepast worden om efficiëntere witte ledlampen te maken die een prettige warme kleur wit uitzenden, al is de stabiliteit hierbij een probleem. De gedoteerde $NaYF_4$ nanodeeltjes kunnen gebruikt worden als lichtgevende labels om dieper in biologisch materialen te kunnen kijken met lichtmicroscopie of om de efficiëntie van zonnecellen te verbeteren.

In dit hoofdstuk worden enkele hoofdzaken uitgelegd om de eigenschappen van de bestudeerde nanodeeltjes beter te begrijpen, inzicht te geven in hoe deze eigenschappen toepassingen kunnen verbeteren en ook om het verrichte onderzoek beter te kunnen volgen. Aan het einde wordt een samenvatting gegeven van het onderzoek dat in dit proefschrift besproken is. De onderwerpen die eerst worden besproken zijn: halfgeleiders en het quantum confinement effect, waarom deeltjes met 'kleurzuivere' emissie nodig zijn, upconversion in lanthaniden, maken van nanodeeltjes, en het volgen van de nanodeeltjes groei met o.a. de verstrooiing van Röntgenstraling.

Halfgeleiders en quantum confinement

De CdSe nanodeeltjes waar we naar kijken bestaan uit honderden tot een paar duizend atomen. Een atoom bestaat uit een positieve kern en een negatieve elektronenwolk. Elektronen in een atoom hebben een bepaalde energie. Dit kan niet iedere willekeurige energie zijn, maar alleen discrete waarden zijn mogelijk. Kleine (quantum) systemen gedragen zich namelijk heel anders dan grote (klassieke) systemen. Een wiel kan met iedere willekeurige snelheid ronddraaien, maar op de kleine schaal gedragen systemen zich volkomen anders; hun eigenschappen kunnen alleen in discrete stappen toenemen; ze kunnen bijvoorbeeld alleen twee, drie, vier, etc. keer zo hard ronddraaien en niets ertussen in. Het systeem is gekwantiseerd. Vergelijkbaar hiermee kunnen elektronen in een atoom niet iedere willekeurige energie aannemen, maar zijn de energieniveaus juist gekwantiseerd.

Vaste stoffen bevatten heel veel atomen (meer dan vele miljarden in één microkristal zo groot als een zandkorreltje) die aan elkaar gebonden zijn via chemische bindingen waarin elektronen gedeeld worden. Het grote aantal chemische bindingen zorgt ervoor dat er heel veel energieniveaus zijn, die in energie dicht bij elkaar liggen, waardoor verdeling van energieniveaus weer continu lijkt. Dit worden energiebanden genoemd. Een vaste stof heeft meerdere energiebanden en afhankelijk van de structuur en samenstelling zullen deze energiebanden wel of niet met elkaar overlappen. Als er geen overlap is, onderstaan er tussen de banden gebieden met verboden energieën die de elektronen niet kunnen aannemen. Dit wordt een band gap (band kloof) genoemd.

De energieniveaus in de energiebanden worden bezet met elektronen. Hierbij worden de laagste energielevels eerst bezet. Als er lege energieniveaus zijn die maar een klein beetje hoger in energie zijn dan de gevulde niveaus, dan kunnen de elektronen makkelijk bewegen door het materiaal en spreken we van geleiders of metalen. Dit komt voor als de energiebanden niet volledig gevuld zijn, of als een gevulde band en lege band overlappen. Metalen hebben dus een bandenstructuur die hieraan voldoet. Als de energiebanden niet overlappen, maar er een bandgap aanwezig is tussen een gevulde en een lege energieband, dan zullen de materialen niet geleiden. Dit soort materialen zijn isolatoren. Als de bandgap klein is, dan is het mogelijk om de stof ge-

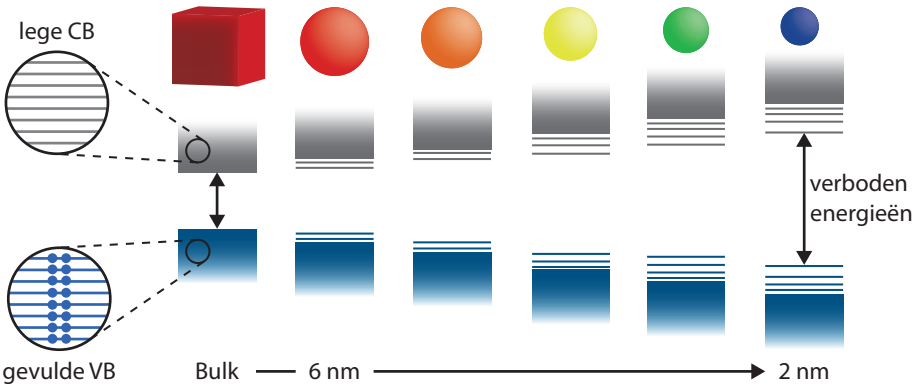

Figuur 2 Schematische weergave van de bandenstructuur van bulk halfgeleidermateriaal (vierkant) en halfgeleider QDs (bollen). De banden bestaan uit energieniveaus die zeer dicht op elkaar liggen en daardoor niet te onderscheiden zijn. In blauw de valentieband (VB) welke is gevuld met elektronen (uitvergroting links) en in grijs de geleidingsband (CB) welke niet gevuld is met elektronen. Naarmate het deeltje kleiner wordt neemt de bandgap toe, dus de licht emissie kan worden aangepast via de grootte van de nanokristallen (zie kleur van de bollen). Naarmate de deeltjes kleiner worden, ontstaan er ook discrete energieniveaus aan de randen van de VB en CB. Deze afbeelding is gebaseerd op referentie [4].

leidend te maken door energie aan het systeem toe te voegen met hitte, elektrische spanning of door het materiaal te beschijnen met licht waardoor elektronen uit de volle band naar de lege kunnen gaan en zo voor een beetje geleiding zorgen. Dit soort materialen worden halfgeleiders genoemd en CdSe is daar een voorbeeld van.

Grote kristallen bestaande uit heel veel atomen worden 'bulk' genoemd. De bandenstructuur van bulk halfgeleidermateriaal wordt schematisch weergegeven aan de linkerkant in Figuur 2. De structuur bestaat uit een volledig gevulde band, de valentieband (VB), waarbij alle energieniveaus bezet zijn met twee elektronen (zie figuur). De lege energieband, de geleidingsband (CB), is gescheiden van de VB door de bandgap met verboden energieën die de elektronen niet kunnen aannemen. Als het materiaal met licht wordt beschenen, dan kan een elektron van een energieniveau uit de VB naar de CB worden gebracht (geëxciteerd worden). Hiervoor moet de energie van het licht (lichtdeeltje of foton) wel gelijk of groter zijn dan de bandgap. Voor CdSe moet de golflengte van het licht bijvoorbeeld korter zijn dan 700 nm. Het licht met deze kortere golflengtes (alle kleuren behalve zeer donkerrood) heeft genoeg energie om het elektron te exciteren en kan geabsorbeerd worden. Het donkerrode en infrarode licht wordt niet geabsorbeerd en zorgt ervoor dat bulk CdSe een donkerrode kleur heeft. Na verloop van tijd zal het elektron terugvallen naar de VB, daarbij wordt de energie weer vrijgegeven met uitzending van een lichtdeeltje met een energie die overeenkomt met het energieverschil tussen de VB en CB (de bandgap). Bulk CdSe kan dus donkerrode lichtdeeltjes uitzenden.

Als we de kristallen van een halfgeleidermateriaal kleiner maken, deeltjes met honderden of duizenden atomen i.p.v. miljarden of miljoenen, dan wordt de bandgap tussen de VB en CB steeds groter. Voor CdSe wordt dit effect zichtbaar voor deeltjes die kleiner zijn dan ongeveer 10 nm. De stof heeft dan niet langer een donkerrode kleur, maar wordt steeds geler van kleur. De kleur licht die wordt uitgezonden als een elektron terugvalt van de CB naar de VB verandert

ook. Dit wordt weergeven in Figuur 2, naarmate de deeltjes kleiner worden, zal de uitgezonden kleur veranderen van rood naar blauw. Zoals hierboven beschreven, worden deze deeltjes quantum dots genoemd. CdSe QDs van 6 nm zenden rood licht uit en CdSe QDs van 2 nm zenden blauw licht uit.

De grootte-afhankelijkheid van de emissiekleur wordt het quantum confinement effect genoemd (quantum opsluitingseffect). De achterliggende natuurkunde is lastig. Kort gezegd zijn de nanodeeltjes kleiner dan de ruimte die de ladingsdragers in bulkmateriaal zouden aannemen. Met ladingsdragers bedoelen we onder andere de elektronen (negatieve lading), maar ook het 'gat' dat achterblijft als we een elektron exciteren van de VB naar de CB. Dit gat, waar geen elektron meer zit, heeft effectief een positieve lading en wordt gezien als een quasi deeltje 'een soort van deeltje'. Een elektron en gat trekken elkaar aan omdat ze een tegengestelde lading hebben. Ze worden daarom vaak samen beschreven als een deeltje, ook een quasi deeltje, dat een exciton genoemd wordt. In het bulk halfgeleider kristal neemt een exciton een ruimte in die vrij groot is en zich uitstrekt over enkele tot tientallen nanometers (de exciton Bohrstraal). Als een halfgeleider kleiner wordt dan de exciton Bohrstraal, dan raakt het exciton steeds meer opgesloten; dit opsluitingseffect heeft als gevolg dat de energie van het exciton en dus de bandgap groter wordt. In Figuur 2 ziet men ook dat, aan de randen van de VB en CB, de energieniveaus verder uit elkaar gaan en er dus discrete niveaus ontstaan in plaats van een continuüm. Dit is ook zichtbaar als we meten welke golflengtes van licht er geabsorbeerd worden door het materiaal. Er zijn duidelijke pieken zichtbaar in een absorptiespectrum van CdSe QDs (zie Hoofdstuk 2, Figuur 2.3B).

Toepassingen van CdSe Nanokristallen

Door het quantum confinement effect is de kleur licht die CdSe QDs uitzenden makkelijk aan te passen. Daarnaast zenden QDs geen brede verdeling aan kleuren (golflengtes) uit, maar juist een zuivere kleur wat we smalbandige emissie noemen. Deze smalbandige emissie is nuttig voor het gebruik van deze deeltjes in ledlampen en beeldschermen. Conventionele materialen die voor witte LEDs en beeldschermen gebruikt worden zenden namelijk vaak licht uit over een breder golflengtegebied, ook golflengtes waarvoor het menselijk oog niet of minder gevoelig is en dit vermindert de efficiëntie van de lichtbron.

Een witte-LED bestaat uit een blauwe LED en luminescerende materialen, fosforen genoemd (bijvoorbeeld YAG:Ce^{3+} en CASN:Eu^{2+}), die een deel van het blauwe LED licht absorberen en omzetten in groen en rood licht. Samen met het doorgelaten blauw geeft dit wit licht. De emissie van deze fosforen is echter vaak niet kleur zuiver en zorgt voor brede pieken in het groene en rode gedeelte van het emissiespectrum. Het emissiespectrum van een witte-LED en de gevoeligheid van het menselijk oog wordt weergegeven in Figuur 3A. In dit figuur is te zien dat een witte-LED veel licht uitzendt met golflengtes langer dan 640 nm, waar de ooggevoeligheid zeer laag wordt.

Echter, voor witte-LED lampen is wel een stofje nodig dat rood licht uitzendt, om een prettige warme-witte kleur te geven in lampen of om een goede kleurweergave te realiseren in beeldschermen. Een prettige warmte tint, hoge efficiëntie en goede kleurweergave kunnen bereikt worden door de smalbandig rode emissie van QDs te gebruiken in LEDs. Het emissiespectrum van rood licht uitzendende QDs wordt weergeven in Figuur 3B in rood. Voor QDs is de kleur licht makkelijk aan te passen met de grootte van de QD en ze hebben een smalbandige emissie

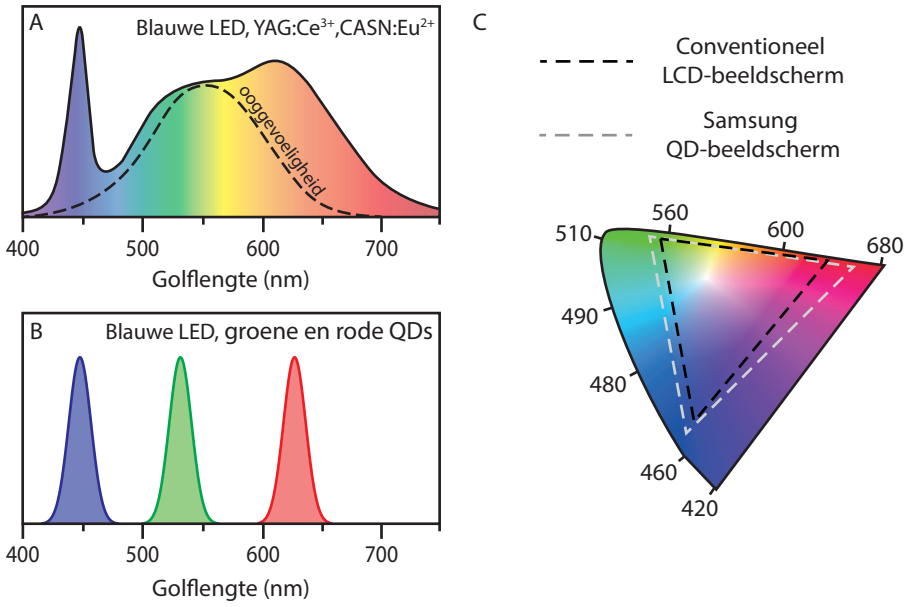

Figuur 3 (A) Spectrum van conventionele ledlamp bestaande uit blauwe LED en de groen-gele en rode fosforen YAG:Ce^{3+} en CASN:Eu^{2+}. De onderbroken lijn geeft de menselijke ooggevoeligheid weer.[5] **(B)** Spectrum van blauwe LED gecombineerd met QDs die groen of rood licht uitzenden. **(C)** Diagram dat het kleurenpalet aangeeft dat gemaakt kan worden door groen, rood en blauw te mengen. De driehoeken geven het kleurenpalet weer dat een conventioneel lcd-beeldscherm kan generen en dat van een Q-LED display van Samsung.[6] Het kleurenpalet van het Q-LED beeldscherm is groter, omdat de blauwe, groene en rode component smalbandig zijn (Spectrum in B) in tegenstelling tot conventionele beeldschermen (spectrum in A samen met kleurenfilters).

en daardoor kan emissie van licht met golflengtes langer dan 640 nm worden beperkt. QDs kunnen zo helpen bij het realiseren van efficiënte warm-witte LEDs.

Voor beeldschermen is het belangrijk dat er zowel een smalbandige blauwe, groene en rode emissie wordt gebruikt. In een beeldscherm zijn de drie basiskleuren nodig om andere kleuren te krijgen door deze drie kleuren te mengen. In lcd-schermen wordt een witte lichtbron gebruikt, zoals de blauwe LED met groen en rode fosforen. De blauwe, groene en rode subpixels worden gerealiseerd met kleurenfilters.

Figuur 3C laat de kleuren zien die gemaakt kunnen worden door groen, blauw en rood te mengen met verschillende verhoudingen. De variatie in kleuren die in een beeldscherm kan worden gemaakt, wordt aangegeven met het kleurenpalet (color gamut). Dit zijn de driehoeken die te zien zijn in Figuur 3C. Hoe groter het kleurenpalet, hoe beter het beeld overeenkomt met de werkelijke kleuren. Het kleurenpalet wordt groter naarmate de drie punten dichter bij de zwarte omkadering komen te liggen (de locus). De locus komt overeen met zuivere golflengtes (monochromatisch) licht. Dit betekent dus dat kleur zuivere emissie van goed gekozen golflengtes blauw, groen en rood licht mooiere beelden zal geven met veel meer verschillende kleuren. Dit kan niet bereikt worden met het spectrum in Figuur 3A en kleurenfilters, maar

wel met een blauwe LEDs in combinatie met smalbandige emissie van groene en rode quantum dots zoals weergeven in Figuur 3B. Ook bij de huidige QD-beeldschermen worden kleurenfilters gebruikt om het groene of rode licht te selecteren, hierbij gaat minder licht verloren dan bij het gebruik van conventionele fosforen.

Quantum dots van een ander materiaal dan CdSe worden al gebruikt in de QLED-displays van Samsung. Het kleurenpalet van de QLED-beeldschermen (Figuur 3C, grijs driehoek) is groter dan van conventionele beeldschermen (Figuur 3C, zwart driehoek). Toch is er nog veel vernieuwing gaande in hoe QDs gebruikt worden in beeldschermen om bijvoorbeeld de beeldkwaliteit te verbeteren of flexibele beeldschermen mogelijk te maken. Bovendien is de emissie van de NPLs nog smalbandiger dan die van QDs en dus zijn deze nanodeeltjes zeer interessant voor witte LEDs en beeldschermen. Hoe smal de emissiebanden zijn kan echter beïnvloed worden door de omgevingstemperatuur en deze temperatuur kan oplopen tot wel 150 °C in LEDs. In hoofdstuk 3 wordt onderzocht wat het effect is van temperatuur op de verbreding van de emissiespectra van CdSe QDs en NPLs.

Upconversion in $NaYF_4$ nanokristallen en toepassingen

Het andere materiaal dat in dit proefschrift onderzocht wordt, zijn $NaYF_4$ nanodeeltjes gedoteerd met lanthanide ionen. De lanthaniden zijn te vinden in de rij elementen die zich onderin het periodiek systeem bevindt, dus van lanthanium tot en met lutetium. De lanthaniden worden ingebouwd tijdens de synthese op de positie van yttrium ionen en zijn verantwoordelijk voor de bijzondere optische eigenschappen van deze nanomaterialen.

De lanthaniden hebben een niet volledig gevulde 4f-schil. In de moderne quantum fysica worden de schillen niet gezien als banen waarin elektronen om de kern draaien, maar als golffuncties die de waarschijnlijkheid beschrijven dat een elektron aangetroffen wordt op een bepaalde afstand van de kern. Deze golffuncties worden orbitalen genoemd. In totaal zijn er zeven verschillende f-orbitalen die bezet kunnen worden met maximaal twee elektronen per orbitaal. Hoe de elektronen verdeeld zijn over de orbitalen heeft invloed op de energie. De lanthanide-ionen krijgen hierdoor veel verschillende energetische toestanden door het grote aantal manieren waarop de elektronen over de 14 beschikbare plaatsen in de 4f orbitalen verdeeld kunnen worden. Deze toestanden, energieniveaus, worden aangeduid met labels die termsymbolen genoemd worden. De laagst energetische toestand (grondtoestand) voor erbium wordt bijvoorbeeld aangeduid met $^4I_{15/2}$. In Figuur 4A zijn de laagste energietoestanden van ytterbium en erbium weergegeven, inclusief het bijbehorende label.

$NaYF_4$ gedoteerd met één van de lanthaniden of een combinatie van lanthaniden kunnen gebruikt worden om laag energetisch licht om te zetten in hoogenergetisch licht. Hierbij is het makkelijker om licht te zien als een deeltje i.p.v. een golf. Zo'n licht deeltje wordt een foton genoemd. Normaal gesproken absorberen materialen een foton en zenden vervolgens een foton uit met dezelfde of een lagere energie waarbij een gedeelte van de energie verloren gaat in de vorm van warmte. De gedoteerde $NaYF_4$ nanodeeltjes kunnen twee fotonen met een lage energie absorberen en deze vervolgens omzetten in één foton met een hogere energie. Bijvoorbeeld, twee ytterbium ionen, in de buurt van een erbium ion, kunnen beide een nabij-infrarood (NIR) foton van ~980 nm absorberen. Dit wordt weergeven in Figuur 4A en 4B met donkerrode pijlen. Door de absorptie verandert de toestand van de ytterbium ionen van de grondtoestand $^2F_{7/2}$ naar de aangeslagen toestand $^2F_{5/2}$. Vervolgens wordt de energie overgedragen naar een erbium ion in

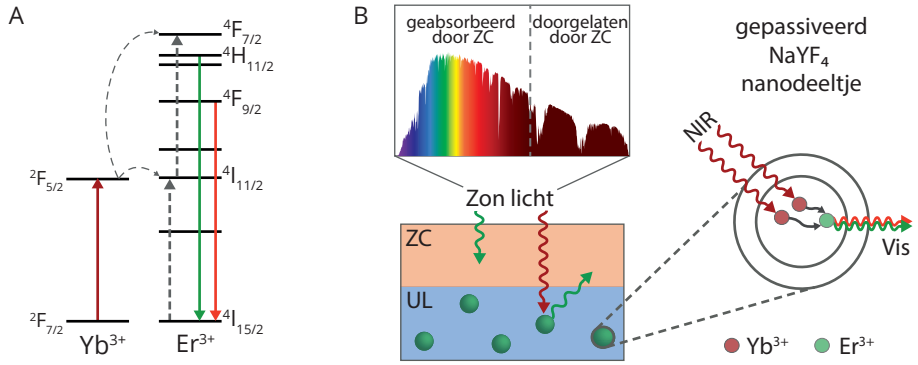

Figuur 4 (A) Energieniveauschema's van ytterbium en erbium. Ytterbium ionen kunnen nabij-infrarood licht (~980 nm) absorberen (donkerrode pijl) en deze energie overdragen aan een erbium ion (grijze onderbroken pijlen) en wordt het erbium ion in twee stappen geëxciteerd naar de $^4F_{7/2}$ toestand via de $^4I_{11/2}$ toestand. Vanuit deze toestand kan het erbium ion terugvallen naar een van de toestanden met een lagere energie en vervolgens een groen of rood foton uitzenden (groene of rode pijl). **(B)** Zonnecel (ZC) gecombineerd met een laag met upconversion nanodeeltjes (UL) zorgen ervoor dat een groter gedeelte van het zonnespectrum benut kan worden. Het gedeelte van het spectrum dat een te lage energie heeft om geabsorbeerd te worden door de zonnecel, wordt omgezet in groen of rood licht door de gedoteerde $NaYF_4$ nanodeeltjes.

de buurt van de ytterbium ionen. Hierbij wordt dit ion aangeslagen naar de $^4I_{11/2}$ en vervolgens de $^4F_{7/2}$ toestand. Vanuit deze toestand zal het erbium relaxeren naar lagergelegen $^4S_{3/2}$ of $^4F_{9/2}$ toestand door de energie af te geven aan vibraties (warmte) en uiteindelijk terugvallen naar de grondtoestand $^4I_{15/2}$ door een groen of rood foton uit te zenden, aangeven met de groene en rode pijlen.

Het proces waarbij twee laag energetische fotonen worden omgezet in een hoogenergetisch foton wordt upconversion genoemd. Upconversion materialen kunnen worden gebruikt om de efficiëntie van zonnecellen te verhogen en zitten ook als echtheidskenmerk in bankbiljetten. Zonnecellen worden gemaakt van een halfgeleidermateriaal, bijvoorbeeld silicium. Deze materialen hebben een bandgap zoals besproken in een voorgaande paragraaf. Alleen fotonen met een hogere energie dan de bandgap, kunnen geabsorbeerd worden door het halfgeleidermateriaal en deze energie wordt vervolgens omgezet door de zonnecel in stroom. Fotonen met een lagere energie worden niet geabsorbeerd en deze zonne-energie kan dus niet worden benut.

Het spectrum van de zon zoals dat het aardoppervlak bereikt is weergegeven in Figuur 4B. In dit spectrum wordt ook weergeven welk gedeelte van het spectrum geabsorbeerd wordt door de zonnecel (ZC) en welk gedeelte wordt doorgelaten. Door een zonnecel te combineren met een laag met upconversion nanodeeltjes (UL) kan het NIR licht (donkerrood Figuur 4B) worden omgezet in groen of rood licht. Dit licht kan vervolgens wel door de zonnecel geabsorbeerd worden, waardoor het donkerrode gebied in het zonnespectrum ook benut wordt en de efficiëntie van zonnecellen verhoogd wordt.

Voor deze en andere toepassingen passiveren we het oppervlak van de nanodeeltjes. Hierbij wordt een laagje $NaYF_4$ zonder lanthaniden om de gedoteerde nanodeeltjes gegroeid. Dit zorgt

ervoor dat de geabsorbeerde energie niet verloren gaat door andere processen aan het oppervlak van de nanodeeltjes en het upconversion proces zo efficiënt mogelijk is.

Synthese van nanodeeltjes

Voor het gebruik van nanodeeltjes in de diverse toepassingen moeten we controle hebben over de groei van deze deeltjes, zodat ze de optimale en reproduceerbare eigenschappen hebben. De groei van nanodeeltjes wordt schematisch weergeven in Figuur 5. Nanodeeltjes worden gemaakt door precursors bij elkaar te voegen. Deze precursors zijn moleculen die bestaan uit de atomen Cd of Se (voor CdSe QDs en NPLs) of Y, Er, Yb, of Na ($NaYF_4$:Yb^{3+},Er^{3+} nanodeeltjes) en daarnaast vaak lange koolwaterstofketens (bestaande uit koolstof, waterstof, en vaak zuurstof atomen). Dit wordt schematisch weergegeven in het eerste ovaal in Figuur 5. Hierbij stellen de oranje bollen selenium voor, blauwe bollen cadmium en de grijze zigzaglijnen de koolwaterstofketens.

Bij hoge temperatuur reageren de precursors met elkaar en vormen kleine clusters van cadmium en selenium atomen. Voornamelijk monomeren worden gevormd (een CdSe eenheid) en soms ook iets grotere clusters (2de ovaal). Vaak worden deze clusters gestabiliseerd door de lange koolwaterstofketens, deze zijn hier weggelaten. Deze eerste fase waarbij monomeren worden gevormd wordt de inductie fase genoemd.

Als de oplossing oververzadigd raakt met CdSe monomeren, zullen er grote clusters van CdSe ontstaan die verder blijven groeien (groene bollen, 3de ovaal). Deze fase wordt de nucleatie fase genoemd. Omdat de deeltjes niet allemaal tegelijk ontstaan zal er een verdeling aan groottes verkregen worden (4de ovaal) tijdens de nucleatiefase. Om deze verdeling zo klein mogelijk te houden is een korte nucleatie fase vaak gunstig. Dit kan bereikt worden door een oplossing met één van de precursor te verhitten en de andere precursor, die op kamertemperatuur is, te injecteren (hot-injection methode). Een andere mogelijkheid is de precursor op kamertemperatuur samen te voegen en vervolgens snel te verhitten (heating-up methode). Een hoge oververzadiging wordt daardoor snel bereikt, er ontstaan daardoor plots heel veel deeltjes, waardoor de concentratie aan CdSe monomeren ook heel snel zakt, en daarmee de oververzadigingsgraad van de oplossing. Op dat moment stopt de nucleatie fase en zullen de stabiele deeltjes verder groeien tijdens de groeifase. Tijdens de groeifase zal de verdeling in grootte nog iets afnemen

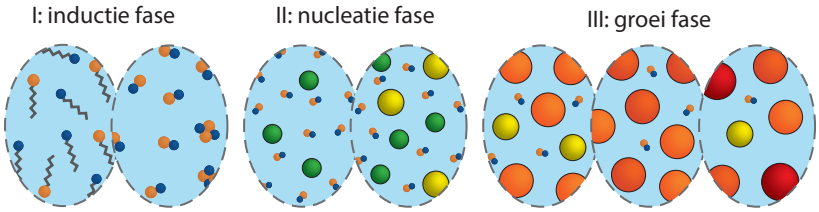

Figuur 5 Schematisch overzicht van de groei van nanodeeltjes. De synthese verloopt volgens drie fasen. 1ste en 2de ovaal (inductie fase): precursors reageren en vormen monomeren en kleine clusters. Hier worden de cadmium en selenium precursors weergeven met blauwe (cadmium) en oranje (selenium) en een lange koolwaterstofketen (grijze zigzaglijnen). In de overige ovalen zijn de koolwaterstofketens weggelaten. 3de en 4de ovaal: tijdens de nucleatie fase ontstaan er grotere stabiele nanodeeltjes (groene bollen) waarvan de grootte toeneemt (gele bollen). 5de en 6de ovaal (groeifase): de monomeer concentratie is flink afgenomen, er ontstaan geen nieuwe deeltjes, maar de bestaande deeltjes groeien verder. 7de ovaal: als de synthese niet tijdig beëindigd wordt en de monomeer concentratie te laag wordt, dan neemt de verdeling in groottes toe.

omdat de kleine deeltjes sneller groeien (5de en 6de ovaal). De concentratie monomeren zal in de groeifase blijven afnemen. Dit heeft echter wel invloed op de stabiliteit van de deeltjes. Als de concentratie monomeren te ver zakt dan zullen de kleinste nanodeeltjes oplossen en de grootste deeltjes verder groeien (7de ovaal). De kleine deeltjes worden als het ware opgegeten door de grote deeltjes. Om een nauwe verdeling aan groottes te krijgen, is het nodig om de synthese voor dit moment te stoppen. Dit kan gedaan worden door de temperatuur snel te verlagen naar kamertemperatuur.

Meten van de vorming en groei van nanodeeltjes

Het model voor groei van nanodeeltjes dat besproken is in de vorige paragraaf dateert al uit de jaren vijftig. Het model klopt niet volledig met de werkelijkheid en kan vaak niet gebruikt worden om de uitkomst van een synthese te voorspellen. Eén van de belangrijkste tekortkomingen van dit model is dat het effect van de koolwaterstofketens niet wordt meegenomen. Deze ketens bevatten namelijk een groep die kan binden aan de atomen op het oppervlak van de nanodeeltjes. De nanodeeltjes in Figuur 5 zijn dus bedekt met een laagje van deze moleculen. Deze lange ketens zorgen ervoor dat de nanodeeltjes niet bij elkaar kunnen komen, waardoor het vormen van bulk kristallen door samensmelten van de nanodeeltjes wordt voorkomen. Daarnaast bepalen de moleculen aan het oppervlak de vloeistoffen die gebruikt kunnen worden om stabiele mengsels van een vloeistof en nanodeeltjes te krijgen (suspensie).

De moleculen aan het oppervlak van nanodeeltjes worden liganden genoemd. Liganden zijn niet per definitie lange koolwaterstofketens, ook geladen atomen (ionen) kunnen ervoor zorgen dat de nanodeeltjes niet samenklonteren. Naast de stabiliserende rol van liganden om samenklontering voorkomen tijdens en na de synthese, hebben ze vaak een rol in de chemische reacties die leiden tot de vorming van monomeren. Ook beïnvloeden ze de groeisnelheid en bepalen ze de vorm van nanodeeltjes omdat ze aan het oppervlak binden. Ze hebben hierdoor veel invloed op de uitkomst van de synthese. Met NMR (de MRI voor moleculen) wordt mooi onderzoek gedaan naar het aantal liganden op het oppervlak van nanodeeltjes en liganden in de oplossing en wordt er gekeken welke chemische bindingen er gevormd worden tijdens de synthese.

Andere technieken zijn vereist om de concentratie, grootte en vorm van de nanodeeltjes tijdens de synthese te onderzoeken. Vaak is hierover nog weinig informatie bekend voor een specifieke synthese methode, omdat het lastig is om dit te onderzoeken. De reacties zijn vaak snel en de deeltjes zijn heel klein. De vorm en grootte kan onderzocht worden met elektronenmicroscopie (zie introductie) door monsters te nemen tijdens de synthese. Het is echter beter om de synthese te volgen zonder deze te verstoren met het nemen van monsters. Dit kan gedaan worden met *in situ* methodes waarbij je iets bestudeert precies waar het gebeurt en niet een monster neemt om dit vervolgens later en buiten de reactieruimte te analyseren. In dit proefschrift zijn verschillende syntheses *in situ* bestudeerd met ultraviolet/zichtbaar licht en röntgenstraling.

De *in situ* opstelling

Om deze *in situ* metingen te kunnen doen, is er een speciale opstelling gemaakt met aangepast glaswerk. Deze opstelling wordt weergegeven in Figuur 6. De opstelling bestaat uit een roerplaat, een speciale driehalskolf en een systeem om vaste stoffen toe te voegen tijdens de synthese. Dit laatste kan ook vervangen worden met een injector voor vloeistoffen voor hot-injection syntheses. Het glaswerk heeft drie halzen, één voor de injector, één voor een thermometer

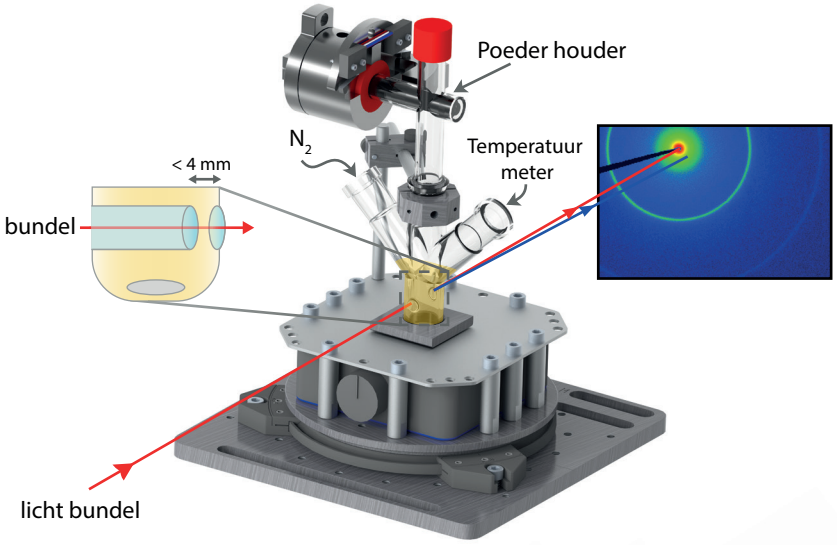

Figuur 6 Opstelling voor *in situ* metingen. Er wordt een speciale driehalskolf gebruikt met een inkeping onderin, zodat de bundel (rode pijl) door minder dan 4 mm van de oplossing heen gaat (zie uitvergroting). De oplossing wordt geroerd met een magnetische roerder. Via de halzen kan een thermometer worden aangesloten en stikstof worden toegevoerd. Bovenop is een poederhouder geplaatst. Het poeder kan op een willekeurig moment tijdens de synthese op afstand worden toegevoegd. Het glaswerk zit in een beschermende metalen bak en wordt verhit met een verwarmingslint (niet in de afbeelding weergegeven). De opstelling kan worden gebruikt om UV/VIS absorptiespectra of verstrooiing van röntgenstralen te meten (blauwe pijl).

en één voor de toevoer van stikstof. Dit laatste is nodig omdat de aanwezigheid van zuurstof de kwaliteit van de nanodeeltjes verlaagt.

De kolf is niet bolvorming aan de onderkant zoals gebruikelijk, maar bevat aan de voorkant een inkeping (zie uitvergroting). Deze inkeping is gemaakt om ervoor te zorgen dat het licht of de röntgenstralen minder dan 4 mm door de oplossing met nanodeeltjes hoeven te reizen. Deze afstand moet niet te groot zijn, anders is er te weinig signaal om de meting te doen doordat te veel licht of röntgenstraling geabsorbeerd wordt. Onder in de kolf bevindt zich een magnetische roerder, om alle precursors goed te mengen en ook een goed beeld te krijgen van het gehele reactie mengsel. Verder zorgt het roeren ervoor dat de deeltjes niet stuk worden gemaakt door langdurige blootstelling aan de hoogenergetische Röntgenstraling.

Een bundel van licht of Röntgenstralen (rode lijn) kan door de kolf geleid worden met de juiste optische elementen (lenzen, spiegels). Na de kolf wordt het signaal gemeten met een detector. In het geval van absorptiemetingen met ultraviolet en zichtbaar licht meten we het spectrum (hoeveelheid absorptie als functie van de golflengte van het licht). Voor de Röntgenmetingen zijn we geïnteresseerd in de röntgenstralen die verstrooid worden door de nanodeeltjes (blauwe lijn). De röntgenstralen die rechtdoor gaan worden geblokkeerd door een 'bundelstopper' om de detector te beschermen. De verstrooide röntgenstralen geven een 2D afbeelding zoals weergegeven in Figuur 6 of 7C. Rood betekent een hoog signaal, veel röntgenstralen worden onder die

hoek verstrooid. Hoe lager het signaal, hoe meer de kleur verschuift naar het blauw. De zwarte lijn in de 2D afbeelding is de bundelstopper, waar alle röntgenstralen worden tegengehouden. Omdat de nanodeeltjes vrij kunnen bewegen, krijgen we een symmetrische afbeelding rond de niet verstrooide bundel (rode lijn). Daarom worden deze data vaak geplot als 1D-data met op de ene as de intensiteit en op de andere as de hoek waaronder de röntgenstralen verstrooid zijn, zoals we later zullen zien in Figuur 7D.

De metingen met de *in situ* opstelling

De vorming van nanodeeltjes van halfgeleidermateriaal kunnen we volgen door te meten welke golflengtes licht geabsorbeerd worden. De kleur van de nanodeeltjes is namelijk afhankelijk van de grootte door het quantum confinement effect. Dit is een relatief goedkope en eenvoudige methode om de synthese te volgen en geeft ook een goed beeld van de synthese zonder dat er ingewikkelde analysemethodes nodig zijn. Het is voor syntheses bij hoge temperatuur helaas niet mogelijk om de grootte van de nanodeeltjes *in situ* te bepalen, omdat de absorptiespectra, de kleuren licht die het nanodeeltjes absorbeert, ook beïnvloed worden door de temperatuur. Als de temperatuur constant is, kan er wel worden waargenomen dat de nanodeeltjes groeien, maar hieraan kunnen we niet direct een deeltjesgrootte koppelen.

Om de concentratie, vorm, grootte en kristalstructuur te bepalen, wordt er in dit proefschrift gebruikt gemaakt van de verstrooiing van röntgenstralen. De atomen, waar de nanodeeltjes uit bestaan die we willen bestuderen (CdSe en $NaYF_4$), zijn netjes geordend in een kristalrooster. Hoe deze ordening er precies uit ziet, is afhankelijk van de kristalstructuur van het materiaal. Een simpel tweedimensionaal rooster is getekend in Figuur 7A, waar de zwarte bollen atomen voorstellen die geordend zijn in lagen. De lagen worden gemarkeerd door de groene lijnen. Röntgenstralen die op de kristallen vallen, kunnen verstrooid worden door elk van de lagen van atomen door interactie met de elektronenwolk van de atomen. Deze verstrooide röntgenstralen kunnen elkaar versterken waardoor er meer signaal onder een bepaalde hoek wordt gemeten, of ze kunnen elkaar juist uitdoven waardoor er geen signaal gemeten wordt onder een bepaalde hoek. Of ze elkaar versterken of uitdoven is afhankelijk van het verschil in afstand die de röntgenstralen hebben afgelegd wanneer ze door verschillende lagen zijn verstrooid. Als deze afstand overeenkomt met de golflengte van het de röntgenstralen (of een meervoud ervan), dan zijn de verstrooide golven in fase (Figuur 7B links). Hierdoor wordt de intensiteit van de röntgenstralen versterkt. Het kan ook voorkomen dat de golven uit fase zijn (Figuur 7B rechts), waardoor ze elkaar uitdoven en er geen signaal meetbaar is.

Het verschil in afgelegde afstand is afhankelijk van de afstand tussen de atoomlagen (Figuur 7C) en ook van de hoek waaronder de röntgenstralen op atoomlagen terecht komen. Door het verstrooiingspatroon als functie van de hoek te meten, kan de afstand tussen de atoomlagen bepaald worden en daarmee de kristalstructuur. De nanodeeltjes kunnen in de oplossing vrij rond bewegen, dus een verstrooiingsmeting bevat informatie over alle verschillende afstanden tussen lagen van atomen. Een voorbeeld van zo'n verstrooiingspatroon wordt weergeven in Figuur 7D in oranje. De scherpe piek worden veroorzaakt door de röntgenstraling die in fase is na verstrooiing. De pieken zijn voorzien met getallen die aangeven door welke atomenlagen (met bijbehorende afstanden tussen atomenlagen) ze veroorzaakt worden. Een voorbeeld hiervan is gegeven in Figuur 7C. In dit figuur worden twee verschillende atoomlagen met andere afstanden weergegeven in blauw en oranje. Omdat het in het voorbeeld om een tweedimensionale structuur gaat worden de vlakken benoemd met twee cijfers in plaats van drie.

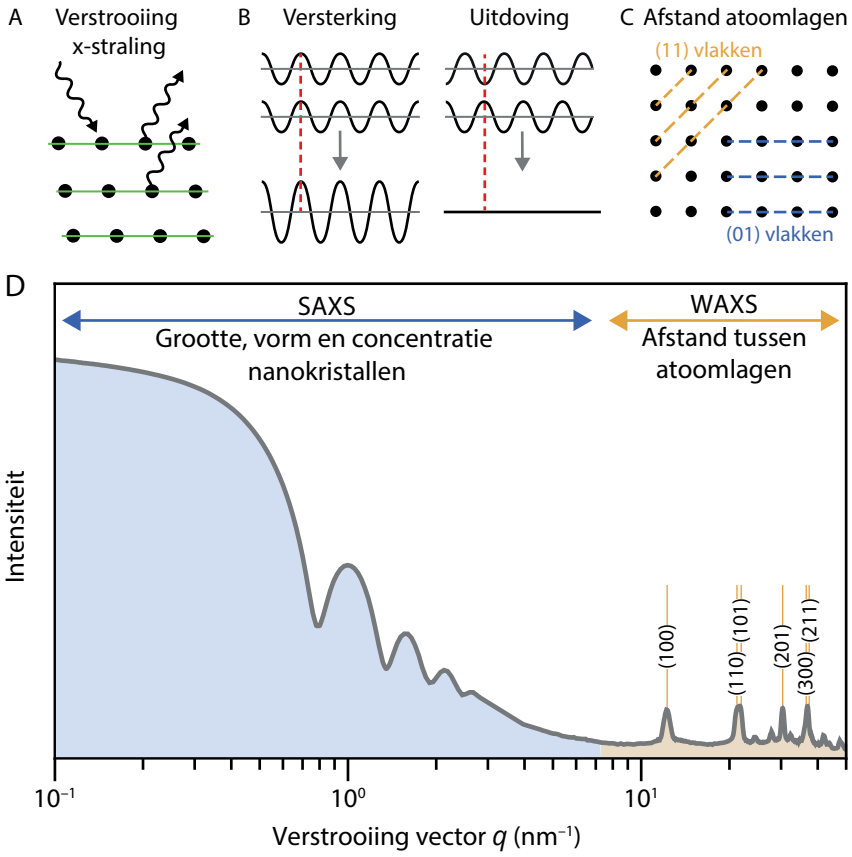

Figuur 7 (A) röntgenstraling wordt verstrooid door verschillende atomenlagen in een kristalstructuur. **(B)** Afhankelijk van het faseverschil tussen de verstrooide röntgenstraling wordt het signaal versterkt (in fase) of uitgedoofd (uit fase). Of het signaal versterkt of uitdooft, is afhankelijk van de afstand tussen de atoomvlakken **(C)**. Deze vlakken worden benoemd met gebruik van getallen (bijvoorbeeld (11) en (01) vlakken) om ze te onderscheiden. **(D)** Het versterken en uitdoven van het signaal zorgt voor een verstrooiingspatroon afhankelijk van de hoek. Het verstrooiingspatroon heeft twee gebieden. Het WAXS-gebied is de verstrooiing onder een grote hoek en geeft informatie over kleine afstanden in de ruimte: afstanden tussen de atomen. Het SAXS-gebied geeft juist informatie over grote afstanden in de ruimte: de grootte, vorm en concentratie van de nanokristallen.

De hoekafhankelijke intensiteit van verstrooide röntgenstralen geeft niet alleen informatie over de kristalstructuur, maar ook helpt het gehele nanodeeltjes te 'zien' in oplossing. Dit komt doordat de elektronendichtheid van de nanodeeltjes veel hoger is dan het oplosmiddel (organische moleculen). Afhankelijk van de vorm, ordening en grootte van de nanodeeltjes worden de röntgenstralen verstrooid met een specifiek patroon. Deze verstrooiing gebeurt onder een veel kleinere hoek dan de verstrooiing door de ordening van de atomen. De techniek waarmee we de nanodeeltjes kunnen meten wordt Small-Angle X-ray Scattering (SAXS, verstrooiing röntgenstralen onder een kleine hoek) genoemd. De kristalstructuur wordt bepaald met

Wide-Angle X-ray scattering (WAXS, verstrooiing röntgenstralen onder grote hoek). Het eendimensionale SAXS-patroon wordt weergeven in blauw in Figuur 7D en het WAXS-patroon, waar al eerder naar verwezen werd, wordt weergeven in oranje. De intensiteit is hier, zoals gebruikelijk, uitgezet tegen de verstrooiingsvector q in plaats van de verstrooiingshoek. Deze twee zijn aan elkaar gerelateerd. Een grotere waarde voor q betekent een grotere verstrooiingshoek en geeft juist informatie over kleine afstanden in de ruimte. Bij grote waarden voor q kijken we dus naar de afstanden tussen de atomen en bij kleine waarden voor q naar de afmetingen van de nanokristallen.

Verstrooiing van röntgenstralen is een zeer krachtige techniek om de kristalstructuur, grootte, concentratie en vorm van de nanodeeltjes te bepalen, maar de analyse is aanzienlijk lastiger dan van bijvoorbeeld absorptiemetingen. In hoofdstuk 4 en 5 worden deze technieken gebruikt om het reactiemechanisme voor de vorming van CdSe NPLs en $NaYF_4$:Yb^{3+},Er^{3+} nanodeeltjes te ontrafelen. Dit wordt gedaan door data zoals in Figuur 7D te vergelijken met wiskundige modellen die de verstrooiingspatronen voor een bepaalde nanodeeltjes vorm en grootte beschrijven. Hiermee kunnen we de vorm bepalen van de deeltjes die aanwezig zijn tijdens de reactie en krijgen we ook informatie over de grootte en concentratie. In sommige gevallen gaan de nanodeeltjes zich ook in oplossing ordenen, zoals ook te zien was op het TEM-plaatje in Figuur 1A. De NPLs vormen geordende systemen en doen dat ook tijdens de synthese. De afstand tussen de nanokristallen kan dan ook uit de gemeten data worden gehaald.

Wat is er onderzocht in dit proefschrift?

De voorgaande paragrafen hebben al een idee gegeven van de onderzochte vraagstukken in dit proefschrift. Ten eerste is er gekeken naar de kleurzuiverheid van het uitgezonden licht van verschillende halfgeleider nanodeeltjes en hoe deze afhangt van de temperatuur. Daarnaast is onderzocht wat het groeimechanisme is van CdSe NPLs en hexagonale $NaYF_4$ nanodeeltjes. Hieronder wordt een samenvatting gegeven van deze hoofdstukken met de belangrijkste bevindingen.

Verbreding van emissie spectra van QDs en NPLs

In hoofdstuk 3 wordt de spectrale verbreding van de emissie spectra voor CdSe NPLs en QDs besproken. NPLs hebben bij kamertemperatuur een veel smaller emissie spectrum dan QDs. Dit komt doordat er altijd variatie is in de grootte van de nanodeeltjes als ze gesynthetiseerd worden. Door het quantum confinement effect hebben deze deeltjes dus allemaal een net iets andere absorptie en emissie maximum, waardoor de spectra van een verzameling aan deeltjes verbreed worden. Deze vorm van verbreding wordt inhomogene verbreding genoemd. Voor NPLs is er alleen quantum confinement in een enkele dimensie, de dikte, omdat de andere twee dimensies te groot zijn voor confinement. Doordat de dikte van de NPLs heel goed gedefinieerd aantal monolagen is, is er voor NPLs geen variatie in het absorptie of emissie maximum tussen verschillende NPLs met dezelfde dikte. Er is voor NPLs daardoor nauwelijks inhomogene verbreding.

Om de nanodeeltjes toe te kunnen passen in bijvoorbeeld lampen of beeldschermen, wordt er een laagje van een ander materiaal om de QDs of NPLs heen gegroeid om het oppervlak te passiveren. Hiervoor wordt vaak zink- of cadmiumsulfide gebruikt. Een schil van dit materiaal om de nanodeeltjes heen verlaagt de kans dat geabsorbeerd licht wordt omgezet in warmte door defecten aan het oppervlak. Echter, als we een schil CdS om de CdSe NPLs synthetiseren

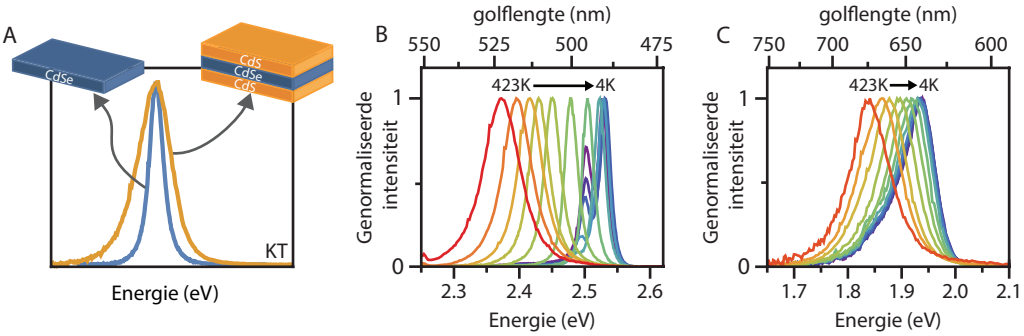

Figuur 8 (A) Emissiespectra van NPLs vertonen smallere pieken dan de spectra van kern-schil NPLs bij kamertemperatuur (KT). De oorzaak hiervan is onderzocht door de verbreding van de spectra te meten als functie van de temperatuur. Een selectie van de resultaten is weergegeven in **B** (NPLs) en **C** (kern-schil NPLs). De spectra zijn gemeten over een groot bereik aan temperaturen van 4 tot 423 kelvin (–269 tot 150°C). De spectra worden breder en de pieken verschuiven naar lagere energie (langere golflentes) als de temperatuur hoger wordt. De verschuiving is sterker voor de NPLs dan voor de kern-schil NPLs.

dan gaat de karakteristieke smalbandige emissie van de NPLs verloren. Dit wordt weergeven in Figuur 8A. In dit figuur zijn de emissie spectra van CdSe NPLs (blauw) en CdSe-CdS kern-schil NPLs (oranje) weergeven en is duidelijk te zien dat het emissiespectrum van de kern-schil deeltjes bij kamertemperatuur (KT) veel breder is.

In de literatuur worden hier verschillende oorzaken voor gegeven. Ten eerste dat er variatie is in dikte van de beschermende schil en/of dat de atomen niet netjes geordend zijn op het grensvlak tussen CdSe en CdS. Dit zijn beide vormen van inhomogene verbreding.[7] Een andere verklaring is dat de kern-schil NPLs een sterkere interactie hebben met de trillingen (vibraties) van het kristal.[8] Een trilling van de atomen in een vaste stof wordt een fonon genoemd. Een geëxciteerd elektron of een exciton (quasi deeltje bestaande uit een elektron en gat) kan interactie hebben met een fonon. Dit zorgt voor verbreding van het spectrum. Bij hoge temperaturen zijn er meer trillingen en zal er dus meer exciton-fonon koppeling plaatsvinden. Daardoor worden de spectra meer verbreed bij hogere temperaturen. Deze vorm van verbreding wordt homogene verbreding genoemd. Hoe sterk de temperatuurafhankelijkheid is, is afhankelijk van het materiaal. Een verklaring voor de verbreding na het groeien van de CdS schil is dat de exciton-fonon koppeling in NPLs met een CdS schil sterker is dan in NPLs zonder schil.

Er zijn dus verschillende verklaringen voor de verbreding. Het onderzoek waarop deze uitspraken zijn gebaseerd betreft vooral analyse van spectra bij lage temperaturen en de sterkte van de koppeling is berekend met een empirisch model. In hoofdstuk 3 is het effect van de temperatuur over een groot temperatuur bereik gemeten van 4 tot 423 K (kelvin) wat overeenkomt met –269 tot 150 °C. We hebben vooral ook naar de verbreding gekeken bij hoge temperatuur, omdat de omgevingstemperatuur in een lamp of beeldscherm flink kan oplopen. Door het grote bereik krijgen we goed inzicht op de bijdrage van homogene verbreding voor de verschillende stoffen. We hebben ook bij 4 K gemeten, omdat het materiaal dan amper trilt. Er zijn weinig fononen om mee te koppelen. Bij deze hele lage temperatuur kunnen we bepalen wat de inhomogene verbreding is voor de verschillende nanodeeltjes.

De resultaten laten zien dat de exciton-fonon koppeling in QDs en NPLs met of zonder schil vergelijkbaar is. Alleen voor hele kleine QDs zonder schil is er een opvallend sterkere koppeling met fononen. De lage temperatuurmetingen laten ook zien dat de inhomogene verbreding voor de kern-schil NPLs groter is dan voor de NPLs zonder schil. De verbreding wordt dus veroorzaakt door dikte variaties in de schil(dikte) of variatie in de ordening van de atomen op het grensvlak tussen CdS en CdSe. Dit kan verholpen worden met andere synthesemethoden. Inmiddels is het onderzoekers ook gelukt om kern-schil NPLs te maken met een betere schil en smallerbandige emissie spectra.[9]

In hoofdstuk 3 worden de eigenschappen van de QDs en NPLs ook vergeleken met materialen die al gebruikt worden in ledlampen en beeldschermen. De emissie van QDs en vooral NPLs is kleurzuiverder dan voor de conventionele materialen, zoals te zien was in Figuur 3B. Dit betekent dat we beeldschermen kunnen maken met een betere kleurweergave, maar vooral ook efficiëntere LEDs en beeldschermen die geen licht uitzenden waar ons oog niet gevoelig voor is. Bij het vergelijken van de nanodeeltjes met de conventionele materialen komen ook nadelen naar voren. Zo zijn de nanodeeltjes minder stabiel bij hoge temperatuur. Hiermee moet dus rekening gehouden worden bij het maken van LEDs en beeldschermen. Ook naar dit probleem wordt op het moment onderzoek gedaan met hoopgevende resultaten.[10]

Een tweede nadeel is dat de kleur van het uitgezonden licht verandert als de temperatuur verandert. Dit is te zien in Figuur 8B en 8C. De spectra verschuiven naar een lagere energie (langere golflengte) als de temperatuur verhoogd wordt. Het effect is het sterkste voor NPLs zonder schil; het maximum van de piek in Figuur 8B verschuift veel meer dan de piek van de kern-schil NPLs in Figuur 8C. Vergeleken met conventionele LED-fosforen is het verschuiven van de pieken als functie van de temperatuur veel sterker in QDs en NPLs. Het is dus belangrijk dat de omgevingstemperatuur bij het gebruik van NPLs of QDs niet te veel schommelt. Conventionele materialen kunnen echter niet op tegen de kleur puurheid en de continue aanpasbaarheid van de uitgezonden kleur licht van CdSe nanodeeltjes. Er moet bij het gebruik van deze deeltjes wel rekening worden gehouden met de regelgeving omtrent de toxiciteit van deze deeltjes.

Groeimechanisme van CdSe NPLs

CdSe NPLs worden gemaakt door cadmium myristaat en selenium (de precursors) te verhitten naar 240^{0}C in het oplosmiddel 1-octadecene en tijdens het verhitten cadmium acetaat toe te voegen bij een temperatuur tussen 190 – 220 ^{0}C. Myristaat en acetaat zijn in deze synthese de liganden en zitten op het oppervlak van de nanodeeltjes. Myristaat heeft een lange koolwaterstofketen (zeventien koolstofatomen) en acetaat en zeer korte koolwaterstof keten (twee koolstofatomen). Waarom en hoe de NPLs vormen en waarom het toevoegen van cadmium-acetaat cruciaal is, wordt nog niet goed begrepen. Dat deze deeltjes in twee richtingen groeien en niet in drie (QDs vormen) is onverwacht, omdat de CdSe NPLs een kubische kristalstructuur hebben. Er is dus eigenlijk niets specifiek anders aan de derde groeirichting vergeleken met de twee andere groeirichtingen, wat deze tweedimensionale (anisotrope) groei ten opzichte van driedimensionale (isotrope) groei zou verklaren.

Daarnaast vormen er naast de NPLs ook QDs tijdens de synthese. Dit zorgt er ten eerste voor dat de NPL-opbrengst van een synthese lager is dan gewenst. Bovendien moeten de QDs in een vervolgstap gescheiden worden van de NPLs wat een arbeidsintensieve taak is en op de grote

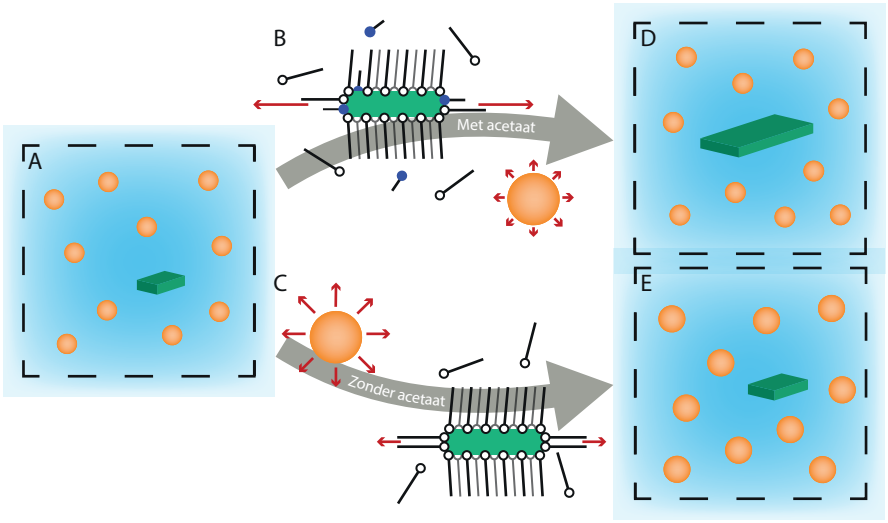

Figuur 9 Groeimechanisme van CdSe NPLs. **(A)** Aan het begin van de synthese worden quantum dots en kleine NPLs (mini-NPLs) gevormd. **(C)** Als geen cadmium acetaat wordt toegevoegd dan groeien de QDs en mini-NPLs met een vergelijkbare snelheid (rode pijlen). **(B)** Met de toevoeging van acetaat, gaan de kleine vlakken van de NPLs snel groeien (lange rode pijl) en ontstaan er grote NPLs en kleine QDs met de toevoeging van cadmium acetaat **(D)** en kleine NPLs en grote QDs zonder de toevoeging van cadmium acetaat **(E)**.

schaal lastig te realiseren. Als we het reactiemechanisme beter begrijpen, dan kan dit inzicht helpen om de synthesemethode aan te passen om de formatie van QDs te voorkomen.

In hoofdstuk 4 bestuderen we de synthesemethode zoals beschreven met en zonder het toevoegen van cadmium acetaat. Hiervoor gebruiken we de opstelling in Figuur 6 om de synthese niet te beïnvloeden. De syntheses zijn *in situ* gevolgd met absorptie spectroscopie en met röntgenverstrooiing (SAXS). Met beide technieken zien we dat er anisotrope groei is, ongeacht of er cadmium acetaat toegevoegd wordt. Zonder acetaat worden er kleine NPLs gevormd (mini-NPLs) en met acetaat zijn de NPLs veel groter. De concentratie van de mini-NPLs in een synthese zonder acetaat is gelijk aan de concentratie NPLs in een synthese met acetaat. Het toevoegen van cadmium acetaat heeft dus geen invloed op de vorming van anisotrope deeltjes maar wel een groot effect op de snelheid van de anisotrope groeit. Zonder toevoeging van cadmium acetaat wordt maar 3% van de CdSe monomeren gebruikt voor de groei van NPLs. Met de toevoeging van acetaat neemt dit percentage toe naar 40% over een gelijke reactietijd van 12 minuten.

De *in situ* metingen laten ook zien dat er heel veel QDs gevormd worden ten opzichte van (mini)-NPLs. Voor ieder NPL zijn er tien QDs aanwezig. Ook op deze ratio heeft het toevoegen van cadmium acetaat geen invloed. Deze verhouding wordt al bepaald voordat cadmium acetaat wordt toegevoegd tijdens de synthese. Deze situatie wordt schematisch weergeven in Figuur 9A. De oranje bollen zijn de QDs en het groene deeltje een mini-NPL.

Figuur 9B en 9C laten de situaties zien wanneer er wel of geen acetaat wordt toegevoegd tijdens het verhitten. De SAXS-metingen laten zien dat zelfs bij hoge temperatuur er een goed geordende laag myristaat liganden zit op de grote vlakken van de mini-NPLs (zie Figuur 9C). Deze laag zorgt ervoor dat aangroei moeilijker is op de grote vlakken. Een verklaring voor de anisotrope groei is dat de myristaat liganden de mini-NPLs stabiliseren en de kans op driedimensionale groei verkleinen. Hogere concentraties aan liganden met een lange koolstofketen lijken volgens andere experimenten ook te zorgen voor meer NPLs, maar bij deze onderzoeken is de concentratie tussen QDs en NPLs niet bepaald.

Er is een model voor de groei van NPLs geopperd in de literatuur.[11] Dit model laat zien dat anisotrope groei van een nanodeeltjes met een kubische kristalstructuur mogelijk is, als het meer energie kost om een NPL een laag dikker te maken, dan om de NPLs te laten groeien in de lengte en breedte. Dit model neemt het effect van liganden niet mee, terwijl onze experimenten laten zien dat deze een belangrijke rol spelen. Van de *in situ* metingen leren we dat acetaat de groei versneld, zowel op grote vlakken van de NPLs als op de kleine vlakken. Zolang het meer energie kost om de NPLs een laag dikker te maken in plaats van te groeien in de andere dimensies, zullen er NPLs vormen. Als er te veel acetaat toegevoegd wordt, dan is er niet langer genoeg verschil in energie tussen driedimensionale groei en tweedimensionale groei en overheerst driedimensionale groei. Zowel acetaat moleculen in het oplosmiddel, als op het oppervlak van de NPLs (Figuur 9B) kunnen de energie voor aangroei verlagen.

Als er niet al te veel acetaat aanwezig is aan het begin van de synthese, dan is de groei op de kleine vlakken van de mini-NPLs veel sneller dan op de grote vlakken en op de QDs. Dit wordt aangegeven met de langere rode pijlen in Figuur 9B. CdSe monomeren worden vooral geconsumeerd door aangroei op de kleine vlakken. Als gevolg hiervan groeien de QDs in Figuur 9B amper (korte rode pijlen), terwijl de QDs wel groeien als er geen acetaat aanwezig is (Figuur 9C). Het gevolg is dat er in een synthese met acetaat grote NPLs vormen en kleine QDs (Figuur 9D), en in een synthese zonder acetaat mini-NPLs vormen en grotere QDs (Figuur 9E). De verhouding tussen de aantallen (mini-)NPLs en QDs blijft onveranderd. Acetaat heeft een belangrijke rol in hoe snel de NPLs groeien, maar niet op de vorming van de NPLs. Deze nieuwe inzichten helpen de synthese aan te passen zodat er in het beginstadium minder QDs vormen, bijvoorbeeld door de concentraties van selenium en cadmium myristaat te variëren.

Groeimechanisme van hexagonale β-fase $NaYF_4$ nanodeeltjes

$NaYF_4$ nanodeeltjes kunnen gesynthetiseerd worden met twee verschillende kristalstructuren, namelijk een kubische of een hexagonale kristalstructuur, die ook wel de α- of β-fase worden genoemd. De α-fase kan bij een lagere temperatuur gevormd worden dan de β-fase. $NaYF_4$ nanodeeltjes met een hexagonale β-fase zijn interessanter, omdat gedoteerde hexagonale deeltjes een hogere upconversion efficiëntie hebben. De β-fase nanodeeltjes worden gemaakt door natrium oleaat, verschillende lanthaniden acetaten, ammonium fluoride (de precursors) te verhitten tot 300 ^{0}C in een mengsel van 1-octadecene (oplosmiddel) en oliezuur (ligand). Tijdens het verhitten worden eerst α-deeltjes gevormd en na langere tijd verhitten bij 300 ^{0}C (meer dan 30 min) worden er uiteindelijk enkele β-deeltjes gevormd. Vervolgens lossen de α-deeltjes volledig op en blijven er alleen β-deeltjes met een zeer kleine variatie in deeltjesgrootte over.

Het is nog niet bekend of de α-deeltjes oplossen en er vervolgens β-deeltjes ontstaan vanuit het opgeloste materiaal, of dat er een verandering van de kristalstructuur plaatsvindt in een

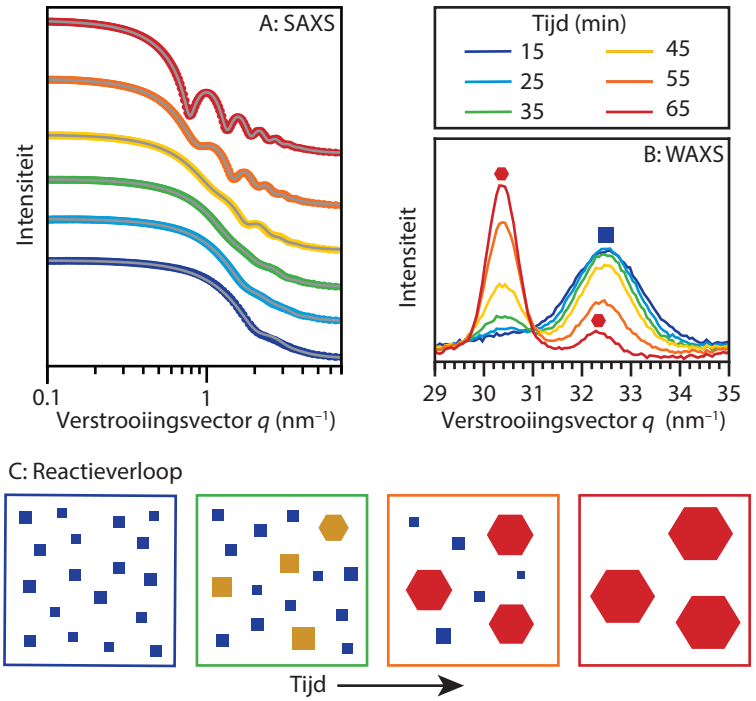

Figuur 10 Röntgenverstrooiing tijdens groei van $NaYF_4$ nanodeeltjes van 15 (blauw) tot 65 (rood) minuten na begin reactie. **(A)** SAXS-metingen met fitcurves van de data om de grootte en concentratie te bepalen. **(B)** WAXS-metingen om de kristalstructuur bepalen. In dit gebied hebben de hexagonale β deeltjes twee pieken (zie rode hexagons) en de kubische α-deeltjes geven één piek (blauwe vierkant). Naarmate de synthese vordert neemt het signaal van de α-deeltjes af en dat van de β-deeltjes toe. **(C)** Schematisch overzicht van het reactieverloop. α-deeltjes worden weergeven met vierkanten en de β-deeltjes met hexagons. Halverwege de reactie zijn er twee verdelingen aan groottes aanwezig (zie groene en oranje vak).

klein aantal α-deeltjes. Ook is het bijzonder dat er maar een kleine variatie is in de grootte van de β-deeltjes aan het einde van de synthese.

Om inzicht te krijgen in het reactiemechanisme hebben we de synthese *in situ* gevolgd in onze zelfgemaakte opstelling. De grootte, vorm en concentratie van de nanodeeltjes hebben we tijdens de reactie bepaald met SAXS (röntgenstraling verstrooiing onder kleine hoek) en de kristalstructuur met WAXS (verstrooiing onder grote hoek). In Figuur 10, staan een aantal verstrooiingspatronen die we gemeten hebben tijdens de synthese. Een kwalitatieve analyse laat een smalle verdeling aan groottes aan het einde van de synthese zien; de minima zijn namelijk veel duidelijker te zien in het rode patroon (einde synthese) dan in het blauwe patroon (begin synthese). In de WAXS-patronen zien we de pieken van de kubische α-deeltjes (blauwe kubus) afnemen en van de hexagonale β-deeltjes (rode hexagon) toenemen (Figuur 10B). Daarmee kunnen we de verandering van kristalstructuur over tijd monitoren.

Als we de SAXS-patronen analyseren zien we in eerste instantie veel α-deeltjes met een gemiddelde grootte van 2 nm en een grote variatie in diameter (Figuur 10C, blauw). Vervolgens

observeren we met SAXS dat er twee verdelingen aan groottes ontstaan tijdens de synthese, schematisch weergeven in Figuur 10C in het groene vierkant met de blauwe en oranje deeltjes (t~35 min). De WAXS-metingen laten echter zien dat dit niet veroorzaakt wordt door het ontstaan van β-deeltjes. Zoals Figuur 10C weergeeft, zijn er zowel grotere kubisch deeltjes als hexagonale deeltjes. De verandering van kristalstructuur vindt vooral plaats in een later stadium van de synthese (Figuur 10C, oranje), waarna de overige α-deeltjes oplossen (Figuur 10C, rood) en β-deeltjes met een diameter van 12 nm overblijven. De synthese verloopt dus anders dan de tot nu toe voorgestelde mechanismen.[12, 13] Een subset van de deeltjes lijkt sneller te groeien dan andere deeltjes.

Met simulaties hebben we laten zien dat we de waargenomen dubbele verdeling aan groottes kunnen krijgen met een grote spreiding aan groei- en oplossnelheden voor verschillende nanodeeltjes. Deze omstandigheden zorgen ervoor dat de allersnelst groeiende deeltjes groeien ten koste van de andere deeltjes. De gemiddeld snelgroeiende/ oplossende deeltjes verdwijnen snel omdat ze oplossen en de sneller groeiende deeltjes het materiaal opnemen. De langzaam groeiende/oplossende deeltjes blijven wel langer aanwezig, omdat ze trager oplossen. Deze deeltjes zijn wel veel kleiner dan de snelgroeiende deeltjes, wat zorgt voor een dubbele verdeling in de grootte.

Onze metingen laten zien dat niet de overgang van de α- naar β-fase verantwoordelijk is voor het oplossen van een gedeelte van de nanodeeltjes en het aangroeien van andere nanodeeltjes, maar een distributie in oplos- en aangroeisnelheden. In een later stadium vindt de overgang naar de stabielere β-fase plaats en verdere aangroei van deze deeltjes en volledig oplossen van de minder stabiele α-fase resulteert in een monodisperse verdeling van β-fase $NaYF_4$ nanodeeltjes. De metingen laten niet zien wat de achterliggende reden is voor de verdeling aan groei/oplossnelheden. Een mogelijkheid is een verschil in soorten atomen aan het oppervlak van een deeltje. Dit kan invloed hebben op de bedekking met liganden aan het oppervlak en de groei- en oplossnelheid beïnvloed, al is dat bij hoge temperatuur een minder aannemelijk. Een andere mogelijkheid is de verhouding tussen de atomen in een nanodeeltjes. Het is bekend dat de Na/Y verhouding het verloop en uitkomst van de synthese sterk beïnvloedt. Deze resultaten sluiten mooi aan op onze metingen; de variatie in de Na/Y ratio tussen nanodeeltjes kan aangroei/oplossnelheden beïnvloeden. Het zou zeer interessant zijn om syntheses met verschillende Na/Y verhoudingen te onderzoeken met de *in situ* opstelling.

Tot slot

De samenvattingen van de experimentele hoofdstukken laten zien dat onderzoek nooit helemaal klaar is. Naast het oplossen van belangrijke problemen ontstaan er vaak weer nieuwe vragen of uitdagingen om de materialen in applicaties te kunnen gebruiken. Het onderzoek heeft ons nieuwe inzichten gegeven die ook door andere onderzoekers gebruikt kunnen worden. Ik hoop dat deze samenvatting voor de lezer zonder achtergrond in nanomaterialen meer inzicht gegeven heeft in het onderzoek dat verricht is, de nieuwe kennis die dit heeft opgeleverd en de theoretische achtergrond erachter.

Referenties

1. Liu, J.; Wang, S.; Kravchyk, K.; Ibáñez, M.; Krumeich, F.; Widmer, R.; Nasiou, D.; Meyns, M.; Llorca, J.; Arbiol, J.; Kovalenko, M. V.; Cabot, A., SnP nanocrystals as anode materials for Na-ion batteries. *Journal of Materials Chemistry A* **2018**, *6* (23), 10958-10966.
2. Moraitis, P.; Schropp, R. E. I.; van Sark, W. G. J. H. M., Nanoparticles for Luminescent Solar Concentrators - A review. *Optical Materials* **2018**, *84*, 636-645.
3. Wahajuddin; Arora, Superparamagnetic iron oxide nanoparticles: magnetic nanoplatforms as drug carriers. *International Journal of Nanomedicine* **2012**, 3445.
4. Rabouw, F. T.; De Mello Donega, C., Excited-State Dynamics in Colloidal Semiconductor Nanocrystals. *Topics in Current Chemistry* **2016**, 374 (5).
5. Vos, J., Colorimetric and Photometric Properties of a 2 Degree Fundamental Observer. *Color Research & Application* **2007**, *3*, 125-128.
6. Samsung Quantum dot, why QD display? https://www.samsungdisplay.com/eng/tech/quantum-dot.jsp (accessed 16 July 2022).
7. Tessier, M. D.; Javaux, C.; Maksimovic, I.; Loriette, V.; Dubertret, B., Spectroscopy of Single CdSe Nanoplatelets. *ACS Nano* **2012**, *6* (8), 6751-6758.
8. Achtstein, A. W.; Marquardt, O.; Scott, R.; Ibrahim, M.; Riedl, T.; Prudnikau, A. V.; Antanovich, A.; Owschimikow, N.; Lindner, J. K. N.; Artemyev, M.; Woggon, U., Impact of Shell Growth on Recombination Dynamics and Exciton–Phonon Interaction in CdSe–CdS Core–Shell Nanoplatelets. *ACS Nano* **2018**, *12* (9), 9476-9483.
9. Rossinelli, A. A.; Riedinger, A.; Marques-Gallego, P.; Knusel, P. N.; Antolinez, F. V.; Norris, D. J., High-temperature growth of thick-shell CdSe/CdS core/shell nanoplatelets. *Chem Commun (Camb)* **2017**, *53* (71), 9938-9941.
10. Estrada, D.; Shimizu, K.; Bohmer, M.; Gangwal, S.; Diederich, T.; Grabowski, S.; Tashjian, G.; Chamberlin, D.; Shchekin, O. B.; Bhardwaj, J., 32-1: On-chip Red Quantum Dots in White LEDs for General Illumination. *SID Symposium Digest of Technical Papers* **2018**, *49* (1), 405-408.
11. Riedinger, A.; Ott, F. D.; Mule, A.; Mazzotti, S.; Knüsel, P. N.; Stephan; Prins, F.; Erwin, S. C.; Norris, D. J., An intrinsic growth instability in isotropic materials leads to quasi-two-dimensional nanoplatelets. *Nature Materials* **2017**, *16* (7), 743-748.
12. May, P. B.; Suter, J. D.; May, P. S.; Berry, M. T., The Dynamics of Nanoparticle Growth and Phase Change During Synthesis of β-NaYF4. *The Journal of Physical Chemistry C* **2016**, *120* (17), 9482-9489.
13. Voss, B.; Haase, M., Intrinsic Focusing of the Particle Size Distribution in Colloids Containing Nanocrystals of Two Different Crystal Phases. *ACS Nano* **2013**, *7* (12), 11242-11254.

Acknowledgements / Dankwoord

Eindelijk is het moment toch echt hier, het einde van mijn promotietraject en het moment dat ik iedereen kan bedanken voor de zeer gewaardeerde wetenschappelijke en niet-wetenschappelijke ondersteuning. Zonder jullie had dit proces niet mogelijk geweest of had ik heel veel leuke en mooie momenten moeten missen.

There are many colleagues at CMI I would like to thank for showing interest in my project, offering help, and creating a pleasant environment to work in. I enjoyed the activities we did together and all the snacks and sweets from your home countries. Writing down all your names feels less personal, so if you read this and I did not thank you personally below, I would still like to thank you for a great time!

De eerste die ik persoonlijk wil bedanken is mijn promotor **Andries**. Het ging allemaal minder soepel dan gehoopt, o.a. met het eerste PhD-project dat na enkele maanden helaas moest worden beëindigd, maar het is uiteindelijk toch goed gekomen met het tweede PhD-project. Bedankt voor je input tijdens mijn promotietijd en de vrijheid om andere weg in te slaan toen bleek dat de opstelling voor het hoofdproject te lang ging duren. Ook heb ik met heel veel plezier spectroscopie en vaste stof werkcolleges geven. Daarnaast wil ik je bedanken voor het creëren van een ontspannen sfeer in de groep, door activiteiten en borrels in de groep te stimuleren, en je humoristische toevoegingen en zelfspot in o.a. de CMI-appgroep. Voor mijn huidige baan is het ook zeer nuttig dat ik een aantal jaar heb kunnen meekijken met iemand die zeer gewaardeerd wordt onder studenten voor het goede onderwijs!

Ook wil ik graag mijn tweede promotor **Daniel** bedanken voor zijn bijdragen aan mijn promotie. Ik heb je kritisch blik altijd gewaardeerd. We hebben eerst vooral meetings gehad toen ik nog bezig was aan de looddeeltjes. Ik vond het prettig dat je niet zomaar overtuigd was, wat ervoor zorgde dat mijn plannen na de meetings beter gedefinieerd waren. Naast je kritische blik, kun je ook heel enthousiast zijn over ideeën en resultaten, ook dit heb ik zeer gewaardeerd. Ik kon de nanoplatelets van mijn masterthesis klaarblijkelijk toch niet loslaten. Bedankt voor je bijdrage aan het hoofdstuk over de groei van deze deeltjes.

Daarnaast wil ik natuurlijk ook graag mijn paranimfen **Tim** en **Maryam** bedanken, omdat jullie mijn paranimfen willen zijn en veel belangrijker voor de leuke tijd die ik met jullie heb gehad tijdens mijn PhD. **Maryam**, I knew very quickly that we would get along, and I am delighted that we became great friends. I swear it is not a case of Stockholm syndrome! It says enough that I had a great time during the four hours at a police station in Barcelona. This statement is simply better without any additional context. I always enjoyed that we would help each other in the lab and could discuss how things were going. I'm also grateful for your words of encouragement during the final stages of writing during the weekends next to a job, which was not easy. Also, thanks for being my personal apartment and job hunter; yes, I should pay you ;)

Tim, wat een avontuur was dit! Ik ben erg blij dat we samen hele succesvolle beamtrips hebben volbracht. Veel voorbereiding, wat in de laatste week voor de NaYF4 trip ook nog leidde tot labwerk tot 23.15h, en heel veel data-analyse achteraf, maar het is allemaal goed gekomen. Ik heb zeer genoten van onze samenwerking, we waren tijdens de beamtrips en op het lab een goede aanvulling op elkaar. Beiden willen we iets moois bereiken, waarvan we overtuigd zijn dat we nette experimenten hebben gedaan en een goede data-analyse. Dit kostte helaas wel veel tijd …, maar uiteindelijk zijn we beiden bijna bij de eindstreep en kunnen we weer leuke dingen doen in

plaats van onze resultaten bespreken. Succes met het afronden van de laatste dingen en ik hoop nog veel spelletjes te spelen en thee te drinken met jou en **Ariëtte**.

Tim and I couldn't have done the beamtrip experiments by ourselves. We could stay awake for many hours, but not days. Therefore, I would really like to thank **Federico**, **Bas**, **Maaike**, **Freddy**, **Thomas**, and **Stijn** for their help. Your enthusiasm and input made the beamtrips extra fun and successful! **Maaike** wil ik nog extra bedanken voor het opofferen van een week om te helpen met voorbereidende experimenten voor de NPLs. Ook jij succes met het afronden van je thesis. **Freddy**, bedankt voor je hulp bij beide projecten. Ik vond het erg prettig dat je kritisch keek naar het NPL-manuscript en SI zonder dat het direct je verantwoordelijkheid was en ook heel erg bedankt voor je betrokkenheid en simulatie berekeningen voor het $NaYF_4$ project.

I would like to thank **Celso** and **Andrei** for their help with the synchrotron proposals. It was an essential step in making sure we could do these experiments. Celso, I have always been very impressed with all your knowledge of NC synthesis, and I'm thankful for all the fruitful discussions that Tim and I had with you around this topic. Andrei, thanks for joining the ESRF X-ray experiments and ensuring I did not miss the progression of the lunar eclipse when I was in the lab and not in the hutch. The beamline scientists at Soleil (**Javier**) and Diamond (**Andy** and **Nick**) deserve special thanks for making sure that our experiments (which were not easy) could be done.

Ik heb ook met veel plezier een aantal studenten mogen begeleiden. **Matt** en **Daphne** bedankt voor jullie urenlange koude metingen op de quantum dots en nanoplatelets. Het waren lange meetdagen, maar ik moest, desondanks, moeite doen om jullie naar huis te krijgen. Bedankt voor jullie bijdrage aan hoofdstuk 3! **Floor** en **Nicolette**, jullie bedankt voor de ICP-metingen en in situ absorptie metingen in hoofdstuk 4. Ik vond het heel fijn dat jullie zo precies te werk gingen, wat zeker nodig was bij dit project. **Nicolette**, ik vond het ook heel fijn dat je bij mij een masterthesis wilde doen. Ik kon je hulp goed gebruiken en je bent echt expert geworden op de in situ absorptie metingen. Bovendien, was het erg leuk je erbij te hebben in het 'zonnetjes team' tijdens de scattering metingen bij Soleil. **Saar** en **Dirk Floris**, bedankt voor jullie experimenten op de looddeeltjes. Helaas liepen deze projecten, ondanks jullie inzet, niet uit op iets waar ik verder mee kon, maar dat kan in de wetenschap ook gebeuren. Jullie allemaal bedankt voor jullie inzet en werk, en excuses als er een korte zenuwinzinking was na het ontvangen van het commentaar op jullie thesis. Vooral in de periode dat we elkaar niet face to face konden zien, had ik misschien niet goed genoeg benadrukt dat het er goed uit ziet en dat ik er vooral grondig naar gekeken had. Veel succes met jullie eigen promotieonderzoek of baan!

Verder wil ik **Hans** en **Chris** nadrukkelijk bedankt voor alle hulp en uitleg bij de TEM en Hans ook voor het helpen bij de metingen op de $NaYF_4$ nanodeeltjes. Dit is een zeer nuttige toevoeging geweest aan ons manuscript. Ook bij CMI wil ook graag alle (ondersteunende) stafleden bedanken. **Peter**, zonder jou zou het echt een drama zijn op het lab. Fijn dat je overal zo snel achteraanging als er iets kapot was of besteld moest worden. Ook dank aan **Hans Ligthart**, je was ook zeer vakkundig, helaas ging je al snel met pensioen toen ik begon met mijn PhD. **Linda** en **Silvia**, het was erg prettig toen we eindelijk een secretariaat hadden en we bij jullie terecht konden. Silvia, ook erg bedankt bij de hulp om mijn uu-account weer terug te krijgen, nadat er per ongeluk een nieuw account zonder mijn weten was aangemaakt. **Stephan**, bedankt voor alle computer gerelateerde zaken en alles te hebben liggen om data van oude computers af te halen. **Ingmar**, ook al hadden we qua onderzoek weinig met elkaar te maken, vond ik je

interesse bij D-group meetings erg prettig en vond ik het ook altijd interessant om te horen wat voor fancy metingen er in de kelder waren gedaan.

Met veel plezier heb ik anderen geholpen met hun projecten. **Joep**, ik vond het fijn dat ik je kon helpen met een aantal QY-metingen op je looddeeltjes en zo een bijdrage kon leveren aan jouw werk. Ook was ik altijd onder de indruk over je kennis over je onderwerpen en je bijdrage aan het attachment team. Also, thanks to all the other people that were part of **team attachment**. Although, in the end, I did not continue with this topic, I enjoyed discussing each other's results and teaching each other about a subtopic of our choice. **Maaike**, **Federico**, and **Quinten**, thanks for the nice time at DESY and the ESRF during your beam trips. **Christa**, het was soms veel werk, maar ik vond het leuk om samen met jou verantwoordelijk te zijn voor ICP-metingen en het onderhoud dat erbij kwam kijken. Later kregen we gelukkig ook hulp van **Bas** en **Kelly**. **Mark** en **Stijn**, bedankt voor de hulp en samenwerking met de correlatie metingen, uiteindelijk was er niet genoeg tijd om het af te maken en heb ik toch een vermoeden dat het universum niet wil dat ik metingen doe met de fancy IR-detector. Jammer, want het waren metingen die mij erg interesseerden. **Aniket** and **Sergio**, the data analysis on your magic-size clusters was challenging but very interesting. It was nice seeing you both in Boston and thanks for inviting Tim and me to give an online talk at ETH. It was nice to have an opportunity to share our results during covid.

Ook heb ik veel kunnen leren van collega's die aan heel andere systemen werkten. Ik wil **Elleke**, **Tim S**, **Robin** en **Jacobine** bedanken voor het met elkaar uitzoeken en aan elkaar uitleg geven over onderwerpen die ons interesseerden in onze 'groepstherapie' sessies. Het was fijn om ruimte te maken om kennis uit te wisselen tussen mensen die op QDs of lanthaniden werkten. It was very useful to discuss difficulties in terms of NC synthesis during the Colloidal Semiconductor QDs Synthesis meetings later in my PhD. I must confess that I forgot the name and remember it as the synthesis club. Thanks, **Serena**, **Maaike**, **Bas**, **Tim P**, **Elleke** for these meetings. I really enjoyed that we actively tried to help each other, instead of struggling on our own.

Bas, **Carlo**, **Elleke**, **Jaco** en **Jara**, bedankt voor de leuke tijd die ik met jullie heb gehad in OL110. Vooral met Bas, Elleke en Carlo heb ik een behoorlijk tijd het kantoor gedeeld, bedankt voor alle discussies, meningen over posters en presentaties, en leuke gesprekken. Bas en Jara, ik was wel een beetje verdrietig toen ik tijdens een teams gesprek de staat van de plant zag die jaren naast me heeft gestaan ;) Jaco, je was een fijne begeleider tijdens mijn masterproject en heb ook genoten van later je collega te zijn bij CMI. **Christiaan**, **Jesper**, **Jur** en **Naud**, bedankt voor jullie gezelligheid tijdens de borrels!

I also had a great time at conferences and really enjoyed renting a big house when we went with multiple people. We enjoyed many dinners together, held some last-minute presentation practice sessions, or stayed an additional weekend to do some sightseeing together. Thank you, **Kelly**, **Anne**, **Annalisa**, and many of the people I mentioned earlier. I also enjoyed the game nights (obviously), the CMI-themed version of Werewolves, joining pub quizzes with colleagues, and group outings. Furthermore, it was great to watch GoT together during lunch and when the episodes became too long, after work and playing a few cutthroat and backstabbing games of GoT the boardgame (**Federico**, of course I will come after you, after you helped me annihilate another player). Thanks all for the great times!

Ik wil ook graag mijn collega's in Wageningen bedanken voor precies genoeg vragen hoe het er mee voor stond met mijn promotie. Het boekje is nu eindelijk af!

Robin, zoals jezelf al zei, wij gaan way back naar het 26ste bestuur. Ik ben met veel plezier je collega geweest, en bewonder je structuur en inzet voor alles waar je aan werkt! Bedankt voor alle kopjes thee bij Proton, discussies en leuke dingen die we naast werk met collega's en vrienden hebben gedaan. Helaas is een derde paranimf niet mogelijk, maar ik denk dat jij het ook fijn vindt om een keer geen verantwoordelijkheden te hebben ;) Ik hoop dat ik samen met jou en **Marlique** nog vele campaign storytelling spellen zal spelen en nu kunnen we verder met discussiëren over onderwijs i.p.v. onderzoek.

Ook **Paul**, **Gerda**, **Bart** en **Stephan** (het complete 26ste), omzettend veel dank voor jullie vriendschap. Jullie zijn de groep mensen, waarbij ik zeker weet dat ik ga huilen van het lachen. Ik zou onze chaos en totale willekeurigheid voor geen goud willen missen. En dan te bedenken dat we zomaar bij elkaar zijn gezet door anderen, en ooit een jaar lang hebben kunnen functioneren.

Ook wil ik alle andere vrienden bedanken (velen van jullie heb ik eerder al genoemd) voor de afleiding, spelletjes spelen, samen taarten bakken, spontaan organiseren van een Proton reünie weekend, en algehele gezelligheid. Ik heb jullie de afgelopen tijd veel minder gezien dan ik zou willen, bedankt voor het begrip, en ik hoop jullie nu weer veel vaker te zien.

Eef, **Elies**, **Karlijn**, **Jans**, **Juul** en **Rebek**, bedankt voor jullie inmiddels decennialange vriendschap. We hebben allemaal ons eigen leventje, maar doen altijd de moeite om elkaar te zien en te ondersteunen wanneer nodig, wat ik zeer bijzonder vind. Mijn DnD genootjes, **Frans**, **Stijn**, **Joanna** en **Robin**, bedankt voor de tweewekelijkse avondje afleiding, dat had ik echt nodig. Ik hoop dat we nog langer op zeer omslachtige manieren bruggen oversteken, NPCs proberen te overtuigen, en gebouwen proberen binnen te komen (misschien moeten we wel gewoon checken of de deur open is).

Ook **mijn familie**, bedankt voor jullie interesse in mijn onderzoek en aanmoediging. **Mijn nichtjes en neefjes**, ondanks het enorme leeftijdsverschil, kunnen we altijd goed met elkaar opschieten. Jullie zijn echt de beste groep om de mol mee te spelen; er zijn al minstens twee mensen beschuldigd wanneer we nog maar net onze ogen open hebben. Ook een escape room (en ter vervanging voor een tijdje among us) is totale chaos. **Nicole**, ik begrijp nog steeds niet hoe je de code wist toen we in de laatste seconden nog cijferslot tegenkwamen. Ook doet het me goed dat **Julia** nu al naar de spelletjeskast loopt. Fijn dat een van mijn favoriete spelletjes, memory (ondanks onze grote collectie), in een lange leeftijdscategorie valt, haha.

Mijn ouders en **oma** ook bedankt voor jullie interesse en ondersteuning de afgelopen jaren. Mijn broers, **Kees** en **Leendert**, bedankt voor de superleuke trip in Vietnam, de vele telefoongesprekken of (online) spelletjes, en dat jullie, inclusief mijn ouders, altijd voor me klaar staan!

List of publications

This thesis is based on the following:

Luminescence Line Broadening of CdSe Nanoplatelets and Quantum Dots for Application in w-LEDs
Johanna C. van der Bok, Daphne M. Dekker, Matt L. J. Peerlings, Bastiaan B. V. Salzmann, and Andries Meijerink, *J. Phys. Chem. C* **2020**, *124*, 22, 12153–12160.

***In Situ* Optical and X-ray Spectroscopy Reveals Evolution toward Mature CdSe Nanoplatelets by Synergetic Action of Myristate and Acetate Ligands**
Johanna C. van der Bok*, P. Tim Prins*, Federico Montanarella, D. Nicolette Maaskant, Floor A. Brzesowsky, Maaike M. van der Sluijs, Bastiaan B. V. Salzmann, Freddy T. Rabouw, Andrei V. Petukhov, Celso De Mello Donega, Daniel Vanmaekelbergh, and Andries Meijerink, *J. Am. Chem. Soc.* **2022**, *144*, 18, 8096–8105.

The formation of NaYF4:Er3+,Yb3+ nanocrystals studied by in situ x-ray scattering: phase transition and size focussing
P. Tim Prins*, Johanna C. van der Bok*, Thomas P. van Swieten, Stijn O.M. Hinterding, Andy J. Smith, Andrei V. Petukhov, Andries Meijerink, Freddy T. Rabouw, *Angew. Chem. Int. Ed.* **2023**, A*ccepted*.

* Authors contributed equally

Other publications:

Growth and Self-Assembly of CsPbBr3 Nanocrystals in the TOPO/PbBr2 Synthesis as Seen with X-ray Scattering
Federico Montanarella, Quinten A. Akkerman, Dennis Bonatz, Maaike M. van der Sluijs, Johanna C. van der Bok, P. Tim Prins, Marcel Aebli, Alf Mews, Daniel Vanmaekelbergh, and Maksym V. Kovalenko, *Nano Lett.* **2023**, *23*, 2, 667–676

Extended Nucleation and Superfocusing in Colloidal Semiconductor Nanocrystal Synthesis
P. Tim Prins, Federico Montanarella, Kim Dümbgen, Yolanda Justo, Johanna C. van der Bok, Stijn O. M. Hinterding, Jaco J. Geuchies, Jorick Maes, Kim De Nolf, Sander Deelen, Hans Meijer, Thomas Zinn, Andrei V. Petukhov, Freddy T. Rabouw, Celso De Mello Donega, Daniel Vanmaekelbergh, and Zeger Hens, *Nano Lett.* **2021**, *21*, 6, 2487–2496.

Unraveling the Growth Mechanism of Magic-Sized Semiconductor Nanocrystals
Aniket S. Mule, Sergio Mazzotti, Aurelio A. Rossinelli, Marianne Aellen, P. Tim Prins, Johanna C. van der Bok, Simon F. Solari, Yannik M. Glauser, Priyank V. Kumar, Andreas Riedinger, and David J. Norris, *J. Am. Chem. Soc.* **2021**, *143*, 4, 2037–2048.

Hybrid Oleate–Iodide Ligand Shell for Air-Stable PbSe Nanocrystals and Superstructures
J. L. Peters, J. C. van der Bok, J. P. Hofmann, and D. Vanmaekelbergh, *Chem. Mater.* **2019**, *31*, 15, 5808–5815.

Temporary Charge Carrier Separation Dominates the Photoluminescence Decay Dynamics of Colloidal CdSe Nanoplatelets
Freddy T. Rabouw, Johanna C. van der Bok, Piernicola Spinicelli, Benoît Mahler, Michel Nasilowski, Silvia Pedetti, Benoît Dubertret, and Daniel Vanmaekelbergh, *Nano Lett.* **2016**, *16*, 3, 2047–2053.

Femtosecond Cooling of Hot Electrons in CdSe Quantum-Well Platelets
Philipp Sippel, Wiebke Albrecht, Johanna C. van der Bok, Relinde J. A. Van Dijk-Moes, Thomas Hannappel, Rainer Eichberger, and Daniel Vanmaekelbergh, *Nano Lett.* **2015**, *15*, 4, 2409–2416.

Conformal and Atomic Characterization of Ultrathin CdSe Platelets with a Helical Shape
Eline M. Hutter, Eva Bladt, Bart Goris, Francesca Pietra, Johanna C. van der Bok, Mark P. Boneschanscher, Celso de Mello Donegá, Sara Bals, and Daniel Vanmaekelbergh, *Nano Lett.* **2014**, *14*, 11, 6257–6262.

List of presentations

***In Situ* Studies of the Formation Mechanism of Nanoparticles** (oral)
Seminar in the group of Prof. Norris at ETH Zurich, online, March 2020

***In situ* X-ray scattering studies on the formation mechanism of nanoparticles** (poster)
ESRF-DUBBLE user meeting, Brussel, March 2020

Nucleation and growth of CdSe Nanoplatelets studied by *in situ* small angle X-ray scattering (oral)
MRS Fall meeting, Boston, USA, December 2019

Spectal Linebroadening of CdSe Nanoplatelets and Quantum Dots for Light Emitting Devices (oral)
MRS Fall meeting, Boston, USA, December 2019

Spectral LineBroadening of CdSe Nanoplatelets and Quantum Dots (poster)
NanoGe Fall Meeting, Torremolinos, Spain, October 2018.

PbSe QD-molecules: Synthesis of nanocrystal oligomers (poster)
WE-Heraeus-Physics School "Exciting nanostructures: Probing and tuning the electronic properties of confined systems", Physikzentrum Bad Honnef, Germany, July 2017.

About the author

Annelies van der Bok was born in Dirksland, The Netherlands, on the 14th of March 1991. She graduated from the CSG Prins Maurits in 2009 and continued to study Chemistry at Utrecht University, The Netherlands. During her bachelor studies, she was a board member of the study association U.S.S. Proton for a year, where she was responsible for external relations, acquisition, excursions, and other educational and recreational events. After obtaining her BSc degree, she enrolled in the master program Nanomaterials: Chemistry and Physics at Utrecht University. Annelies performed her master thesis research at the Condensed Matter and Interfaces (CMI) group under the supervision of Jaco Geuchies and Daniel Vanmaekelbergh. She studied the synthesis of heterostructures, ion-exchange, and optical properties of cadmium-based nanoplatelets. Afterward, she did a half-year internship at TNO in Eindhoven, where she worked on anti-reflection coating based on cellulose nanocrystals. In 2015, she obtained her MSc degree *cum laude*.

In May 2016, she started as a PhD researcher at CMI under the supervision of Andries Meijerink and Daniel Vanmaekelbergh. The results of this research are published in this thesis and peer-reviewed scientific journals, and presented at international conferences. During her PhD project, Annelies supervised six bachelor and master students and was a teaching assistant for first- and second-year courses on spectroscopy, inorganic and solid state chemistry, and analytical lab skills. Furthermore, she led the practicals for the module Nanomaterials organized by Junior College Utrecht (JCU) for high school students. In 2017, she presented her research to primary school students during the 'KNCV Vuurvliegen' contest organized by C3. From 2016 to 2018, she was secretary of the Debye PhD committee, which organizes social and scientific activities for the PhDs of the Debye Institute of Nanomaterial Science. Since January 2021, she has a shared position as a lecturer at the Biophysics and Organic Chemistry research groups at Wageningen University and Research.